AN EXPERIMENTAL STUDY OF PHYSICAL PROPERTY CHANGES IN CRUSTAL ROCKS UNDERGOING TRIAXIAL DEFORMATION

by

MARK RAYMOND AYLING

A thesis submitted to the University of London
for the degree of Doctor of Philosophy

August 1991

Department of Geological Sciences
University College London

ABSTRACT

A laboratory investigation has been undertaken to examine changes in a number of physical parameters of deforming brittle rocks. The experiments were carried out in a pressure-balanced, gas-medium triaxial cell, which is capable of simulating lower crustal conditions. During sample deformation, contemporaneous measurements were made of differential stress, axial strain, compressional wave velocity (Vp), shear wave velocity (Vs) and received elastic waveforms, which were stored for later analysis. In an alternative operational mode, simultaneous measurements were made of differential stress, axial strain, acoustic emission (AE) statistics and porosity changes through direct pore volumometry. Four different sedimentary rocks have been systematically examined: Darley Dale sandstone, Gosford sandstone, Solenhofen limestone and Tennessee sandstone, at confining pressures up to 200MPa and at ambient temperature.

A number of major improvements have been made to the triaxial deformation system and to the electronic data acquisition and control equipment during this study. Specifically, the commissioning and performance evaluation of a newly-built servo-hydraulic actuator is described. The integration of a more powerful control and data-logging computer with new elastic wave velocity measurement and display equipment is also described. An important aspect of this developmental stage of the study was the enhancement of the acoustic signal transmission/reception system which allowed simultaneous measurements of both Vp and Vs to be made; therefore, transducer theory is considered in detail. Also during the course of this study, a new servo-controlled pore-fluid pressure intensifier and volumometer was commissioned. This device was interfaced with the triaxial cell so that direct measurements of changes in sample porosity could be made during deformation.

Simultaneous compressional and shear wave velocity measurements were carried out on Darley Dale sandstone samples at confining pressures ranging from 30MPa up to 200MPa. Under initial deviatoric loading Vp and Vs increase slightly (1% to 5%) with Vp increasing relatively more than Vs. As dilatancy ensued, Vp and Vs both decrease (generally from 8% to 20%) with Vs decreasing more sharply and proportionately more

than Vp. In general, as the confining pressures were increased, the velocity increases became less and the velocity decreases became more gradual. Similar trends were observed for the Gosford sandstone tested under comparable conditions. These velocity changes are interpreted in terms of a model of microcrack populations closing and opening as a function of stress, strain and time. The recording of both velocities simultaneously has enabled changes in the effective moduli (including the dynamic Young's modulus, and dynamic Poisson's ratio) along with the crack density parameter (ε) to be estimated. The changes in these parameters are discussed for Darley Dale sandstone samples showing both catastrophic brittle deformation and pseudo-ductile deformation. As dilatant cracking occurs the effective Poisson's ratio increases, and this is interpreted as resulting from inelastic radial strains. At the same time the effective Young's modulus decreases, and the vertical crack density parameter (which reflects the cracking aligned in the axis of maximum stress) also increases. Furthermore, for the first time, these measurements have allowed seismic Q values to be determined for a deforming rock sample using the spectral ratio method. The seismic Q values for a Darley Dale sandstone sample at 50MPa confining pressure were found to increase sharply under initial deviatoric loading to approximately twice their initial values, and then to decrease steeply as dilatant crack growth occurred.

Velocity measurements on Solenhofen limestone samples at confining pressures up to 200MPa are also reported. However, in contrast to the results for the sandstones, Vp was found to decrease proportionately more than Vs during ductile deformation. This result is interpreted as showing plastic processes may be occurring in this rock type, at least at elevated confining pressures.

Experiments were also carried out at 50MPa confining pressure on samples of Tennessee sandstone in order to examine the effect of its strong bedding on the mechanical and acoustic properties of the rock when the bedding was orientated parallel and perpendicular to the maximum stress direction. The rock was found to be markedly stronger and failure to be less brittle when the bedding plane is perpendicular to the axis of maximum load.

Results from drained and undrained water saturated tests conducted at 100MPa confining pressure on samples of Darley Dale sandstone and Solenhofen limestone are also described. These results show that the strength of sandstone is reduced markedly by

the presence of interstitial water. Sandstones are weakest in the undrained tests.

Experiments were also carried out in which the pore-fluid pressure was maintained at a constant level by means of the servo-controlled pore-fluid pressure intensifier. Three tests are described in detail for Darley Dale sandstone samples exhibiting catastrophic localised failure, distributed pseudo-ductile deformation, and a failure mode transitional between these two. The strength of the sample showing localised brittle failure is comparable to that seen for dry samples of this rock at equivalent effective confining pressures. However, the stress drop after peak stress is less in the saturated sample. The strengths of the samples showing transitional and pseudo-ductile behaviour are less than would be expected from application of the simple effective stress law. This discrepancy is considered to be the result of incomplete sample drainage causing local pore-fluid gradients which reduce the effective confining pressure. AE waveforms were recorded and stored for the test on the sample exhibiting localised brittle deformation. The amplitude spectra of these waveforms show that after peak stress the amplitude of the waveforms increase by an order of magnitude, and the dominant frequency in the waveforms decreased substantially. These observations are interpreted as reflecting an increase in the crack source dimensions following peak stress. Direct porosity change measurements which were also made during these tests, are brought together with crack density values determined for dry Darley Dale sandstone samples under comparable effective confining pressures to determine, for the first time, the crack aspect ratio of dilatant cracking accumulating during brittle and pseudo-ductile deformation.

The experiments performed during this study have led to further insights into the damage processes involved in brittle deformation and failure of rocks. These insights have enabled a new delineation of the stages of brittle failure to be made for Darley Dale sandstone. It is considered that this delineation can be held as general for many brittle upper-crustal rocks. The linking of far-field acoustic monitoring techniques and the in situ stress field, the evolving state of damage, and the fluid transport properties of rock, is of great importance in many areas of geological interest, including earthquake source processes, oil exploration and exploitation, and nuclear waste disposal.

CONTENTS page

LIST OF FIGURES

LIST OF TABLES

page

ACKNOWLEDGEMENTS

Firstly, I would like to thank my supervisors Drs S.A.F. Murrell and P.G. Meredith for their enthusiasm and encouragement throughout this project. I would especially like to thank them for their efforts in obtaining for me a grant for my third year. Also, P.G.M. showed great patience in correcting faulty grammar in early drafts of this thesis.

I would also like to mention my colleagues in the Rock and Ice Physics Laboratory to whom I am indebted;

Dr. C. Jones who was generous with his time and advice during the early stages of this project

Dr. P. Sammonds who helped with designing maintaining and refurbishing the triaxial cell.

Dr. M.A. Rist for kindly reading my thesis, and for his very useful criticisms.

M.D. Read for continual cups of coffee and long discussions about most things except rock physics.

Mr. J.P. Bowles and N. Hughes for their invaluable technical support. Especially J.P.B. for his knowledge and help in designing pieces of equipment and for his help in repairing others, and N.H. for computing advice.

I would also like to thank the following for their thorough reading of my thesis and for their useful advice: Drs. Meredith, Murrell, Rist, Sammonds, and especially Ms. S. P. McGurk who gave up a week of her holiday to check the grammar.

In the Department of Geological Sciences I would like to thank Prof. M. Audley-Charles for his continuing support of the Rock and Ice Physics Group.

This project was funded for two years by the Natural Environmental Research Council

(NERC) in conjunction with British Petroleum (BP) as part of a Co-operative Award in Sciences of the Environment (CASE). The third year of this project was funded jointly by BP and the Thomas Whitherton-Butts scholarship.

My special thanks go to Susan and Marianne McGurk who provided me with rent-free accommodation during many months of writing up this thesis. I would also like to thank them for their patience and understanding during the days when it looked as if this thesis would never end. I could never begin to repay this debt of kindness.

Above all, my sincerest thanks go to Susan McGurk without whom this thesis would not have been possible, and who suffered the intolerable intrusion of this thesis into her life. I shall be forever grateful for her concern and support during this difficult period.

CHAPTER 1

1.1 INTRODUCTION.

Understanding the brittle deformation of rocks is of fundamental importance in many areas of geological interest, these include oil exploration and exploitation, earthquake source physics, nuclear waste disposal, nappe emplacement, geothermal heat extraction and deep engineering projects amongst others. The macroscopic mechanical response of rocks is controlled by processes that occur at the grain, crystal and atomic scale. Therefore, a clear understanding of the microprocesses involved in rock deformation is essential in understanding many large-scale geological processes. In order to simulate the crustal conditions of confining pressure, temperature, deviatoric stress and pore fluid migration in the laboratory, a triaxial cell is commonly used. Simply, this superimposes a deviatoric stress upon a hydrostatic pressure. The mechanical response of the rock under different stress and environmental conditions can then be readily examined. The main advantage of such an apparatus is that precise control of the environmental conditions during deformation can be maintained. Far-field geophysical interrogation techniques can also be employed during deformation. These enable direct comparisons to be made between changes in rock physical properties (rock strength, elastic response, dilatancy, pore-fluid volume/pressure changes and permeability) and changes seen in the far-field investigation methods (elastic wave velocities, elastic wave attenuation, acoustic emissions, and electrolytic conductivity). Generally, for rocks in situ, far-field investigations provide the only data available (mainly from seismic compressional wave velocity changes) and from this, information can be estimated about the stress regime, density, elastic compliance and the porosity and permeability of the rock at depth.

A very important aim of research in this area is ultimately to be able to determine the fluid transport properties of a rock from its mechanical, physical, acoustic and electrical properties. This would have particular importance to the oil and waste disposal industries, where a great deal of money could be saved if far-field interrogation techniques could yield a better understanding of the fluid storage capacity and permeability of rock at depth.

It is very difficult to extrapolate the results obtained on samples of centimetre

dimensions and deformed at strain rates of the order of $10^{-5}s^{-1}$ to geological situations where deformation can occur over kilometre scales and at strain rates down to $10^{-14}s^{-1}$. However, it is well known that many geological features (including shear faulting) are scale-invariant over many orders of magnitude (Shaw & Gartner, 1986). It may be the case that a simple fractal-type scaling law will be appropriate for comparing laboratory and field data (see Main et al., 1990). This, however, is outside the scope of the present study.

The historical development of triaxial testing can be traced through a series of important technical developments. Adams (1910) carried out the first systematic triaxial tests. The ductile flow of Carrara marble was examined, with different confining pressures being simulated by tightly fitting iron jackets of different thicknesses. Von Karmen (1911) developed an apparatus which incorporated all of the essential features of a modern triaxial cell. A glycerine medium was used to transmit a confining pressure to a sample surrounded by a soft brass jacket. Further developments were made by Griggs (1936), who used a yoked piston arrangement so that the confining pressure remained constant during ram advancement. Heard (1963) first used a low friction ball screw actuator to apply a deviatoric stress, and Carter et al. (1964) describe a solid medium, six piston, true-triaxial cell.

The triaxial cell used in this project is a high pressure/high temperature gas-medium apparatus which has now been in use for over 20 years. It was designed by Dr S.A.F. Murrell and is located in the Rock and Ice Physics Laboratory in the Department of Geological Sciences at U.C.L. The cell can approximate lower crustal pressure and temperature conditions, being capable of attaining 1.4GPa and 1000°C. However, during this study, experiments were performed at room temperature and generally at the lower end of the pressure range of the cell. A cylindrical rock sample 45mm long by 15mm diameter is located between the top and bottom rams in the pressure vessel. A thin-walled copper jacket seals the sample from the gas confining medium. The top ram is of a stepped-balance design so that only a differential stress is required to deform the sample. Sample strain is measured externally using two linear variable differential transducers, with a correction made for elastic response of the ram.

At the start of this project a nominally constant deformation rate was obtained using a simple ball-screw actuator which advanced at a constant displacement rate. During this study, the ball-screw actuator was replaced by a specially designed, highly responsive, servo-hydraulic actuator. The previous controlling computer was also replaced, upgrading the data logging speed and storage capacity. Also a digitising oscilloscope with an integral plotter, and two new counter-timers were interfaced with the existing equipment. Prior to this study, simultaneous measurements of differential stress, axial strain, acoustic emission rate and compressional wave velocity changes were routinely made on a deforming sample (see Jones, 1989; Jones & Murrell, 1990). The capabilities of the equipment have now been enhanced so that, in addition to the previously measured parameters, measurements can also be made simultaneously of the compressional and shear wave velocities, and acoustic waveforms can be captured. Independent pore fluid pressure/volume control has also been introduced. This was achieved by using a newly-built pore-fluid pressure intensifier. For the first time changes in seismic Q has been determined for both the compressional and shear wave arrivals travelling through a triaxially deformed rock sample. The experimental data processing and analysis has been extended to model the changes in crack densities, crack alignment, and crack aspect ratios.

1.2 Background to this project.

It has long been known that the presence of microcracks strongly affects the mechanical and fluid transport qualities of a rock. This has been demonstrated primarily for hydrostatic laboratory experiments including, by amongst others, Brace and Orange (1968) for electrical resistivity, Nur and Simmons (1969a) for compressional and shear wave acoustic studies, Walsh (1981) for hydraulic permeability, and Johnston & Toksoz (1980) for seismic attenuation. However, studies on triaxially deformed samples are fewer and much more restricted in the number of parameters measured at any one time. Lockner et al. (1977), looked at the change in travel times for compressional and shear waves which travelled radially across a deforming rock sample. They also considered the change in amplitude of the first arrival. Hadley (1975a) and Gupta (1973) reported changes in velocity of the compressional and shear waves along the major stress axis for uniaxially deformed Westerly granite and Indiana limestone, respectively.

In this present study, systematic experiments have been performed to measure changes in the compressional and shear wave velocities through deforming rock samples at different confining pressures. Four different sedimentary rocks have been investigated. The results for velocity measurements have been modelled to determine crack density changes, and elastic moduli changes in the samples are also considered. Results from pore volume change experiments have been brought together with crack density parameter changes to model, for the first time, changes in the pore aspect ratios of deforming sandstone samples. Finally, extensive measurement of rock physical parameter changes during brittle deformation has led to a new delineation of regimes of brittle deformation to be proposed. The points at which cracking initiates, cracks coalescence, and the onset of final crack linkage at macroscopic failure are explicitly described.

1.3 Arrangement of this thesis.

In Chapter 2, the experimental evidence for the mechanical behaviour of rocks under different conditions of confining pressure, temperature, pore fluid pressure, and strain rate is briefly reviewed. Theoretical brittle failure models are then considered in detail, as are experimental and theoretical acoustic studies (including acoustic emission analysis, acoustic wave velocity measurements, crack density modelling, and attenuation studies). The general characteristics of brittle rock deformation are then updated and summarised.

Chapter 3 provides an outline of the experimental equipment. Particular emphasis is given to equipment upgrading that was carried out during this study. This includes the complete replacement of the original ball-screw actuator system by a specifically designed servo-hydraulic actuator, and the integration of a new pore fluid pressure intensifier with the triaxial deformation system.

Chapter 4 describes the integration of a more powerful data acquisition and control computer, along with new electronic data acquisition equipment into the existing acoustic measurement system. A crucial part of this study included improving the acoustic signal such that simultaneous compression and shear wave velocity measurements could be made during triaxial deformation. This necessitated a detailed study of transducer theory and application, which is also discussed in this chapter.

Chapter 5 describes the experimental procedures and testing techniques used in this study. The frequency response of the waveform capture system is also discussed. Experimental accuracy and data reduction is briefly discussed. The anisotropic crack density model of Soga et al. (1978), as adapted for the specific velocity measurements made in this study, is discussed in detail. The spectral ratio method for determining seismic Q is also examined.

Chapter 6 introduces the experimental results. It summarises the test conditions and outlines the format of the presentation of the experimental results. All of the experiments performed are tabulated. Twenty-seven experiments are discussed in detail in this thesis, out of a total of 93 performed.

Chapters 7 to 13 describe and discuss the experimental results. Chapters 7 to 10 analyse the mechanical response and elastic wave velocity changes through samples of Darley Dale sandstone, Gosford sandstone, and Solenhofen limestone. Chapter 11 examines velocity anisotropy in samples of Tennessee sandstone. Chapter 12 describes acoustic velocity changes during deformation of water-saturated samples. Chapter 13 describes results from constant pore fluid pressure experiments which made use of the servo-controlled pore fluid pressure intensifier.

Chapter 14 is the discussion and conclusion chapter. In this chapter, crack density changes calculated from acoustic velocity data are brought together for the first time with pore volume changes. As a result, changes in the crack aspect ratio of new dilatant cracks in deforming rock samples can be determined. Also in this chapter a new characterisation of the stages of brittle deformation and failure is proposed. The limitations of the experimental procedure are also discussed.

The results of this thesis when considered in a wider geological context are further discussed. Finally, proposals for future experiments, machine development and processing techniques are given. How this work could be extended with the new large-volume rock deformation and physical property measurement system recently commissioned by the Rock and Ice Physics Group at U.C.L., is also briefly, discussed.

CHAPTER 2

EXPERIMENTAL OBSERVATIONS OF ROCK FAILURE, BRITTLE FAILURE THEORIES, ACOUSTIC STUDIES AND ATTENUATION MECHANISMS.

2:1 Introduction.

The mechanical response of rock is dependent upon factors such as the presence, nature and pressure of pore fluids, ambient temperature, confining pressure, deviatoric stress, and strain rate. The way in which these affect the brittle deformation and failure of rocks is central to understanding the fundamental physical processes involved. The first section of this chapter aims to draw some general conclusions about the mechanical response of rocks from previous experimental studies. This field of study is well documented now, and good reviews can be found in Paterson (1978) and Jaeger & Cook (1979). There are, however, two broad areas of specific interest to this study worthy of further examination in some detail. The first of these is the theory of failure in brittle solids. The second covers the wide range of acoustic studies and modelling, including acoustic emissions studies, acoustic velocity studies (and the corollary of crack density modelling), and attenuation studies. Finally, at the end of this chapter, the generalised characteristics of brittle deformation in rocks, as determined from mechanical and acoustic studies, is given.

Most of the experimental data on rocks under crustal conditions have been obtained using the conventional triaxial test. In such a test all the principal stresses are non-zero and usually compressive. In usual operation a deviatoric stress is superimposed upon a hydrostatic pressure. If the principal stresses are $\sigma1,\sigma2,\sigma3$ with $\sigma1\geq\sigma2\geq\sigma3$, then in the conventional triaxial test the stress system is $\sigma1>\sigma2=\sigma3$; where compression is taken as positive. When all three principal stresses are controlled independently such a test is called a true triaxial or polyaxial test. As is common practice, in this thesis the conventional triaxial test is referred to simply as the triaxial test.

It is useful, at this point, to define what is meant by brittle and ductile failure, since there is commonly much confusion over these definitions. Macroscopically the behaviour of a deforming rock specimen can be described either as brittle, ductile or transitional. Although there is some latitude in the definition of brittle failure, Murrell

(1965) describes brittle failure as occurring when deformation is essentially elastic before failure. There may, however, be regions of anelastic deformation but these should be small when compared to the elastic range. Ductility is similarly defined loosely as the condition under which a rock can sustain significant permanent deformation without catastrophic failure. Heard (1960) defined ductility as the ability to sustain at least 3-5% strain prior to fracture.

2:2 Macroscopic experimental observations of rock deformation.

Many experimental studies have shown that the strength of brittle rocks is highly dependent upon the confining pressure. As the confining pressure increases the brittle strength of rock specimens increase, with the increase being nonlinear and usually concave towards the increasing confining pressure axis (e.g. Byerlee, 1967a). General macroscopic observations have also shown that the manner in which brittle rocks fail is highly dependent on the confining pressure under which the rock is deformed. Increasing confining pressure also suppresses brittle fracture with the rock behaviour progressing through a brittle-ductile transition zone to finally exhibit fully ductile behaviour if a sufficiently high confining pressure is reached. Three broad modes of brittle rock failure have been seen to occur, these are shown schematically in fig. 2:1 and are described below:

a) At zero confining pressure rock specimens fail as a result of unstable tensile crack growth predominately parallel to the stress axis. This is termed slabbing or axial splitting.

b) The application of even a modest confining pressure can suppress this uninhibited crack growth, failure then occurs as a shear fracture or as a pair of conjugate shears. The fracture plane is generally at an angle of 20-30° to the axis of maximum compression. There is some evidence to suggest this angle increases with increasing confining pressure (e.g. Griggs, 1936; Paterson, 1958; Wawersik & Fairhurst, 1970). With increasing confining pressure the fracture plane generally broadens from a distinct fault to become an increasingly wide zone of distributed damage.

c) At very high confining pressure this damage zone broadens into an homogeneous zone of distributed microcracking that encompasses much of the specimen, which then undergoes pseudo-ductile cataclastic flow. In this case, the specimen commonly work

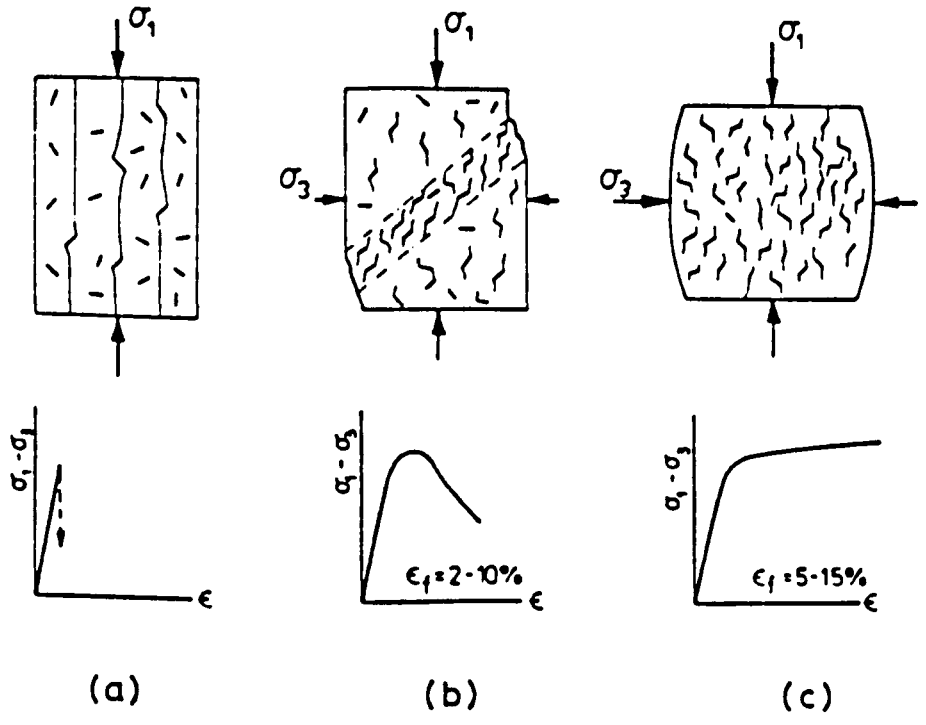

Fig. 2:1 Typical failure modes of brittle materials under axial compression, and a function of confining pressure (such that $\sigma_1>\sigma_2=\sigma_3$). (a) Uniaxial compression ($\sigma_2=\sigma_3=0$) causes failure by slabbing. (b) modest confining pressures lead to failure by a well defined, inclined shear plane. (c) Higher confining pressures lead to distributed homogeneous microcracking. From Ashby & Hallam, 1986.

hardens with substantial dilatancy and barrelling. Deformation is taken up by sliding on a network of microcracks, further strain can lead to individual clasts loosening and rotating.

It is important to note at this point that ductility describes only an ability to undergo a substantial change of shape without fracture and does not take into account the type of mechanism causing it. Cataclastic flow (flow with distributed microcracking) is essentially a brittle mechanism microscopically and is dependent upon friction between sliding surfaces. Cataclastic flow results in a permanent volume increase in the rock. This leads to two diagnostic features for cataclasis: Firstly, it is highly pressure dependent; this results from higher confining pressures increasing the normal force, and thus friction, between grains. Secondly, it is associated with a nonelastic volumetric increase, termed dilatancy. Other mechanisms that cause ductility are plasticity, twinning, cleavage slip, twin plane gliding or diffusional flow, all of which involve little or no volume change. The rock type, ambient pressure and temperature conditions will determine which mechanism is dominant in the ductile phase. Generally, more than one mechanism may be occurring at any one time.

Brittle fracture generally shows little temperature dependence (Paterson, 1978), although complications can arise as the brittle-ductile transition is approached. This complication is caused by the change in relative importance of different deformational mechanisms; notably the increasing importance of plasticity with temperature. There exists, however, the special case of high temperature embrittlement. This occurs when a mineralogic change involving dehydration reactions occurs in response to increasing temperature and results in the release of a fluid phase. The fluid phase then introduces a local pore fluid pressure rise which reduces the effective confining pressure, thus allowing the sample to fail brittly. This mechanism has been observed in rocks containing serpentinite and gypsum (Murrell & Ismail, 1976a; Jones, 1989).

There is a similarly small strain rate dependence of brittle fracture. For example, in uniaxial tests a two orders of magnitude increase in strain rate gives approximately only a 10% increase in fracture stress in limestones and igneous rocks (e.g. Serdengecti & Boozer, 1961; Brace & Martin, 1968).

The influence of pore fluid pressure on rock failure has been investigated using two important experimental techniques. In the first case, the pore fluid pressure is kept constant and the volume of the fluid either entering or expelled from the sample reflects changes in the porosity of the specimen (Murrell, 1963, 1965); this is termed "drained" conditions. Alternatively, the pore fluid volume can be maintained at a constant level, and changes in the pore fluid pressure can be monitored (Heck, 1972); this is termed "undrained" conditions. The mechanical effect of a pressurised pore fluid is usually described in terms of the "effective stress" law. This simply states that each component of principal stress is reduced by an amount equal to the pore pressure and is referred to as "Terzaghi's principle". This has been found generally to be experimentally valid (Murrell, 1965). Mathematically the effective stress can be written as:

$$\sigma_{ij\ effective} = \sigma_{ij} - \alpha p d_{ij} \qquad (2:1)$$

Where p is the pore pressure d_{ij} is the Kroneker delta, σij is the total macroscopic stress tensor and α is a constant. For Terzaghi's simple effective stress law to hold, $\alpha = 1$. However, α can be seen to depart from 1 under certain circumstances. For example, if the rock permeability is low and the internal pore pressure cannot equilibrate throughout the rock, if fluid saturation is incomplete, or if the fluid is chemically active. Consequently Handin et al. (1963) concluded that the strength and ductility of a rock is dependent on the effective stress (i.e. controlled by Terzaghi's principle) only if certain conditions are met. These can be summarised as;

i) the fluid is inert and its only effect on the sample is mechanical,

ii) the permeability is sufficient to allow the pore pressure to remain constant throughout the sample and,

iii) the pore space remains connected to ensure the pore pressure is transmitted throughout the rock.

Paterson (1978, p80) refers to a "critical strain rate" above which Terzaghi's effective stress rule is not obeyed; that is, condition (ii) is violated. This critical strain rate

is integrally dependent on both rock permeability and fluid viscosity. Rutter (1972a) found that for Solenhofen limestone with a water interstitial fluid, the critical strain rate was 10^{-6} $s^{-1;}$ for Westerly granite it has been shown to be 10^{-7} s^{-1} (Brace, 1969a); and for sandstone 10^{-4} s^{-1} (Brace & Martin, 1968). If permeability is low the test conditions will approach those met in the undrained test. Under these conditions an increase in porosity can lead to a decrease in pore fluid pressure, leading in turn to an increase in the effective confining pressure. A greater differential stress is then needed for deformation than when a constant pore fluid pressure is maintained. This effect is known as "dilatancy hardening" and is discussed by Scholz (1990).

It has been shown by many authors that the presence of even the smallest amount of fluid especially in silicious rocks and calcareous rocks has a weakening effect on the rock (e.g. Murrell, 1965; Rutter, 1972b). In quartz rich rocks it is suggested (Atkinson & Meredith, 1983) that interstitial water has the specific chemical weakening role by assisting to break Si-O bonds. Atkinson & Meredith (1987a,b) give a good review of subcritical crack growth in response to fluid chemical activity.

An extremely widely observed phenomenon is that prior to brittle rupture rocks often exhibit non-elastic behaviour. Dilatancy is an inelastic increase in volume suffered by a rock sample during deformation. There is not necessarily an absolute increase in volume of the sample but only an increase relative to the elastic compaction of the rock. In general, non-elastic deformation results from either localised plastic yields or from microfracturing (Paterson, 1978, p113). Some workers (e.g. Edmond & Paterson, 1972) have shown that materials such as rock salt and marble are either non-dilatant or only marginally so; this implies plastic processes are involved in the deformation of these rocks. However, most brittle rocks suffer significant dilatancy caused by microfracturing. There are three experimental techniques that have been used to measure dilatancy directly:

a) The most widely used method is to apply electrical resistance strain gauges to the sample (e.g. Brace et al., 1966). These directly measure the radial expansion and axial contraction of the sample. Volumetric strain is then calculated from $e_{volume}=e_{axial}+2e_{radial}$; where e is strain. This method, however, assumes that strains throughout the sample are homogeneous. There is also some evidence that strain gauges give localised support to the

sample causing uneven stress distributions.

b) In the second method a fluid surrounds a jacketed sample in a dilatometer. The amount of fluid expelled in response to the deforming sample is then measured. Fluid displacement caused by the advancing ram can be compensated for by a yoke arrangement (e.g. Edmond & Paterson, 1972). The dilatancy is determined by subtracting the elastic volumetric change determined by the elastic constants of the rock. Edmond & Paterson (1972) performed a series of extremely difficult experiments using this technique on a variety of rocks at confining pressures up to 800MPa.

c) The third method measures the change in pore fluid volume of a sample during deformation. This method requires the rock sample to remain sufficiently permeable throughout the test. The technique effectively measures the connected porosity which is assumed to be equal to the dilatancy once elastic effects have been corrected for.

Fig. 2:2 shows strain data from Brace et al. (1966). Dilatancy is considered to begin at the point at which the volumetric strain curve deviates from linearity. In highly porous rocks this onset may be somewhat subjective. Dilatancy tends to commence at between 30% and 70% of the peak stress. It is generally accepted that, as first suggested by Brace et al. (1966), the onset of dilatancy marks the initiation of new crack growth. Brace et al. also noted that an increase in compressibility (decrease in stiffness) occurs radially in deforming rock specimens. This suggest that new dilatant cracks are orientated predominately with their long axis parallel to the direction of maximum compressive stress.

2:2:1 Microscopic observations.

There is little direct observational evidence of the processes of crack initiation, propagation and coalescence in deforming rocks. The main reason for this is the difficulty in preparing samples for conventional microscopic techniques. There have been a number of studies using different optical techniques which have attempted to observe directly the internal structure of rock samples. These include: (i) the use of conventional optical microscopes (e.g. Simmons & Richter, 1976); the performance of this technique can be enhanced by decorating the cracks with dyes (Thill, 1973); (ii) transmission electron microscopy (TEM) (Martin & Durham, 1975); and (iii) scanning electron microscopy

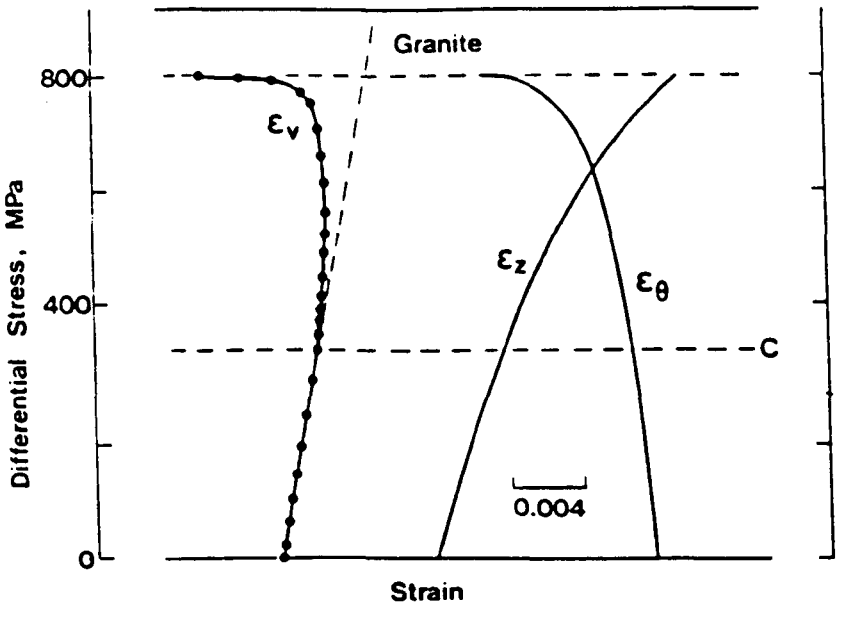

Fig. 2:2 Dilatancy in a triaxially deformed Westerly granite at 100MPa confining pressure. εv is the volumetric strain, εz the axial strain and εo the circumferential strain. Compression is taken as positive, therefore volume increase is to the left. C marks the point of the onset of dilatancy. (After Brace et al., 1966).

(SEM) (Fonseka et al., 1985). Rock samples have also been injected with molten Woods metal. Following this process, the rock can then be dissolved away using acids (Zheng et al., 1987), leaving a metal caste of the pore and crack structure.

It is perhaps useful at this point to distinguish between pores and microcracks in a physical way. Pores are essentially equidimensional and occupy intergranular spaces in sedimentary rocks and also occur as fluid inclusions in igneous and metamorphic rocks. Simmons & Richter (1976) described a microcrack as being elongate, with length to width ratio (i.e. (**c/a**), where **a** and **c** are the maximum and minimum dimensions of the crack; and is called the aspect ratio) of less than 10^{-2} but typically between 10^{-3}-10^{-5}. Cracks can be grain boundary, intergranular, intragranular or transgranular in nature. A comprehensive review of microcracks in rocks is given by Kranz (1983).

In some studies (e.g. Hallbaur et al., 1973; Hadley, 1976b; Fonseka et al., 1985) rock samples have been loaded up to a known percentage of failure stress, before being unloaded for examination of the induced cracking using SEM techniques. The important results of all these studies can be summarized as follows:

i) For granites undergoing uniaxial compression most of the initial cracking is parallel to the axis of compression (Bombalakis, 1973) although some are inclined at an angle of about 35°. Both intergranular and transgranular are present.

ii) The crack distribution is fairly homogeneous at low strains although the crack density is lower toward the sample ends (Hadley, 1976b).

iii) At low stresses, grain boundary cracking is predominant but at higher stresses transgranular cracking becomes dominant (Hadley, 1976b).

iv) Axial cracking continues to be dominant even after peak stress (Wawersik & Brace, 1971). Sometime after peak stress localized shear fracturing occurs.

v) In more brittle rocks, preliminary microcracking is less pronounced due to greater homogeneity, especially in fine grained rocks. In the most extreme cases (e.g. Solenhofen limestone with a grain size of <0.01mm) samples appeared to fail by shear

fracturing without any precursory axial cracking (Houpert, 1974b).

vi) Although some studies (i.e. Fonseka et al., 1985) have noted that crack formation by shearing action (or "wing-cracks"; see section 2:3). Others such as Wawersik & Brace found that these were not common.

2:3 Theories of brittle failure.

An important aspect of this study was attempting to reconcile observed rock deformation characteristics with theoretical brittle failure models. The development of theoretical models is traced in this section with particular emphasis given to more recent models. Attempts have been made for most of this century to model mathematically the physical characteristics of brittle failure in crystalline materials. These range from simple empirical methods that do not consider the mechanisms involved, to the most sophisticated recent models which track the progress of damage through regions of anelasticity and crack linkage to post peak deformational behaviour. Most theoretical models are based on the premise that even under a regime of global compression there will be regions of local tension where cracks will nucleate and grow. These regions will act as stress concentrators, resulting in microcracking given a sufficient level of deforming stress. The way in which these cracks initiate, grow, interact and link is looked at physically by the most recent theories. Generally, the theories describing brittle deformation fall into three broad groupings.

1) Empirical theories which attempt to fit a mathematical expression to experimental data. This may allow a limited extrapolation of the data to predict behaviour under inaccessible physical conditions. These theories however, give no insight into the physical processes that may be occurring.

2) Micromechanical theories which look at the growth of a single crack in an otherwise homogeneous and infinite surrounding medium. These are termed "crack initiation theories".

3) "Damage mechanics" theories, which use a single variable or set of variables to describe the changing internal structures (e.g. crack structures) of a deforming material. At their most advanced these theories attempt to profile the complete process of deformation and failure leading from crack initiation to crack growth and interaction and finally to the inception of macroscopic failure.

A brief survey of the relevant literature is presented below with particular attention given to more recent developments. Good reviews of the theories outlined in 1) and 2) above are given in Jaeger & Cook (1979). The conventions used are those common

in the geological literature, where the compressive fields are taken as positive and tensile fields as negative. When considering a stress field within a finite body it is usual to define principal stress axes along which only normal stresses ($\sigma_1,\sigma_2,\sigma_3$) act, the shear stresses are zero on planes normal to these axes. The convention $\sigma_1>\sigma_2>\sigma_3$ is used.

2:3:1 Empirical theories.

One of the earliest theories was proposed by Coulomb in 1773, yet this theory still retains considerable importance today. The Coulomb Criterion states simply that shear failure will occur when the shear stress tending to cause failure in a plane overcomes some inherent strength of the rock. This strength is called the cohesion. Mathematically the criterion takes the form,

$$\tau = S_o + \mu\sigma_n \qquad (2:2)$$

where σ_n and τ are the normal and shear stresses respectively, acting on the fracture plane. S_o is the inherent cohesive shear strength of the material and μ is the coefficient of internal friction. The formulation of the two-dimensional case yields the failure envelope,

$$\sigma_1[(\mu^2+1)^{½} - \mu] - \sigma_3[(\mu^2+1)^{½} + \mu] = 2S_o \qquad (2:3)$$

which is a linear failure relationship in σ_3, σ_1 space. The intercept on the σ_1 axis is,

$$C_o = 2S_o[(\mu^2+1)^{½} + \mu] \qquad (2:4)$$

where C_o is the uniaxial compressive strength. However, as it is implicitly assumed in eqn. 2:2 that σ_n is positive, the intercept on the σ_1 axis cannot be considered to be the uniaxial tensile strength. The linear line in σ_1,σ_3 space is truncated by the line $\sigma_3=-T_o$, for $\sigma_1<C_o[1-C_oT_o/4S_o^2]$. Where T_o is the tensile strength. The Coulomb theory has several important consequences. Firstly the failure plane is predicted to develop at an angle to the σ_1 axis of,

$$\Theta = \tfrac{1}{2}\tan^{-1}(1/\mu) \qquad (2:5)$$

Most rocks have a μ value between 0.5 and 1.0, these give fracture angles between 32° and 22.5°; such angles are seen experimentally (see, for example this study, table 6:1). Furthermore, the ratio of the uniaxial compressive strength to the uniaxial tensile strength C_o/T_o is given by;

$$C_o/T_o = (\mu^2+1)^{\frac{1}{2}} + \mu/(\mu^2+1)^{\frac{1}{2}} - \mu. \qquad (2:6)$$

For values of μ ranging from 0.5 to 1.0, C_o/T_o will vary between 2.7 and 5.8. These are low compared with experimental observations which suggest the uniaxial compressive strength of most rocks is about 10 to 20 times greater than their uniaxial tensile strength (Paterson, 1978).

In 1900 Mohr proposed a general failure criterion,

$$\tau = f(\sigma_n) \qquad (2:7)$$

where f is some experimentally derived function. The failure envelope for a particular material is determined by the locus of the Mohr stress circles constructed from the σ_1,σ_3 conditions at failure. Therefore, by experimentally determining the strength of a brittle material at different confining pressures, a failure envelope can be constructed. This envelope can then be extrapolated to predict the failure conditions under pressures unobtainable experimentally. The angle of fracture is determined by the normal to the Mohr envelope. The envelope is concave downwards (Murrell, 1965), so as the mean stress ($\frac{1}{2}(\sigma_1+\sigma_3)$or hydrostatic pressure) is increased the plane the fracture subtends to the axial (σ_1) direction is seen to increase. This appears to be consistent with experimental observations (section 2:1).

2:3:2 Crack initiation theories.

The apparent low experimental strength of solids when compared to the derived theoretical strength was addressed by Griffith (1920). Griffith proposed that all brittle materials contain microscopic cracks which act as stress, strain, and strain energy concentrators. These sharp microscopic cracks are referred to as "Griffith flaws". He used

an energy argument to determine conditions for initiation of crack growth. The crack would grow or heal depending on the relative values of three energy contributors to the system. A crack would only grow if the surface energy of the new crack surface was less than the sum of the change in potential energy arising from the release of stored energy contained in the cracked body and the work done by the loading system, thus decreasing the overall energy of the system.

Griffith (1924) then went on to consider crack initiation in a biaxial stress field with open cavities. Instead of an energy argument he looked at the stress concentrations at the tips of minute cracks. Crack growth occurs when the maximum stress near the tip of the most favourably orientated crack reaches some value characteristic of the material. The Griffith Criterion is represented by;

$$(\sigma_1-\sigma_3)^2 = 8T_o(\sigma_1+\sigma_3) \; ; \text{ if } \sigma_1+3\sigma_3 > 0 \qquad (2:8)$$

$$\sigma_3 = -T_o \qquad ; \text{ if } \sigma_1+3\sigma_3 < 0 \qquad (2:9)$$

where To is the uniaxial tensile strength. The first equation describes crack initiation under predominantly compressive conditions and the second describes tensile failure. In tension the new crack will grow in an unstable manner and, therefore, crack initiation can be considered to be synonymous with failure. However, in compression crack growth is generally stable, requiring a positive increment in stress to promote further crack growth. Therefore eqn. 2:8 cannot be considered a failure criterion. Murrell (1958), however, points out that in a general way the Griffith Criterion may be considered as a failure criterion for very brittle materials such as glass, some rocks and concrete.

In (two-dimensional) principal stress space the Griffith Criterion is represented by a straight line portion (ABC, fig. 2:3), and the parabolic portion (CDE) which touches the line ABC at the point $C_o,(3T_o,-T_o)$. The predicted ratio of the uniaxial compressive strength to the uniaxial tensile strength is eight. Although this value is an improvement on that obtained from the Coulomb Criterion, it is still less than that observed experimentally.

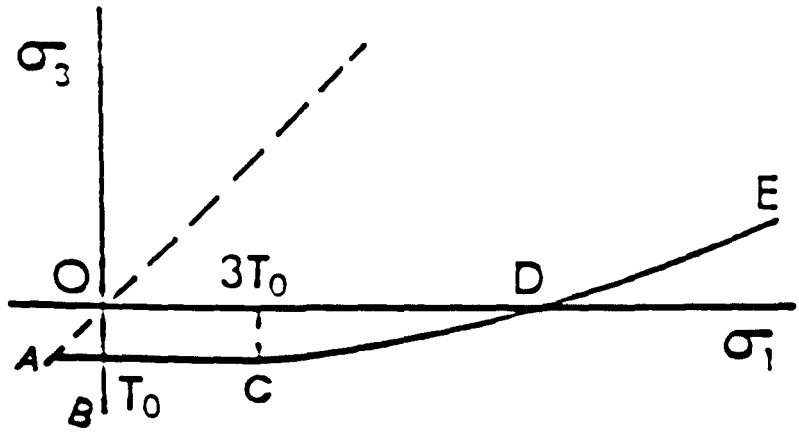

Fig. 2:3 The two-dimensional principal stress space (σ_1, σ_3) representation of the Griffith crack initiation criterion.

Murrell (1963) provided an empirical extension of the two-dimensional Griffith Criterion to the three-dimensional case. Generalising the three-dimensional situation by rotating the two-dimensional parabolic crack initiation curve to become a paraboloid of revolution about the axis line $\sigma_1=\sigma_2=\sigma_3$. The paraboloid is truncated by the mutually perpendicular planes;

$$\sigma_1 = -T_o \quad \sigma_2 = -T_o \quad \sigma_3 = -T_o \qquad (2:10)$$

The extended Griffith Criterion is then;

$$(\sigma_2-\sigma_3)^2 + (\sigma_3-\sigma_1)^2 + (\sigma_1-\sigma_2)^2 = 24T_o(\sigma_1+\sigma_2+\sigma_3) \qquad (2:11)$$

The predicted ratio of the uniaxial compressive strength to uniaxial tensile strength is twelve. This brings the value into the lower range of experimentally observed values. This criterion also shows a dependence of strength on the intermediate principal stress σ_2. Murrell (1963, 1965) has shown experimentally that rock strength, in general, increases with increasing intermediate stress.

The assumption behind the Griffith Criterion neglects the closure of cracks that would be expected under sufficiently high compressive stresses. The Modified Griffith Theory, first proposed by McClintock & Walsh (1962) and Murrell (1964), takes into account the frictional interaction between closed crack faces. Its effect is to leave the early part of the curve ABCDE (fig 2:3) unaltered (the cracks remaining open at low σ_3,σ_1 values). A transition will then occur (mathematically examined by McClintock & Walsh (1962)), when cracks are closed the theory becomes identical to the Coulomb Theory giving a linear Mohr envelope. Mathematically this can be expressed as;

$$\sigma_1[(\mu^2+1)^{1/2}-\mu] - \sigma_2[(\mu^2+1)^{1/2}+\mu] = 4T_o \qquad (2:12)$$

$$\sigma_c=0$$

where σ_c is the normal compressive stress required to close the cracks. As can be seen, this is equivalent to the Coulomb Theory (eqn. 2:3) with the coefficient of

internal friction tan ϕ equal to the coefficient of sliding friction on the crack faces. This also gives a physical meaning to the ambiguous Coulomb concept of internal friction. The cohesion S_o is replaced by $2T_o$.

The three-dimensional extension of the two-dimensional Griffith Theory by Murrell (1963) was the result of geometrical completeness. A full three dimensional treatment has been carried out for open elliptical cracks by Murrell & Digby (1970i) and for closed cracks (with an internal pore pressure) by Murrell & Digby (1970ii). Murrell & Digby (1970i) first considered open traction-free cracks subject to an arbitrary uniform triaxial stress system. The principal axes of the cavities are a,b,c, where a>b>>c; no crack interaction is considered. The maximum values of the stress on the walls of the cavity are determined and then the orientation of the cracks with respect to the stress field are varied to maximise these values. This enables the orientation of the cracks most responsive to the stress field to be found. The new cracks will grow out of plane of the initial crack since the maximum stress values do not lie along the axes of the crack. This yields a crack initiation curve (for the case a=b, or penny-shaped cracks),

$$(\sigma_1-\sigma_3)^2 - 2(2-v)T_o(\sigma_1+\sigma_3) = U(4-U)(2-U)^2T_o^2 \qquad (2:13)$$

for $\sigma_1 > -A^*\sigma_3$ (or a predominantly compressive system)

where A^* is a constant of order 1 when v=0.3, and U is Poisson's ratio. An important consequence of eqn. 2:13 is its independence from the intermediate stress.

For closed cracks suffering surface traction Murrell & Digby (1970ii) obtained a crack initiation relationship of;

$$((1+\mu^2)^{1/2}-\mu)(\sigma_1-\sigma_3) = a'T_o(1+\sigma_c/T_o)^{1/2}+2\mu(\sigma_3-\sigma_c) \qquad (2:14)$$

where σ_c is the stress required to close the cracks and a' is a constant (2(2-U) for penny shaped cracks). Again the result is independent of the intermediate stress. These results are entirely complementary in form to the two-dimensional Griffith Criterion and the Modified Griffith Criterion. That is, the results for closed cracks show a linear relationship (in σ_1,σ_3 space) moving into a parabolic relationship for open cracks. It

should be noted that the Griffith and Murrell relationships shown above are concerned only with isolated cracks and give no indication of the effects of crack interaction and linkage.

2:3:3 Damage mechanics models.

Damage mechanics models follow the same common reasoning as the Griffith Criteria. Specifically they consider an isolated flaw in an otherwise homogeneous medium, which is rotated with respect to the principal stress axis to maximise the tensile forces at the crack tips. Cracks then occur at a high angle to the initial flaw ("wing cracks"). These cracks grow when the stress intensity factor K becomes greater than the fracture toughness Kc, of the surrounding medium. The stress intensity factor K describes three modes of deformation at the crack tip. Ki describes the stress field associated with displacement normal to the crack plane (that is, opening or tensile cracking). Kii describes the stress field associated with displacement parallel to crack plane and normal to the edge (shearing-in-plane) and Kiii the stress field associated with displacement parallel to the crack plane and parallel to the edge (twisting-in-plane). The stress intensity factor Ki is derived from considering the stress field around a crack tip isolated in a linear elastic body. For polar coordinates r,Θ the stress perpendicular to the crack line (σ) is,

$$\sigma = K/(2\pi r)^{1/2} f(\Theta) \qquad (2:15)$$

where $f(\Theta)$ is a known function of the angle Θ. A review of stress intensity parameters is given by Lawn & Wilshaw (1975b). This equation shows that the stress field around the crack tip can be completely specified if a value of K is known. K contains all the essential information to enable the stress field to be described, i.e. the loading and crack geometry. Inelasticity at the crack tip is handled theoretically by considering sufficiently small areas of elasticity.

Nemat-Nasser & Horii (1982) and Horii & Nemat-Nasser (1985) provide a complete model which incorporates all of the experimentally observed characteristics of brittle failure. The role of confining pressure and temperature on failure are also examined. Theoretical results are compared to simple experiments performed on slits introduced into blocks of Columbia resin (CR39). The authors develop three main regions

to the argument, axial crack growth, faulting, and the brittle/ductile transition. An exact formulation of the elastic boundary problem for a single flaw in a homogeneous medium with curved wing cracks is given by Horii & Nemat-Nasser (1985) in terms of singular integral equations. However, an analytical solution for the simplified state of straight wing cracks at an angle Θ to the stress axis σ_1 is given by Horii & Nemat-Nasser (1986). The stress intensity factors Ki and Kii are estimated at the crack tips. The analytical results show a good correlation with the exact solution. The Ki stress intensity is maximised with respect to Θ and crack initiation occurs when $Ki \geq K_c$ where K_c is opening mode fracture toughness. They show that the stress for initiation of cracking is inversely proportional to $\sqrt{c}$ (where 2c is the initial crack length). Hence the larger flaws will provide the sites for initial cracking.

Figs. 2:4a,b,c. show results from tests performed on blocks of CR39 resin. A line of closely-spaced, small cracks is angled across the specimen, large cracks are spaced sparsely and (more or less) at random. Although intuitively the line of small cracks appear weaker, cracks initiate from the larger cracks under uniaxial conditions in fig. 2:4b as predicted by the model. When interaction effects are considered the elastic boundary problem becomes very complex. A full numerical solution is provided by Horii & Nemat-Nasser (1985). Again, the stress intensity factor at the crack tips is calculated and Θ is chosen such that $Ki/\sqrt{(\sigma_1(\pi c))}$ is maximised. The inception of the fault occurs when the favourably orientated cracks grow and interact. Fig. 2:4c shows how the application of even a modest confining pressure can suppress axial cracking which first initiates from the large cracks. Secondary cracking from the smaller cracks then occurs resulting in faulting.

Ashby & Hallam (1986) and Sammis & Ashby (1986), use a combination of fracture mechanics and beam theory to determine crack growth and crack interaction processes. They further consider the interaction of growing cracks with the free surface of a finite sample. Such a method leads to a framework of damage mechanics which allows experimentally feasible stress/strain curves to be compiled. Ashby & Hallam (1986) provide an approximate analytical examination of crack growth from preexisting two-dimensional flaws. Sammis & Ashby (1986) use the same method to develop cracking from two-dimensional holes and three-dimensional spherical pores, and also show simple

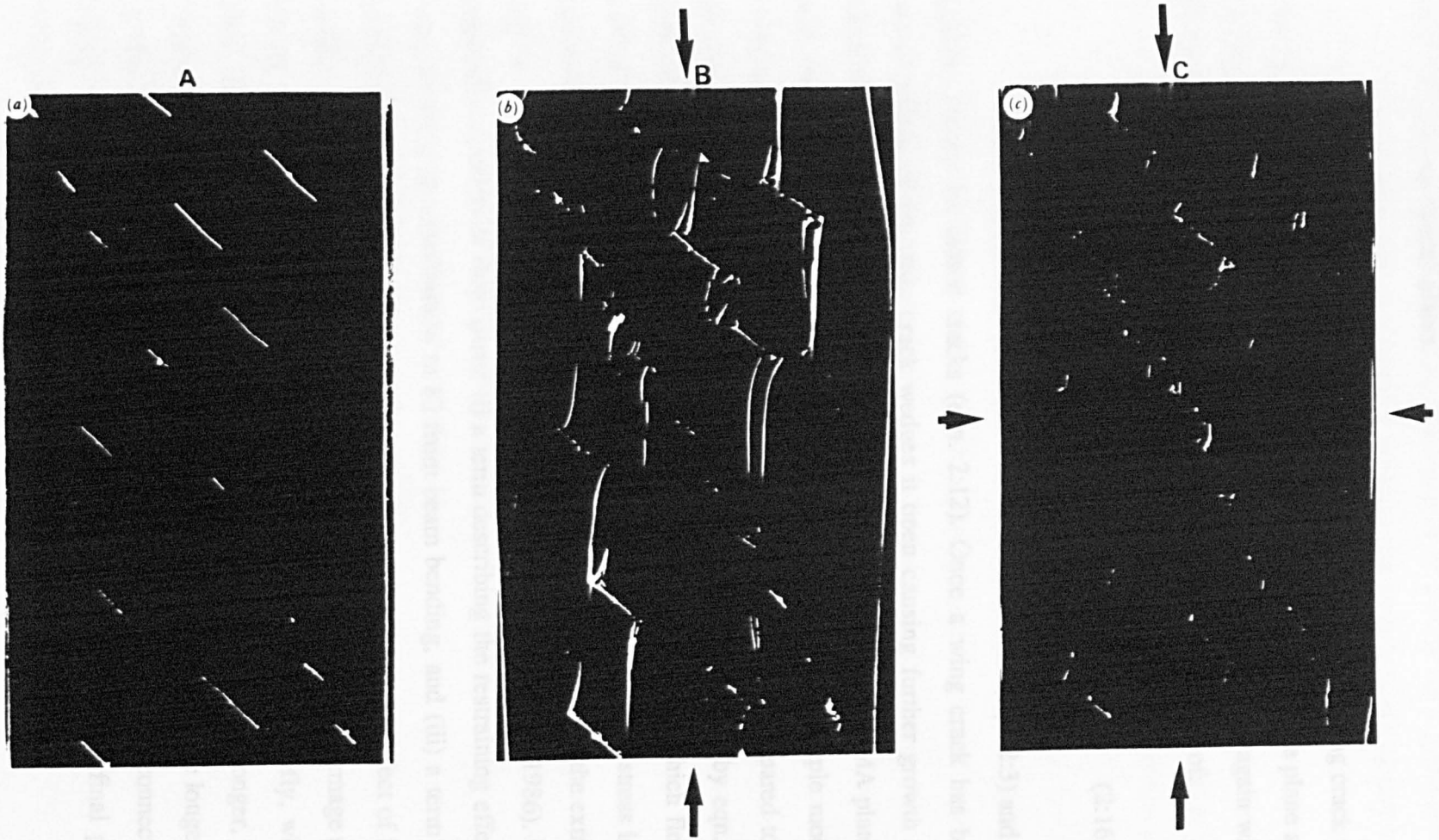

1:1

Fig. 2:4 Blocks of Columbia resin with a series of artificial small flaws angle across the specimen, and several larger flaws, (a). (b) shows axial splitting originating from the larger flaws in response to uniaxial compression. (c) shows shear failure by linkage of the smaller flaws in response to axial compression but with a lateral confinement, (from Horii & Nemat-Nasser, 1985a).

experimental data in which idealised flaws are introduced in blocks of glass and PMMA (polymethylmethacrylate) plates.

Ashby & Hallam (1986) considered the initiation of a wing crack in an infinite plate. The stress intensity Ki at the crack tip is derived by finding the plane at angle Θ on which the tensile stress is maximum. This stress is then maximised again with respect to the flaw orientation angle μ, leading to a crack initiation condition of;

$$\sigma_1((1+\mu^2)^{1/2}-\mu)-\sigma_3((1+\mu^2)^{1/2}+\mu)=(3/[\pi a])^{-1/2}K_{IC} \qquad (2:16)$$

which has the same form as the Coulomb Criterion (eqn. 2:3) and the Modified Griffith Theory for closed cracks (eqn. 2:12). Once a wing crack has been initiated, further sliding of the main crack wedges it open causing further growth until Ki falls below Kc. The authors noted that the wing cracks in deforming PMMA plates accelerated with the bowing of the plates. They, therefore, considered the simple model of a plate containing a central angled crack the length of which is small compared to the width of the sample. The stress intensity at the crack tip can then be given by eqn. 2:16. Cracks then grow vertically, splitting the plates into two vertical beams which flex in response to further loading. The outward bending of the beams increases the stress intensity at the crack tip making the crack grow further. The authors then calculated the extra contribution due to beam flexure, (see equation (8) of Ashby & Hallam, 1986). The resulting expression consists of three parts; (i) a term describing the restraining effect of σ_3, (ii) a term showing the contribution to Ki from beam bending, and (iii) a term correcting for changing geometry of the sample. This expression describes the effect of having a finite sample size. Crack interaction is approached through the ideas of damage mechanics, i.e. the mechanics of an array of cracks growing and interacting. Briefly, when cracks are short they are considered to act as described above. As they get longer, however, they interpenetrate dividing the solid into a series of beams which become longer and narrower as the cracks extend. These beams are handled as a network of connected struts. The theory stops short of following through crack interaction to the final phase of crack behaviour at failure.

The work of Sammis & Ashby (1986) uses the same basic method as described above but extends the work to consider crack growth from three-dimensional pore

structures. They determine stress/strain curves resulting from progressive crack growth and interaction. The stress and the Young's modulus of a body for a given level of cracking are calculated; then from the Young's modulus the sample straining can be determined. As axial cracking ensues the modulus of the sample decreases, i.e. the sample becomes more compliant. Since cracks are aligned the sample becomes anisotropic. The modulus in the maximum principal stress direction will then differ from that in either of the other two principal directions. An energy argument is used to relate the change in potential energy of the system caused by cracking to the Young's modulus of the sample.

Other damage mechanics models have been proposed, notably by Costin (1983, 1985). The Costin (1985) model uses the same analytical approach as Horii & Nemat-Nasser (1985). The results for individual cracks are generalized to model a suite of cracks by assuming that an array of small microcracks behaves in a similar way to a single "equivalent" large crack. He considers the worst case scenario of collinear arrays of interacting cracks. As the cracks become more closely spaced the stress intensity factor is amplified. This results in cracks growing under a lower applied stress. The deformation can thus be followed theoretically for a limited region of post-peak strain softening. Failure is considered to occur when crack interaction dominates the deformation. This model also incorporates a time-dependent component by allowing the effects of "stress corrosion" by chemically active fluids at crack tips to be analysed. In such an environment cracks can grow subcritically at values of K well below Kc.

2:4 Acoustic interrogation techniques and theoretical crack density determinations.

As rock samples are being deformed, far-field techniques can be employed to monitor internal changes within the rock. Inferences can then be made as to the mechanisms that may be governing the deformation. These methods are extremely important not only in the laboratory but also in the field where they allow investigations of the stress regimes at depth. The laboratory situation provides a unique opportunity to use acoustic investigation techniques while also directly monitoring or controlling the stress and strain regimes operating on a deforming rock sample. Experimental and theoretical acoustic investigations are now examined in detail, these include acoustic emission studies, elastic wave velocity studies, crack density determinations and attenuation studies.

2:4:1 Acoustic emissions.

Acoustic emissions (AEs) result from a sudden local stress relaxation that produces a burst of energy. This stress relaxation can be caused by crack propagation, abrupt twinning or by dislocation mechanisms. Generally, in highly stressed samples of a brittle material, acoustic emissions predominately result from microcracking and is often referred to as "microseismic activity". In recent years the analysis of acoustic emission events has advanced significantly. Initially acoustic events were merely counted (e.g. Obert & Duvall, 1942; Scholz, 1968a). However, present day analysis includes the study of the relative amplitude distribution of the events (Meredith & Atkinson, 1983; Fonseka et al., 1985; Main et al., 1990), frequency analysis of amplitude spectra (Ohnaka & Mogi, 1982; Maeda, 1981; Sondergeld & Estey, 1981), analysis of source mechanisms (Yanagidani et al., 1985) and source location (Sondergeld & Estey, 1981; Yanagidani et al., 1985).

Acoustic emissions tend to occur mostly in the frequency range 100kHz-10MHz (Byerlee, 1974). As a rock sample is loaded there are several distinct stages of characteristic AE activity. Upon initial loading there is a flurry of low frequency acoustic activity, this is typically associated with the closing of favourably orientated low aspect

ratio cracks (Ohnaka & Mogi, 1981). There then follows a period of little or no AE activity, where deformation is primarily controlled by elastic processes and the stress/strain curve is linear. At somewhere between 30% and 50% of the peak stress the acoustic emission rate tends to show a rapid increase. This has been associated by many authors (e.g. Scholz, 1968a) with the onset of dilatancy, defined as a deviation of the axial stress/volumetric strain curve from linearity. However, the onset of the AE must to some extent be a function of the sensitivity of the recording equipment. Ohnaka & Mogi (1981) reported observations of AE activity starting prior to dilatancy. It is, however, generally recognised that the onset of dilatancy can be correlated with a sharp increase in AE activity. As macroscopic failure is approached the AE rate further increases. Frequency analysis shows that emissions tend to have an increased lower frequency content immediately prior to failure (Ohnaka & Mogi, 1981). There are two possible explanations for this: Firstly, as the rock becomes more heterogenous with accelerated microcracking, the high frequency components of the AEs could be preferentially attenuated. Secondly, the crack sources are becoming larger and subsequently are generating lower frequency components (Savage, 1972). It seems likely, however, that both mechanisms will be occurring at the same time.

Source location experiments show that there is significant inhomogeneity in the spatial distribution of AE events during rock deformation. Yanagidani et al. (1985) noted an absence of AE events in the vicinity of the end caps in compression tests. This is probably the result of the added frictional constraint imposed on the sample at contact with the loading rams. However, throughout the main body of the sample the distribution of AE events was fairly homogeneous until failure is approached. Prior to failure significant heterogeneity in the location of AE events occurs, with clustering around a weak spot. In some cases this region has been linked with the site of final failure (Lockner & Byerlee, 1977). Both Sondergeld & Estey (1981) and Nishizawa et al. (1985) note this heterogeneity before failure in uniaxial tests on granite. This occurs at about 80% of the failure stress with abrupt migration of the AE events to cluster at surface sites. Nishizawa et al. (1985) explain this in terms of stress corrosion cracking where subcritical crack growth is environmentally induced. This appears to be borne out by Lockner & Byerlee (1980) who noted a much later localisation of events in triaxial tests. There can be envisaged a dual effect operating in triaxial tests to suppress localisation of AE activity. Firstly, by jacketing the sample protection is given from moisture infiltration, and

secondly, the application of confining pressure reduces the effect of cracks clustering about initial heterogeneities in the sample.

The first motions of a number of AE events have been examined by Maeda (1981), Sondergeld & Estey (1981) and Nishizawa et al. (1985) for events recorded at several different transducers located over the sample surface. These studies show that none of the recorded waveforms had a compressional first motion at all of the transducers. Purely tensile cracking would be expected to produce a positive pressure pulse in all radial directions. Therefore, it is concluded that all microfracturing must include some element of shear. At present no one has been able to determine a precise source mechanism from the recorded waveforms of AE events in rocks.

The importance of a statistical approach to AE analysis has been highlighted by Yanagidani et al. (1985). The way of describing relative amplitude distributions is the seismic b-value. A log-log plot of the cumulative (or discrete) number of events versus amplitude is determined. The negative slope of the monotonically decreasing part of the plot then gives the b-value (e.g. Fonseka et al., 1985; Jones, 1989; Main et al., 1990). Jones (1989) has studied experimentally, and Main et al. (1990) theoretically, the changes in seismic b-value during brittle failure and cataclastic flow. In the faulting case the seismic b-value decreases steadily reaching a minimum value of around 0.5 at failure, after which it regains an intermediate value. For cataclastic flow the seismic b-value decreases as the sample reaches peak stress. However, in the post failure regime the AE activity remains high and the seismic b-value remains low (but never as low as the critical value of 0.5). A decreasing b-value reflects a relative increase in the number of large events in the AE distribution profile. This result correlates well with the previous interpretation of the increase in low frequency components of the AE events at this point. However, as pointed out by Sondergeld & Estey (1981), if strong spatial clustering occurs prior to failure the AE distribution is no longer random and in such cases the definition of a b-value then becomes unclear.

2:4:2 Elastic wave velocities in rocks.

It is well known that cracks or defects in a solid reduce the elastic modulus of the material (e.g. Walsh, 1965; O'Connell & Budiansky, 1974) and as a consequence the velocity of elastic waves propagating through the material are also reduced. The velocity of an interrogating elastic wave is not only affected by the number of cracks in a rock but also their size, degree of alignment, their aspect ratio, and the presence, type and degree of saturation of an interstitial fluid.

The velocity of sound through a laboratory rock sample can be measured using a variety of techniques. The one used in this study is the pulse-transmission method described by Birch (1960). This method measures the time of flight of an elastic wave propagating through the rock sample. Usually only the first arrival is considered. However, more sophisticated methods use wave matching techniques (Mattaboni & Shreiber, 1974). Other methods use resonating bars (Thill & Peng, 1974), or resonating rock spheres (Birch, 1967). Winkler & Plona (1982) have described a pulse echo technique in which the rock sample is situated between two lucite buffers.

The response of pore and crack structures within rock specimens to hydrostatic pressure have been examined by many authors (for example, Birch, 1960; Nur & Simmons, 1969a; Hadley, 1976b; Lo et al., 1988; Jones, 1989; Xu & King, 1990). It is well established that application of even a modest confining pressure (<200MPa) closes most of the low aspect ratio cracks in the rock and increases the velocities of both the compressional wave velocity (Vp) and the shear wave velocity (Vs) travelling through the sample. These velocities can be used to estimate the moduli of the rock in its crack-free state. Spherical pores are little affected by hydrostatic pressure, until the point is reached where pore crushing occurs. Under increasing hydrostatic confining pressure both Vp and Vs increase rapidly, but this rate of increase is reduced above about 100MPa confining pressure. The form of the curve (velocity against confining pressure) is concave to the increasing pressure (e.g. Nur & Simmons, 1969a; Volarovich & Budnikov, 1979). If the changes in both Vp and Vs are known, then the dynamic elastic constants, Young's modulus and Poisson's ratio can be easily calculated using standard equations (e.g. Jaeger & Cook, 1976, p188; Nur, 1990; Thill & Peng, 1974).

Seismic anisotropy is a common phenomenon in rocks and has been examined

by a number of authors (a selection of investigations are briefly discussed below). There are, primarily, two causes of such anisotropy; (i) crystallographic alignment and (ii) microcrack alignment. The dual effects of mineral and microcrack alignment can be separated by considering the velocity changes in the three principal directions of a rock, under increasing hydrostatic pressure. Residual anisotropy at high confining pressure is attributed to mineral alignment. Kern & Fakhimi (1975) and Kern (1978) looked at the effect of high pressures and temperatures on peridotite, amphibolite, serpentinite and Yule marble. Although Birch (1960) found that most rocks gradually lose their primary velocity anisotropy as hydrostatic pressure is increased, it was found that an anisotropy of about 10% remained even at 1GPa in serpentinite. This was considered to be the result of alignment of sheet silicates. The marble showed an alignment of calcite crystals with a concentration parallel to the c-axis, where Vp is low. Lo et al. (1988) examined the effect of increasing confining pressure on bedded sandstones and shales, and determined that the initial anisotropy under ambient conditions was due to both aligned cracking and mineral alignment. Using similar reasoning, Sayers (1990) has described a method of determining in situ stress conditions at depth from cored rock samples. By increasing the confining pressure on these samples in the laboratory, a point is reached where the velocity anisotropy becomes insignificant. The in situ stress conditions are then considered to have been reproduced. There are two implicit assumptions in the Sayers method. Firstly, that all the seismic anisotropy is a result of microcracking caused by stress relaxation of the cored sample as it is brought to the surface. Secondly, that the rock was uniformly homogeneous and isotropic at depth.

A number of authors have examined the stress induced compressional wave velocity anisotropy in deforming samples (Nur & Simmons, 1969b; Gupta, 1973; Bonner, 1974; Hadley, 1975a; Lockner et al., 1977; Soga et al., 1978). The results of these studies can be interpreted in terms of crack populations closing and opening. In dry rocks, upon initial deviatoric loading both Vp and Vs increase (measured along the unique axis); Vp somewhat more than Vs. This is interpreted as being due to the closure of favourably orientated cracks, i.e. those lying in a plane perpendicular to the maximum principal stress axis. Between 30% and 70% of the peak stress Vp begins to decrease. Vp measured perpendicular to the loading axis decreases more than that measured along the axis (Lockner et al., 1977). Changes in Vs along the axial direction are not well known. However, Gupta (1973) reports little change in either axial Vp or Vs for uniaxial tests on

a fine grained limestone. Hadley (1975a) examined changes in both axial Vp and Vs in a uniaxially deformed granite, and also found little change in either velocity prior to failure. The changes in Vs propagating perpendicular to the axis of maximum compression depend crucially upon the direction of wave polarisation. The shear wave polarised parallel to the stress axis is influenced less than the wave polarised perpendicular to the axis (Lockner et al., 1977). Generally shear waves normal to the maximum stress axis are affected less than the compressional wave travelling in this direction. The decrease in velocities in all directions indicates the onset of dilatancy. The preferential decrease in radial Vp relative to axial Vp suggests that dilatant cracks are preferentially aligned in the major axis of compression.

It follows then, that even an initially isotropic rock will become increasingly anisotropic as it is progressively deformed. How such anisotropy affects the Vp/Vs ratios in three mutually perpendicular directions has been discussed in detail by Paterson (1978, pp. 127-129). The effect of dilatancy-induced anisotropy on Vp/Vs ratios in a transversely isotropic system is summarised in a diagram taken from Hadley (1975a), fig 2:5. The data used in this diagram were obtained from uniaxial tests on granite. The Vp/Vs ratio increases slightly in the axial direction but decreases markedly perpendicular to the maximum stress axis.

Although axial symmetry is often assumed in triaxial deformation, recent evidence suggests that this assumption may be violated as failure is approached. Yukutake (1989) measured the compressional wave velocity along 20 different travel paths across a rock specimen. These velocity measurements were then inverted to reconstruct zones of damage using algebraic reconstruction techniques (ART). His results suggest that surface damage and asymmetric development of dilatancy could be important before failure for uniaxial tests on granite. Such localisation of damage is suppressed to some extent in triaxial tests.

Crampin & McGonigle (1981), and Crampin (1981) have discussed the importance of shear wave splitting resulting from shear wave propagation in an anisotropic medium. However, this will not occur if the direction of propagation is along the axis of rotational symmetry (Paterson, 1978), and is therefore not important in this study.

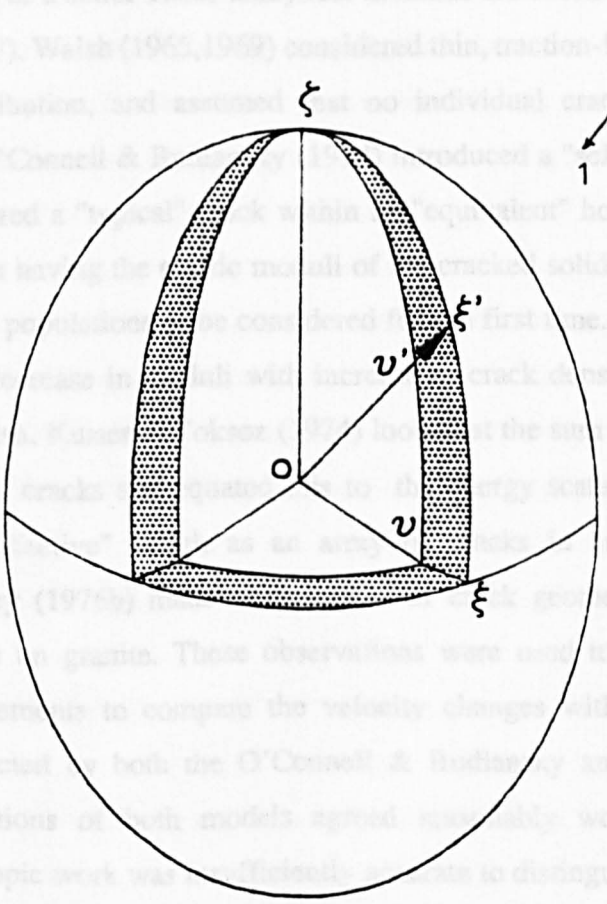

$$\zeta = (V_{p3}/V_{s31})/(V_{p3_o}/V_{s31_o}) = 1.01$$

$$\xi = (V_{p1}/V_{s12})/(V_{p1_o}/V_{s12_o}) = 0.97$$

$$\upsilon = (V_{p1}/V_{s13})/(V_{p1_o}/V_{s13_o}) = 0.95$$

Fig. 2:5 Surface plot of the Vp/Vs ratio changes seen for a uniaxially deformed granite, (after Hadley, 1975a). Note that Vp/Vs in the compressive axis (3) will increase slightly, whereas in the radial directions it will decrease. THE ZERO SUFFIX DENOTES VELOCITIES THROUGH THE UNDEFORMED SAMPLE.

2:4:3 Crack density models.

There have been several analytical theories presented which describe the effect of cracks on the elastic moduli of a solid. These analytical methods are based on the now classical work of Eshelby (1957). Walsh (1965,1969) considered thin, traction-free, penny-shaped cracks of dilute distribution, and assumed that no individual crack had any influence on its neighbours. O'Connell & Budiansky (1974) introduced a "self consistent scheme" (SCS) which considered a "typical" crack within an "equivalent" homogeneous medium, but with this medium having the elastic moduli of the cracked solid. This latter approach allowed dense crack populations to be considered for the first time. The theory predicts a much more rapid decrease in moduli with increase in crack density than the non-interactive models of Walsh. Kuster & Toksoz (1974) looked at the sum of scattered wave energy from an array of cracks and equated this to the energy scattered from a single crack of the same "effective" length as an array of cracks in an otherwise homogeneous medium. Hadley (1976b) made observations of crack geometry using a scanning electron microscope on granite. These observations were used together with independent porosity measurements to compare the velocity changes with increasing hydrostatic pressure as predicted by both the O'Connell & Budiansky and Kuster & Toksoz models. The predictions of both models agreed reasonably well with the observations, but the microscopic work was insufficiently accurate to distinguish between the models.

Other models have considered cracks that are not ellipsoidal (penny-shaped), for example, Mavko & Nur (1978) and Walsh & Grosenbaugh (1979). However, these do not lend themselves to the calculation of the effective shear modulus (G). Since both compressional and shear wave velocities depend on G, these theories are not examined here. It has been shown that it is not only the number of cracks in a solid which effect the elastic wave velocities, but also their shape and orientation. Walsh (1965) determined that the effective elastic moduli are proportional to the cube of the crack length. He also showed that elongated cracks have a greater effect on the moduli (and hence the seismic velocities) than more rounded cracks for the same orientations and crack volumes. O'Connell & Budiansky (1974) used a single dimensionless parameter to describe the cracking in a solid, called the crack density parameter, ε, where;

$$\varepsilon = N\langle a^3 \rangle = 3\phi/4\pi\langle\alpha\rangle \qquad (2:17)$$

for the case where thin penny-shaped cracks are randomly orientated in the solid (a≈b>>c where a and b are the major axes of a crack and c is the crack thickness), <a> is a mean major axis of the ellipsoid. ϕ is the volume of cracks per unit volume of solid and α is the aspect ratio (c/a). The authors note that there is very little difference between the effect of spheroidal cracks and penny-shaped cracks of random orientation on the calculated values of the elastic moduli.

Zimmerman & King (1985) examined the changes in crack density parameters as a result of hydrostatic pressure using the experimental velocity measurements of Birch (1960) and Simmons (1964). They used an approximate solution developed by Bruner (1976) to an exact solution of Salganik (1973). They used the relationships;

$$E/E_o = \exp(-16\varepsilon/9) \qquad (2:18)$$

$$U/U_o = \exp(-16\varepsilon/10) \qquad (2:19)$$

where E is the Young's modulus, ε the crack density and U the Poisson's ratio. The subscript o denotes the properties of the uncracked solid.

Experimentally it has been shown that crack alignment has a significant effect on the elastic wave velocities through rocks (for example, Wang & Lin, 1974; Lockner et al., 1977; Soga et al., 1978; Lo et al., 1988). It is also well known that nonhydrostatic loading causes anisotropic dilatancy in brittle solids. Initial deviatoric loading preferentially closes cracks with their long axes perpendicular to the axis of maximum compression. Further loading leads to the growth of predominately axial cracks (Brace & Bombolaski, 1963; Brace et al., 1966; Scholz, 1968). Therefore in analyzing triaxially deformed samples, anisotropy will be expected to play an important role. Anisotropic crack density models are much more complex than those which consider only random cracking. With the experimental set-up used in this study the velocities of the elastic waves travelling along the maximum stress axis can be measured. This limited velocity data makes it impossible to use many of the anisotropic models. However, by making certain assumptions, a linear crack density model for aligned microcracking in an

otherwise homogeneous surround given by Soga et al. (1978), can be used. The adaptation of the Soga et al. method to the specific case of the limited velocity measurements made in this study is explicitly examined in section 5:6:1. Briefly, Soga et al. (1978) use the numerical analysis of Anderson et al. (1974) which examines the velocities travelling along three mutually orthogonal axes of an elliptical crack in an isotropic surround. Soga et al. then sum the effects of three mutually orthogonal crack arrays.

The Soga et al. model has been questioned by Nishizawa (1982) who used instead a step-wise iterative process developed by Yamamoto et al. (1981). Small incremental increases in crack volume are assumed to occur in an elastic medium, thus enabling the effects of large crack densities to be analysed. The Nishizawa model predicts a smaller anisotropy than that given by Anderson et al. (1974). Fig. 2:6 shows a comparison of the linear Soga et al. model with the Nishizawa model. The graph shows the change in velocity resulting from an increase in the crack density parameter. In this diagram, the notation is that x denotes the unique axis in a transversely isotropic system x,y,z. The axes of interest in this case are then Vxx and Vxz or Vxy. The two models begin to diverge for crack densities greater than about 0.1, they remain in reasonably good agreement up to a density of 0.3 (i.e. within about 10% error). Unfortunately the Nishizawa model is not presented in a form readily applicable to the experimental data of this study.

More recently, Sayers (1988a,b, 1990, and references therein) has presented a model for crack anisotropy in a rock, using a Crack Orientation Distribution Function (CODF). This function gives the probability of a crack having a given orientation with respect to a reference frame, and can be used to calculate variations of velocity for elastic waves in the long wavelength limit. Given velocity measurements, an inversion can be made to obtain the microcrack orientation distribution function. Coefficients of a series expansion of the CODF in generalized spherical harmonics are obtained to the fourth order for the angular variation of velocity. This allows construction of microfracture pole figures. The Sayers method has considerable potential for characterising crack development during deformation, but analysis requires the simultaneous measurement of velocities along three mutually perpendicular axes.

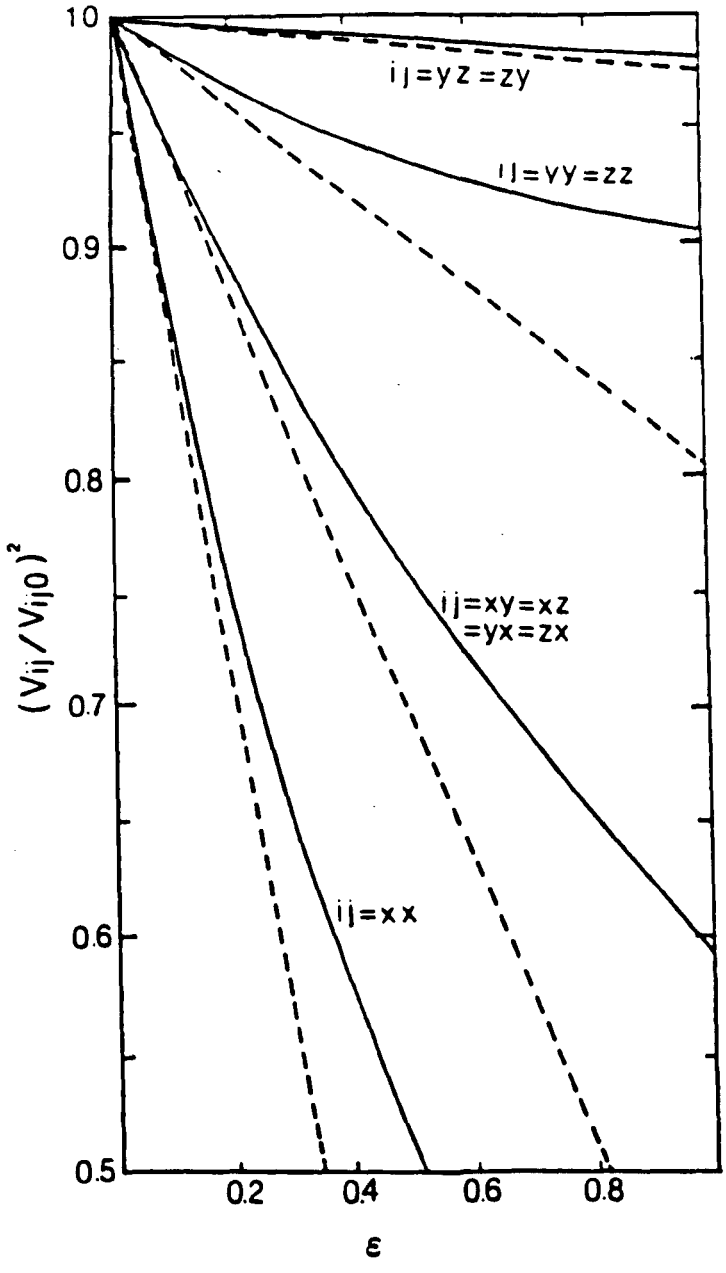

Fig. 2:6 Change of $(V_{ij}/V_{ijo})^2$ as a function of crack density parameter ε. The dashed lines are the linear fit of Soga et al. (1978) to Anderson et al's (1974) numerical analysis. The solid lines are determined by Nishizawa (1982) using a step wise iterative method. Soga et al. determined failure to occur when the crack density in the direction of the unique axis reached 0.3, about 10% error is seen between the models at this point, (from Nishizawa, 1982).

2:5 Attenuation studies.

Seismic studies have perhaps been the most productive geophysical method used to investigate the constitution of the interior of the earth. Yet of the two aspects of seismic studies, velocity and attenuation, velocity has provided by far the bulk of this information. This is perhaps because good quality attenuation data is difficult to collect and even more difficult to interpret in terms of rock properties. The propagation of acoustic waves is essentially an elastic process, whereas rock failure is basically a non-elastic process. Therefore, the link between acoustic wave velocity and rock strength is only indirect. However, attenuation is a non-elastic process and therefore may be expected to be even more sensitive to internal changes in a rock sample than acoustic velocities. Attenuation mechanisms have been extensively reviewed by others (e.g. Winkler & Nur, 1982; Johnston et al., 1979), and this section is only meant as brief review of some of the important conclusions.

A fundamental feature of a stress wave propagating in all solids is the absorption of energy which results in a change of shape of the transient waveform and a degradation of its amplitude with distance. This degradation is due to two well-known effects:

1) "Intrinsic attenuation", which is a process that involves energy loss. Several mechanisms have been proposed as responsible for this process. These include simple friction at grain boundaries and across microcrack surfaces (Walsh, 1966), relative motion of matrix and fluid inclusions (Biot, 1956a,b), intercrack squirting (Mavko & Nur, 1975; O'Connell & Budiansky, 1977), partial saturation effects such as gas pocket squeezing (White, 1975), and a range of mechanisms which might only reasonably be considered to be significant in the mantle, such as systems undergoing phase changes (Spetzler & Anderson, 1968), atomic diffusion, and 'high-temperature internal friction background' (Jackson & Anderson, 1970).

2) "Apparent attenuation", where the processes are elastic and involve no energy loss but which still effect the shape and integrity of the waveform. These include geometric spreading, multiple reflections, mode conversions and scattering. Scattering becomes important as the wavelength of the seismic wave approaches the dimensions of

the heterogeneities. It is considered that other geometric effects can be eliminated by careful experimental technique (see section 5:7).

The measured attenuation is the sum of the intrinsic and apparent components. Therefore, in order to determine the intrinsic attenuation of the wave, the apparent attenuation needs to be corrected for; this can be very difficult. Attenuation can be defined either by the internal friction parameter (Q^{-1}) or its reciprocal the quality factor (Q). Where;

$$Q = (1/2\pi)\Delta W/W \qquad (2:20)$$

W is the total amount of energy stored per unit volume per cycle and ΔW is that part of w dissipated per cycle.

2:5:1 Laboratory measurement techniques.

In the laboratory, attenuation is measured by one of several techniques. These include the resonant bar method where transducers excite a bar of material at various resonant frequencies and the phase and amplitude of the decay with time is measured (Thill & Peng, 1974). A second technique involving the comparison of the amplitudes of waves reflected from the top and bottom of a sample that is situated between two lucite buffer rods has been described by Winkler & Plona (1982). However, the most common method is the spectral ratio technique (Toksoz et al., 1976, Sears & Bonner, 1981), which is analogous to the pulse-transmission method used to determine elastic wave velocities (section 2:4:2). The waveforms are recorded for later analysis. This technique is most suited for use in a pressure vessel with jacketed and saturated samples, provided corrections can be made for geometrical factors. Different laboratory methods determine different attenuation parameters. The quantities most commonly found in the literature are either (i) the attenuation coefficient α for plane waves propagating in an infinite medium, (ii) the logarithmic decrement δ, or (iii) the dissipation factor Q^{-1}. These parameters are related through the relationship;

$$Q = \pi f/\alpha V = \pi/\delta \qquad (2:21)$$

where V is the wave velocity and f the frequency.

2:5:2 Attenuation mechanisms.

1) Frictional sliding.

There is an intuitive attraction to simple Coulomb friction as an attenuation mechanism, since the sliding surfaces of grains or minerals can easily be envisaged, and similar sliding is often seen on macroscopic fracture surfaces. In this mechanism a passing elastic wave causes sliding at grain boundaries and across crack faces thereby doing work against friction and converting seismic energy into heat. It can be seen that this mechanism would be essentially frequency independent (i.e. the rate of occurrence of slip has negligible effect on the amount of energy loss) but would be highly amplitude dependent (with the strain amplitude effectively describing the amount of slip). This is termed a nonlinear mechanism, because of its strain amplitude dependence.

Detailed models of frictional sliding have been proposed by several authors. Walsh (1966) formulated a mathematical model for thin, penny-shaped, randomly orientated cracks in which sliding occurs between smooth crack faces. At least some portion of the crack faces need to be in contact with each other. When either a compressional or shear wave passes, the contact surfaces will be subjected to oscillatory stresses resolved into shear and normal components depending on the surface orientation. Sliding will then occur on the favourably orientated crack faces providing the static coefficient of friction is overcome. The main problem with the Walsh model is that it requires an unrealistically large spectrum of cracks per grain (Savage, 1969). Mavko (1979) extended the Walsh model to include irregular contact surfaces. Contact occurs initially only at the crack tips but as confining pressure is applied the elastic surfaces deform and the area of contact increases. The resulting normal stress on the contact surface is variable, and consequently the frictional stress is variable. As a wave passes, the applied shear stress will almost always exceed the frictional coefficient over at least a small region near the contact edges causing frictional sliding. Walsh & Grosenbaugh (1979) have proposed a model which again assumes irregular crack surfaces. However, the distribution of the asperity heights is taken to be nearly Gaussian in nature. The strain amplitude dependence in this model shows that for low strain amplitudes work is done on the low contact tail end of the distribution. Since the distribution here is relatively flat, Q would appear independent of amplitude. As strain amplitudes increase work is done on the contact near the peak of the crack area distribution and Q would appear to decrease.

2) Other Solid Phase losses.

At high pressures and temperatures, other solid phase mechanisms may be important. These include; damped resonance of pinned dislocation segments, dislocation unpinning, motion of dislocation kinks, atomic diffusion, grain boundary relaxation and vacancy diffusion (Mavko et al., 1979). However, these mechanisms are not thought to be important in the upper crust. An extensive review of these mechanisms is given by Jackson & Anderson (1970).

3) Attenuation due to viscosity and flow of saturating fluids.

Briefly, there are two sets of processes thought to be important where pore fluid occurs. Firstly, those which occur on the "local" pore-scale level, and secondly, mechanisms which envisage the rock matrix moving as a whole with respect to a saturating fluid. The former includes such processes as local pressure gradients caused by varying pore geometry or the passing seismic wave, and gas bubble squeezing. Work is then done in moving fluid from place to place. These and other grain scale attenuation mechanisms are discussed in detail by Johnston et al. (1979). The latter fluid-attenuation mechanisms have been modelled by Biot (1956a,b), who developed a comprehensive theory of wave attenuation in a two phase medium. Attenuation results from the viscous interaction of the rock framework and the fluid and is considered to be significant in porous rocks and at the higher acoustic frequencies.

2:5:3 Laboratory and field observations.

1) Frequency dependence.

It is commonly held that attenuation is essentially frequency independent for both laboratory and field measurements over a wide range of frequencies, 10^{-2}-10^{7}Hz, (for example, McDonal et al., 1958; Peselnick & Outerbridge, 1961; Knopoff, 1964; Attewal & Ramana, 1966; Pandit & Savage, 1973; Hamilton, 1972; Sheriff, 1975; Johnston & Toksoz, 1980). Although constant Q (frequency independent) attenuation is widely accepted, it is unlikely that a single attenuation mechanism is responsible over the whole range of frequencies. Indeed, it has been pointed out (Jackson & Anderson, 1970) that many of the physical mechanisms responsible for attenuation in the mantle (e.g. damped resonance, static hysteresis, thermoelastic relaxation etc.) have a strong frequency dependence. Jackson and Anderson note that a distribution of chemical and physical

properties might weaken this frequency dependence, so that a multiphase, multicomponent system with a spectrum of inhomogeneity sizes would show only a weak frequency dependence. However, frictional sliding is essentially a frequency independent mechanism.

2) Strain Amplitude dependence.

Whether attenuation is linear or nonlinear has been found to be crucially dependent upon the strain amplitude of the interrogating wave (Gordon & Davies, 1966; Winkler et al., 1979; Johnston & Toksoz, 1980). Generally attenuation is found to be highly nonlinear for large strain amplitudes (that is $>10^{-6}$), and low confining pressures (<100MPa; Johnston & Toksoz, 1980). Some work (e.g. Johnston et al., 1979) has also shown that if the strain amplitude is increased further, the attenuation again becomes linear. In the field, seismic waves have frequencies that are typically less than a few kHz, and propagate at strains much less than 10^{-6}. Also, the rocks they propagate through will generally be subject to high confining pressures. Therefore nonlinear attenuation will be suppressed. Since grain boundary friction is the most likely source of nonlinear, amplitude-dependent attenuation, the implication is that friction may not be a dominant mechanism of energy dissipation under crustal conditions. Savage (1969) also points out that, for typical strain amplitudes of seismic waves and for reasonable crack dimensions, the slip across crack faces is less than the interatomic spacing and, therefore, cannot be described in terms of conventional frictional sliding. However, under laboratory conditions, frictional sliding is the most likely cause of attenuation in deforming samples. This is because frictional sliding is most likely to occur under the conditions of low confining pressures and high strain amplitudes (Winkler et al., 1979). The strain amplitudes associated with ultrasonic testing are in the range 10^{-6}-10^{-3} (Barasch, 1970).

3) Pressure and temperature dependence.

Generally, attenuation decreases with increasing pressure (e.g. Winkler et al., 1979; Toksoz et al., 1980). The rate of decrease in attenuation is greatest at low confining pressures and levels off at high confining pressures. The rate of change in Q is approximately the same for both P and S waves (Johnston & Toksoz, 1980), and is analogous to the similar effect seen for velocity with increasing confining pressures (Birch, 1960; Nur & Simmons, 1969a; Toksoz et al., 1976; Jones, 1989). However, the increase in Q is much larger than that seen for velocity. Johnston & Toksoz (1980)

reported the observation that only a few percent increase in velocity is reflected in an increase in Q of up to 60%.

Both field and laboratory observations for the temperature dependence of attenuation are very scarce. However, Gordon & Davies (1968) found that Q is generally independent of temperature at low homologous temperatures. Johnston and Toksoz (1980) noted that Q decreased sharply in Berea sandstone, at temperatures above 400°C. This was considered to be the result of thermal expansion coefficient mismatch between grains causing intergrangular cracking.

2:5:4 Summary of attenuation characteristics.

The characteristics of attenuation in response to changes in the surrounding physical environment can be summarised as follows.

1) Q appears to be frequency independent for most conditions (attenuation coefficient α is proportional to f^1).

2) Q is linear at small strain amplitudes, but is strain amplitude dependent at higher strains($>10^{-6}$).

3) Attenuation in water saturated rocks is greater than that in dry rocks.

4) The primary mechanism for attenuation in laboratory ultrasonic tests appears to be friction.

5) Attenuation decreases (Q increases) with increasing confining pressures; the rate of increase being greater at lower confining pressures.

6) In fluid saturated porous rock, attenuation due to fluid phase flow is secondary to the role of friction (Johnston et al., 1979). At ultrasonic frequencies, the Biot-type fluid flow mechanism while not necessarily dominant, may play an important role in overall attenuation at high pressures. Squirt flow may be important at lower frequencies and in partially saturated rocks.

It is worth pointing out that since the attenuation coefficient is defined by $\alpha=\pi f/QV$, and that the velocity of S waves is lower than P waves, the attenuation per unit distance of S waves is higher than that for P waves for both dry and water saturated cases.

2:6 Summary of brittle rock behaviour.

Brittle behaviour of rocks can be characterised through various well defined stages of development; this was first attempted by Brace (1964a). In any one experiment not all the stages will necessarily be present. However, it has proved a useful summary of brittle behaviour. Paterson (1978, pp157-159) gives a four stage description of brittle behaviour, however, it seems appropriate for the tests performed in this study to extend this subdivision to five stages (following Jones, 1989). The Paterson delineation is considerably updated and re-evaluated in the light of recent acoustic work. Fig 2:7 shows a schematic stress/strain curve for a deforming brittle rock. The subdivisions outlined below are marked on the diagram.

Stage 1.

This is characterised by a concave upwards trend in the stress/strain curve. This stage is most pronounced in porous rocks at low confining pressures. It may, however, be completely absent for low porosity and very brittle rocks. Vp parallel to the differential stress axis will increase, while Vp perpendicular to this axis is relatively unaffected. Vs perpendicular to this axis will either show no increase or a small increase depending on the direction of polarization (an increase may be seen for shear wave polarised in the axis of compression). Acoustic emission activity is low and contains a significant quantity of low frequency components.

This region is considered to mark the closing of favourably orientated microcracks making the rock stiffer and causing an increase in the effective Young's modulus along the major axis of compression.

Stage 2.

This stage describes predominantly elastic deformation. The stress/strain curve is linear, and cycling involves little or no hysteresis. In highly porous rocks this region may be indistinct or even absent. However, for most brittle rocks at moderate confining pressures, an elastic region appears to be justified. Vp and Vs both parallel and perpendicular to the maximum stress axis remain fairly constant. There is little or no acoustic emission activity.

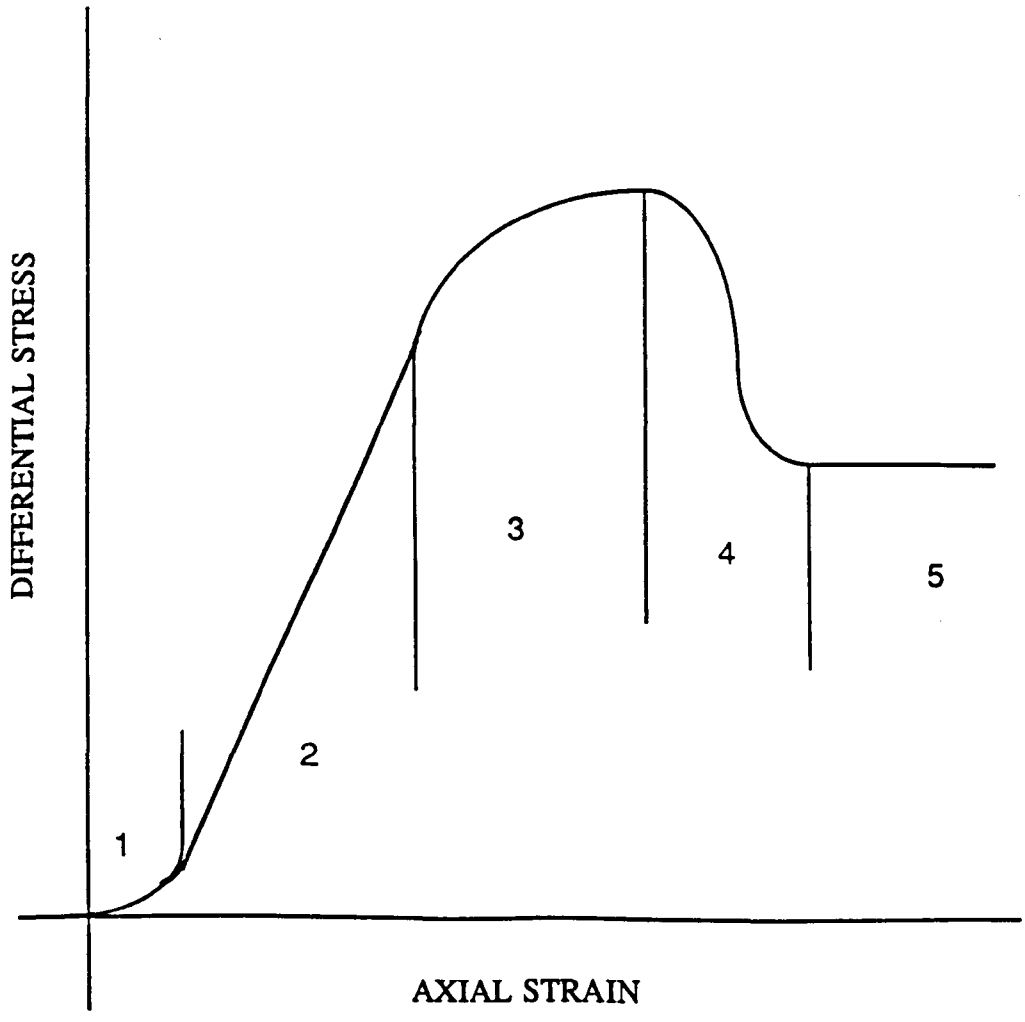

Fig. 2:7 A synoptic view of brittle failure. The stages 1 to **5** outlined in the text are delineated on an idealised stress/strain curve.

This is a region of predominantly elastic deformation of the rock matrix and is essentially reversible.

Stage 3.

The stress/strain curve clearly deviates from linearity becoming concave downwards. Deformation, however, remains stable, a positive increment in stress being needed for an increase in sample strain. Vp both parallel and perpendicular to the major stress axis decrease, the latter decreasing significantly more than the former. Vs propagating perpendicular to the deviatoric loading axis also decreases moderately if polarised perpendicular to this axis. The shear wave polarised parallel to this axis is little affected. The acoustic emission rate increases exponentially and the sample becomes dilatant.

This stage marks the onset of new microcrack growth, most of which is in the axial direction. The cracking is fairly well distributed throughout the sample except very near the ram ends, where it is virtually absent. The extent of crack interaction is not known. The rock is becoming more compliant with the effective Young's modulus decreasing. The effective Young's modulus perpendicular to the major stress axis decreases at a faster rate than the modulus parallel to this axis. The microcracking is markedly anisotropic but there remains a generally homogeneous crack distribution.

Stage 4.

The rock shows a marked reduction in its load bearing capacity, this may or may not result in catastrophic failure of the specimen. This will be determined by the relative stiffness of the machine and sample (section 3:5). The acoustic emission may show an apparent quiescence and the seismic b-value may tend from an erratic pattern to a well constrained low of about 0.5. Elastic wave velocity in all directions continues to decrease, often at a slightly accelerating rate.

This region is thought to mark the onset of accelerated crack growth. During this phase cracks coalesce to form a macroscopic failure surface prior to dynamic failure including a stress drop. There is some evidence that cracking activity is preferentially

occurring along the plane of the eventual failure surface. All elastic wave velocities must now be considered to represent some sort of average value along an inhomogeneous travel path.

Stage 5.

After failure there is a period of stable sliding along the fracture plane. The stress/strain curve will then level off to an approximately constant value. The AE activity reduces to an intermediate level, and the seismic-b value regains an intermediate value. The elastic wave velocities in all directions remain approximately constant.

The acoustic emission activity is probably due to movement of fault asperities across each other rather than continued cracking (as the elastic wave velocities remain constant). The level of AE activity is then probably pressure dependent. No significant wearing of the fault occurs over small strains and the dynamic coefficient of friction remains approximately constant.

CHAPTER 3

TRIAXIAL DEFORMATION AND PORE PRESSURE SYSTEMS.

3:1 Introduction.

The triaxial cell used in this study is that described by Edmond & Murrell (1973), Ismail (1974) and Jones (1989). It is a conventional gas-medium rig with a stepped balanced ram. The design specifications have been described in detail by the above authors. During the course of this study substantial modifications to the triaxial loading and physical measurement systems have been made. Specifically, the motor driven actuator has been replaced by a highly responsive servo-controlled actuator. The commissioning of the new actuator is discussed in detail in this chapter. The upgrading of the acoustic measurement system is discussed in detail in Chapter 4.

A general review of triaxial testing is given by Paterson (1978), and a detailed description of a state of the art triaxial cell is given by Sammonds et al. (1991). For a review of the practical problems encountered during triaxial testing see Tullis & Tullis (1986).

3:2 A brief description of the triaxial system.

Fig. 3:1 shows schematically the thick walled pressure vessel at U.C.L. A jacketed right cylindrical specimen (15mm diameter by 45mm long) is located between upper and lower rams. Loading is by means of a stepped balanced ram; this design requires a complicated moving seal arrangement. The rams are hollow and allow access to the sample ends. Most commonly piezoelectric transducers are located in the ram ends and electrical feed-throughs allow access to the outside of the vessel (fig 3:2). The hollow ram arrangement has also been used in this study to allow fluid access to the sample, thus allowing pore pressure/volume changes to be measured.

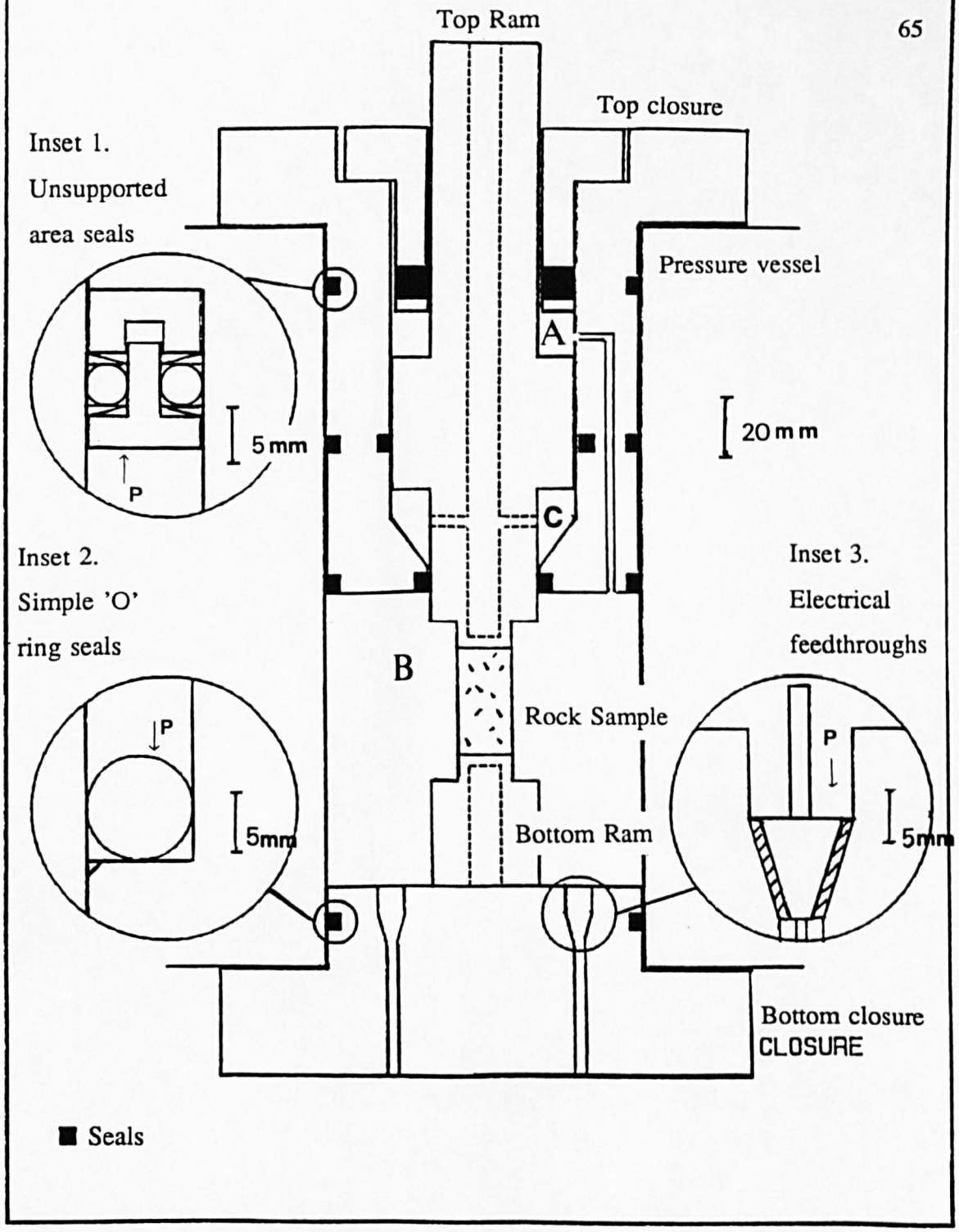

Fig. 3:1 Schematic drawing of the triaxial cell at U.C.L., showing the pressure vessel, the closures and the rams. The seals are also shown. The balanced ram requires a complex arrangement of moving seals. The confining pressure (B) is bled to the ram annulus (A), C is at atmospheric pressure. Detail of the ram ends and the transducer location are shown in fig. 3:2. The diagram has a horizontal exaggeration of 1.5 (from Jones, 1989).

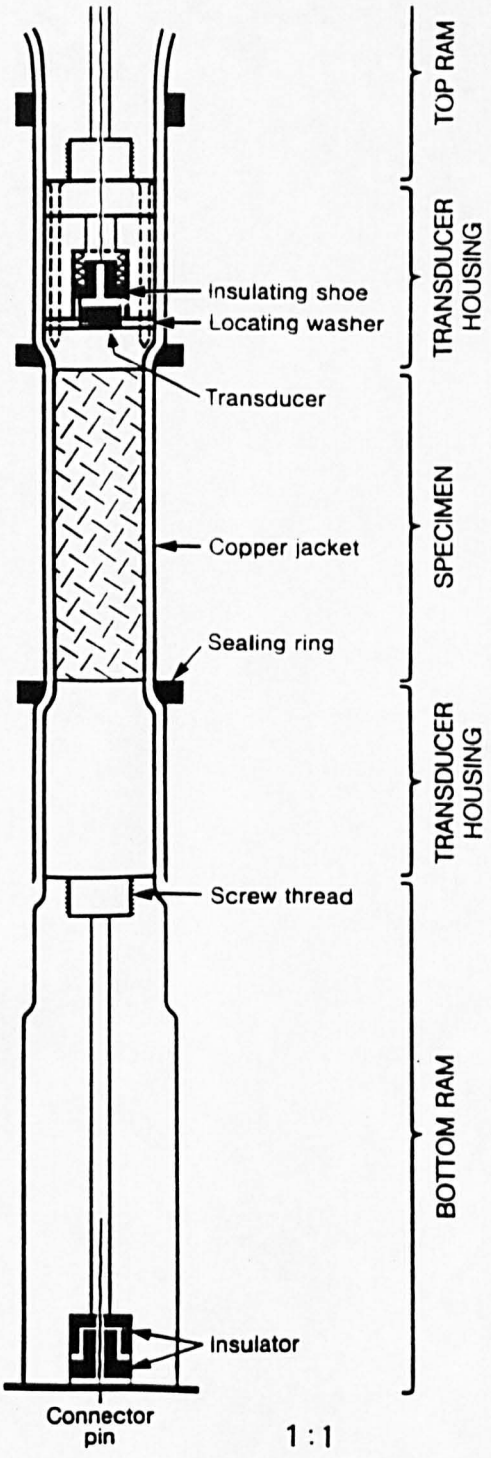

Fig. 3:2 A detailed view of the hollow ram ends and the jackèted sample. The transducers are placed near the ram/sample interface, electrical contact with the transducer is made via a brass "shoe" which is securely fixed using silver conducting paint and is held in place with a spring.

The vessel is designed to operate at pressures up to 1.4GPa and an internal furnace allows temperatures of up to 1000°C to be attained. The confining pressure is supplied by a three stage compressor pump built by Harwood Engineering of Massachusetts, U.S.A. Oxygen-free nitrogen is used as the pressure medium. The design and operation of this pump is described in detail by Jones (1989). The vessel is a dual block design, and comprises of two concentric rings with an interference fit. The outer body was heated and the liner cooled to achieve the fit. This induces an initial hoop compression in the liner and hoop extension in the outer body, which distributes the induced stress resulting from internal pressure more evenly. The stresses induced in the vessel remain within the elastic limit of the vessel up to the maximum design pressure. The working volume within the vessel is 80mm diameter by 294mm long. Retaining nuts are required to hold the end plugs in against the internal pressure. The end plugs form a seal between the ram and the vessel and also afford access to the vessel.

Leak-free sealing needs to be effective in three general areas in a triaxial cell, and each of these requires a different approach.

1) Closure seals. These consist of both static and moving seals which seal the closure against the vessel interior and the ram. Between the closures and the vessel there are four static seals; and between the top closure and the ram there are three moving seals. The moving seals need to be both virtually frictionless and leak-free. With gas medium vessels this can be difficult. Bridgeman-type unsupported area seals (described by Holloway, 1971) are used. These seals consist of an 'O' ring backed by two wedge shaped anti-extrusion rings made from soft steel and beryllium copper.

2) Electrical feed-through seals. These allow electrical connections made inside the vessel for the furnace and the acoustic transducer to be taken outside. Twelve feed-throughs are available. In such seals, the wire must remain electrically isolated from the vessel. This is achieved using thin sheaths of a hard epoxy resin based plastic called Vespel.

3) Jacket seals. The copper jacket separates the specimen from the confining medium. Sealing the jacket is important to prevent the confining medium penetrating the sample. It must also prevent the transfer of chemical species between the gas and the rock. A soft copper jacket seals to the bottom ram once and the upper ram twice (fig. 3:2). The jacket is sealed at the ram ends and above the transducer housing on the top ram. This is necessary as the top transducer is vented to atmosphere. The seal is effected by tightly fitting rings which squeeze the jacket between the ram and the ring. The seal is made against a rising portion of the ram diameter. The inside diameter of the rings is 0.1mm smaller than the outside diameter of the jacketed ram, which gives a reliable interference fit.

The upper ram is of a balanced single-stepped design. The piston has an annular portion along its length of larger diameter than the main ram. The annular area of the top shoulder is equal to the cross-sectional area of the ram inside the working volume of the pressure vessel. The confining pressure experienced by the sample is bled through galleries to the top shoulder of the ram annulus. Thus when a confining pressure is exerted on the sample the piston will experience a net zero force. Therefore, hydrostatic pressure does not have to be overcome in order to deform the sample; the load applied by the load cell is merely the deviatoric force. This enables small axial loads to be measured accurately, while also allowing high differential stresses to be applied. The load cell does measure seal friction, which is usually very small when compared to the strength of the rock. Seal friction can be calculated and simply subtracted from the differential stress. However, in practice it is easy to note the seal friction on an analogue plot of load against axial strain, and then simply remove it using software. The upper ram is made of hardened D2 tool steel and has a maximum load capacity of 600MPa, and a maximum temperature capability of 600°C. A new upper ram was designed during this project to enable pore fluid pressure/volume measurements to be made on a deforming sample. The new ram has a high pressure fitting which allows the high pressure tubing from a newly-built, servo-controlled pore fluid pressure intensifier and volumometer (see section 3:7) to seal effectively at the ram end (fig. 3:3). This "marrying" of the triaxial deformation system and the new pore fluid pressure equipment allowed for the first time, pore fluid volume change experiments to be performed in the triaxial cell.

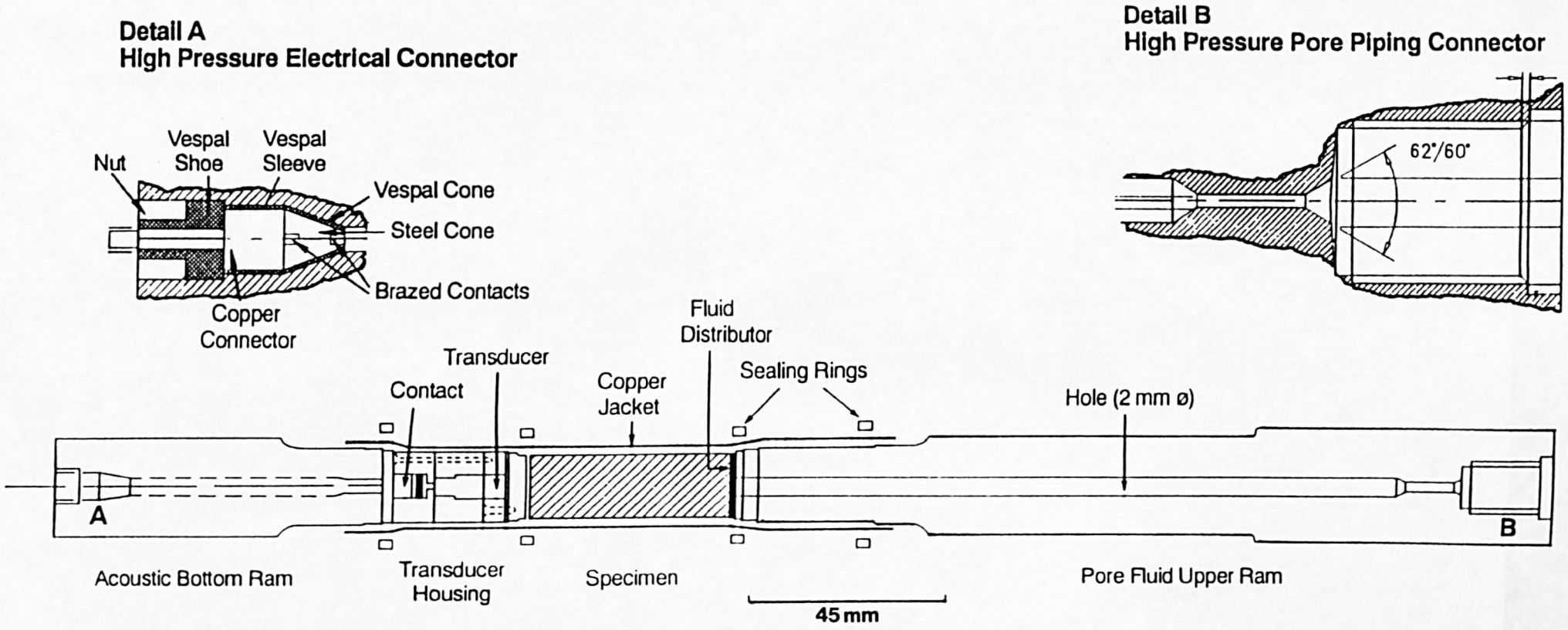

Fig. 3:3 A diagram of the sample and the new upper ram with the pore fluid inlet connector; used in constant pore fluid pressure tests with contemporaneous acoustic measurements.

The sample jacket is made by a series of annealing and stretching steps using brass formers which shape the jacket to the ram ends. The ram assembly is held together by the jacket, while a press is used to force the jacket sealing rings into place. This process also ensures that the assembly is vertically aligned (fig. 3:4). The complete ram assembly is then lowered into the pressure vessel. The top collar is dropped over the ram, and the breach nut secured. An external 20Tonne load cell and actuator are placed in series with the ram assembly. Strain is measured externally using Linear Variable Differential Transformers (LVDTs).

3:3 The loading system.

Initially, the loading system consisted of a constant speed motor driven through reduction gears. A magnetic clutch engaged a recirculating ball screw actuator. Thus rotary motion provided by the electric motor was converted to longitudinal motion which deformed the sample at a constant displacement rate. The displacement rate could be selected between 0.3mm/s and 10^{-8}mm/s by adding or removing sets of radial gears from the gear box. The advantage of such a system is that a wide range of strain rates can be chosen and it also provides a very stable displacement at the slower rates. However, because the motor drives at a constant speed, a constant strain rate is maintained only when the sample deforms in a linear-elastic manner. During the course of this study, a completely new 200kN capacity, servo-controlled hydraulic loading system was designed to replace the ball screw actuator. The system was designed in conjunction with Servotechnique of Middlessex, England. The system proved difficult to commission, and various modifications were necessary before it performed to the desired specification. The commissioning of this unit, carried out by the author, is discussed in some detail.

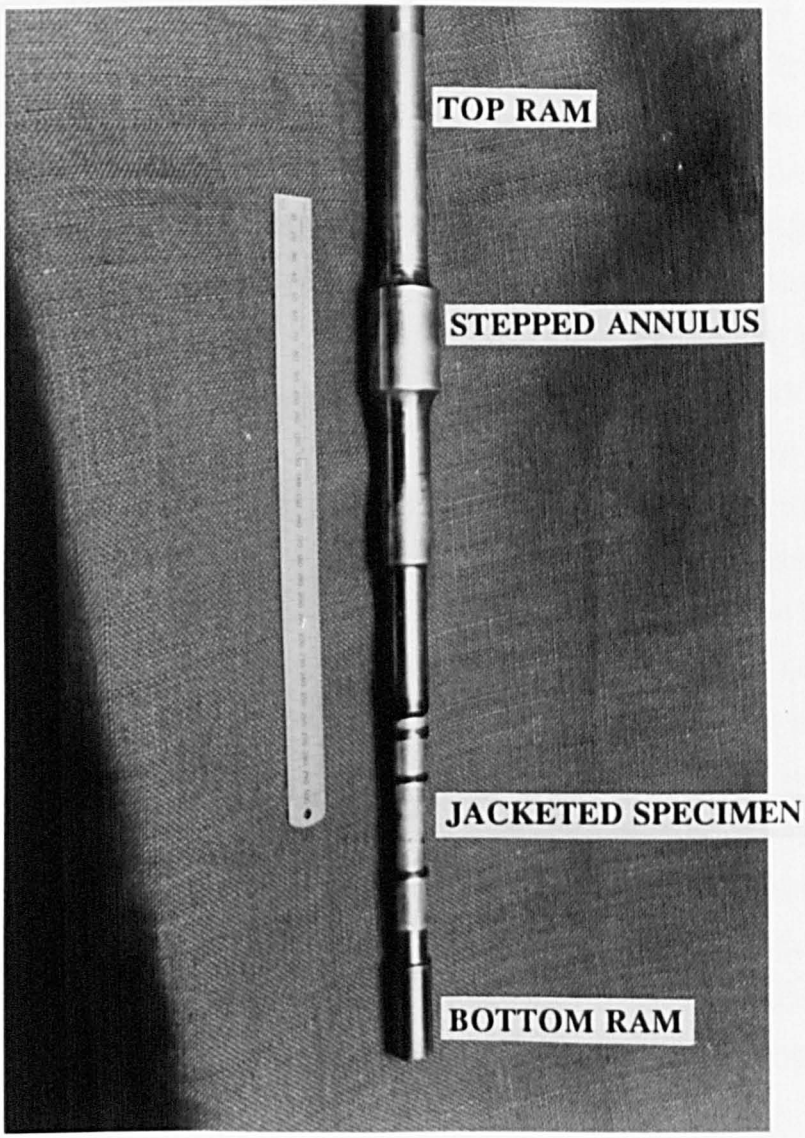

Fig. 3:4 The ram assembly consisting of the top and bottom rams, held together in alignment with the jacketed specimen by the sealing rings.

3:4 The servo-hydraulic actuator.

Fig 3:5 shows the servo-hydraulic actuator, and the pressure vessel. The hydraulic ram can apply a load up to 200kN. The servo-controller works by comparing a received signal from either a LVDT (when under strain control) or from the load cell (if under load control) with an internally generated reference signal. The servo-valve then, upon command from the servo-controller, proportions oil flow from the hydraulic power supply so as to position the actuator rapidly. This can be achieved within tens of milliseconds for small displacements. A locating pin ensures the actuator is directly in series with the ram assembly, before loading begins. The actuator slides into position on roller bearings, and is moved to the side to allow access to the ram. When the actuator is in position above the ram it is bolted down using four bolts which are tightened to a torque of 200Nm. This provides a very rigid assembly. Fig. 3:6 shows the servo-hydraulic actuator in series with the external load cell, and the upper ram. The external LVDTs used to maintain strain control are also shown. The electronic control panel for the servo-hydraulic actuator allows deformation to be under either strain, load or displacement control. Control can be passed between load, strain or displacement when the donor and receiving modes are balanced. This means no rapid repositioning of the actuator occurs as a consequence of changing between control modes. Balance is achieved by adjusting a potentiometer on the mode to which control is to be passed, and is indicated by two lights above the potentiometer illuminated with equal intensity. Transfer of control then automatically takes place in a stable manner. Each control has a 5%, 20% or 100% selectable range which means that full scale deflection is then 5%, 20% or 100% of the maximum capacity of the control. This allows, for example, much greater sensitivity in displacement control, when only small scale displacements are required. Test limits can be set in both load and displacement control. In strain control tests external LVDTs are used as source for the feedback signal to the servo-control unit. The electronic unit is fully computer programmable, therefore preselected deformation paths can be followed. Test limits can also be set on either of the three control modes. Furthermore, the limits can be set to become operational after a preselected stress, strain/displacement coordinate has been passed. This enables the limits to become operational in the post peak stress regime, i.e. on the negative slope of a deformation curve.

Fig. 3:5 The pressure vessel and newly-commissioned servo-hydraulic actuator inside the steel safety cubicle.

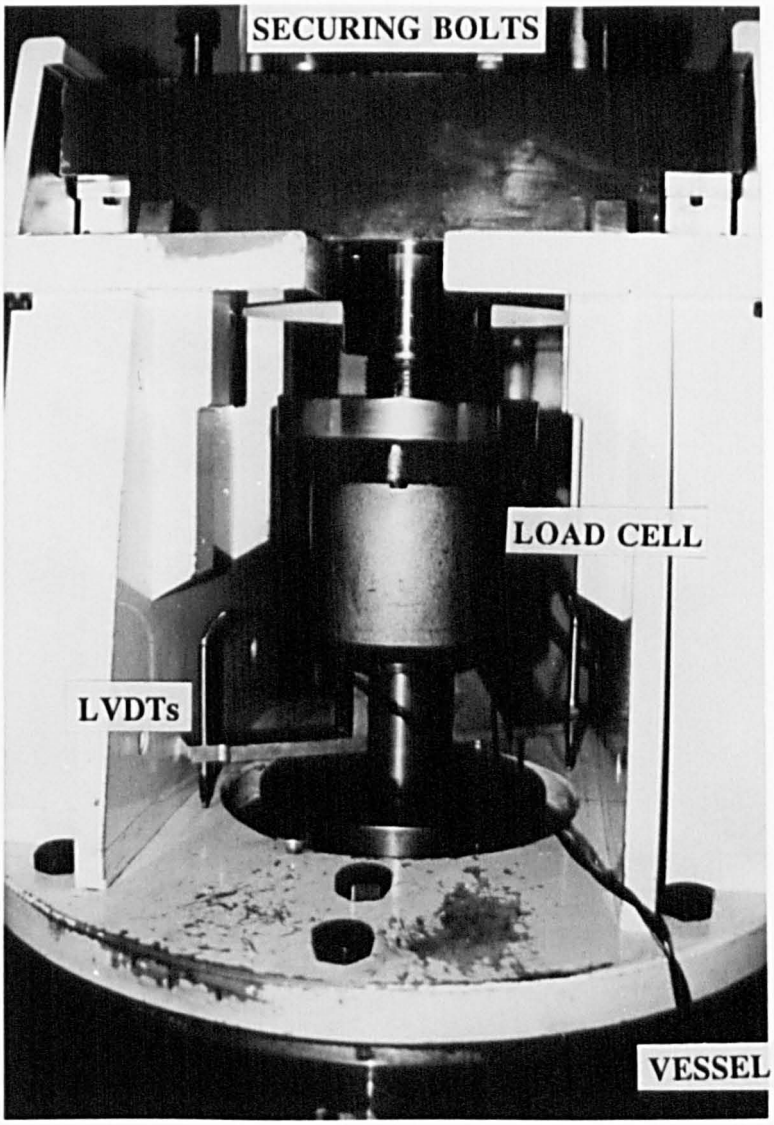

Fig. 3:6 The rigid servo-hydraulic actuator assembly along with the external load cell and LVDTs.

3:5 Machine stiffness.

The stiffness of a deformation system has been shown to have particular influence on the deformation path and point of failure in brittle rocks (e.g. Wawersik & Fairhurst, 1970). Premature failure of the specimen is a common consequence of an inadequately stiff machine. Generally, the stiffness of an elastic body can be thought of as either the force per unit displacement required to deform the body in a particular direction, or can be related to the amount of energy stored per unit displacement. As a rock specimen is loaded tensile stresses arise in the external frame that attaches the actuator to the vessel, these arise as a reaction to the compressive strength of the sample. The ram also experiences compressive forces and as the rock weakens the external frame and the ram will elastically unload. The rate at which the testing machine unloads is of crucial importance in examining the post-peak, strain softening of the specimen. This problem is discussed in detail in Rist et al. (1991), and is only outlined here. Following Rist et al., fig. 3:7 shows a force/displacement curve, ABCD, for a typical brittle rock. The portion B-C represents strain softening of the sample, that is, where the sample can support only a decreasing load with increasing sample strain. The drop in load from Fb to Fc requires energy to be absorbed by the sample in the form of an inelastic strain increase in the specimen. If the unloading path of the testing machine is represented by B-E, then the additional energy represented by the area BEC will be absorbed by the specimen. This can lead to premature catastrophic failure of the sample. However, if the unloading path is steeper than that of the sample (that is, if the machine is stiffer than the sample), then the machine will be able to unload at a faster rate than the specimen and the true sample deformation path can be followed. However, with some very brittle rocks, even very stiff machines will not be able completely to follow the strain softening path. This is because catastrophic failure of the sample can occur by conversion of elastic strain within the sample itself to permanent deformation without any advance of the loading piston.

In servo-controlled machines the effective stiffness is obtained by a control loop. In constant strain rate tests (those carried out in this study) this is achieved by controlling the rate of advance of the actuator by comparing a feedback signal from a LVDT with a programmed signal. The most desirable way to achieve a constant strain rate

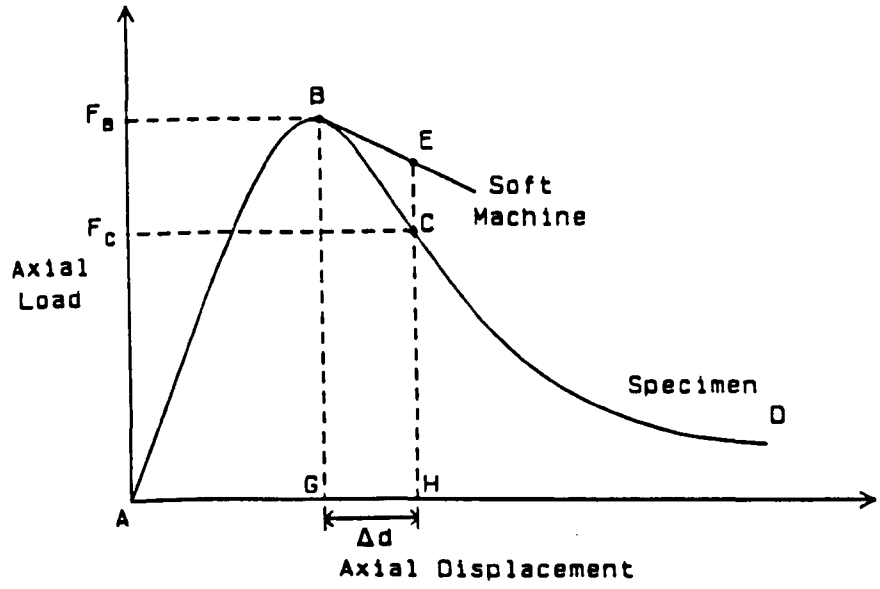

Fig. 3:7 A simplified load-displacement curve for a brittle rock, showing the post-peak softening of the sample. An unloading curve for a relatively soft testing machine is also shown for reference (from, Rist et al., 1991).

is to directly measure specimen strain by using displacement transducers directly mounted on the specimen. However, this is very difficult with jacketed samples (see Jones, 1989). In the present system, strain is measured externally using LVDTs which are located at the top of the upper ram. In order to compensate for the elastic deformation of the ram (and to effectively emulate an infinitely stiff machine), a ram deformation compensation circuit was incorporated into the new deformation system. This circuit was first designed for use on the ice-testing system at U.C.L. (Sammonds et al., 1991), and has been successfully used in the examination of the brittle failure of laboratory ice (see Rist et al., 1991). In this system a known proportion of the load signal is subtracted from the displacement signal, thus correcting for the elastic deformation of the ram. Previously, the amount of ram deformation (calculated by a series of calibration tests described by Jones, 1989) was removed from the externally measured strain by software in post-experiment analysis.

Calibration of the ram deformation circuit was carried out using a steel dummy specimen. Simply, a material of known elastic modulus is loaded by the testing machine, the ram deformation circuit is then dialled-in. When the resultant elastic response of the actuator-ram-sample string has the gradient of the known sample, then the elastic response of the test machine has been removed. Fig. 3:8 shows the plotted Young's modulus of steel (available from tables). The modulus response of the dummy sample, with and without the ram deformation circuit switched in, is also shown. It can be seen that the elastic deformation of the ram and loading system can be successfully removed using this method.

3:6 Commissioning the servo-hydraulic actuator.

There were a number of problems that needed to be overcome before the servo-controller worked to specification. These are outlined below:

1) Firstly, it was difficult to isolate electronically the controlling electronics from other electrical control and data acquisition equipment. Amplifiers used to improve the acoustic signal were seen to interfere severely with the stability of the servo-controller. Electrical

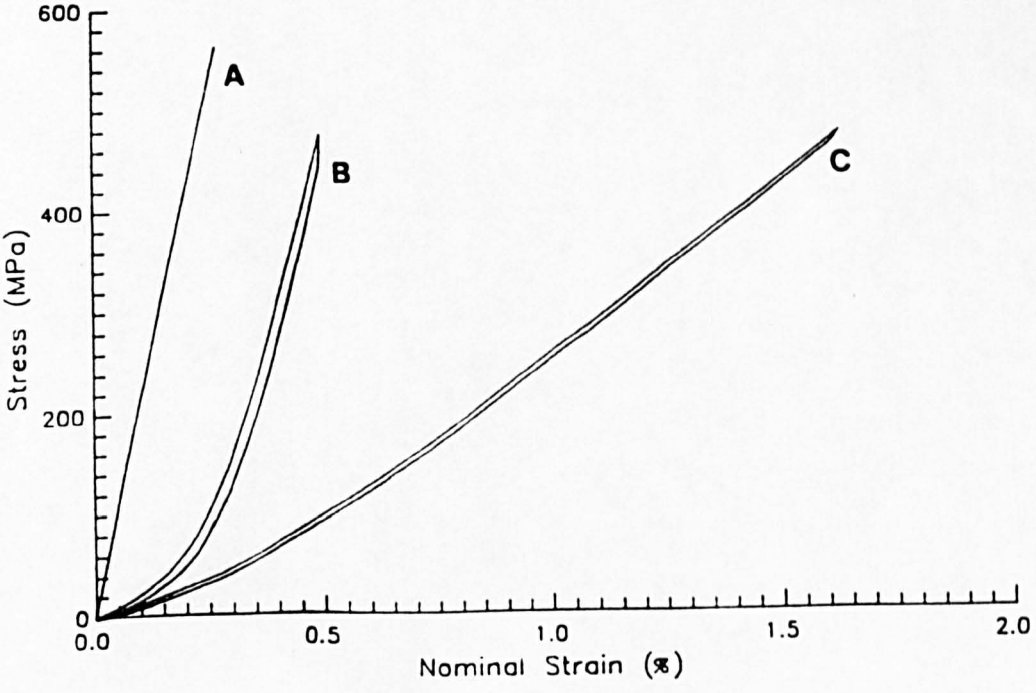

Fig. 3:8 Calibration tests on a steel dummy specimen, with the displacement modification circuit switched in (B) and out (C). The Young's modulus of the steel specimen is plotted for comparative purposes (A).

air pumps used to keep a safety valve shut in the main pressure pump were also seen to cause large voltage spikes on the load readings when they switched in. In order to minimise these effects the air pumps were fitted with electrical suppressers. Also all the electrical equipment was securely tied to a common earth using copper braid.

2) The servo-controller was seen to interfere significantly with the received acoustic waveform, causing both short and long wavelength noise to be superimposed on the waveform. It was difficult to determine whether the source of this interference was electrical or mechanical, however, it was strongly suspected to be mechanical. In a very stiff machine hydraulic vibration could easily be picked up by the transducers in the ram ends and converted into spurious electrical noise. Two methods were proposed to overcome this: (i) A transducer could be attached to the outside of the vessel, assuming it experienced similar noise patterns to the internal transducers an electrical subtracting circuit could then be used to remove the background noise from the acoustic pulse. (ii) Alternatively, a band-pass filter centred about the resonant frequency of the transducers could be used. It was found that a simple band-pass filter built in-house by the author was adequate to remove the interference. Although this reduced the overall amplitude of the received wave by about 30% the high frequency noise was reduced by more than 80%, and the longer wavelength noise was completely removed.

3) At first the stress/strain curves obtained using this equipment had a "stepped" appearance. This was especially noticeable for the stiffer rocks where relatively large stress increases were seen for small strain increments. After consultation with the manufacturers it was decided to upgrade the central processor board in the servo-control unit, increasing it from a 12-bit to 16-bit board with an integral smoothing function. These modifications completely removed the stepped appearance of the stress/strain curves.

4) System stability proved very difficult especially for rocks at high confining pressures. The instability was reduced by careful adjustment of the "loop-gain" circuit on the particular control mode used (in this case strain control) to a low level. This prevented the servo-controller from hunting back and forth for a value it continually overshoots. However, this by no means eliminated the instability. Previously, with the screw jack

actuator, the load cell contacted upon a simple cap that rested on the ram end. This cap had a single arm which held the external LVDT. In the highly active servo-controlled system the LVDT is used as a reference feedback signal during constant strain rate tests. As the load cell impinged on the end cap the ram experienced some frictional resistance causing flexing of the arm, this in turn led to the servo-controller becoming caught in violent feedback loops. This was overcome by placing a second identical arm holding a second identical LVDT diametrically opposite the first. The two LVDT readings were then averaged, and the averaged signal was used as the closed-loop reference signal. The end cap was also redesigned so that it could be held securely to the ram by brass screws. This has completely alleviated the system instability.

5) The ram deformation circuit described in the previous section has proved difficult to adapt to triaxial rock deformation. The ram deformation circuit subtracts a proportion of the load signal from the feedback strain signal. This is achieved by the manual adjustment of a potentiometer scaled in "percentage of the load voltage" signal. The proportion of load subtracted is calibrated for the amount of elastic strain the system experiences at a set load. It was found, however, that at high confining pressures where seal friction is large, the load increases in trying to overcome friction without a corresponding strain increment. The circuit then attempts to subtract a percentage of the increasing load signal from the zero strain signal. This results in a negative signal and the system becomes unstable. To overcome this, a second potentiometer was installed to allow a load offset to be selected below which the deformation correction circuit would not be switched in. Therefore, at each confining pressure the seal friction could be calculated, and a threshold could be set at which the correction circuit would become operable. This was partially successful, as it proved to be stable only at low confining pressures. The potentiometer which was situated directly on the actuator unit was taken outside the safety cubicle. Then during tests at high confining pressures the ram deformation could be manually dialled in. This improved matters but full ram deformation could not be corrected for before instability again became a problem. The reason for this unpredictability is thought to be the oscillatory nature of the ram/seal friction. This problem is unlikely to be fully overcome using external LVDTs. A modified upper ram is presently being designed to allow direct strain gauging of the sample.

3:7 The pore-fluid pressure intensifier.

The newly-developed pore pressure device was again built by Servotechnique and was commissioned by M.D. Read; a full description of which is given by Read et al. (1990). The fluid pressure intensifier can be used to generate pore pressures up to 700MPa. It has three modes of operation; (i) it can be used to monitor pore volume changes at constant fluid pressure, (ii) to measure pore fluid pressure changes at constant fluid volume, or (iii) it can be used to make permeability measurements. Essentially, a double ended piston moves within two closely coupled pressure vessels of different diameter and operating pressures. The pressure induced on the high pressure side of the piston is controlled by movement of the low pressure side. This low pressure piston is double acting, and its movement is controlled by an electronic servo-control unit. The feedback signal to the servo-control system is via either a displacement or pressure transducer depending on whether constant pore volume or constant pore fluid pressure is required.

CHAPTER 4

ACOUSTIC PROPERTY MEASUREMENT SYSTEM USED IN CONJUNCTION WITH THE TRIAXIAL DEFORMATION SYSTEM.

4:1 Introduction.

Fig. 4:1 shows a block diagram of the acoustic measurement instrumentation and the electronic recording and control equipment used in conjunction with the triaxial cell. All of the major electrical devices are described briefly, but a more detailed description is given for equipment newly-integrated into the system as part of this study. These new developments include; integration of a more powerful data acquisition and control computer (for which extensive equipment control and logging software was written), two universal counter-timers, a digitising oscilloscope, and an on-line plotter. Following improvements to the acoustic signal generation/receiving system, simultaneous compressional and shear wave velocity measurements were able to be made during triaxial deformation. This is an important advancement because the additional recorded parameter (i.e. shear wave velocity) allows damage processes to be modelled. The improvement in acoustic signal quality was achieved by optimising transducer performance after considering, in detail, transducer theory. Transducer performance is also discussed in this chapter.

4:2 Electronic, acoustic and data control equipment.

A Hewlett Packard HP214B pulse generator is utilised to produce a high voltage (up to 100V) rectangular pulse with a rise time of a few nanoseconds. The pulse width is selectable between 25ns and 10ms, and has a repetition rate selectable between 10Hz and 10MHz. The usual experimental settings used were; 100V pulse amplitude, 1μs pulse width, and 100Hz repetition rate. The pulse generator also emits a trigger pulse coincident with the leading edge of the rectangular pulse. This is used as the zero time reference for the electronic acoustic velocity measurement equipment, i.e. the counter-

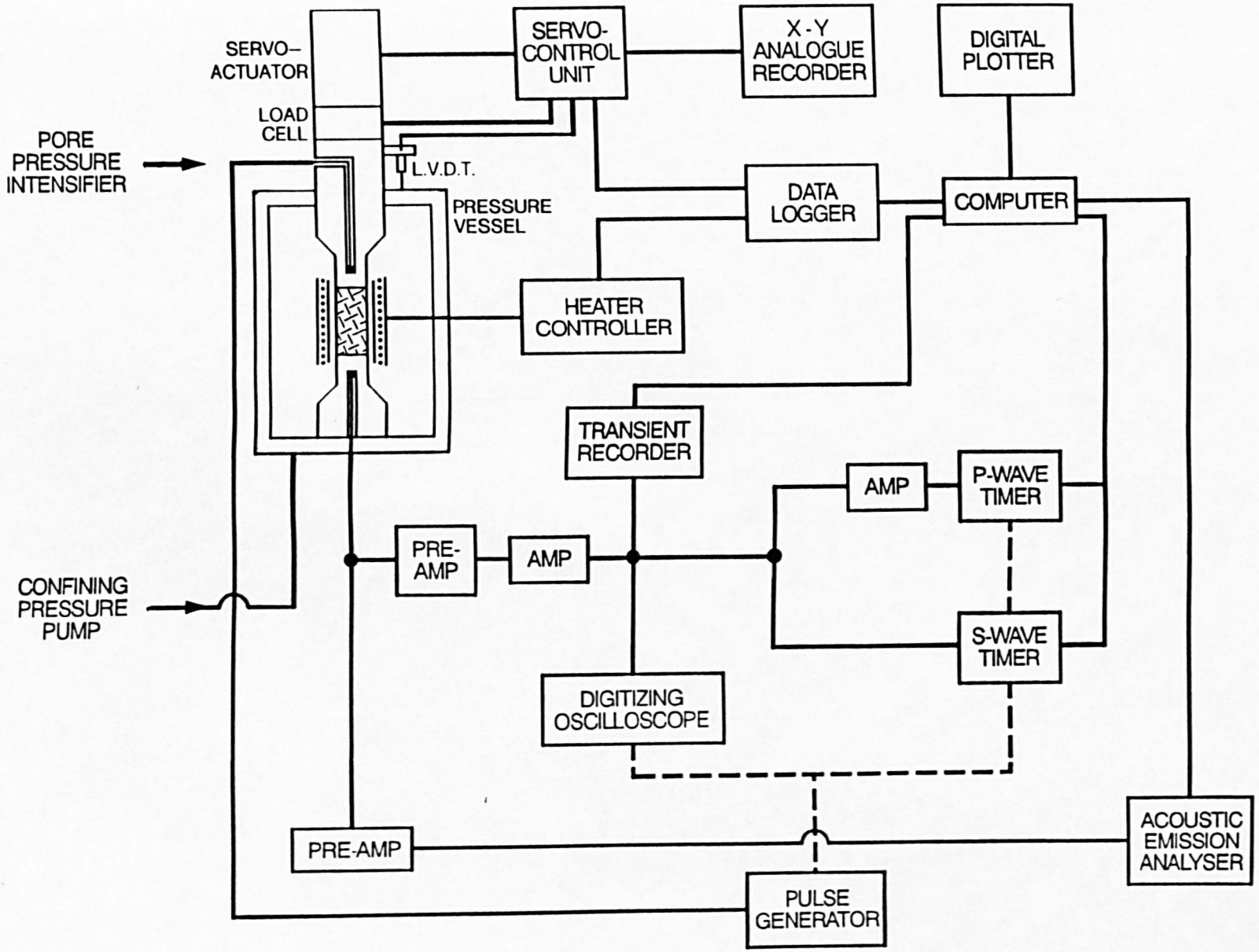

Fig. 4:1 Block diagram showing the electrical control and monitoring equipment, along with the acoustic generation and measurement instrumentation, used in conjunction with the triaxial deformation apparatus.

timers, the transient recorder and the oscilloscope.

Two Hewlett Packard HP5334B Universal counter-timers, were integrated into the acoustic measurement system during the course of this study. These devices have several switchable functions including frequency, rise time, 100 gate average and delay time recording. However, only the travel time function, which measures the time difference between two pulses, was used. The trigger pulse (from the pulse generator) was put into input A, and the acoustic waveform into input B. The internal clock in the counters are triggered when the amplitude of the waves put into the inputs (A and B) cross a pre-set voltage trigger level. The counter-timers then measured the time difference between inputs A and B. A reading can be taken every 100ms, and has an accuracy of 0.01μs.

The data acquisition system used is a Hewlett Packard HP3497A data control and acquisition unit; this is essentially a high speed analogue/digital converter. It has 20 channels with voltage ranges 0-0.1V, 0-10V, and 0-100V. The instrument is used to log the conditioned voltage output of the load cell and the strain LVDTs. The voltage range usually used is 0-0.1V, and the accuracy on this range is ±4μV.

A Datalab DL912 transient recorder was used to record complete waveforms. The recorder has two channels each with a 4Kbyte memory. The digitising rate is selectable between 500Hz and 20MHz which gives a time interval between each digitised point ranging from 2ms to 50ns. The peak-to-peak amplitude range is selectable from 0.05V to 20V. The digitised waveform is stored as a string of ASCII characters and can be logged by the computer via a parallel interface.

The oscilloscope used was a Hewlett Packard model HP54501A. This is a 100MHz digitising oscilloscope, and is fully computer programmable via a HP-IB interface. The oscilloscope and ancillary HP plotter were integrated into the system by the author. The oscilloscope is used to display the elastic waves propagating through the rock specimen in the triaxial cell. The computer logs the travel time measured by the counter-timers (which are set to trigger on the first arrival of each wave; see Chapter 5) and then

moves a cursor on the oscilloscope to this value via a parallel information-bus. This gives a continually updated display of the position on the waveform at which the counter-timers are triggering. The oscilloscope is usually set to display the mean of 128 waveforms, this takes only a few seconds to update. If extraneous noise is random then the summation of N waveforms reduces the noise by $1/\sqrt{N}$. In usual operation a hard-copy of the oscilloscope display is taken every 300s. The hard-copy is produced by sending a control command to the oscilloscope to down-load the digitised waveform to the HP plotter. This provides a readily usable display of waveform and trigger point. The digitised waveform can also be easily stored on computer.

The data acquisition and control computer used in this study was an Opus III, which is an IBM compatible PC. It has a 20Mbyte hard disk and its speed is switchable between 7MHz and 12Mhz. It is fitted with a CIL serial interface card and two parallel ports. A printer is used to provide a continuous hard-copy printout of the data during logging. This computer was integrated into the measurement and control system to replace the previous HP86 desktop computer which used 30Kbyte data storage cassettes. These cassettes had insufficient storage capacity when waveform recording was introduced. Data logging programs were written by the author, to interface the computer with essentially incompatible logging equipment. This caused several specific computing problems relating to interface commands and control speeds which are not discussed here.

The acoustic emission monitoring system used was Dunegan/Endevco series 3000 equipment. This is a modular system, and the following three modules were used in this study: (i) a 921 amplitude detector, (ii) a 920A amplitude analyser and, (iii) a 950 computer interface. Signals from the AE transducer located within the hollow bottom ram are first amplified by a pre-amplifier that is close-coupled to the triaxial system. The pre-amplifier has a fixed gain of 40dB and incorporates a high-pass filter with a 3dB cut-off at 100kHz. Signals are further amplified in the main body of the recording equipment by a wide-range logarithmic amplifier. This, in turn, drives a threshold comparator and a peak voltage detector. The voltage detector becomes operable when the peak voltage of an event exceeds the threshold (usually set just above the background noise level which is normally in the range of 28dB to 30dB). The acoustic events are then summed and the

peak voltages of these events are stored as cumulative totals in amplitude bins of range 0-100dB and of resolution 1dB. For detailed descriptions of this equipment, and its use in experimental rock and ice deformation see Jones (1989) and Rist (1990).

4:3 Wave generation and transducer performance.

As has been previously stated, one important aspect of this project has been the upgrading of the acoustic measurement system to enable simultaneous compressional and shear wave measurements to be made. This development required an in-depth consideration of transducer and wave propagation theory. As shown in fig. 3:2 (see page 66), piezoelectric transducers are located in the hollow ends of the loading rams; these rams impinge on the ends of the rock sample and the time of flight of the longitudinal and/or transverse wave can be measured. It can easily be realised that a wave propagating through a rock cylinder will be a complicated function of time and position the full analysis of which would be extremely difficult. However, there are a few general features that can be noted: (i) The first arrival will always be the direct compressional wave, and it will travel with the velocity of a compressional wave travelling through an infinite medium (provided certain wavelength:sample-width conditions are met, see section 5:6). (ii) Because of the geometry of the sample/transducer system, the source is neither a point source nor a plane wave source. It is, however, nearer to a point source as the width of the transducer is of the order of the wavelength of the propagating wave. (iii) Although waveguide effects will occur resulting in a waveform extended by multiple reflections and mode conversions, these will not interfere with the direct P wave arrival but could effect the S wave onset if of sufficient amplitude. However, it appears that the mode conversions preceding the shear onset are of low amplitude and usually the S wave onset is easily identifiable (see fig. 4:2 on page 91).

4:3:1 Types of transducer available.

It is well known that piezoelectric properties are inherent in some naturally occurring minerals such as quartz, Rochelle salt, tourmaline and barium titanate, and are linked to a certain type of crystal asymmetry. A pressure distortion of the crystal can lead to a redistribution of the charge elements in the lattice, the net result of which is the appearance of charges on the surface of the material. It is possible to select the crystals in such a way that deformation in a particular direction is maximised. For compressional wave transducers this will mean maximising their thickness expansion, and for shear wave transducers this will mean maximising their thickness-shear deformation. In general, both these actions are usually present simultaneously. In some crystals, however, expansion in one direction is not equalled in magnitude by a compensating contraction in another direction, and a net volume change occurs. These materials are obviously the better materials to use to achieve a pure waveform.

The transducers first used in this study were lithium niobate crystals with a resonant frequency centred around 1MHz (obtained through Roditi International and manufactured in the U.S.A. Valpey Fischer Inc.). The faces were gold coated and fine polished for good electrical and acoustic contact. These crystals have a high Curie temperature, and hence can be used effectively in experiments conducted at temperatures up to about 700°C (Jones, 1989). These transducers were perfectly adequate for P wave velocity measurements, where a signal-to-noise ratio of about 15:1 could be achieved, and provided a peak-to-peak amplitude of about 12V after amplification. However, the lithium niobate shear crystals produced a wave of poorer characteristics, with a signal-to-noise ratio of only about 5:1 and an amplitude of only about 2V after amplification. The shear wave onset was also almost completely obscured by a precursory compressional arrival.

Polycrystalline ceramic materials have been successfully used by others as piezoelectric transducer elements (e.g. Toksoz et al., 1976, and his co-worker publications). Polycrystalline materials do not have piezoelectric properties in their original state, since generally crystal orientation will be random and if a sufficiently large number of crystals are present then the net distortion will be zero. However, some

ferroelectric materials can be induced to have a net piezoelectric effect by placing the material in a suitably large electric field. The underlying polarising mechanism is a domain alignment analogous to that seen for ferromagnetic materials placed in a magnetic field. By their nature, such materials are limited to relatively low temperature use. Even at relatively low temperatures phase changes can occur removing the domain alignment. However, ceramic transducers appear to provide a much more efficient acoustic generation and measurement system, than do single crystal transducers. PZT is a lead zirconate titanate ceramic and is the most commonly reported ceramic transducer. It is common practise in virtually all ultrasonic testing equipment to use the same piezoelectric material for both the transmitting and receiving transducers (e.g. Birch, 1960; Toksoz et al., 1976; Thill, 1973). However, Silk (1984) points out that certain piezoelectric materials are either better as transmitters or receivers. Therefore, in order to optimise the overall efficiency of an acoustic system, different materials should be chosen for transmitting and receiving. The arguments put forward by Silk are followed closely in the following discussion.

Silk (1984, pp.10-11) discusses a method proposed by Callerame et al. (1979) of representing a piezoelectric material in terms of a transmitter efficiency parameter (Y_T) and a receiver efficiency parameter (Y_R). The product of $Y_T Y_R$ represents the overall performance of using any transmitter/receiver pair. The efficiency parameters are defined in terms of their electromagnetic coupling coefficient (k), the dielectric constant (ε) and the compressional wave velocity through the material. However, the important term is the dielectric constant (ε), as Y_T is proportional to $(\varepsilon_{33})^{1/4}$ and Y_R to $1/(\varepsilon_{33})^{1/4}$. Therefore, a good transmitter should have a large dielectric constant, and a good receiver a low dielectric constant. Physically, this occurs because the surface displacement of a piezoelectric material increases for a given voltage with an increase in ε. Hence ε increases the transmission qualities of the material. However, an increase in ε also produces a corresponding increase in the capacitance of the material. Therefore reducing the electrical output for a given surface strain, hence reducing the receiving qualities. Table 4:1 is taken from Silk (1984) and lists the efficiencies of some common piezoelectric materials normalised to quartz.

	Y_T	Y_R	Y_TY_R
Quartz	1.0	1.0	1.0
$LiNbO_3$	2.8	0.54	1.54
PZT-5A	70.0	0.21	14.6
PVDF	6.9	1.35	9.3
Lead Metaniobate	32	-	-

Table 4:1. Efficiencies of transducer materials normalised to quartz (from, Silk, 1984).

The best transmitters are clearly the ceramic, lead zirconate titanate (PZT), and lead metaniobate. The best receivers are Polyvinylidene fluoride (PVDF), quartz and lithium niobate ($LiNob_3$). However, PVDF, a stretched polymer, is difficult to obtain commercially.

The transducer pairings decided upon for this study were PZT-5A (compressional) and PZT-7A (shear) as transmitters, and lithium niobate as receivers. The efficiency of this pairing (Y_TY_R) is ≈37, compared to the previous transducer pairing of lithium niobate transducers which had an efficiency of 1.54. Therefore, a 20 fold increase in efficiency was achieved simply by careful selection of transducer materials. The ceramic transducers were again obtained from Valpey Fischer. PZT-7A shear wave transducers were chosen because they had the best shear coupling coefficients. PZT-5A was chosen for the compressional wave transducers because they showed good efficiency and excellent time stability characteristics. These transducers can be subjected to a maximum rated hydrostatic pressure of 140MPa, but have a low Curie temperature of only 350°C. This obviously precludes their use in high temperature experiments.

The improved transducer efficiency resulting from these changes allowed simultaneous P and S wave velocity measurements to be made using only the shear-

transducer-generated waveform. The slightly impure mode of oscillation of the shear wave transducer produces a P wave forerunner of sufficient amplitude to trigger a counter-timer. This compressional forerunner is a commonly reported phenomenon (e.g. Hadley, 1975a; Lockner et al., 1977; Brookes, 1984; Prof. M.S. King, personal communication, Imperial College London). Waveforms produced by shear wave transducers have been used by Brookes to make simultaneous P and S wave measurements under hydrostatic conditions, and by Hadley for uniaxial tests on granite. However, this is the first time the method has been used to systematically examine the changes in simultaneously measured P and S wave velocities for a series of rocks undergoing triaxial deformation at different confining pressures.

An example of a typical waveform produced by the shear wave transducers is shown in fig. 4:2. This is a waveform produced by shear wave transducers and travelling through a sandstone at a moderate confining pressure. The waveforms are most clearly defined when travelling through very fine grained rocks subjected to high confining pressures. This is probably the result of better acoustic contacts across the ram/sample interfaces, and also the lack of heterogeneities within the rock. However, the onset of the S wave in fig. 4:2 is clear and is marked by an abrupt "knee" in the waveform immediately followed by a large amplitude arrival. The waveform is re-amplified to clearly see the compressional wave onset (see Chapter 5).

4:3:2 Waveform characteristics.

An ideal acoustic waveform would have a sharp onset yet have as short a duration as possible. To reduce the length of the received waveform in the time domain either its frequency band-width can be increased or the rate of decay of the "tail" of the wave can be increased. The former can be achieved by "backing" the transducer with an energy absorbing material. The latter can be achieved by using higher frequency transducers; high frequencies have a greater attenuation per unit distance of travel than low frequencies. Both of these methods, however, reduce the useful energy of the signal, and a balance needs to be achieved between the desire for a short waveform and a good

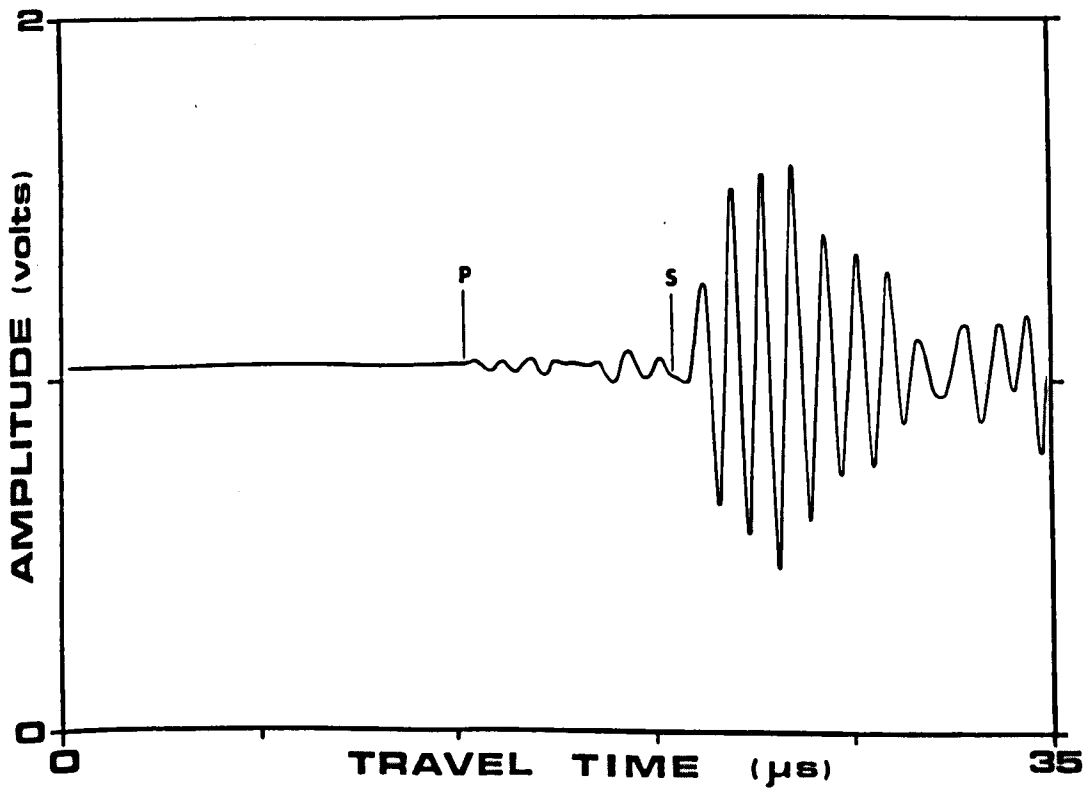

Fig. 4:2 A typical shear wave transducer generated signal. This was recorded for Darley Dale sandstone at 50MPa confining pressure (experiment DDA1). A low amplitude compressional wave forerunner can be seen (this part of the signal is re-amplified before it is used for triggering the P wave counter-timer). The onset of the shear wave is marked by a sharp change in direction of a preceding smooth waveform, and is followed by the first large amplitude shear arrival. The polarity of the S wave onset is the same as the P wave onset.

first arrival.

For velocity measurements, a good onset of the first arrival is of paramount importance, and therefore unbacked shear wave transducers were most commonly used in this study. However, for the specific case of acoustic emission (AE) measurements it is more important to have as little ringing of the receiver transducer as possible. This is because subsequent events could be masked by the reverberating tail of a previous event.

The ideal backing material is one with efficient transfer qualities, allowing as much energy out of the back face of the transducer as possible while also absorbing this energy. Plastics and rubbers are good absorbers in the MHz range but have a low acoustic impedance when compared with piezoelectric materials. Therefore, energy transfer would be relatively inefficient between the transducer and these backing materials. Metals have acoustic impedances close to those of many transducer materials, but they are poor absorbers. The most commonly used backing materials, at present, are high density metal powders suspended in an organic base (e.g. Araldite). Tungsten is often used as it has a high acoustic impedance and is relatively inert. The effect of the metal in suspension is to improve the acoustic impedance match between the transducer and the backing while the organic body provides the damping role. A small block of tungsten loaded epoxy was kindly supplied for use in this study by Dr. L. Bond (Mechanical Engineering Dept., U.C.L.). Space is restricted in the ends of the loading rams where the transducers are situated (fig. 3:2, page 66), so only a few millimetres of the material could be bonded to the rear of the transducers. Because of its receiving qualities a backed lithium niobate compressional transducer was used for logging acoustic emissions. Figs. 4:3a,b show compressional waves received by transducers both with and without acoustic backing material, respectively. It can be seen that even a small amount of backing material can reduce the reverberating tail of an acoustic waveform substantially, although the peak amplitude of the wave is also reduced.

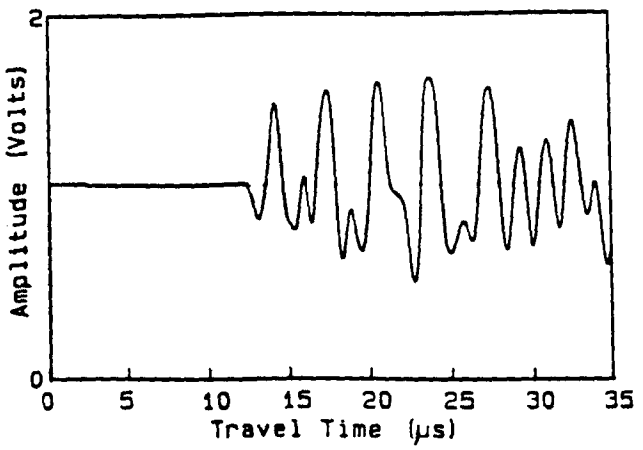

a

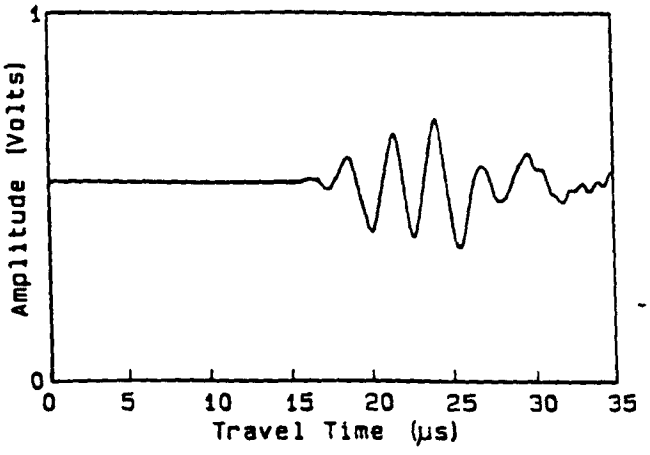

b

Figs. 4:3a,b These diagrams show a compressional waveform from (a) unbacked transducers and (b) from transducers backed with tungsten loaded epoxy. The backed waveform is more attenuated and shows limited "ringing".

4:3:3 Transducer bonding.

The most important factor affecting the reproducibility of a pulse shape is the variation in thickness and the patchiness of the bonding. The transducer is bonded to the transducer housing at the front face using epoxy resin. This is applied sparingly and then the transducer is pressed firmly into position and worked in slow circles to remove air bubbles and ensure an even bonding surface. A bond line of thickness less than one hundredth of a wavelength is desirable to reduce the effect of the bond on the wave (Dr. L. Bond personal communication, U.C.L.). It is estimated the thickness of the bond achieved by this method is less than 0.05mm, and the wavelength of the shear and compressional waves are ≈3.5mm and ≈6mm through the ram ends, respectively.

CHAPTER 5

EXPERIMENTAL PROCEDURE AND DATA REDUCTION METHODS

5:1 Introduction.

There are, at present, three main operational arrangements used with the triaxial system at U.C.L.. Each arrangement enables a specific set of physical property measurements to be made on a deforming rock sample. Limited access to the sample prohibits all the physical property measurements to be made at the same time. The physical parameters that can be measured are; differential stress, axial strain, compressional and shear wave velocities, acoustic emission (AE) rate and amplitude distribution, waveform capture, and independent pore fluid pressure/volume control. The three operational modes used in this study, are described in section 5:4. Equations used in data reduction and elastic moduli determinations are discussed in section 5:6. A detailed account is given of the adaption of the anisotropic crack density model of Soga et al. (1978) to the specific case of the limited velocity measurements possible in this present study (section 5:6:1). Furthermore, the spectral ratio method used to determine seismic Q is discussed (section 5:6:2). Firstly, however, a brief outline is given of sample preparation and sample assembly; detailed accounts of these can be found in Ismail (1974), Jones (1989) and Murrell (1990).

5:2 Sample preparation.

Rock cores of approximately 50mm in length are cut using a diamond-impregnated rotary core barrel of 15mm internal diameter. Excess material is cut off using a diamond saw. The cores are then lapped by hand, using first a coarse and then a fine carborundum powder, until the ends are parallel to within ±0.02mm and the length is 45±1mm. The samples are finally washed in distilled water and placed in an oven at 70°C

and left to dry for at least 48hours. Samples to be saturated are placed in a desiccator which is evacuated to a vacuum of 10^{-3}Tor. Distilled water is then introduced into the desiccator to saturate the sample. Increased saturation is achieved by then re-evacuating with the vacuum pump. Samples are then stored under water for various periods of time depending on their porosity and permeability. The rocks used in this study were generally saturated in a vacuum for a few hours. The samples were weighed air-dry and then re-weighed suspended by a thin wire in water. The sample porosity was then determined using the standard method outlined by Carmichael (1989, p142).

5:3 Sample assembly.

The manufacture of the copper jacket which sheaths the sample is a difficult process. First, thin-walled copper tubing is cut to length and annealed. Then a series of brass formers of increasing diameter are used to shape the jacket to fit the ram ends. The jacket is then placed over the lower ram and the single sealing ring is forced into place using a specially designed vertical press. The sample is then inserted into the jacket, with thin brass discs placed between the sample and the ram ends (these discs reduce the frictional restraining effects of the ram ends on the sample, and also provide a good acoustic contact at the ram/sample interface). The top ram is pushed into the jacket, with the press ensuring that the top ram/sample/lower ram lie along a common axis. Finally, two sealing rings are forced into place, and the assembly is then ready to be loaded into the vessel.

When shear wave transducers are used (see operational mode (2) section 5:4:1) there is the additional difficulty of aligning the directions of polarisation of the transducers. The shear wave transducers used have small flats ground onto their circumference to indicate the polarisation direction. The orientation of the transducers within the ram ends needs to be represented outside the rams so that the transducers can be aligned during ram assembly. The line of the transducer orientation is taken outside the rams using a straight-edge (usually a razor blade) and a fine line of engineers dye. A specially designed system of clamps and guide rods then ensures that the transducers are

aligned in the vertical press as the jacket sealing rings secure the assembly. It is estimated that the shear transducers can be aligned to better than 2° using this method.

5:4 The physical property measurement arrangements.

There are three primary physical property measurement arrangements that can be used with the present system. The first of these was in routine use before this study began, having been developed by Jones (1989) after initial work by Dr. R. Colston. The other two arrangements were developed during the course of this study. The three arrangements are:

1) The simultaneous measurement of differential stress, axial strain, compressional wave velocity, and acoustic emission rate and amplitude distribution during triaxial deformation.

2) The simultaneous measurement of differential stress, axial strain, compressional and shear wave velocity, and acoustic waveform capture during triaxial deformation.

3) The simultaneous measurement of differential stress, axial strain, acoustic emission rate and amplitude distribution, acoustic emission waveform capture, and pore fluid pressure/volume changes during triaxial deformation.

5:4:1 Description of operational mode (2).

Under this arrangement, shear wave transducers of 1MHz resonant frequency are located in both the top and bottom ram ends (fig. 3:2, see page 66). An unbacked PZT-7A transducer is used as a transmitter and a lithium niobate transducer as receiver. The time of flight of both the main shear wave and the compressional wave forerunner are measured, using the counter-timers. Corrections are made for the travel time through the ram ends, and for sample shortening during deformation.

In this mode of operation, the pulse generator is set to produce a 100V rectangular pulse which strains the transducer located in the top ram. This, in turn, produces a mechanical wave which propagates across the sample. The lower transducer converts this wave back to an electrical signal. The resulting electrical signal has a peak-to-peak amplitude of about 300mV at this stage. The signal is immediately amplified by a fixed-gain, low-noise 10dB header-amplifier. This amplifier was designed by Dr. J. Weight (City University) to be used specifically with this type of transducer. The amplified signal is taken out of the safety cubicle by shielded coaxial cable. The signal is then passed through a band-pass filter, with a band-width of 100kHz-1.5Mhz, and the filtered signal is re-amplified by a variable-gain amplifier. The S wave signal has a peak-to-peak amplitude of about 12V, and the P wave signal about 1V to 2V at this stage.

The signal is then split with one signal being taken directly to one of the counter-timers, the transient recorder and the digitising oscilloscope. This signal shows the full waveform shape, and is used to measure the shear wave velocity. It is also stored for future amplitude analysis. The first large shear wave peak is used to trigger the counter-timer. The recording equipment is initialised by a trigger output from the pulse generator. Cursors on the oscilloscope show the exact trigger position of the counter-timers on the acoustic waveform. Using the oscilloscope an accurate correction can be made for the "missed" onset of the wave (that is, the time difference between the actual onset and the trigger position). This time correction is monitored throughout the test, and can be varied to account for any change in waveform shape that may occur during the test. This correction is generally less than 1μs and can be measured to an accuracy of 0.02μs. The trigger position is set on the steepest part of the first arrival, because any change in waveform shape will be least at this point. The computer continually updates the cursor position on the oscilloscope every 100μs. The travel time is logged 100 times per logging interval (normally 30s), the mean and standard deviation of these travel times are calculated and stored on the computer. If the standard deviation is greater than 0.03μs the data is considered too noisy and rejected. Every 300s a hard copy of the oscilloscope display is taken.

The second part of the split signal is amplified a third time using a second variable-gain amplifier. This "over-amplifies" the shear arrival and distorts its shape. However, the P wave arrival is amplified to a height of about 10V without distortion, and a signal:noise ratio of about 10:1 is generally obtained. The first large compressional wave arrival is then used to trigger the second counter-timer. The computer moves a second cursor on the oscilloscope display to continually update the trigger position. Corrections for the missed onset are made in the same way as for the shear wave. A similar accuracy is obtained for the P wave onset as for the S wave onset. This wave is also sampled 100 times per logging interval. Both variable-gain amplifiers were built in-house by Dr. R. Colston and are described in detail by Jones (1989).

5:4:2 Description of operational mode (3).

Contemporaneous acoustic emission rate, acoustic emission amplitude distribution, and pore fluid pressure/volume measurements were possible after a newly-built servo-controlled pore fluid pressure intensifier was integrated into the triaxial deformation system (section 3:7). High pressure tubing connects this device, located outside the safety cubicle, to a newly-designed upper ram (fig. 3:3). This ram affords a leak-free seal between the high pressure pore piping and the ram end. Thus free-fluid access to the sample is obtained. A grooved disc interposed between the sample and the upper loading ram distributes the pore fluid evenly across the face of the sample. The lower ram assembly is similar to that used in operational mode (2), but makes use of a compressional lithium niobate transducer backed with a pellet of tungsten doped epoxy to receive AE signals. The acoustic emissions picked up by this transducer are immediately amplified, before being passed to the AE analyser, where individual events are recognised, and their peak amplitudes recorded.

In pore-fluid control experiments, the confining pressure is applied before the pore fluid pressure is applied, which is then left to equilibrate (this usually takes only a few minutes). Pore pressure data is logged using a CIL data logger, the data logger is set by the computer to take the mean of 2048 voltage readings, this takes about 20s. M.D.

Read (U.C.L.) supervised the use of the pore fluid pressure intensifier device during these experiments.

5:5 Frequency response of the elastic waveform capture arrangement.

The frequency response of the waveform capture system has been examined. Shear waves were pulsed through a sample of very high Q material, of the same dimensions as the rock samples. An aluminium sample was used as it has a Q≈150,000. The assumption is made that intrinsic attenuation of the waveform through the sample is negligible, so that consequently the frequency spectrum of the recorded wave can be considered to be the result of the band limitations of the transducer/amplifier/recording arrangement. The digitising rate used was 20MHz and each waveform was 4096 data points long. A Fast Fourier Transform (FFT) was performed on the waveform using ASYSTANT software (ASYST Software Technologies Inc., N.Y., U.S.A.). Figs. 5:1a,b show the amplitude spectra of the P and S wave arrivals, respectively. The frequency spectrum of both waveforms are reasonably wide. The shear wave shows high energy levels between 400kHz and 1.3MHz, with a peak amplitude at a frequency of 900kHz. The compressional wave shows high energy levels between 600kHz and 1.4MHz, centred about 1.1MHz. These results are in good agreement with those of other authors (e.g. Xu & King, 1990). The amplitude of the P wave arrival is about one tenth of that seen for the shear wave, and the frequency of the P wave is slightly higher than that seen in the shear wave.

The frequency response of the equipment is of prime importance when amplitude analysis is carried out on captured waveforms. If the frequency content of a waveform changes significantly during a test, an amplitude change may be induced by merely moving out of the frequency response range of the equipment. It is important, therefore, to separate real amplitude changes from those induced by the response limitations of the recording equipment.

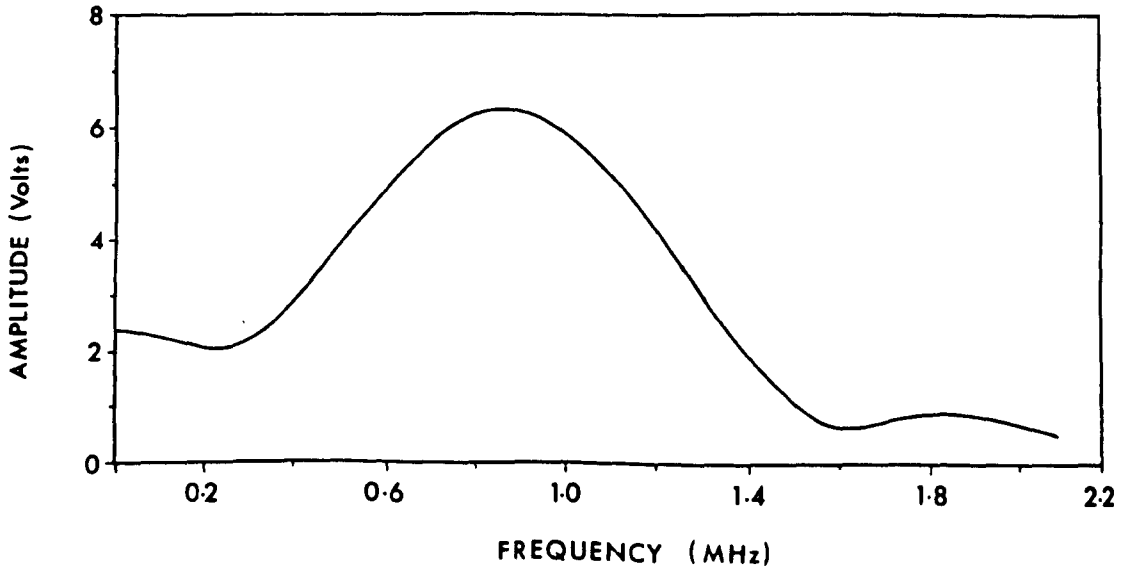

a

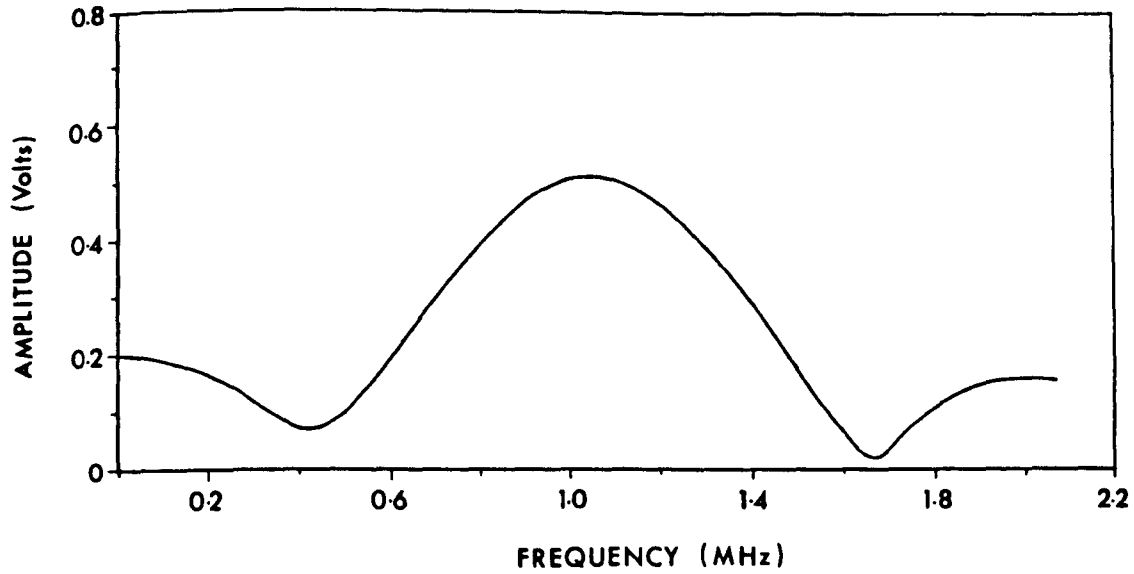

b

Figs. 5:1a,b These show the amplitude spectra of the shear (a) and compressional (b) waveforms that have travelled through an aluminium specimen. Both show reasonably wide frequency bands, the compressional wave is of slightly higher frequency than the shear wave; this has been noted by others (see text).

5:6 Data accuracy and data reduction.

In order to obtain the travel times of the elastic waves through the rock sample two corrections need to be made. Firstly, a correction is made for the missed onset (section 5:4:1), and secondly, for the travel time of the waves through the ram ends. As is common practice in rock mechanics (see for example, Brookes, 1984), this latter correction was determined by placing the ram ends directly together and noting the travel times at atmospheric pressure. The corrections were 2.71±0.05μs and 4.10±0.05μs for the compressional and shear waves respectively. No attempt was made to correct for the changing thickness of the end caps with increasing confining pressure or differential stress. This second correction is considered to be insignificantly small (Jones, 1989). The uncertainty in picking the first arrival of the acoustic waves has previously been discussed by Jones (1989); the absolute error in the velocity measurements is considered to be ±1.5% (see previous reference). The error in the normalised velocities (which are considered in this study) are typically ±0.1%.

Once the compressional and shear wave velocities have been determined, well known equations can be used to calculate the effective dynamic Young's modulus, the dynamic Poisson's ratio, bulk and shear moduli, and the Vp/Vs ratio. It is important to remember that as the rock sample is progressively deformed the sample will undergo stress induced anisotropy. Therefore, these calculated values can at best be considered "effective" or only having meaning in the direction of measurement and do not reflect a value for the specimen as a whole. The equations used to calculate the moduli are strictly valid only for a homogeneous, isotropic medium and, therefore, represent the actual moduli of the rock only at the beginning of the test (that is under hydrostatic pressure). As the rock deforms the calculated moduli will reflect not only the extent of microcracking but also the alignment of this cracking. The dynamic elastic moduli equations (5:1-5:4) have been discussed by others (e.g. Fjaer et al., 1990) in terms of their applicability to cases where stress-induced anisotropy occurs. Furthermore, previous work (section 2:4:1) suggests that prior to macroscopic failure microcracking becomes concentrated near the site of final failure. Therefore, the elastic wave velocities (and subsequently, the dynamic moduli) must be considered average values and in some way

related to the propagation path. The equations used to determine the elastic moduli are given by Jaeger & Cook (1979, pp185) as:

$$E_D = V_s^2 p[3(Vp/Vs)^2-4]/[(Vp/Vs)^2-1] \quad (5:1)$$

$$U_D = \tfrac{1}{2}[(Vp/Vs)^2-2]/[(Vp/Vs)^2-1] \quad (5:2)$$

$$K_D = p(Vp^2-4Vs^2/3) \quad (5:3)$$

$$G_D = pVs^2 \quad (5:4)$$

Where E_D is the dynamic Young's modulus, U_D is the dynamic Poisson's ratio, K_D is the bulk modulus, G_D is the shear modulus, and p the density. Assuming a 1.5% error in velocity measurements, and taking maximum velocities of Vp≈6km/s and Vs≈3.6km/s, this gives an uncertainty in E of ±10%, in U of ±6%, in K of ±6%, and in G of ±8% (after Thill & Peng, 1974). Velocity changes can be induced in a sample by changes in the bulk density during deformation (see eqns. 5:1-5:4). Jones (1989) has calculated that the density changes for the rocks used in this study will introduce no more than 1% variation in the velocity measurements.

It is important to note that these equations are derived from the expression for the velocity of compressional waves in an extended medium given by:

$$Vp = [E(1-U)/p(1+U)(1-2U)]^{\frac{1}{2}} \quad (5:5)$$

The equation for the shear wave velocity (from eqn. 5:4) is the same for an extended medium and for a long bar. However, the compressional wave velocity in a long bar is:

$$Vp = (E/p)^{\frac{1}{2}} \quad (5:6)$$

The compressional wave velocity is greater in a long bar than in an extended medium. The long bar formula comes into play if the wavelength of the propagating wave is greater than the diameter of the specimen (Jaeger & Cook, 1979, p185). The ASTM Standards Report (1988) suggests that the diameter of the specimen should be greater than five times the wavelength of the compressional wave. In the worst case, the sample diameter is between three and four wavelengths in this study. However, Jaeger & Cook (1979, p184) state that if care is taken to pick the first onset of the P arrival, then a wavelength:sample-diameter ratio of 3:1 is sufficient for the assumption of an extended medium to be valid.

Care also needs to be taken when comparing static and dynamic moduli values as it has been noted that the values of dynamic moduli can be much higher than those of static moduli (Jaeger & Cook, 1979, p185; Fjaer et al., 1990). However, this is most noticeable in porous, weakly-cemented rocks. This inequality has been explained in terms of the difference in strain rate and in energy loss due to non-elastic processes in the dynamic and static measurement techniques.

The crack density parameter for a deforming sample can be determined using two methods: Firstly, by a method outlined by O'Connell & Budiansky (1974) which considers only random crack distributions, and secondly, by using a method outlined by Soga et al. (1978) in which crack anisotropy can be modelled. This latter method is discussed in detail in the following section (5:6:1). O'Connell & Budiansky described the properties of a damaged volume in terms of the crack density parameter. The parameter ε is given by;

$$\varepsilon = \langle Na^3 \rangle \qquad (5:7)$$

where a is a mean major axis of the ellipsoidal crack, and N is the number of cracks per unit volume. The crack density parameter for a random distribution of penny-shaped cracks can be described as a function of Poisson's ratio (after Yukutake, 1989);

$$\varepsilon = 45/16[(Uo-U)(2-U)]/[(1-U^2)(10Uo-3UoU-U)] \qquad (5:8)$$

where Uo is the Poisson's ratio of the uncracked solid, and U is the effective Poisson's ratio of the cracked solid. By substituting eqn. 5:2 into eqn. 5:8 the effective crack density can be expressed in terms of Vp and Vs. Furthermore, the Vp and Vs values for the uncracked rock can be approximated by the initial Vp and Vs values recorded through the rock at high confining pressures.

5:6:1 Crack density determinations for anisotropic cracking.

The method of Soga et al. (1978), outlined in section 2:4:3, can be adapted so that the horizontal and vertical crack density parameters (εz, εx) can be determined simply by using the axial velocity measurements made in this study. When cracking is no longer random, velocity changes can no longer be described by a single parameter like ε. Anderson et al. (1974) showed numerically that for aligned ellipsoidal cracks (i.e. a=b>c) there are six independent velocities lying along the three principal axes. Fig. 5:2 summarises the elastic wave velocities (determined by Anderson et al.) along three orthogonal axes of a single penny-shaped, air-filled crack in an isotropic solid assuming moduli and density appropriate for granite. Briefly, the P wave travelling perpendicular to the crack plane is more affected than the P wave travelling in the plane of the crack. The two shear waves (SV,SH) travelling perpendicular to the crack plane are equally affected. The shear wave travelling in the plane of the crack but polarised perpendicular to the crack (SV) is affected more than the shear wave travelling in the crack plane but also polarised in that plane (SH). Following from Anderson et al's numerical analysis, Soga et al. (1978) plotted the square of normalised elastic wave velocities against various crack density values for aligned penny-shaped cracks. These plots were found to be linear and four independent coefficients (a_1,a_2,b_1,b_2) were determined from the gradients of these plots (fig. 8 in Soga et al., 1978). The six independent velocities (in the three orthogonal directions; one perpendicular to the crack planes, and two parallel to the crack planes) are given below for an array of penny-shaped cracks aligned perpendicular to the i axis; see fig. 5:3.

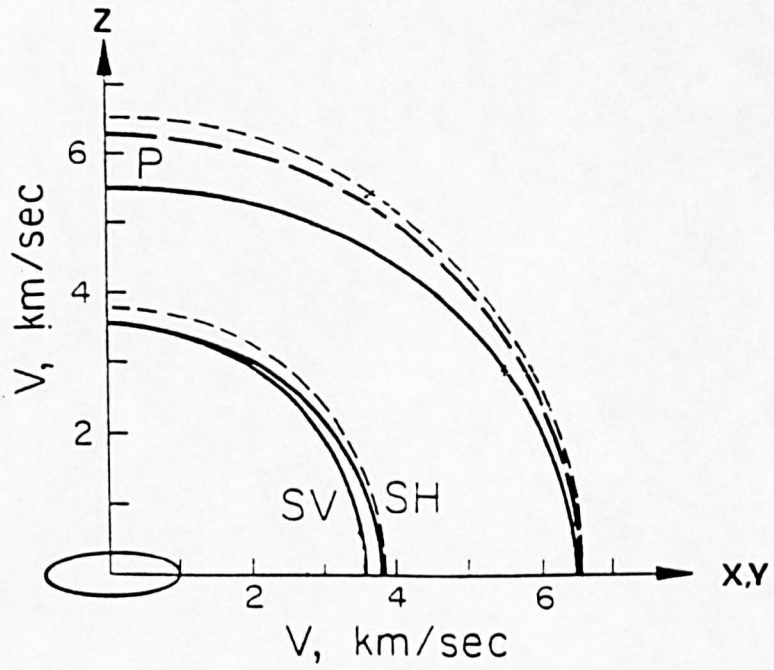

Fig. 5:2 Diagram showing the velocities of elastic waves through an elliptical crack as a function of angle and fluid properties. The porosity is 0.01, the aspect ratio is 0.05, the bulk moduli of the fluid phase is 0.1kb (simulating gas filled pores; solid lines) and 100kb (simulating fluid filled pores; long dashed lines), the rigidity modulus of the solid is 39GPa. The short dashed lines give the velocities through the isotropic uncracked solid (from Anderson et al., 1974).

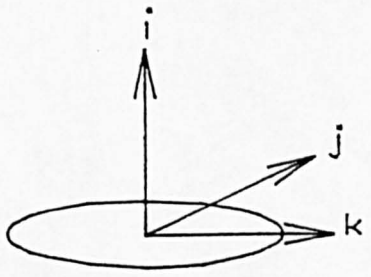

Fig. 5:3 An elliptical crack showing the axes convention used in eqns. 5:9-5:14 in the text.

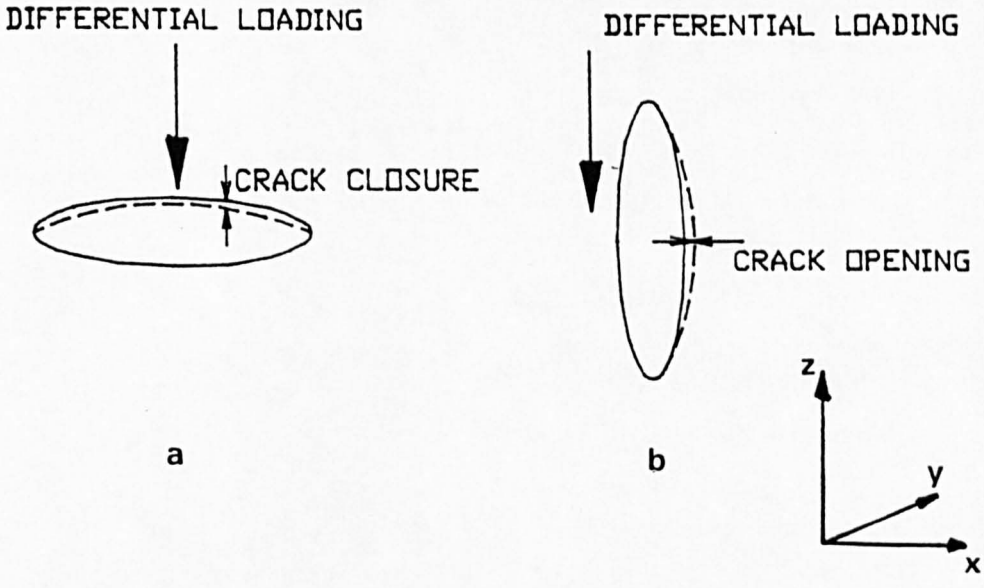

Figs. 5:4a,b These diagrams show the idealised form of the crack closure (a), and dilatant crack opening (b), occurring in a deforming rock specimen.

$$(Vii/Viio)^2 = 1 - a_1\,\varepsilon i \qquad (5:9)$$

$$(Vjj/Vjjo)^2 = 1 - a_2\,\varepsilon i \qquad (5:10)$$

$$(Vij/Vijo)^2 = 1 - b_1\,\varepsilon i \qquad (5:11)$$

$$(Vik/Viko)^2 = 1 - b_1\,\varepsilon i \qquad (5:12)$$

$$(Vjk/Vjko)^2 = 1 - b_2\,\varepsilon i \qquad (5:13)$$

$$(Vji/Vjio)^2 = 1 - b_1\,\varepsilon i \qquad (5:14)$$

The first suffix denotes the direction of propagation and the second suffix denotes the direction of displacement; the suffix o denotes the velocity through the uncracked solid. The above equations are the same as eqns. (2)-(7) given by Soga et al. (1978), but with the change of notation where i≡x, j≡y, k≡z. These equations highlight some important features; Vij=Vik, which is as expected, however, Vij=Vji and it is not intuitively apparent why this should be so. Soga et al. go on to suggest that cracking in a deforming rock sample can be reasonably well represented by three sets of aligned cracks with the crack densities εi, εj and εk; where these crack densities represent arrays of aligned, penny-shaped cracks which lie in planes perpendicular to the axes i, j, and k, respectively. These cracks are superimposed on an otherwise homogeneous and isotropic solid, and the densities are dilute such that cracks do not interact. The total effect of the crack arrays on the velocities of waves interrogating the solid is determined by the sum of the crack arrays. The effect of any cracking occurring obliquely to the specified axes is vectorially divided between the mutually orthogonal crack arrays. Following Soga et al. (1978), this idea can be adapted for use in the specific case of the tests carried out in this study.

Firstly, the coordinate system is chosen such that the unique differential loading axis is the z-axis, with the other two mutually orthogonal axes being x and y. Secondly, it is reasonable to assume cylindrical symmetry of the sample at least until macroscopic failure is approached (Hadley, 1975a). Thirdly, a simple analogue of the complicated processes of crack closure and crack opening during triaxial deformation of a rock, is assumed. That is, upon initial deviatoric loading of the sample cracks aligned perpendicular to the z axis will tend to close (fig. 5:4a). The effect that these cracks closing will have on the axial Vp and Vs can be found by using eqns. 5:9, and 5:11 or 5:12;

$$(Vzz/Vzzo)^2 = 1 - a_1 \varepsilon z \qquad (5:15)$$

$$(Vzx/Vzxo)^2 = (Vzy/Vzyo)^2 = 1 - b_1 \varepsilon z \qquad (5:16)$$

Where Vzz is the compressional wave velocity in the axial direction and Vzx (which=Vzy) is the axial shear wave; εz (the horizontal crack density parameter) represents the crack density of aligned penny-shaped cracks lying in a plane perpendicular to the z axis.

Upon further differential loading dilatant cracking is modelled by the opening of axially orientated cracking (see fig. 5:4b). The contribution that this makes to the axial Vp (from eqn. 5:10) is;

$$(Vzz/Vzzo)^2 = 1 - a_2 \varepsilon x \qquad (5:17)$$

Where εx (the vertical crack density parameter) is the crack density of an array of aligned cracks in a plane perpendicular to the x axis. However, the effect this axial cracking will have on the axial shear wave velocity is more complicated. The shear wave velocity changes to a greater or lesser extent depending on the wave polarisation with respect to the axially orientated penny-shaped cracks. If the wave is travelling in the plane of the cracks and is also polarised in this plane, then the velocity is given by eqn. (5:13). If the shear wave is travelling in the plane of the cracks but polarised perpendicular to them then the velocity is given by eqn. (5:14). The real situation is probably best represented by fig. 5:5, where crack normals are random in the x,y plane. If cracking is random in the x,y plane then for any particle motion direction of an axial shear wave, the motion can be considered to be parallel to half the cracks and perpendicular to the other half. Therefore, from eqns. (5:13) and (5:14) above, the axial shear wave velocity can be represented by;

$$(Vzx/Vzxo)^2 = 1 - \tfrac{1}{2}(b_1 + b_2) \varepsilon x \qquad (5:18)$$

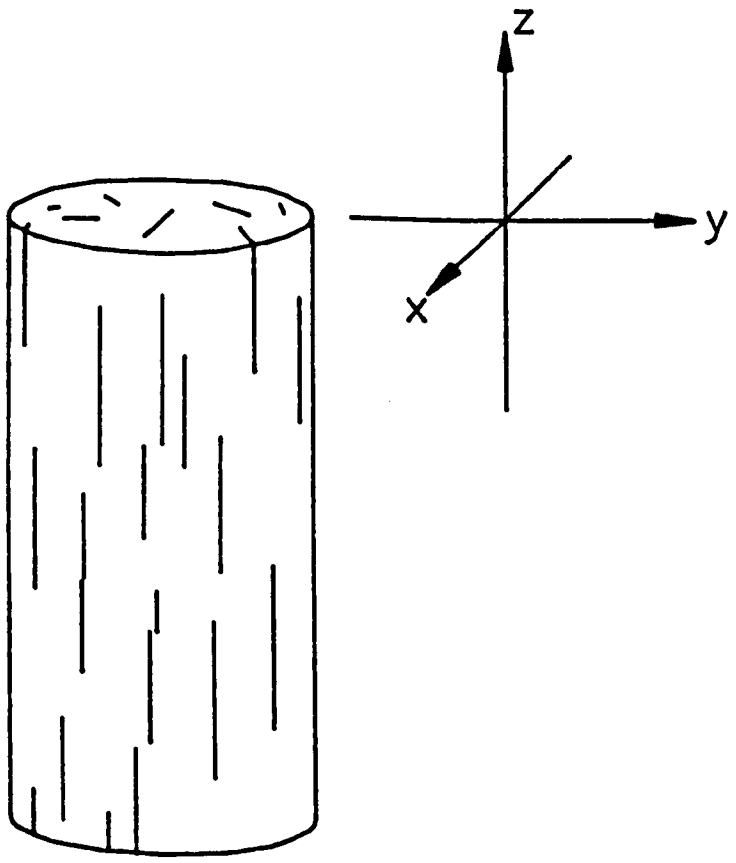

Fig. 5:5 This diagram shows an analogue model of the most likely form of dilatant cracking occurring in a triaxially deformed rock. Elliptical (penny-shaped) cracks are presumed to occur with one major axis aligned along the unique compressional axis (z-axis), and with the crack normals random in the x,y plane.

The net effect of the opening and closing of the vertical and horizontal crack arrays on the axial Vp and Vs is simply the sum of the individual contribution of each crack array. Therefore, by combining eqns. (5:15) and (5:17) above, the axial compressional wave velocity is given by;

$$(Vp/Vpo)^2 = 1 - (a_1\,\varepsilon z + a_2\,\varepsilon x) \qquad (5:19)$$

and the axial shear wave velocity is determined by combining equations (5:16) and (5:18);

$$(Vs/Vso)^2 = 1 - (b_1\,\varepsilon z + \tfrac{1}{2}(b_1+b_2)\,\varepsilon x) \qquad (5:20)$$

Because Vp and Vs are measured continuously throughout the tests carried out in this study, the changes in horizontal crack density parameter (εz) and the vertical crack density parameter (εx) can be determined from eqns. (5:19) and (5:20). By rearranging eqns. (5:19) and (5:20) and substituting in the constants (where a_1=1.452, a_2=0.192, b_1=0.601, b_2=0.025; the initial conditions for which these constants were determined are discussed below), it can be shown that;

$$\varepsilon x = 4.28\,(1-(Vs/Vso)^2) - 1.77\,(1-(Vp/Vpo)^2) \qquad (5:21)$$

$$\varepsilon z = 0.92\,(1-(Vp/Vpo)^2) - 0.57\,(1-(Vs/Vso)^2) \qquad (5:22)$$

There are a two important consequences which follow from eqns. (5:21) and (5:22): Firstly, as horizontal cracks close (i.e. εz decreases), Vp will increase relative to Vs. Secondly, as axial cracks open (and εx increases), Vs will decrease proportionately more than Vp.

It should be noted that Anderson et al.'s (1974) analysis is implicity based on the work of Eshelby (1957) and is strictly valid only for low porosity rocks (i.e. porosity of only a few percent). Also, the numerical analysis from which Soga et al. (1978) determined the constants was based on the assumption of a crack-free solid which was

homogeneous, isotropic and had a rigidity modulus of 39GPa and a density of 2.7g/cm^3. The crack-free density of a rock can be represented by the grain density of the rock. The grain density of Darley Dale sandstone has been calculated to be 2.62g/cm^3, using the method outlined by Carmichael (1989, p141). The crack-free rigidity modulus of Darley Dale sandstone (determined using eqn. 5:4 and the shear wave velocity recorded at 200MPa confining pressure; 2.83±0.04km/s) is ≈21±1.5GPa. In eqns. 5:21 and 5:22 the constants determine the actual crack density parameter values for a given shear and compressional wave velocity pair. However, the shape of the crack density change curve (that is, where the crack density parameters are normalised to their initial values) will depend on the relative values of Vp and Vs. In this study, generally only the change in crack density parameters are considered, in which case the discrepancy between the rigidity modulus assumed in Anderson et al's calculation and the actual modulus of Darley Dale sandstone is considered not to be significant. In Chapter 14 the actual crack density parameters are used to estimate the change in average crack aspect ratios for a deforming rock sample.

5:6:2 Method used to determine seismic Q.

The method used to determine seismic Q in this study is essentially the spectral ratio method described by Toksoz et al. (1976). However, this method was developed for measurements under hydrostatic conditions. Under such conditions the change in sample size relative to a reference sample (in response to an applied hydrostatic pressure), is small. However, in triaxial deformation experiments the rock sample can be subjected to up to 10% axial shortening (even though most commonly it is less than 5%). It is also assumed by Toksoz et al. that the elastic waves interrogating the sample are plane waves. This is not the case with the present experimental set-up. The method of Toksoz et al., and the assumptions implicit in the method, are discussed below.

The spectral ratio method requires two experiments to be carried out under identical conditions; one on a rock sample and another on a reference sample of exactly equal dimensions. The reference sample needs to be of a material of very high Q. The

amplitudes of elastic waves from the two experiments are then compared. It is assumed that the amplitude of the wave passing through the reference sample is only negligibly affected by its very high intrinsic Q. It is also assumed that geometric effects are the same for each sample. Thus, the geometric effects can be removed from the attenuation measurement, and the intrinsic Q of the rock can be determined.

The amplitude of a plane wave can be represented by;

$$A_1(f) = G_1(x)\, e^{-\alpha 1(f)x}\, e^{i(2\pi ft - k1x)} \qquad (5:23)$$

$$A_2(f) = G_2(x)\, e^{-\alpha 2(f)x}\, e^{i(2\pi ft - k2x)} \qquad (5:24)$$

where A is the amplitude, f is the frequency, x the distance travelled, k the wavenumber (which = $2\pi f/V$), and V the velocity. G(x) is a geometrical factor which includes wavefront spreading, reflections, etc. $\alpha(f)$ is the frequency dependent attenuation coefficient. The subscripts 1 and 2 refer to the reference and rock sample, respectively. From the arguments presented in section 2:5:5 it is reasonable to assume that in the frequency range 0.1-1Mhz, α is a linear function of frequency, although, as pointed out by Xu & King (1990), the method itself tests this assumption. Therefore,

$$\alpha(f) = \tau.f \qquad (5:25)$$

where τ is a constant, and is related to Q by,

$$Q = \pi/\tau.V\ . \qquad (5:26)$$

When the geometry of the rock and reference samples are the same then G_1 and G_2 can be considered as frequency-independent scaling factors. Hence, the ratio of the Fourier amplitudes is,

$$A_1/A_2 = G_1/G_2\, e^{-(\tau 1 - \tau 2)x} \qquad (5:27)$$

which can be rewritten as,

$$\ln(A_1/A_2) = (\tau 1 - \tau 2)xf + \ln(G_1/G_2). \qquad (5:28)$$

Eqn. 5:28 can be represented by a straight line plot of $\ln(A_1/A_2)$ against f, the slope of which allows $(\tau 1 - \tau 2)$ to be determined. If the Q of the reference sample is very large (i.e. $Q \approx \infty$) then $\tau 1 \rightarrow 0$ and $\tau 2$ can be determined directly from the slope of straight line plot. In this study the reference sample was made from aluminium (which as previously stated has a Q of about 150,000); the Q of crustal rocks is usually <200. Therefore, by taking $\tau 1 = 0$ an error of less than 0.2% is introduced.

It should be noted that as the wavelength of the interrogating elastic waves approaches that of the inhomogeneities of the rock sample then scattering may become important. In this case the $\ln(A_1/A_2)$ versus frequency relationship will no longer be linear. However, Xu & King (1990) point out that in cases of non-linear frequency dependence of α, it is necessary to determine Q over a slightly reduced frequency range, assuming Q is constant within this range.

Two important considerations when adapting the above method for triaxial tests are: (i) In the experimental arrangement used in this study, the elastic wave has a spherical component; and (ii) the rock sample changes in length during deviatoric loading. These two points can be addressed in the following manner. By considering the elastic waveforms travelling through an axially loaded aluminium reference sample, an estimate of the amplitude dependence of the elastic waves to differential loading and axial shortening can be obtained. A plane wave travelling in an infinite medium will retain its shape along its axis of travel, however, the amplitude of a spherical wave is inversely proportional to the radius of its travel, r (Jaeger & Cook, 1979). Therefore, for small strains, it would not be expected that significant amplitude dependence due to shortening would be seen.

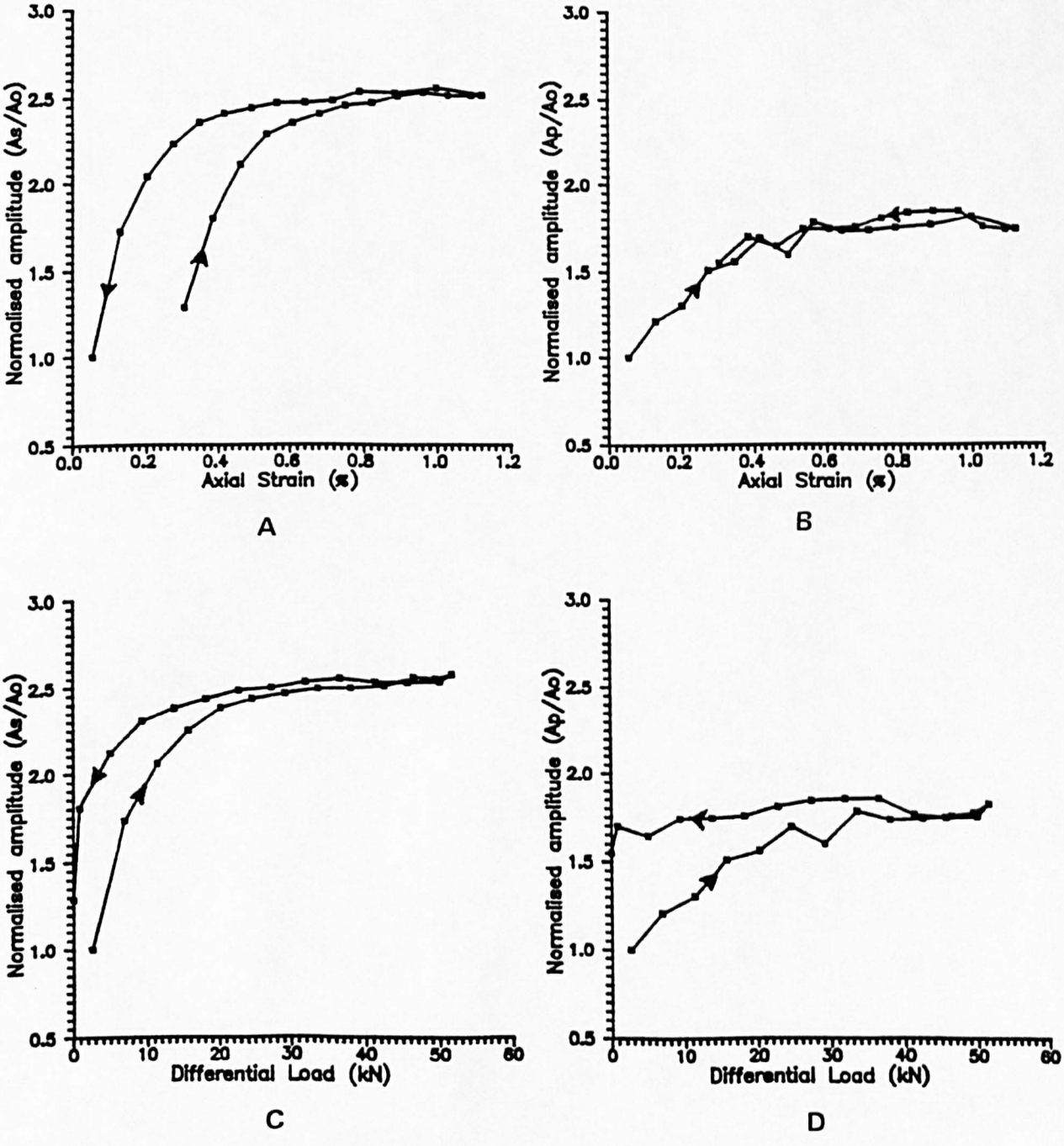

Figs. 5:6a,b,c,d These diagrams show the amplitude dependence of the shear wave on strain (a) and load (c), and the amplitude dependence of compressional wave on strain (b) and load (d), travelling through an Aluminium dummy sample.

Figs. 5:6a,b show the amplitude/strain dependence of the shear and compressional waves travelling through a uniaxially loaded aluminium sample, respectively. Figs. 5:6c,d show the amplitude/load dependence of the shear and compressional waves, respectively. It can be seen that after about 0.5% strain the amplitude of both the P and S arrivals becomes effectively strain-independent to at least 1.2% strain. The total strain was limited by the sample's elastic range. However, this appears to confirm that for small strains, the difference in length between the rock and reference sample will not have much effect on the Q calculation. The initial rise in amplitude would appear to be the result of the initial improvement in contact as the sample is axially loaded. This is confirmed by figs. 5:6b,d which show that the amplitude has a strong initial load-dependence. From contact to 20kN load, the compressional wave amplitude increases by 50% and the shear wave by about 150%. Above this load value, however, the wave amplitudes remain essentially constant. The shear wave is much more sensitive to changes in the sample/ram contact surface than the compressional wave. However, there may also be an effect on G_2 relative to G_1 as the rock sample deforms. This is because the sample will not only shorten, but the sample will also change shape. In the most extreme cases of pseudo-ductile deformation the rock sample will barrel, thus affecting the form of the internal reflections described by G_2. The effect of this shape change, however, at small strains is not considered to be important. This is because only the first arrivals of the compressional and shear waves are considered in the seismic Q determinations. The compressional first arrival will have travelled directly through the sample and will not therefore be affected by internal reflections. The shear arrival is also clearly seen with only relatively low amplitude disturbances preceding its onset (see fig. 4:2, page 88).

5:7 Experimental repeatability.

Experimental repeatability has been discussed by Jones (1989) and in published work by Meredith et al. (1990) and Jones & Murrell (1990). All these investigators have shown that both the mechanical response and acoustic measurements made on the rock samples are highly repeatable using the same deformation system as used in this study.

Common features are seen for tests carried out on the same material and under the same conditions. This repeatability is important, as it allows individual tests to be analysed in detail and their results to be considered general (for a particular rock and particular ambient test conditions). Furthermore, in this study (except in Chapter 12), series of experiments were conducted on the same rock at different confining pressures. Systematic mechanical and acoustic changes can be seen through these series of experiments; this internal consistency further increases confidence in any one test result.

CHAPTER 6

INTRODUCTION TO THE EXPERIMENTAL RESULTS

In total 93 experiments were performed during this study. Brief details of all the experiments performed are listed in table 6:1 for completeness. Results from 27 of these experiments are discussed in detail in the following chapters. These experiments best highlight the damage mechanisms that occur during rock deformation. The prime cause of experimental difficulties, initially, resulted from developing the acoustic velocity measurement technique. Later, difficulties in commissioning the new servo-controlled loading system caused many tests to be aborted. Throughout the study problems were encountered in sealing the jacket and/or the vessel. Incomplete sealing of the specimen from the confining medium is common with this type of equipment and in this project was the cause of failure of approximately one in five tests.

All the experiments performed during this project were essentially constant strain rate tests, carried out at a nominal strain rate of $10^{-5}s^{-1}$. The average duration of each test was about 2hrs. The data logging interval was fixed at 30s, and waveforms were digitised and stored every 10 logging intervals. The rate of digitisation of the recorded waveforms was 20MHz. In the following section "stress" refers to differential stress (σ_1-σ_3), unless otherwise stated and "strain" refers to axial sample strain. All the tests were carried out at ambient temperature. The test specimens were cylindrical samples nominally 15mm in diameter and 45mm long. The ends of the samples had a parallelism of better than 0.02mm.

The experimental results are described in Chapters 7-13, with chapter 14 giving a general summary of the work and a briefly outlining the wider perspective of the work. Chapters 7 to 12 describe simultaneous compressional and shear wave velocity changes through deforming samples of four different sedimentary rocks, under different confining pressures. Chapter 7 phenomenologically describes the mechanical response and elastic wave velocity changes of Darley Dale sandstone (which has been extensively investigated in this laboratory by others, e.g. Murrell, 1965; Ismail & Murrell, 1976; Jones and Murrell, 1990) at confining pressures up to 200MPa. Chapter 8 examines more closely the mechanisms of failure in this rock with typical examples of catastrophic brittle failure and

pseudo-ductile deformation. Changes in the moduli of the rock are examined as well as inferred crack density changes and attenuation studies. Chapter 9 examines, for comparative purposes, the deformation of Gosford sandstone, a rock previously studied in detail by Edmond & Paterson (1972). Chapter 10 studies the mechanical and acoustic characteristics of the well-known Solenhofen limestone. Chapter 11, examines elastic wave velocity anisotropy in Tennessee sandstone; a fine grained rock with a strong bedding plane. Chapter 12 describes elastic wave velocity changes through wet and dry sandstone and limestone samples. Chapter 13 describes three constant pore fluid pressure tests on Darley Dale sandstone using the newly-built pore-fluid pressure intensifier and volumometer described in section 3:7. This chapter reports typical examples of the pore fluid volume changes during brittle deformation, pseudo-ductile deformation and the brittle-ductile transition seen in Darley Dale sandstone samples. In Chapter 14 the acoustic velocity measurements and the constant pore fluid pressure experiments are brought together, and for the first time, the changes in pore aspect ratio of dilatant cracks can be estimated during both brittle and ductile deformation of Darley dale sandstone.

Table 6:1. Tabulation of the experiments carried out in this study.

KEY TO ROCK TYPES
DD - Darley dale sandstone **SL** - Solenhofen limestone **GS** - Gosford sandstone **UM** - Kambalda ultramafic **TS** - Tennesee sandstone
KEY TO PARAMETERS LOGGED
AE - Acoustic emissions **P** - Compressional wave velocity **S** - Shear wave velocity

Specimen nos.	Material	Effective pressure (MPa)	Observation	Parameters	Mode of failure
GS1	GS	50	jacket leaked	P,S	test aborted
GS2	GS	50	good acoustic sig	P,S	no impress in jacket
GS3	GS	30	good acoustic sig	P,S	no impress in jacket
GS4	GS	15	good acoustic sig	P,S	shear at 33° to σ_1
GS5	GS	25	good acoustic sig	P,S	no impress in jacket
GS6	GS	100	good acoustic sig	P,S	no impress in jacket
GS10	GS	200	good acoustic sig	P,S	no impress in jacket
TEN1	TS	100	good acoustic sig	P,S	shear at 25° to σ_1
TEN2	TS	200	good acoustic sig	P,S	not taken to failure
TEN3	TS	100	bedding $\perp$ to axis	P,S	not taken to failure
TEN4	TS	50	bedding $\perp$ to axis	P,S	shear at 30° to σ_1
TEN5	TS	50	bedding $\parallel$ to axis	P,S	shear at 31° to σ_1

TEN6	TS	50	bedding ∥ to axis	P,S	shear at 30° to σ_1
TEN7	TS	50	bedding ⊥ to axis	P,S	shear at 28° to σ_1
TEN8	TS	50	bedding ∥ to axis	P,S	shear at 28° to σ_1
UM1	UM	100	talc veins of 1mm	P,S	shear at 35° to σ_1
UM2	UM	150	no visible veins	P,S	shear at 37° to σ_1
UM3	UM	250	no visible veins	P,S	shear at 42° to σ_1
UM4	UM	450	no visible veins	P,S	shear at 45° to σ_1
UM7	UM	700	no visible veins	P,S	shear at 45° to σ_1
MSL2	SL	50	poor acoustic sig	S	shear at 12° to σ_1
MSL5	SL	200	jacket leaked		
MSL6	SL	50	poor acoustic sig	S	shear at 16° to σ_1
MSL8	SL	150	jacket leaked		
MSL10	SL	50	poor acoustic sig	S	shear at 17° to σ_1
MSL11	SL	100	jacket leaked ?	S	shear at 20° to σ_1
SL1-3	SL	50	poor acoustic sig	S	conj. fract. at 20°σ_1
SL4	SL	50	actuator ramp malfunction		
SL5	SL	50	saw cut tests ; experimenting with trans		
SL6	SL	50	saw cut tests ; poor acoustic signal		
SL7	SL	50	saw cut test	P,S	
SL8	SL	100	jacket leaked		
SL10	SL	100	jacket leaked		
SL11	SL	50	saw cut test	poor acoustic signal	
SLAP4	SL	50	good acoustic sig	P,S	shear at 20° to σ_1

table 6:1 continued

SLAP5	SL	100	good acoustic sig	P,S	shear at 30° to σ_1
SLAP6	SL	75	good acoustic sig	P,S	shear at 28° to σ_1
S320	SL	150	good acoustic sig	P,S	no clear impress
S322	SL	100	good acoustic sig	P,S	shear at 30° to σ_1
S323	SL	75	poor acoustic sig	P,S	jacket leaked
S324	SL	75	good acoustic sig	P,S	shear at 27° to σ_1
S517	SL	175	poor sig	S	no clear impress
S518	SL	200	good acoustic sig	P,S	no clear impress
SL121	SL	100	sat.- undrained	P,S	no clear impress
SLS32	SL	100	sat.- undrained	P,S	no clear impress
D520	DD	100	sat.- undrained	P,S	shear at 32° to σ_1
DD100S	DD	100	sat-drained	P,S	no clear impress
DDS128	DD	100	sat.-undrained	P,S	no clear impress
PERM1	TS	Pc-50, Pp-12	const. pore press	AE	shear at 28° to σ_1
PERM2	DD	Pc-110,Pp-10	const. pore press	AE	no clear impress
PERM4	DD	Pc-60, Pp-12	const. pore press	AE	shear at 18° to σ_1
PERM8	DD	Pc-80, Pp-30	const. pore press	AE	no clear impress
PERM11	DD	Pc-50, Pp-20	const. pore press	AE	shear at 25° to σ_1
PERM12	DD	Pc-80, Pp-50	const. pore press	AE	shear at 25° to σ_1
PERM13	DD	Pc-60, Pp-15	const. pore press	AE	shear at 33° to σ_1
PERM17	DD	Pc-50, Pp-25	const. pore press	AE	shear at 30° to σ_1

table 6:1 continued

PERM20	DD	Pc-30, Pp-20	const. pore press	AE	shear at 27° to σ_1
PERM21	DD	Pc-30, Pp-10	const. pore press	AE	shear at 34° to σ_1
PERM25	DD	Pc-150,Pp-50	const. pore press	AE	no clear impress
UMPORE	UM	Pc-100,Pp-30	const. pore press	AE	shear at 30° to σ_1
GSPERM	GS	Pc-30, Pp-10	const. pore press	AE	no clear impress
WG1	DD	40	poor signal -jacket leaked		
WG2	DD	50	poor signal		shear at 38° to σ_1
WG3	DD	50	poor signal		shear at 30° to σ_1
MS1	DD				shear at 36° to σ_1
MS2	DD				shear at 26° to σ_1
MS3	DD		poor signal -jacket leaked		
MS6	DD	100	poor signal		
MS7	DD	200	poor signal		
MS10	DD	200		S	short'ng & barrelling
MS12	DD	100	reas. signal	P,S	" "
MS14	DD	200	signal lost		" "
MS17	DD	50			shear at 24° to σ_1
MS19	DD	30	reas. signal	P,S	shear at 22° to σ_1
DDs90.1	DD	50	ram deformation circuit in - unstable		
DDs90.2	DD	150	" " " "		
DDA1	DD	50	good acoustic sig	P,S	shear at 18° to σ_1

table 6:1 continued

DDA2	DD	75	good acoustic sig	P,S	no clear fracture
D48	DD	150	" " "	P,S	no clear fracture
D49	DD	75	" " "	S	no clear impress
D519	DD	100	" " "	P,S	slight barrelling
D500	DD	500	trans. malfunc.		barrelling
D59	DD	200	good acoustic sig	P,S	"
DDO1C	DD	50	saw cut test	P,S	
DDO2C	DD	50	"	"	
DDO3C	DD	50	"	"	
DDO5C	DD	50	"	"	leaked
S321	DD	50	"	"	leaked
S118	DD	50	"	"	
SDD1	DD	50	"	"	
SD12	DD	50	"	"	leaked
SD13	DD	50	"	"	good test
SD14	DD	50	"	test aborted	
SD15	DD	50	"	"	good test
SD17	DD	50	"	"	

table 6:1 continued

CHAPTER 7

ELASTIC WAVE VELOCITY MEASUREMENTS ON DARLEY DALE SANDSTONE.

7:1 Introduction.

A series of triaxial deformation experiments were carried out on samples of Darley Dale sandstone at confining pressures 30MPa, 50MPa, 75MPa, 100MPa, 150MPa and 200MPa. Extensive laboratory investigations have been reported for this rock, notably by Murrell (1963, 1965) and Murrell & Ismail (1976). Jones & Murrell (1990) have also reported compressional wave velocity changes through triaxially deformed samples of Darley Dale sandstone. However, this is the first time that simultaneous Vp and Vs measurements have been presented for this rock. A description of the important features of the stress/strain curves and elastic wave velocity changes seen at each confining pressure is given. This is followed by a detailed interpretation of these phenomenological observations in terms of changing damage mechanisms such as crack closure, crack initiation, crack growth and crack coalescence.

In the first of the experiments described in this chapter (MS19) the shear and compressional wave velocities were measured on two different rock samples under identical conditions. This was necessary as at low confining pressures good acoustic velocity data is difficult to obtain because of poor acoustic contact at the ram/sample interface. The peak stresses of the two tests were then normalised with respect to strain (and the velocity data scaled accordingly). In all the other velocity measurements reported in this thesis the compressional and shear wave velocities were measured simultaneously on the same sample.

7:2 The stress/strain curves and elastic wave velocity changes.

Fig. 7:1 shows the stress/strain curve and elastic wave velocity changes for a sample deformed with a confining pressure of 30MPa (experiment MS19). Initially the curve shows a concave upwards form. There follows a brief period of linearity, although its precise delineation is fairly subjective. The sample very soon becomes anelastic (at

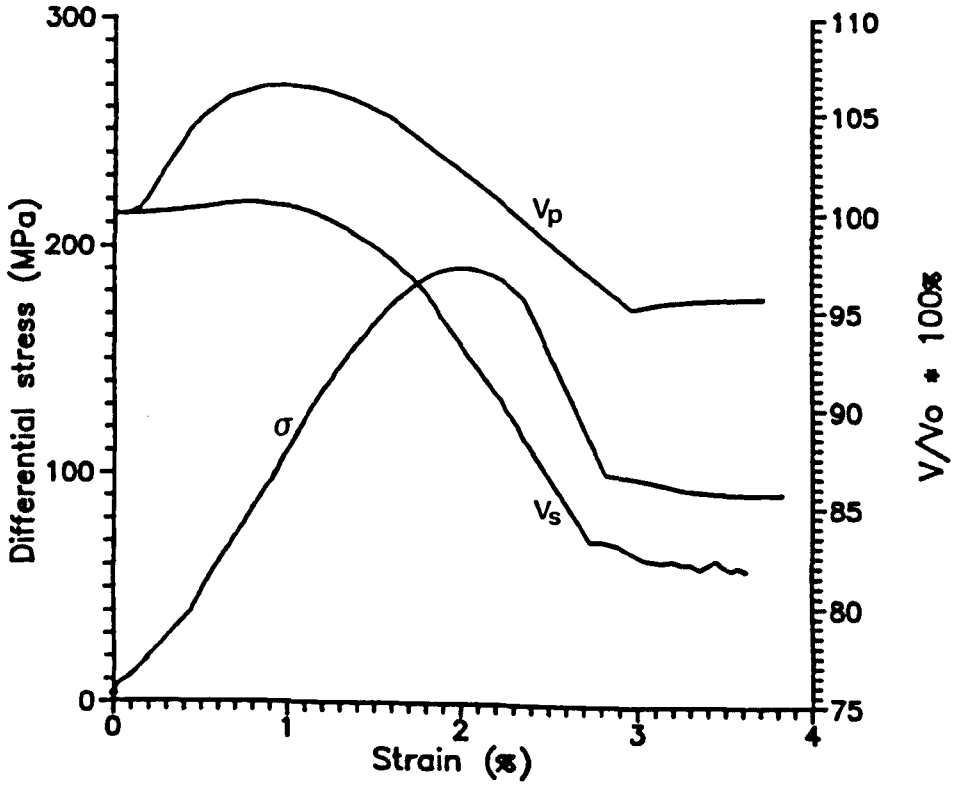

Fig. 7:1 The stress/strain curve and velocity changes for a Darley Dale sandstone sample deformed at 30MPa confining pressure (test nos. MS19).

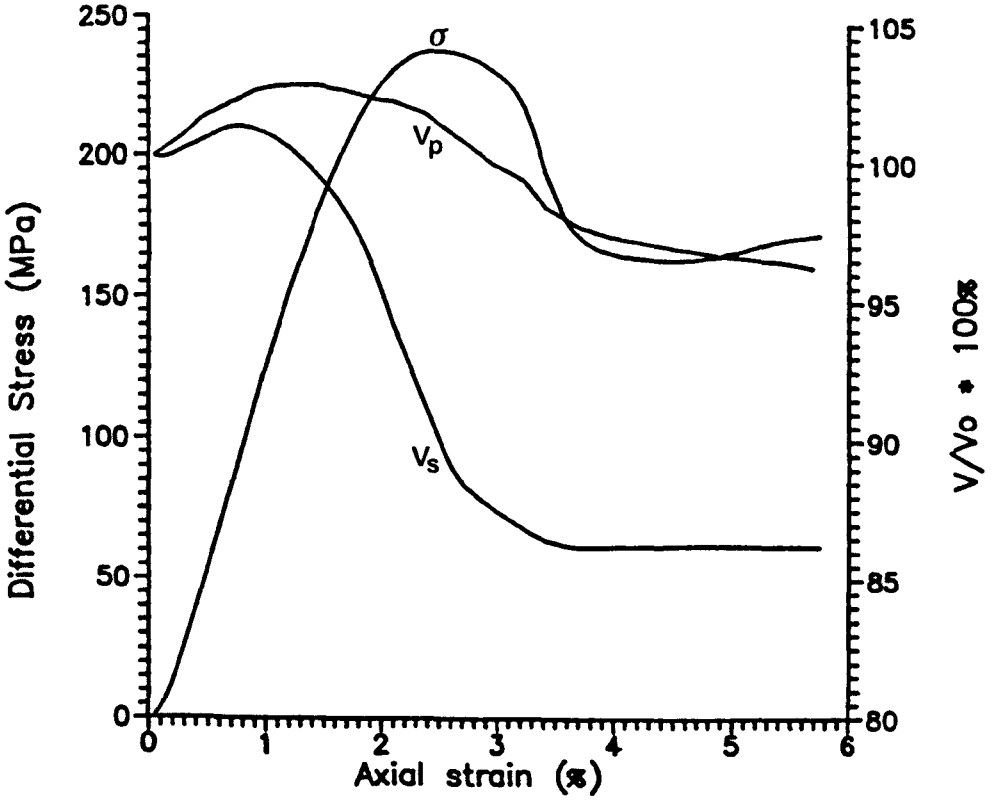

Fig. 7:2 The stress/strain curve and velocity changes for a Darley Dale sandstone sample deformed at 50MPa confining pressure (test nos. DDA1).

≈1.2% strain), and reaches a peak stress of 190MPa at about 2% strain. There is a period of stable roll over, and at about 2.4% strain the rock fails catastrophically resulting in a dynamic stress drop of just under 100MPa. Finally, there occurs a period of stable sliding along the failure plane. Examination of the sample after testing revealed a distinct fracture plane angled at ≈22° to the major stress axis. The angle of failure was measured from the impression of the fault in the soft copper jacket. Both the compressional and shear wave velocities (recorded continuously during this test, and normalised to their respective initial values) show an initial increase; Vp significantly more than Vs. They peak at around 1% strain. As the sample becomes anelastic both Vp and Vs decrease sharply; Vs at a faster rate than Vp. After macroscopic failure both the velocities remain approximately constant.

At 50MPa confining pressure (experiment DDA1) the stress/strain curve (fig. 7:2) shows only a slight initial period of upward concavity. There follows a period of sustained linearity. The curve begins to deviate from linearity at ≈1% strain; an increased peak stress of 240MPa is reached. The sample then strain softens before failing catastrophically at about 3.2% strain (this is marked by an instantaneous stress drop of 50MPa). After failure axial shortening is taken up by sliding on the fault. Examination of the deformed sample showed a failure plane angled at ≈30° to the major axis of compression. Both Vp and Vs rise initially; again Vp increases proportionately more than Vs. These compressional and shear wave velocity increases are less than seen in test MS19. Vs begins to decrease at ≈0.8% strain, while Vp has a broader peak and appears not to begin to decrease until after ≈1.3% strain. Both the compressional and shear wave velocities decrease at a slower rate than seen previously.

At 75MPa confining pressure (experiment D49) the stress/strain curve (fig. 7:3) again shows a slight initial upward turn, this gives way to a reasonably well determined linear gradient. The curve gradually deviates from linearity at around 1.2% strain, anelasticity becomes significant at ≈2% strain. An increased peak stress is seen (≈300MPa), and the sample can sustain this high differential load up to significant strains. Examination of the sample after the experiment showed no clear fault impression in the sample jacket; but there was no apparent barrelling of the sample. A slight increase in the compressional wave velocity is seen, forming a broad, low peak. Vp decreases with a shallow gradient sometime after 1% strain. Vs reaches a low peak at ≈1% strain after which it decreases much more sharply than Vp.

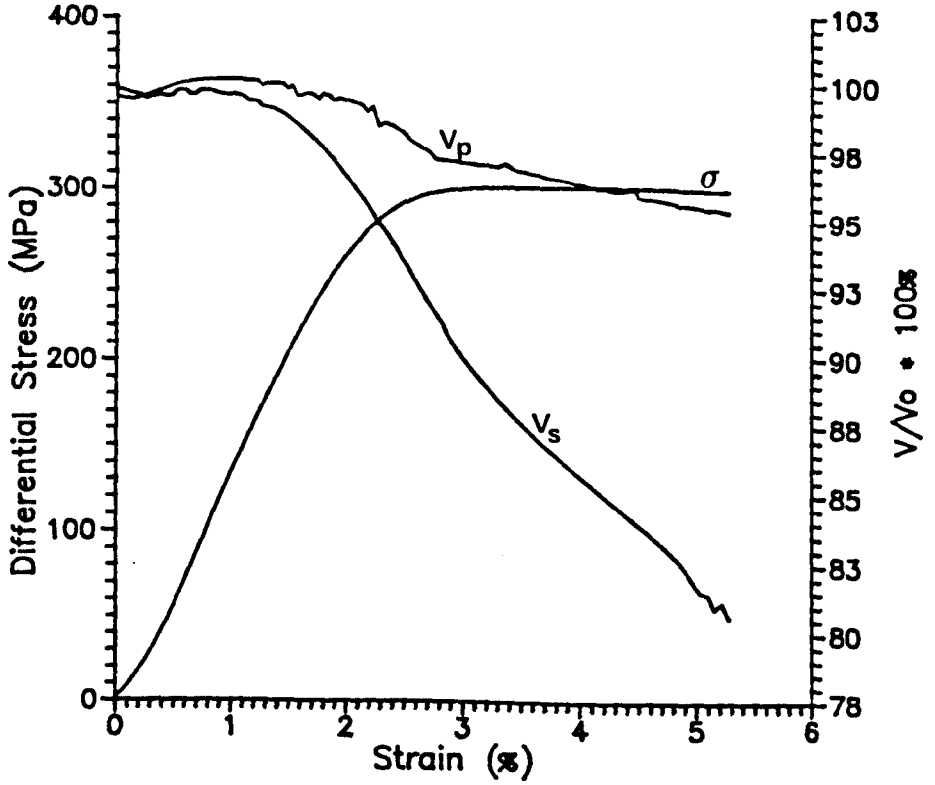

Fig. 7:3 The stress/strain curve and velocity changes for a Darley Dale sandstone sample deformed at 75MPa confining pressure (test nos. D49).

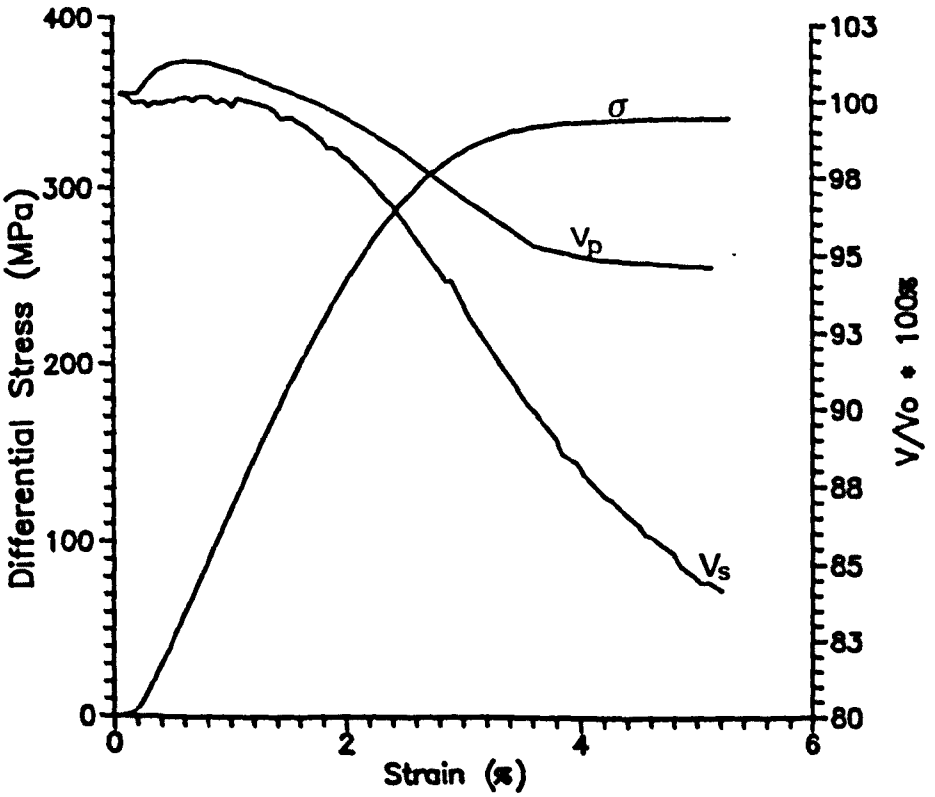

Fig. 7:4 The stress/strain curve and velocity changes for a Darley Dale sandstone sample deformed at 100MPa confining pressure (test nos. MS12).

Fig. 7:4 shows the stress/strain curve and elastic wave velocity changes for 100MPa confining pressure (experiment MS12). Little initial upward concavity is seen upon loading. A distinct linear loading curve is seen, this begins to deviate from linearity at around 1.4% strain. The sample becomes significantly anelastic after about 2% strain. A peak stress of just less than 350MPa is reached. Vp shows a small initial increase, and then decreases at a slow rate. Vs remains reasonably constant before decreasing as the sample becomes anelastic; Vs clearly decreases at a faster rate than Vp. Again both the Vp and Vs decreases are less than at lower confining pressures.

The stress/strain curve for 150MPa confining pressure (D48) increases linearly after initial loading (fig 7:5). The precise point at which the curve begins to deviate from linearity is difficult to determine, but appears to be around 1.5% strain. The curve then rolls over to a peak stress of ≈370MPa. The sample sustains this high differential load up to considerable strains (>10%). The compressional wave velocity increases marginally (fig. 7:5), and then decreases at a slow rate. The shear wave shows a narrow peak at around 1% strain and then decreases more steeply than the compressional wave. The velocities continue to decrease during ductile behaviour showing that progressive damage is occurring in the sample.

At 200MPa confining pressure the stress/strain curve (fig. 7:6; experiment D59) shows a steep initial elastic climb. At around 1.6% strain the curve graduates into an anelastic phase. The sample shows marked strain hardening and reaches a peak stress of over 450MPa. Both Vp and Vs show a slight decrease upon initial differential loading. Vp then increases slightly to form a low broad peak at ≈2.5% strain, it then decreases gently. The shear wave velocity shows no initial increase at all, but begins to decrease significantly at ≈1% strain.

7:3 Discussion.

Some of the essential features of the mechanical response of this rock with increasing confining pressure are best highlighted by using fig. 7:7a which shows the "family" of stress/strain curves for all these tests. These features have been well documented by others (e.g. Murrell 1963, Ismail 1974). An increase in confining pressures results in; (i) an increase in peak stress, (ii) a reduced stress drop, (iii) a slight increase

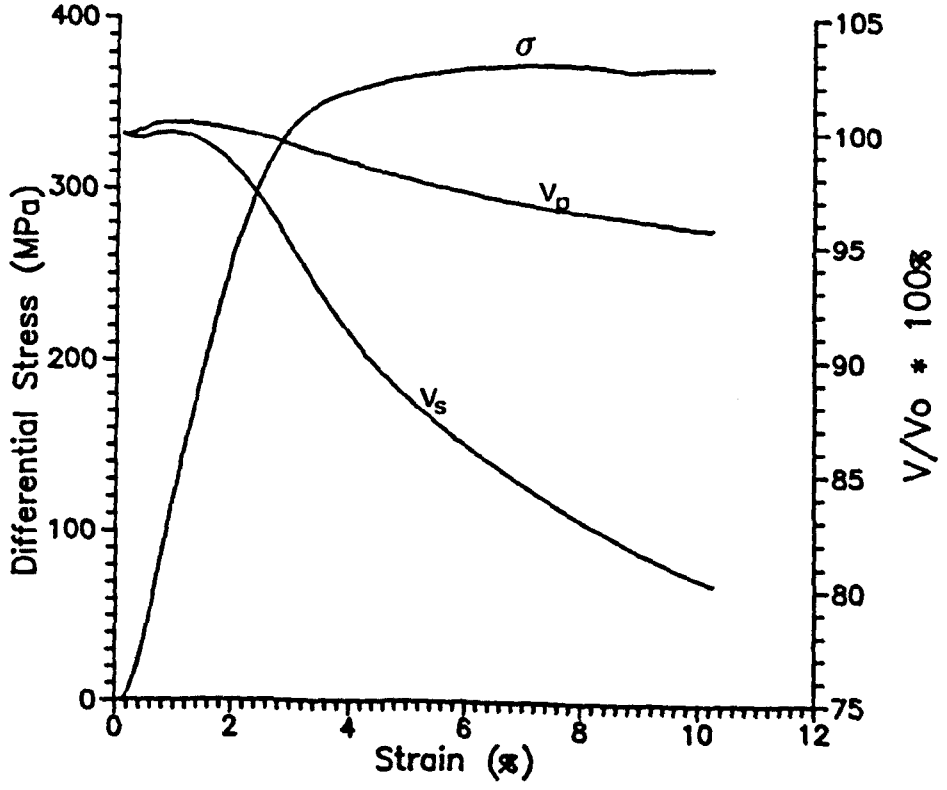

Fig. 7:5 The stress/strain curve and velocity changes for a Darley Dale sandstone sample deformed at 150MPa confining pressure (test nos. D48).

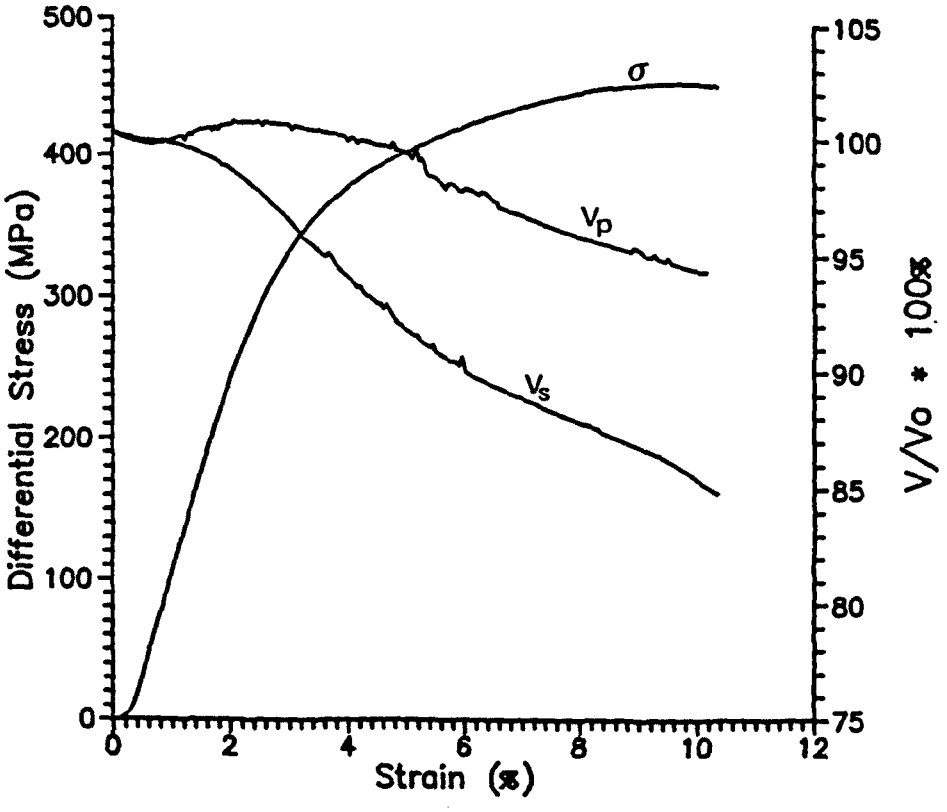

Fig. 7:6 The stress/strain curve and velocity changes for a Darley Dale sandstone sample deformed at 200MPa confining pressure (test nos. D59).

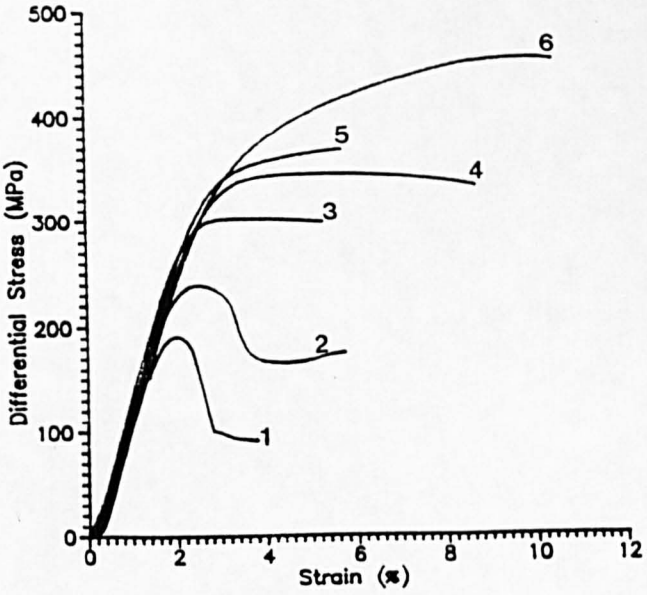

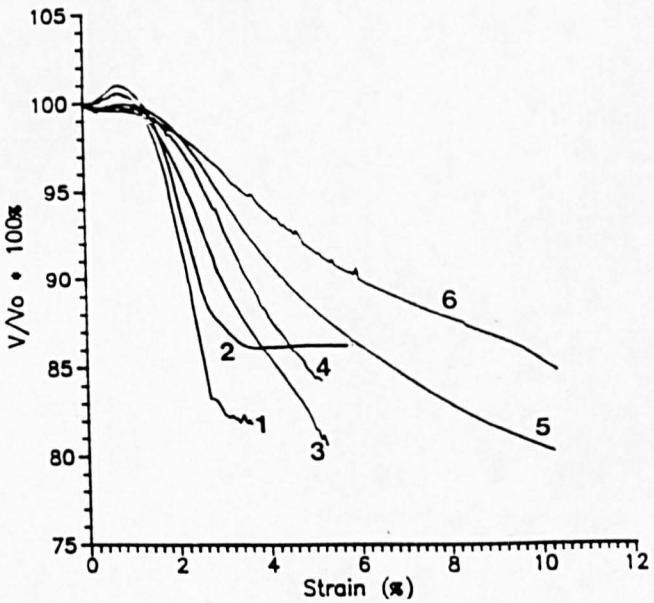

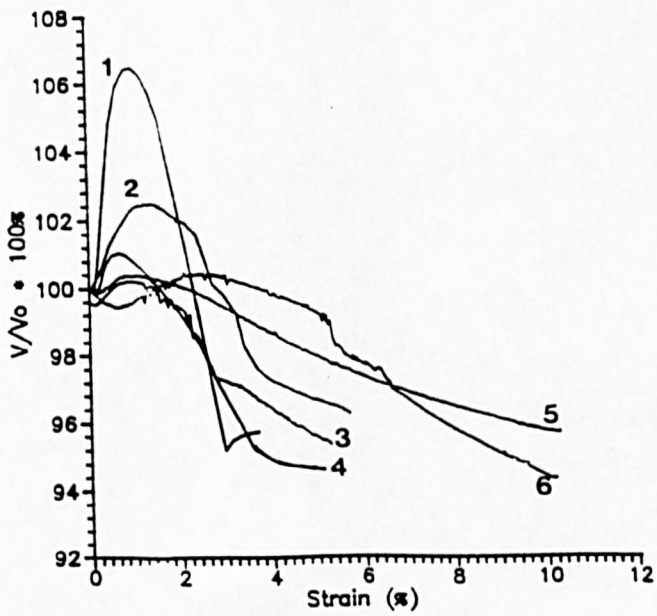

Figs. 7:7a,b,c These diagrams show the family of stress/strain curves (a), shear wave velocity changes (b), and compressional wave velocity changes (c), for Darley Dale sandstone at confining pressures, 30MPa (curve 1), 50MPa (curve 2), 75MPa (curve 3), 100MPa (curve 4), 150MPa (curve 5) and 200MPa (curve 6).

in the tangent modulus, (iv) an increase in the value of strain at which peak stress occurs, and (v) the rock failure mode changing from failure on a single fault to distributed cracking and eventual cataclastic flow. However, these experiments also highlight important new points. Figs. 7:7b,c show the change in the shear and compressional wave velocities with increasing confining pressure. With increasing confining pressure the velocities show less initial increase, a broader peak, and a slower rate of decrease with strain (these features are most obvious in shear wave velocity changes). In all cases upon differential loading, Vp increases proportionately more than Vs. Furthermore, there is a greater decrease in shear wave velocity relative to the compressional wave velocity in all the experiments. How the mechanical response of the rock along with the elastic wave velocity changes can be used to infer mechanisms of damage is discussed below.

At low to moderate confining pressures, initial differential loading causes an upward concavity in the stress/strain curve, and an increase in both Vp and Vs. This period is interpreted as the initial closing of favourably orientated cracks of generally low aspect ratio (i.e. thin cracks). As confining pressure increases a greater proportion of these cracks will already be closed by the hydrostatic pressure alone, making this period less distinct. The closing of these cracks under differential loading will cause a slight stiffening of the sample, and an upward concavity of the stress/strain curve. Crack closure also increases the moduli of the sample resulting in an increase in both Vp and Vs. Cracks with their long axis perpendicular to the loading axis will close preferentially, causing Vp to increase relative to Vs (following from the theoretical analysis of Anderson et al., 1974; see fig. 5:2). Upon further loading the stress/strain curve becomes quasi-linear, during this stage the compressional wave velocity shows a broad peak, the shear wave velocity shows a narrower peak and begins to decrease. This stage of apparent specimen elasticity may result from either predominantly elastic processes such as crack bowing, or from the superposition of two inelastic processes such as a balance between crack closure and crack growth. Since the shear wave velocity decreases more sharply, and begins to decrease earlier than the compressional wave velocity, it appears that crack opening or crack growth is predominantly orientated in the axial direction (that is along the sample length or along the axis of major compression). As the stress/strain response of the sample becomes significantly anelastic, Vp begins to decrease gently while Vs decreases more sharply. The sample is now becoming increasingly anisotropic with the radial moduli decreasing rapidly while in the axial direction the sample remains relatively stiff. The

stress/strain curves roll over to peak stress, and then the sample strain softens. Cracking continues during this period although we cannot be certain at what point crack linkage and coalescence occurs. Finally, following coalescence the rock fails macroscopically on an inclined fracture plane.

A brittle-ductile transition, loosely defined by Heard (1960), occurs where the sample can sustain high loads at significant strains without catastrophic failure. This transition appears to occur at around 75MPa confining pressure for this rock.

As the confining pressure is increased, the initial upward concavity of the stress/strain curve becomes insignificant; the crack porosity is then considered to be mostly closed. The stress/strain curve rises with a well defined linear gradient. During this period there is little change in Vp or Vs. This may suggest that during the linear climb of the stress/strain curve anelastic cracking is suppressed and with increasing confining pressure, elastic processes of pore closure and crack opening are promoted. It should be noted that although most of the low aspect ratio cracks will be closed at high confining pressures (about 200MPa for this rock; Jones, 1989), the more spherical pore space will not be closed. Spherical pores are much more difficult to close by hydrostatic pressure alone. Pores also have much less effect on the elastic wave velocities (e.g. Walsh, 1965; O'Connell & Budiansky, 1974). After the linear stress/strain climb the sample becomes significantly anelastic and the stress/strain curve rolls over. This roll over is then followed by strain hardening of the sample. During this period the elastic wave velocities continue to decrease, but at a slower rate than at lower confining pressures. Following from, for example Horii & Nemat-Nasser (1986) it has been shown that smaller cracks reduce the modulus of a solid (and thus the elastic wave velocity) less than longer cracks. Therefore, elevated confining pressures appear to suppress unlimited crack growth and coalescence. The shear wave velocity still preferentially decreases relative to the compressional wave velocity (although less so than at lower confining pressures). This suggests that axial cracking is still an important mechanism of failure in this rock even at elevated confining pressures.

In summary therefore, the changes in the compressional and shear wave velocities in the above tests can be explained by a series of temporal distributions of different microcrack populations opening and closing. That is, as the sample is initially loaded, favourably orientated cracks (i.e. those with their long axis perpendicular to the loading axis) are closed, causing an upward concavity in the stress/strain response and an increase in both the compressional and shear wave velocities (Vp increasing rather more than Vs). A quasi-elastic period then follows with a linear stress/strain response where crack closure and opening is approximately balanced; this may or may not be an elastic process. At higher confining pressures the processes may become increasingly elastic. Crack growth is preferentially orientated in the major axis of compression. As the sample becomes noticeably anelastic, axial crack growth and extension occurs. It is not clear from this phenomenological study at which stage unstable crack growth and coalescence occurs. This important aspect of rock failure is examined in Chapter 8.

CHAPTER 8

DETAILED ANALYSIS AND MODELLING OF SEISMIC VELOCITIES AND CRACK DENSITIES.

8:1 Introduction.

In this chapter further, more detailed analysis is carried out of results from the two experiments performed at 50MPa and 150MPa confining pressures on Darley Dale sandstone (experiments DDA1 and D48, respectively), and which were described phenomenologically in Chapter 7. The experiment carried out at 50MPa confining pressure, shows all the stages of "classic" brittle failure outlined in section 2:6, while the experiment at 150MPa confining pressure, shows the typical pseudo-ductile behaviour seen for this rock (i.e. a well defined linear stress/strain response, roll over, and then strain hardening). The results of the latter experiment (D48) are described mainly by comparison with those of the former (DDA1). The change in the elastic moduli of the samples are discussed in this section. As the rock sample is progressively deformed, it becomes increasingly anisotropic and the calculated moduli will increasingly only have meaning in the direction in which the velocity is measured (that is, along the differential loading axis). Because of this, the calculated moduli are referred to as "effective moduli" and should, in general, be considered as directional quantities. Also later in this chapter, the change in horizontally and vertically orientated crack density parameters are determined. Furthermore, waveform storage has enabled seismic Qp and Qs to be determined.

The stress/strain curves and velocity changes for the two experiments DDA1 and D48 are reproduced in figs. 8:1 and 8:11 for reference purposes.

8:2 The Vp/Vs ratio for DDA1.

The changes in the Vp/Vs ratio are discussed here as it has been previously cited as an important earthquake precursor (Aggarwal et al., 1973). Initially, there is a slight upwards concavity of the Vp/Vs ratio (fig. 8:2), there then follows a short period

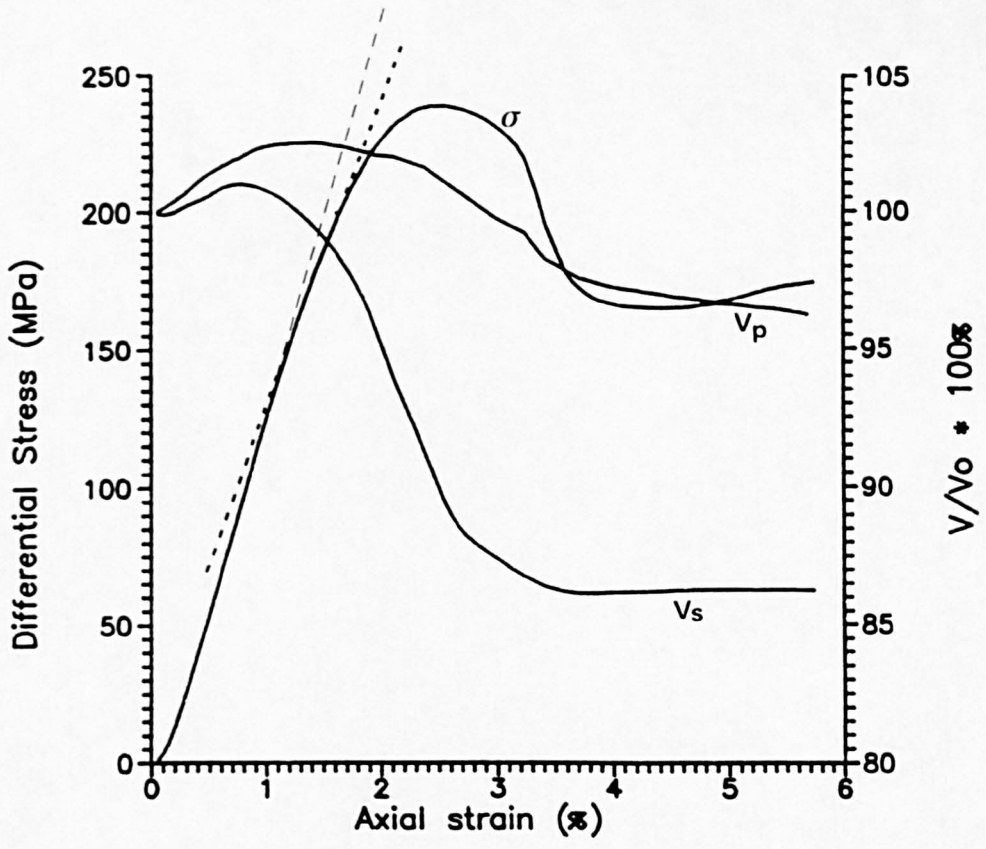

Fig. 8:1 The stress/strain curve and velocity changes for a Darley Dale sandstone deformed at 50MPa confining pressure (DDA1); reproduced from Chapter 7 for reference purposes.

NOTE: In the following diagrams in this thesis gradients referred to in the text are marked by dashed lines for ease of reference.

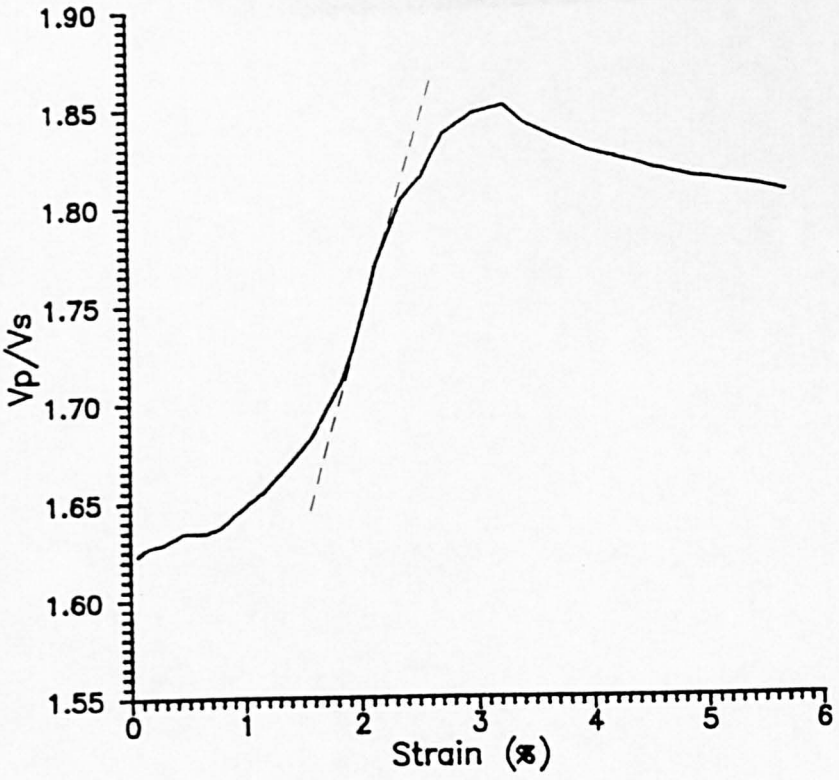

Fig. 8:2 The Vp/Vs ratio for experiment DDA1.

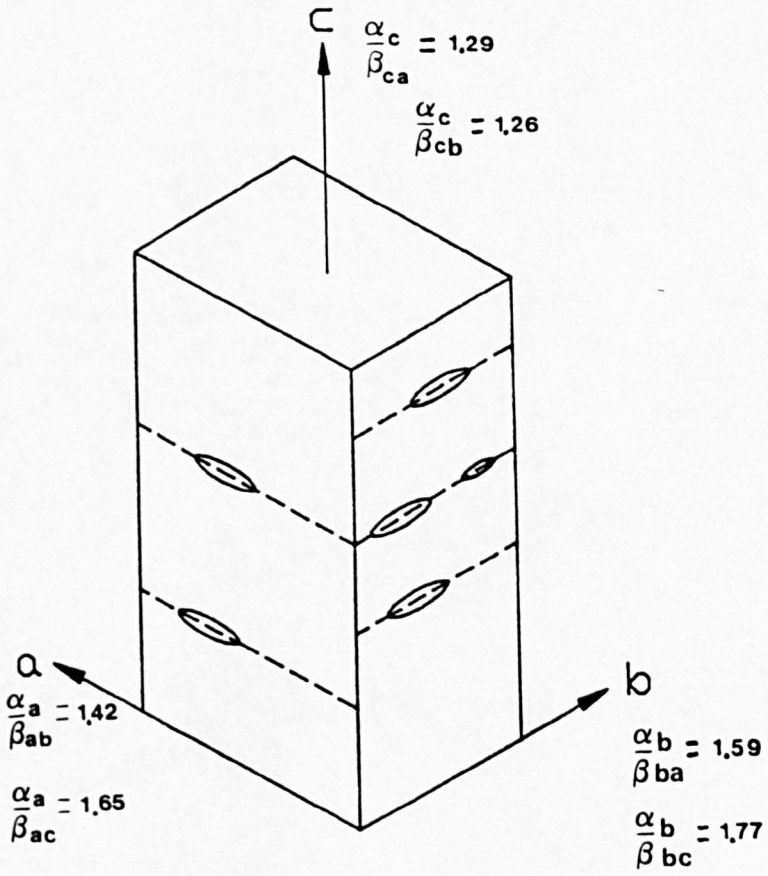

Fig. 8:3 Diagram showing the velocity anisotropy found in Alpine gneisses by Wang & Lin (1974). α and ß are compressional and shear wave velocities respectively. The first suffix denotes the direction of propagation and the second suffix denotes the direction of polarisation, (drawn using information from Wang & Lin, 1974).

of approximate linearity (between 1.9% and 2.2% strain). The Vp/Vs ratio reaches a peak at 3.2% strain, this approximately coincides with macroscopic failure of the sample. The ratio then drops slightly and continues to decrease at a shallow rate.

The period of Vp/Vs linearity coincides with the region where the stress/strain curve rolls over towards peak stress and where both Vp and Vs are decreasing (Vs steeply). A linear increase in Vp/Vs with strain implies that cracks are growing by a set amount for a positive strain increment. Crack growth thus appears, to some extent, to be a strain-linear process and not stress-linear as might be expected.

An increase in the axial Vp/Vs ratio would be expected for an axisymmetric sample with axial cracking (Hadley, 1975a; see fig. 2:5). Others have noted that aligned cracking effects the Vp/Vs ratio; and that this ratio is dependent upon the polarisation of the shear wave with respect to the cracking. For example, Wang & Lin (1974) looked at the velocity anisotropy in gneisses. Fig. 8:3 summarises the information contained in their paper. α_{ij} and β_{ij} being Vp and Vs; the first suffix denotes the direction of propagation and the second suffix the direction of polarisation. The cracks are thought to lie in the plane of the foliation, which is perpendicular to the **c** axis. The velocity ratios in the **c** direction are very similar and therefore hexagonal symmetry can be assumed. In the respective **a** and **b** directions of propagation the velocities are very different, and depend on the orientation of the S waves. Assuming that shear waves travelling in the plane of an elliptical crack and also polarised in this plane are little affected by the crack (Anderson et al., 1974), then these will approximate the shear velocity through the uncracked solid. The effect of crack anisotropy, i.e. the difference between α_b/β_{ba} (or α_a/β_{ab}) and α_b/β_{bc} (or α_a/β_{ac}) results in a velocity ratio anisotropy in the **a** direction of 14% and similarly in the **b** direction it is 11%. This fits in well with the order of increase in Vp/Vs (i.e. 12-13%) seen experimentally here.

8:3 The "effective dynamic Young's modulus" for DDA1.

The effective dynamic Young's modulus (E_{eff}) increases slightly from 34GPa to 35GPa upon initial deviatoric loading (fig. 8:4). It then decreases smoothly to a value of 27.5GPa at ≈3.5% strain, after which it remains constant. Initially, as cracks close, the sample stiffens causing an increase in E_{eff}. As dilatancy ensues, the sample becomes more

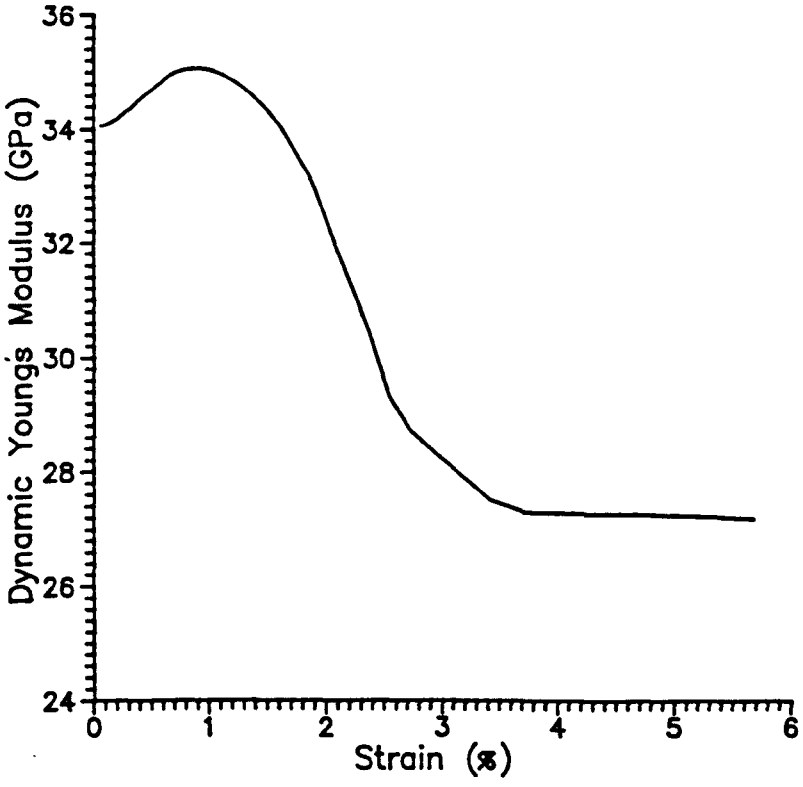

Fig. 8:4 The effective dynamic Young's modulus for experiment DDA1.

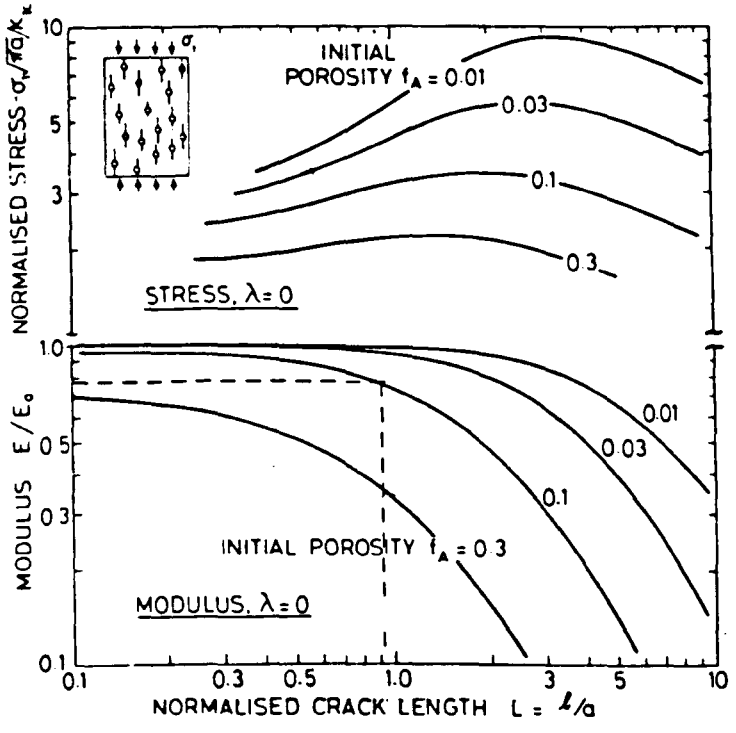

Fig. 8:5 The change in axial stress and Young's modulus as cracks grow and interact. l is the length of the wing crack, and 2a is the size of the initial pore (from Sammis & Ashby, 1986).

compliant causing $E_{eff.}$ to decrease. It should be noted that as crack growth is predominantly axial, then the modulus perpendicular to the loading axis will be expected to decrease at a faster rate than that measured along the differential loading axis.

Sammis & Ashby (1986) used a damage mechanics model to look at the change in Young's modulus of a solid with axially orientated cracks growing from spherical pores (section 2:3). Fig. 8:5 shows the predicted change in the axial Young's modulus calculated in response to the growth and interaction of axial cracks. The model considers anisotropic crack growth aligned along the loading axis. Note that in this model crack instability occurs when L=2 (L=**l**/**a**; where **l** is the crack length and **a** is the pore radius), if the grain size is considered to be of the order of the pore size. Instability then occurs when the length of axial cracks become the order of the grain size. Eo in the figure refers to the Young's modulus of the uncracked solid. This can be approximated reasonably well by the peak value of the dynamic Young's modulus obtained in this experiment (≈35GPa). The fall in modulus during the test (or E/Eo) is 0.22. For a rock of initial porosity of 10% (0.1) a drop in the normalised modulus to 0.78 gives a normalised crack length of L≈0.9. This means that in this experiment crack growth appears to become unstable when the axial cracks grow to about half the grain size (this is smaller than the length predicted by the model). The most probable explanation for this is that, because the velocities are averaged over the whole sample length, crack growth is locally approaching L=2 (probably near the site of final failure), whereas in other regions, such as near the sample ends, cracking may be virtually absent.

8:4 The "effective dynamic Poisson's ratio" for DDA1.

As might be expected from eqn. 5:2 the effective dynamic Poisson's ratio change curve is very similar in form to the Vp/Vs curve. The Poisson's ratio (fig. 8:6) rises from an initial value of 0.19 to a peak of about 0.29 at sample failure (≈3.3% strain). It then decreases slightly.

By equating the static and dynamic Poisson's ratio, an estimate of the volumetric strain of the sample can be determined. This is because the product of the dynamic Poisson's ratio and the axial strain yield the radial strain (i.e. the static Poisson's ratio is $-e_2/e_1$ where e_2 is the radial strain and e_1 the axial strain): the volumetric strain is then simply e_1+2e_2 assuming cylindrical symmetry. If compression is taken as positive,

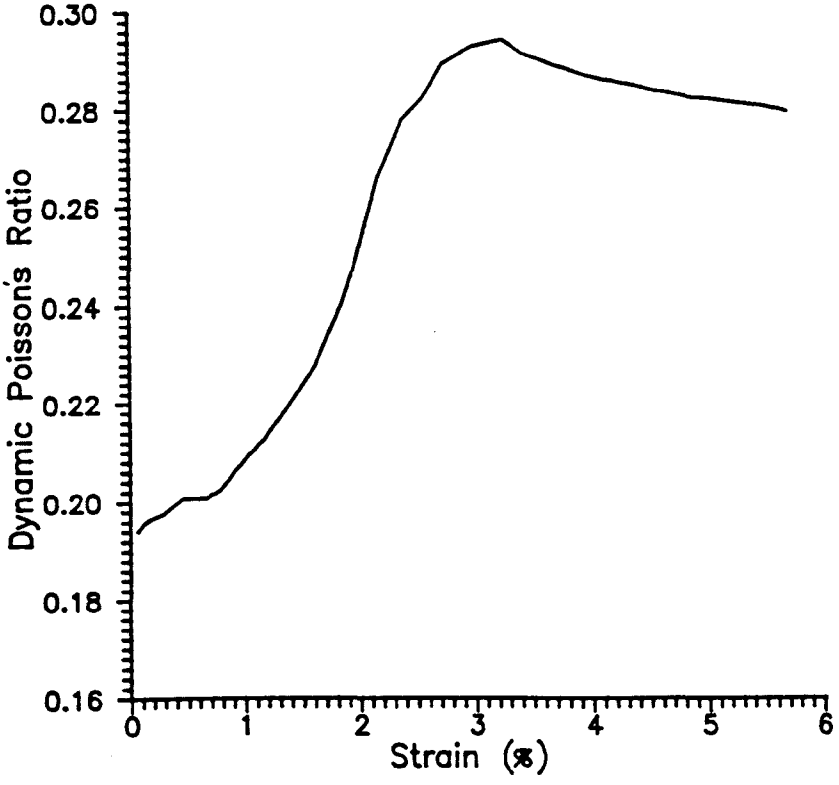

Fig. 8:6 The effective dynamic Poisson's ratio for experiment DDA1.

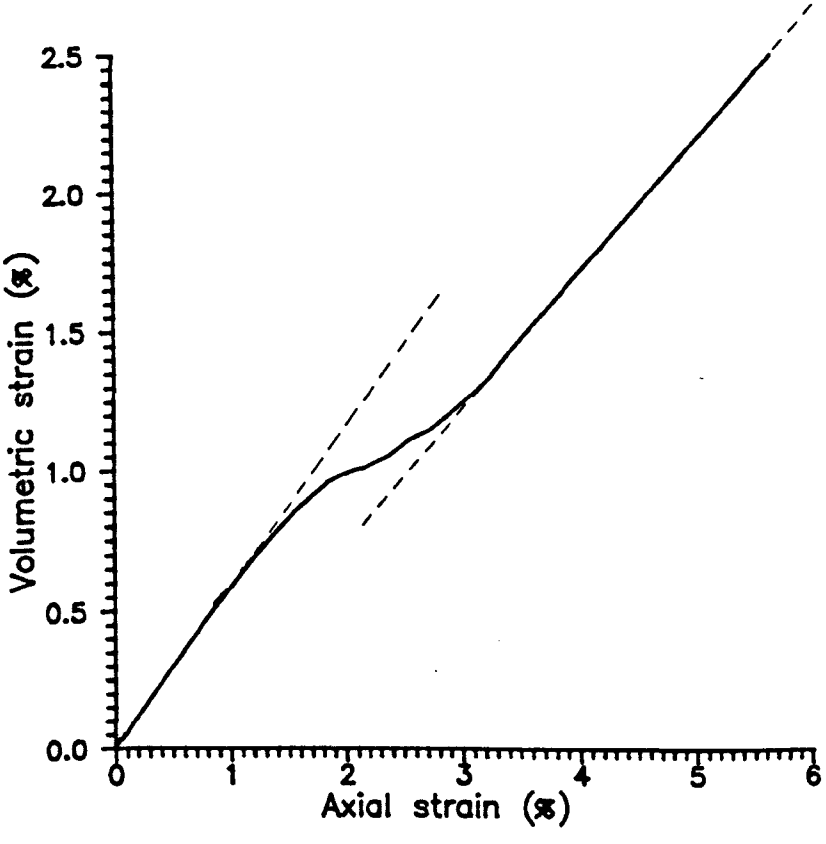

Fig. 8:7 The calculated volumetric-strain/axial-strain plot for experiment DDA1 (see text for details).

then an increase in Poisson's ratio reflects an increase in radial strain relative to axial shortening i.e. dilatancy. An increase in Poisson's ratio of 50% (at 3% axial strain) represents an average increase in the radial strain of ≈4.5%. This corresponds to an average increase in sample radius of ≈0.67mm. This appears reasonable, but is difficult to confirm by post-experimental examination because of variation in jacket thickness, and significantly inhomogeneous dilatancy of the sample. However, micrometer measurements of the sample after failure gave a difference between the initial and final sample diameters of about 1mm, consistent with the above figure.

Fig. 8:7 shows a plot of calculated volumetric strain against measured axial strain. The curve shows an initial well-defined period of elastic sample straining. Inelastic sample straining then begins at ≈1.2% strain, coinciding with the stress/strain curve showing sample anelasticity (fig. 8:1). The slope of the volumetric/axial strain plot then becomes shallower, reflecting an increase in radial expansion relative to axial contraction. Rapid dilatancy appears to occur above about 1.9% strain and coincides with the stress/strain curve showing significant anelasticity. Above about 3% strain, the curve again resumes a linear increase, however at a slightly reduced rate. The form of this curve is in very good agreement with a plot presented by Jaeger & Cook (1979, p82, Fig.4.2.5), which shows volumetric strain against axial strain determined for a sandstone by a method similar to the dilatometer method (section 2:2).

A major problem with equating the dynamic and static Poisson's ratio to estimate the volumetric strain, is that it relates a vector quantity like velocity to a scalar quantity like volume change. As cracking becomes increasingly anisotropic volumetric strains determined by this method will become less valid. However, the method provides a useful measure of the onset of dilatancy. To accurately determine the true volumetric strain, elastic wave velocities should ideally have to be measured along all three principal axes simultaneously.

8:5 The change in crack densities for DDA1.

Fig. 8:8 shows the change in crack density parameter calculated using the model of O'Connell & Budiansky (1974), valid for a random, dense population of penny-shaped cracks (previously discussed in sections 2:4:3 and 5:6). The curve decreases

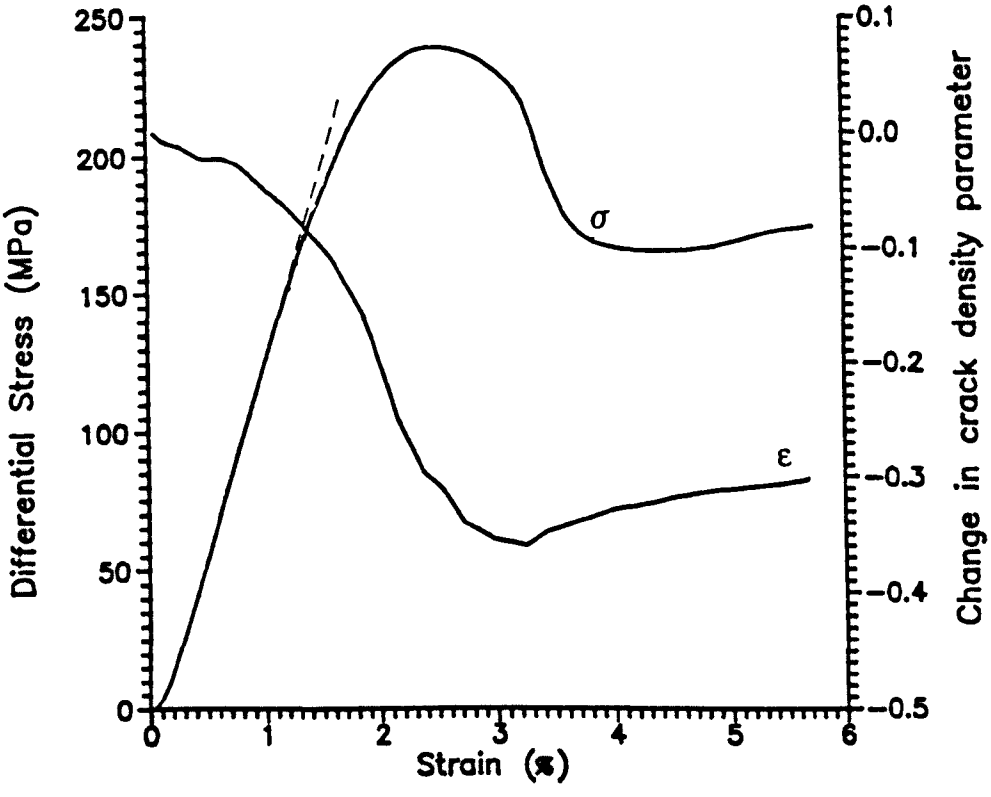

Fig. 8:8 The change in crack density parameter ε for experiment DDA1, determined using the O'Connell & Budiansky (1974) method valid for random, densely populated cracks.

slightly upon initial differential loading, then as the sample becomes anelastic the crack density parameter falls sharply. After macroscopic failure the crack density parameter increases slightly. This model suggests that crack closure is occurring while the acoustic velocities are falling and the sample is becoming more compliant. The reason for this is probably that the model predicts that Vp will be affected more than Vs (for random cracking). As Vs actually decreases more steeply than Vp in the experiment, a reduction in the crack density parameter is determined. Thus the importance of considering crack anisotropy when analysing velocity data is highlighted by this example, since the calculated result is inconsistent with all the experimental observations.

A more suitable model which considers crack alignment and anisotropy has previously been presented by Soga et al. (1978) and adapted for use in this study (see section 5:6:1). In this model, anisotropic crack populations can be superimposed to determine their cumulative effect on acoustic wave velocities measured in any direction. Even with the restrictions of the present experimental arrangement, both the vertical crack density parameter (εx) and the horizontal crack density parameter (εz), can be determined. εz is the crack density function for cracks with their long axis perpendicular to the z, or major compressive, axis. εx denotes the crack density function for cracks with their long axis perpendicular to the x or y axis (which are equivalent in the axisymmetric case). Inclined cracking will be vectorially distributed between εx and εz.

The εx and εz curves, determined from the velocity data are presented in figs. 8:9a,b. Both parameters show a very slight decrease upon initial differential loading (εx is probably affected by the closing of inclined cracks). εx begins to rise at about 0.8% strain. It then increases rapidly, reaching a peak value at 3.2% strain. This graph illustrates two important features. Firstly, the onset of dilatancy is more easily identifiable using the εx plot than the stress/strain curve where interpreting the onset of dilatancy is fairly subjective. Secondly, peak dilatancy occurs noticeably after peak stress and very close to the point of macroscopic failure. After failure, during frictional sliding, dilatancy remains essentially constant.

The εz curve shows much less change than εx. This is as expected from the mechanical response of the sample, and from the acoustic velocity measurements which show only a relatively small increase upon initial differential loading. εz decreases at a

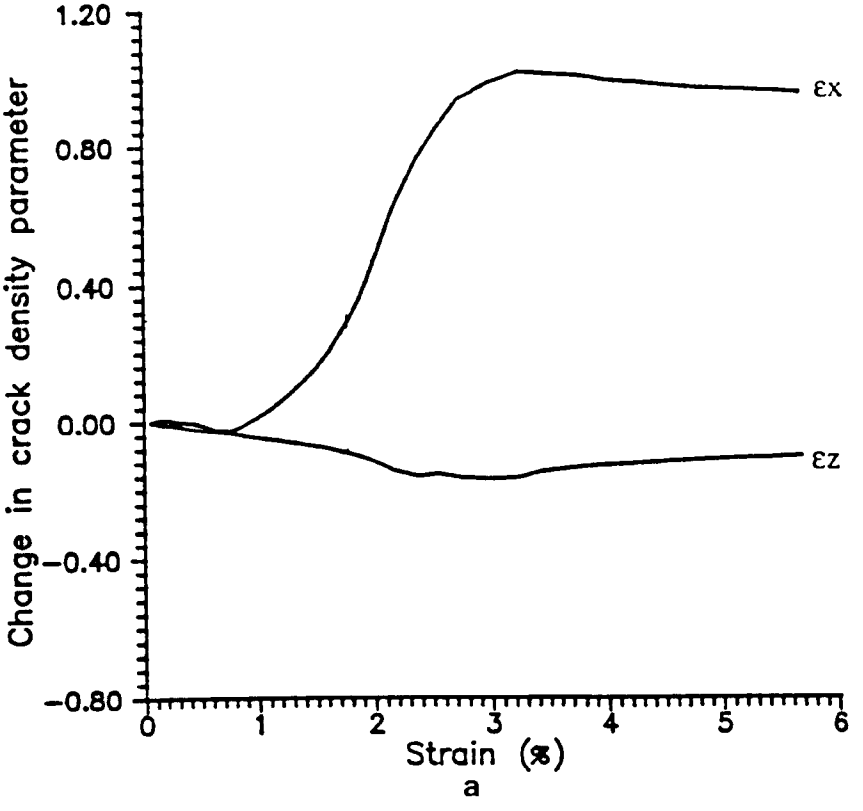

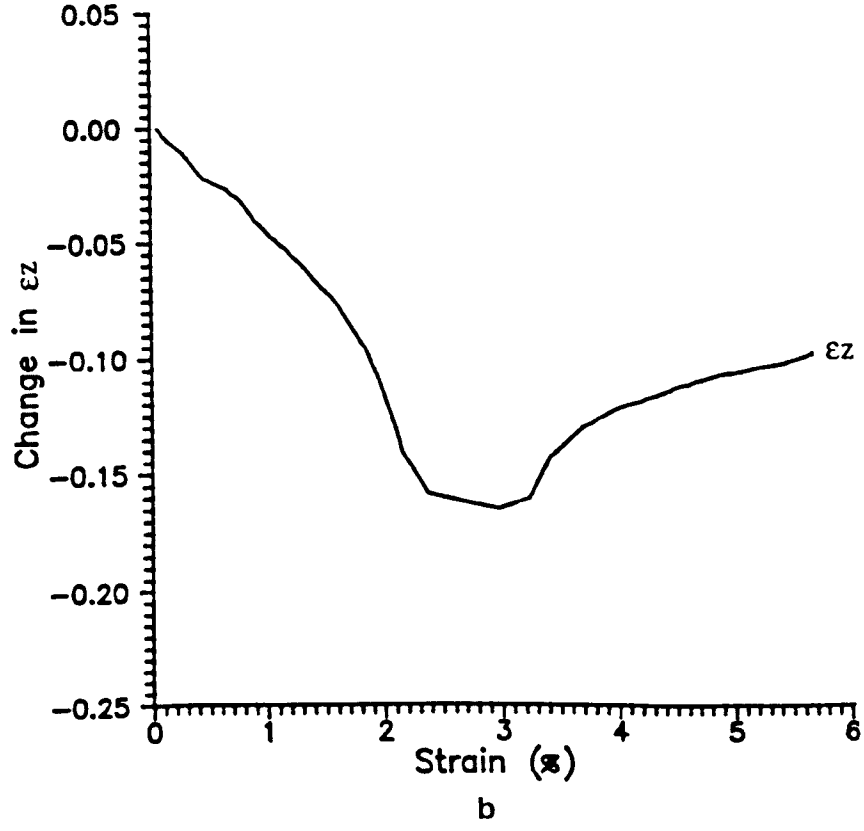

Figs. 8:9a,b The change in the vertical (or axial) crack density parameter εx (a) and the horizontal crack density parameter εz (a,b) for experiment DDA1. These were calculated using the Soga et al. (1978) linear crack density model which considers aligned crack populations. εz in (b) is merely the εz data in (a) plotted on a larger scale.

reasonably constant rate until about 2.3% strain, or approximately at peak stress (fig. 8:9b merely shows εz plotted on a larger scale to show its detailed form). It then remains constant before increasing sharply at about 3.2% strain (macroscopic failure). This graph is significant since it suggests that axial cracking dominates deformation until right up to the point of macroscopic failure. Inclined cracking (which is suggested by the increase in εz) appears to be virtually contemporaneous with macroscopic failure of the sample.

8:6 The seismic Q values for DDA1.

The received elastic waveforms were digitised and stored approximately every 300s. The digitising rate was 20MHz, and each waveform was 4096 data points long. The seismic Q values were determined from the P wave first arrival (Qp) and the S wave first arrival (Qs), using the method described by Toksoz et al. (1976). The first arrivals of each waveform were picked by hand. These wavelets were then separated from the rest of the recorded waveform. The wavelets were then extended with leading and tailing zeros until each waveform was 1024 points long (the FFT algorithm requires the waveform to be 2^n data points long, where n is an integer). A waveform that is long in the time domain is required to ensure a smooth function in the frequency domain, because each point on the spectrum in the frequency domain is 1/T apart, where T is the effective length of a discrete and repetitive waveform in the time domain. The amplitude spectra of each waveform were then determined using the ASYSTANT software. Q is then finally determined using the method outlined in section 5:6:2.

The seismic Q values determined from the P wave (Qp) and the S wave (Qs) are shown in fig. 8:10. The initial Q values lie between ≈25 and 40. These values appear to be reasonable. Johnston et al. (1979) give Q values for a variety of sandstones to be between 10 and 52, determined using different laboratory techniques. Upon loading Qp and Qs rise smoothly to peak values of about 45 and 72, respectively. This increase occurs not only during the initial compactive phase (as seen on the stress/strain curve and the elastic wave velocity data) but also during the linear elastic stress climb. This increase probably results from both sample compaction and from improving acoustic contact at the ram/sample interface. From section 5:6:2 it has been shown that an improving acoustic contact can have a dramatic effect on the wave amplitudes. It was also seen that Q is not

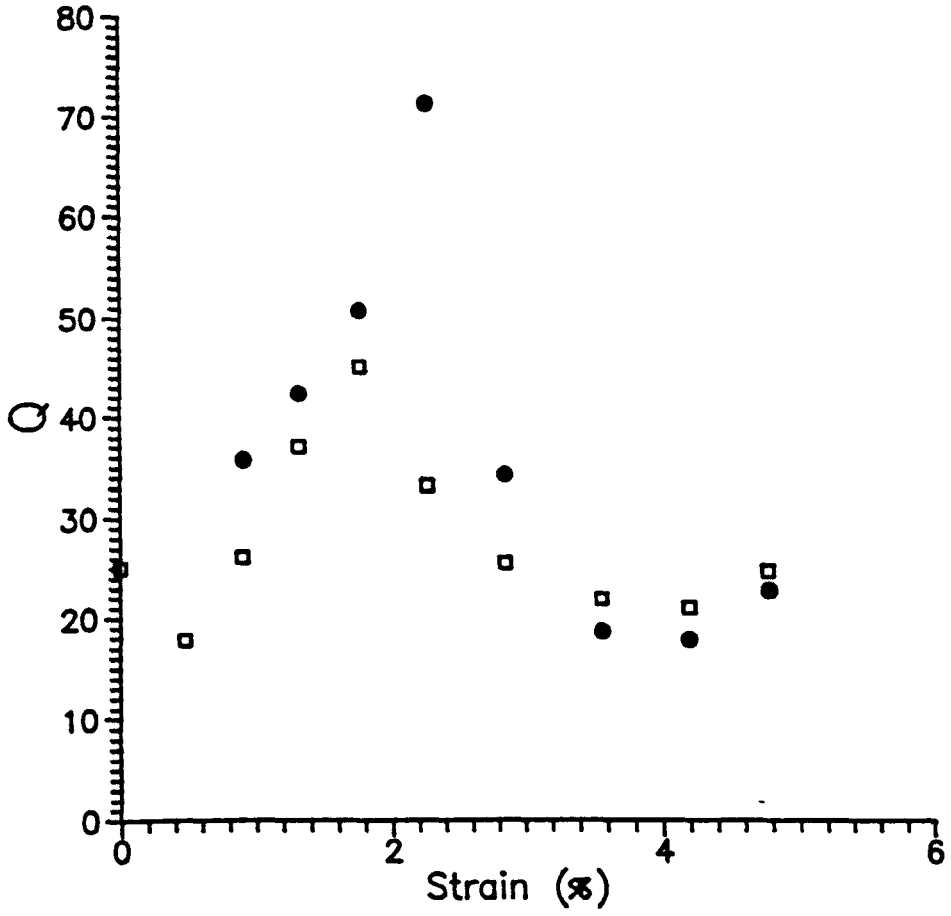

Fig. 8:10 The seismic Qp and Qs values for experiment DDA1 determined using the spectral ratios method. ●- Qs □-Qp

very strain sensitive for small strains, but is strongly load dependent to a stress of about 30MPa. This stress level is overcome by the hydrostatic pressure alone, yet there is still a large increase in Q upon differential loading. Concurrent pore and crack closure will change the acoustic impedance between the rams and the rock, and an estimate of the load at which crack closure is mostly complete can be obtained from hydrostatic velocity measurements made by Jones (1989). These measurements show that most of the cracks in Darley Dale sandstone are closed by about 200MPa hydrostatic pressure. Hence at a confining pressure of around 50MPa, all acoustically sensitive cracking should be closed at around 150MPa differential stress. This stress value is reached between 1.0 and 1.5% strain. However, the Q values continue to rise until the combined differential and hydrostatic stress is about 300MPa. This suggests that attenuation is more sensitive to internal changes in the rock microstructure than are velocity measurements. Acoustic emission location experiments (sections 2:4:1) suggest that dilatant cracking occurs mainly away from the ram ends. Thus the acoustic impedance across the sample/ram contact should remain constant after crack closure, and most importantly, during crack opening.

Qp falls from a peak value of 45 at 1.8% strain to a value of about 23. Qs has a peak value of about 70 at 2% strain, and then falls to less than 20. These changes represent a decrease in Qp of about 50% and in Qs of about 70%; compared to decreases in Vp and Vs of only a few percent and 12%, respectively, from their maximum values. This difference in sensitivity between the velocity and attenuation measurements, although large, is not unexpected. For example, Johnston & Toksoz (1980) report cracking that caused a 1% change in velocity but at the same time caused a 60% change in Q. Qs falls more steeply than Qp mirroring the steeper fall seen in Vs relative to Vp. It is not clear why Qs should reach a higher peak value than Qp, although it is known that shear waves are more sensitive to changes in the contact conditions than are compressional waves (section 5:6:2).

An important aspect of these attenuation measurements is that it is essentially a measure of anelastic processes, whereas velocity is essentially dependent upon changes in the elastic properties of the rock. Therefore, simultaneous elastic wave velocity measurements and Q value measurements potentially offer a useful way to distinguish between elastic and anelastic crack opening in a deforming rock sample.

8:7 A review of the physical changes for the Darley dale sandstone sample deformed at 150MPa confining pressure (experiment D48).

The experiment discussed here (D48) is described phenomenologically in Chapter 7, and the stress/strain curve and velocity changes are shown in (fig. 8:11).

The Vp/Vs ratio (fig. 8:12) for this experiment shows a similar initial value as for experiment DDA1. It remains fairly constant during the linear stress/strain response of the sample, and then increases from ≈1.6 to 1.75, between 2-4% strain. After about 4% strain the rate of increase becomes less. The total increase in Vp/Vs is about 16%, this is more than is seen in experiment DDA1, although the total axial strains are also larger in experiment D48. Also, the Vp/Vs ratio continues to increase throughout the test, whereas in experiment DDA1 the ratio decreases after dynamic sample failure.

The initial value of effective dynamic Young's modulus (fig. 8:13) is slightly higher than the peak modulus value seen in the previous test (40GPa±4GPa and 35GPa±3.5GPa, respectively). However, there is approximately 10% error in the calculation of Young's modulus where the elastic wave velocities are measured to an accuracy of ±1% (section 5:6). Therefore, these values are within the experimental error of the system. Taking 35GPa rather than 40GPa as the uncracked modulus in the crack length determination (section 8:4) makes little difference to the calculated mean crack length. The effective modulus begins to decrease after ≈1% strain, the rate of decrease is steepest between 2.6-4% strain. This coincides with the maximum rate of curvature in the stress/strain curve. The total modulus decrease during the experiment is about 28%, this is slightly more than in experiment DDA1.

The effective dynamic Poisson's ratio (fig. 8:14) remains fairly constant until the sample becomes anelastic (≈1.4% strain). The rate of increase is maximum between about 2.2% and 3.8% strain, and reflects the period of most rapid dilatancy. The calculated volumetric strain curve (fig. 8:15) shows a linear increase up until ≈ 2% strain, after which a shallower, but linear, increase is seen. This linearity probably reflects a period of stable crack growth.

Fig. 8:16 shows the vertical (εx) and horizontal (εz) crack density parameter changes. There is very little change in εz; this again confirms that most of the cracks are

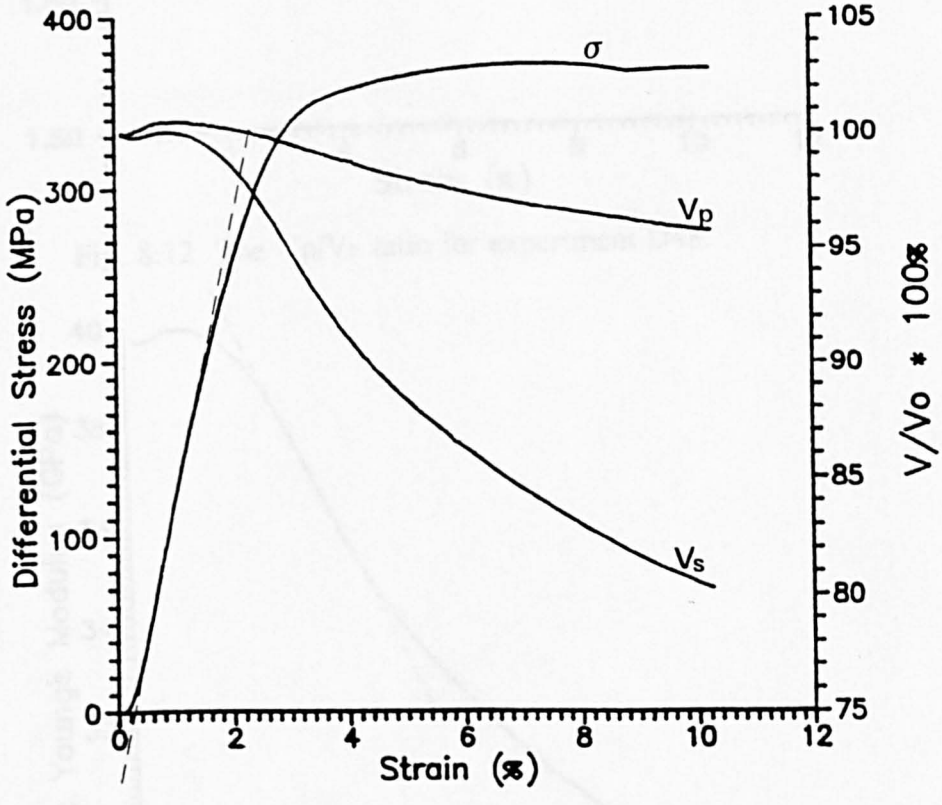

Fig. 8:11 The stress/strain curve and velocity changes for a Darley Dale sandstone deformed at 150MPa confining pressure (D48); reproduced from Chapter 7 for reference purposes.

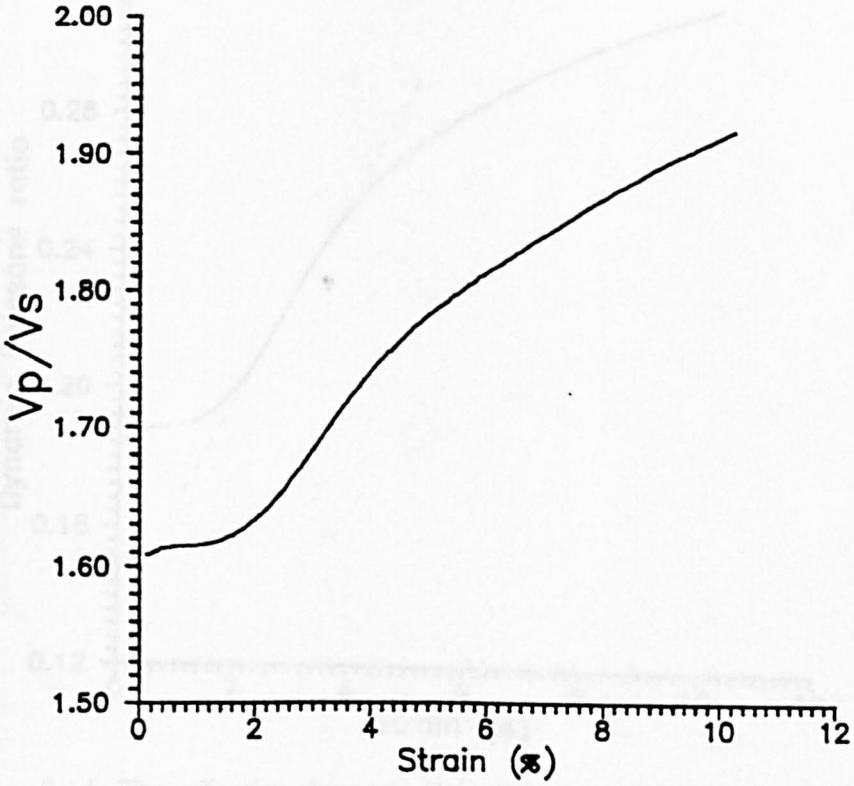

Fig. 8:12 The Vp/Vs ratio for experiment D48.

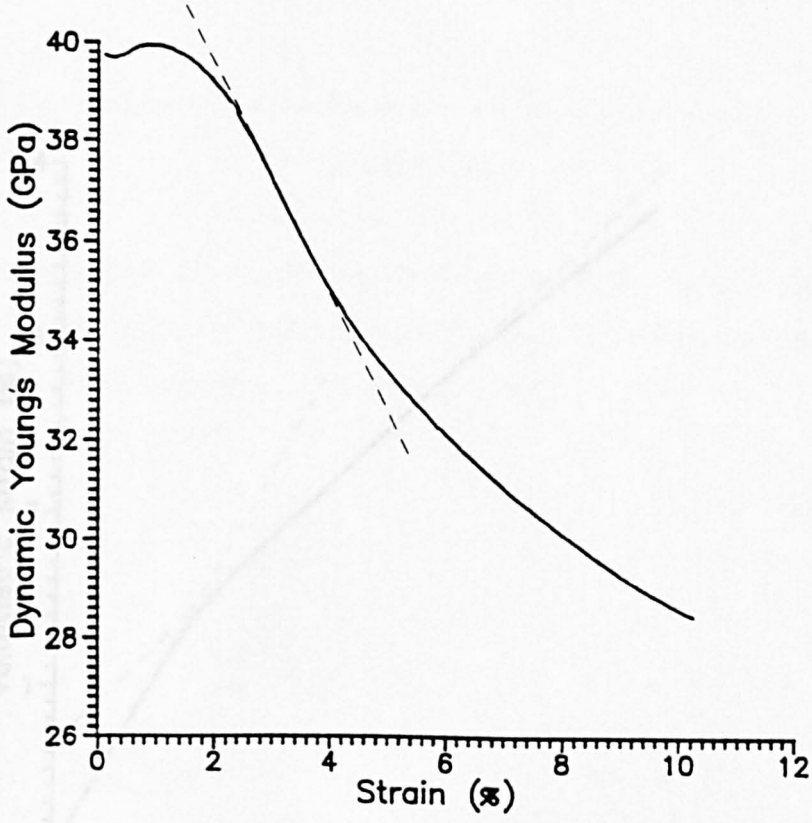

Fig. 8:13 The effective dynamic Young's modulus for experiment D48.

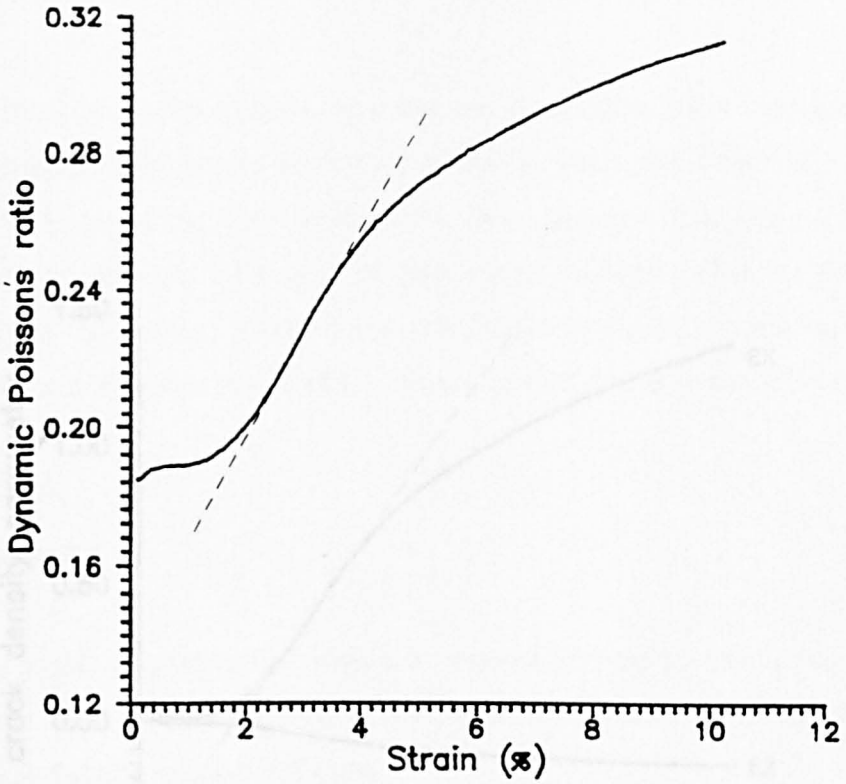

Fig. 8:14 The effective dynamic Poisson's ratio for experiment D48.

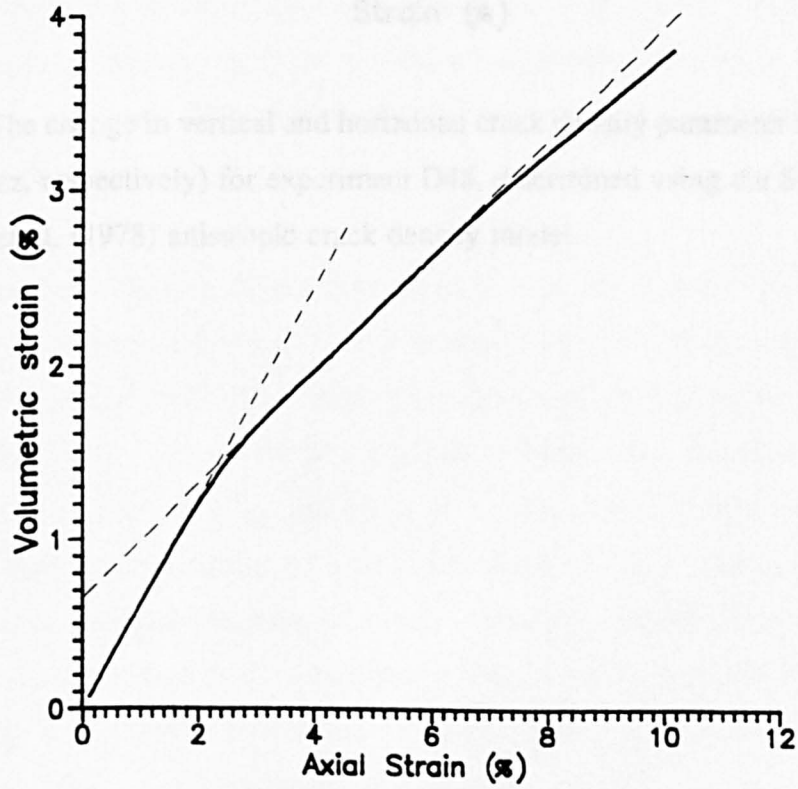

Fig. 8:15 The calculated volumetric-strain/axial-strain plot for experiment D48.

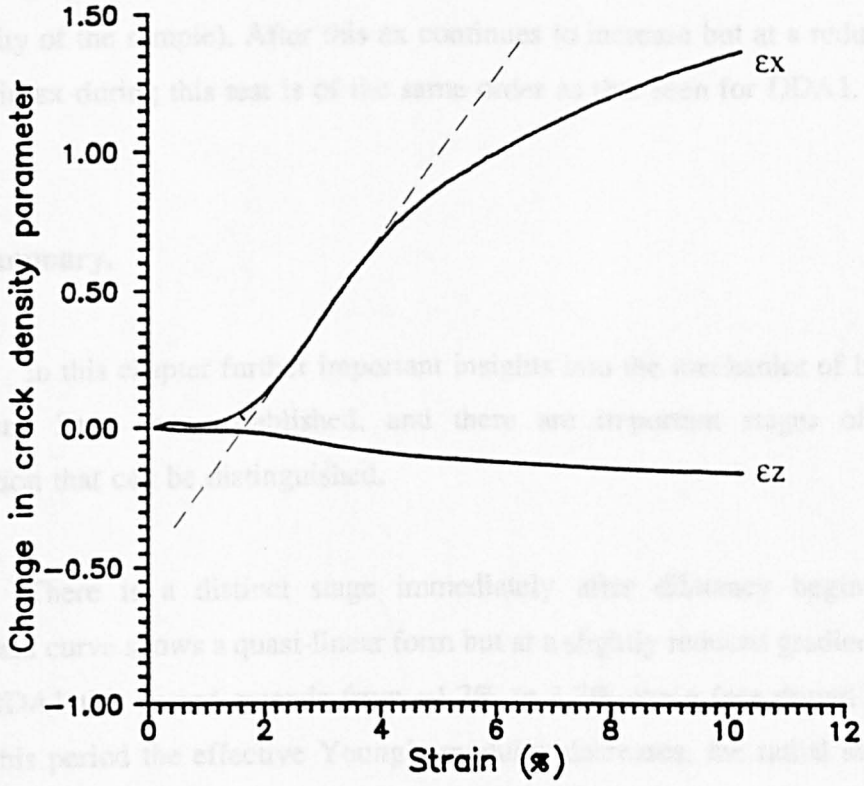

Fig. 8:16 The change in vertical and horizontal crack density parameter (εx, εz, respectively) for experiment D48, determined using the Soga et al. (1978) anistropic crack density model.

closed in this rock at these confining pressures. εx remains fairly constant during initial differential loading, but begins to increase after ≈1% strain which coincides approximately with the deviation of the stress/strain curve from linearity. The steepest increase in εx occurs roughly between 2.4% and 4% strain (and coincides with the most significant anelasticity of the sample). After this εx continues to increase but at a reduced rate. The increase in εx during this test is of the same order as that seen for DDA1.

8:8 Summary.

In this chapter further important insights into the mechanics of brittle fracture and failure have been established, and there are important stages of brittle rock deformation that can be distinguished.

There is a distinct stage immediately after dilatancy begins, where the stress/strain curve shows a quasi-linear form but at a slightly reduced gradient than before. In test DDA1 this period extends from ≈1.2% to 1.7% strain (see dotted line fig. 8:1). During this period the effective Young's modulus decreases, the radial strain increases relative to axial shortening, and the vertical crack density parameter (εx) increases; seismic Q also increases. This stage probably reflects crack initiation, but is prior to significant crack growth.

Another important stage occurs where significant anelasticity of the sample is seen, and the stress/strain curve rolls over to peak stress (≈1.7-2.5% strain in DDA1). The volumetric/axial strain curve shows significant dilatancy, εx increases sharply, and the moduli of the sample decrease steeply. Seismic Q values also decrease sharply. Since O'Connell & Budiansky (1974) and Horii & Nemat-Nasser (1985) have shown the greatest decrease in the modulus of a solid is caused by larger cracks. Then it seems reasonable to assume that the point of crack coalescence would cause the most rapid decrease in elastic moduli and subsequently, the sharpest decrease in elastic wave velocities. Fig. 8:17 shows a plot of the differential of the shear velocity change curve with respect to strain. The point of greatest shear wave change occurs between 2% and 2.5% axial strain. This coincides with significant anelasticity of the sample, and occurs just before peak stress. Therefore, it appears that accelerated crack growth and linkage are

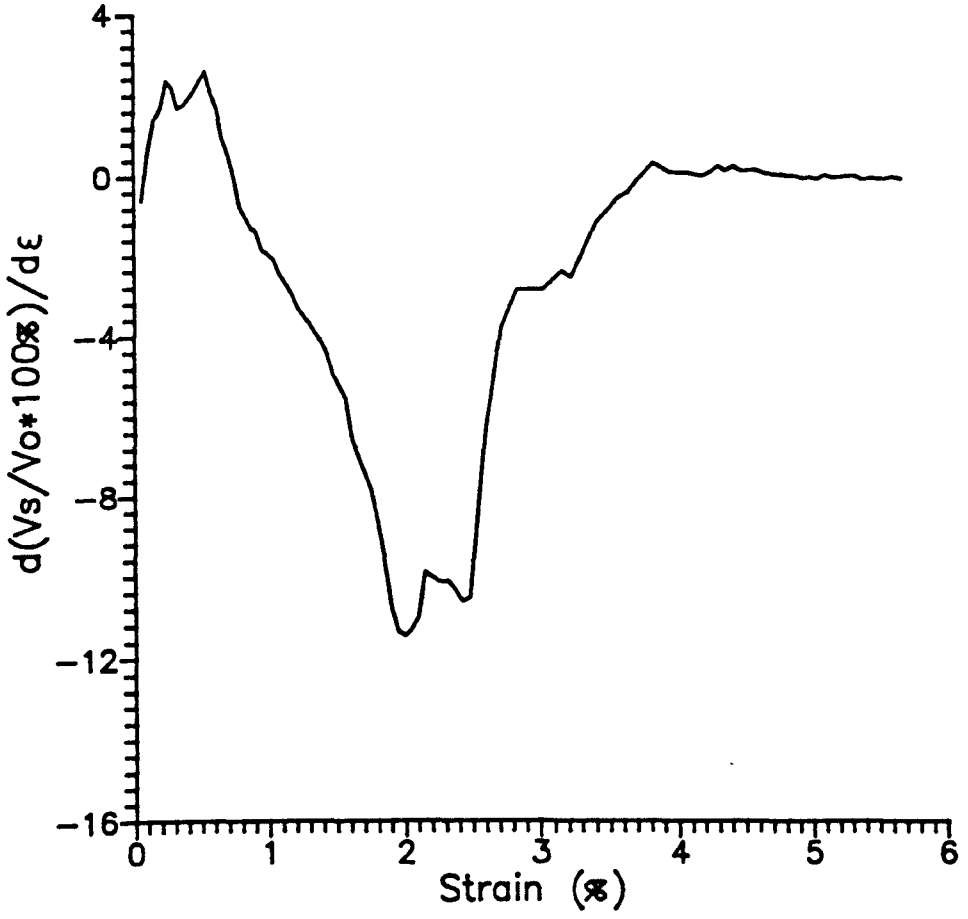

8:17 Differential plot of the shear wave velocity change curve with respect to axial strain.

occurring just prior to peak stress. Although the Sammis & Ashby model suggests that cracks are too small at this stage for crack linkage to occur, it is most probable that linkage is occurring locally in the most damaged areas of the rock.

After peak stress in experiment DDA1, the sample strain softens and then fails macroscopically. The rate of decrease in the shear wave velocity becomes less after peak stress. The maximum in Poisson's ratio coincides with macroscopic failure, and the vertical crack density parameter (εx) also peaks at failure. These two observations imply that maximum dilatancy occurs as the sample fails catastrophically. The cracking remains predominantly axial in nature until immediately before failure. The plot of horizontal crack densities (εz) suggests that the onset of inclined cracking and macroscopic failure of the sample are virtually synchronous.

The above stages are discussed more fully and clarified in Chapter 14, where additional information from direct volumometry is used to elucidate damage processes.

The forms of the physical parameter curves for the experiment D48 (i.e. showing phenomenologically ductile deformation) are as expected. Firstly, there is little sign of pore closure upon initial differential loading. Secondly, the linear climb of the stress/strain curve is predominantly the result of elastic processes. Thirdly, after the sample has reached peak stress and the sample strains at constant stress, damage continues to occur in the sample in a stable manner. This is indicated by the continued decrease in moduli and increase in the vertical crack density parameter.

CHAPTER 9

ELASTIC WAVE VELOCITY MEASUREMENTS ON GOSFORD SANDSTONE.

9.1 Introduction.

A series of experiments have been performed on Gosford sandstone for comparative purposes with Darley Dale sandstone. Both materials are medium grained sandstones and are of similar porosities (see Appendix 1). Edmond and Paterson (1972) have presented stress/strain curves and volumetric strain plots for Gosford sandstone (determined using the dilatometer method), at confining pressures of 100MPa, 200MPa, 400MPa and 600MPa. At these confining pressures, the rock is well within its pseudo-ductile regime. This is the first time the brittle response of the rock has been presented and also the first time elastic wave velocity measurements have been reported for this material.

9:2 The stress/strain response and velocity changes.

The experimental results are discussed only briefly, because many of the essential phenomenological features of the stress/strain curves and elastic wave velocity curves are similar to those discussed in Chapter 7 for Darley Dale sandstone. However, a closer analysis of the results suggests that Gosford sandstone may be deforming in a notably different way to Darley Dale sandstone. Figs. 9:1a,b,c show the family of stress/strain curves, and the compressional and shear wave velocity changes.

The stress/strain curve for the sample deformed at 15MPa confining pressure (experiment GS4) shows only a slight upward concavity upon initial differential loading. The stress peaks sharply at about 120MPa. After a short strain softening phase the sample fails catastrophically; a stress drop of about 30MPa is observed. Examination of the sample after failure showed a fracture plane angled at about 33° to the differential loading axis. Both the compressional and shear wave velocities show similar large increases of about 4% as the sample is initially loaded. The velocities begin to decrease as the sample becomes anelastic; Vs is more affected than Vp.

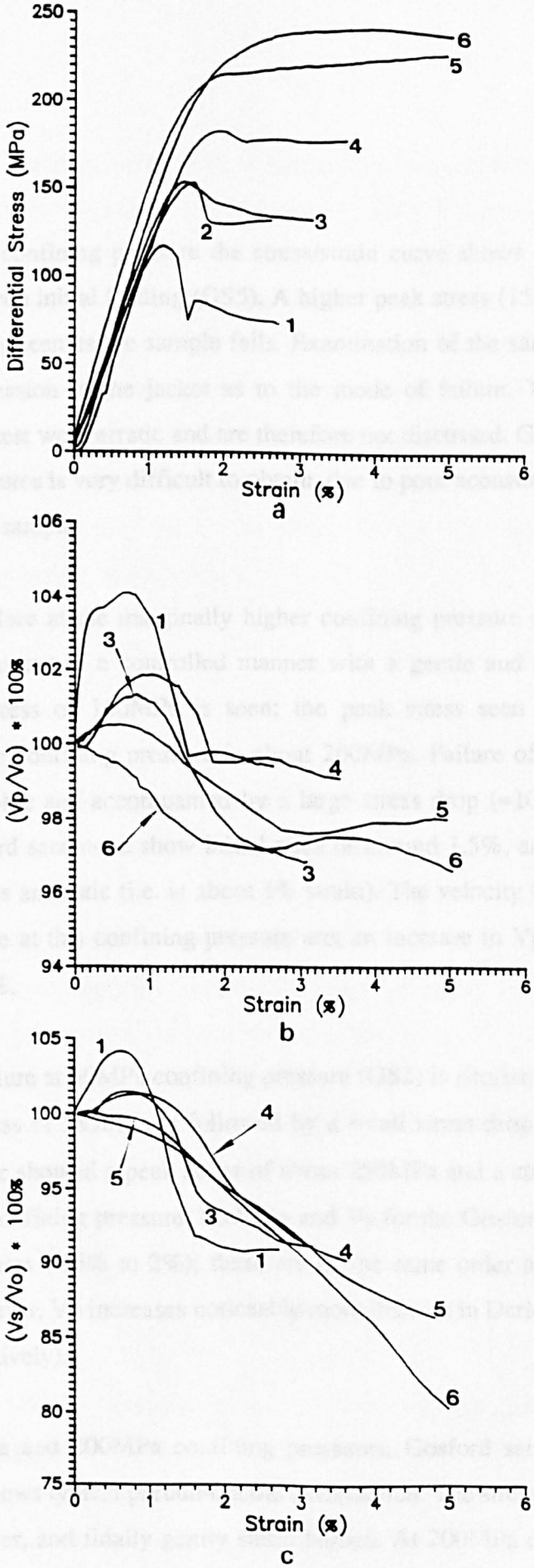

Figs. 9:1a,b,c The family of stress/strain curves (a), the changes in compressional wave velocity (b), and the changes in shear wave velocity for Gosford sandstone at confining pressures 15MPa, 25MPa, 30MPa, 50MPa, 100MPa and 200MPa. Curve 1 represents parameter changes at 15MPa, 2 at 25MPa, 3 at 30MPa, 4 at 50MPa, 5 at 100MPa, and 6 at 200MPa.

At 25MPa confining pressure the stress/strain curve shows little evidence of sample compaction upon initial loading (GS5). A higher peak stress (150MPa) and lower stress drop (20MPa) is seen as the sample fails. Examination of the sample after failure shows no clear impression in the jacket as to the mode of failure. The velocity data measured during this test were erratic and are therefore not discussed. Good velocity data at low confining pressures is very difficult to obtain, due to poor acoustic contact between the ram ends and the sample.

Sample failure at the marginally higher confining pressure of 30MPa (GS3), however, appears to occur in a controlled manner with a gentle and continuous strain softening. A peak stress of 150MPa is seen; the peak stress seen for Darley Dale sandstone at the same confining pressure is about 200MPa. Failure of the Darley Dale sandstone is catastrophic and accompanied by a large stress drop (≈100MPa). Both Vp and Vs for the Gosford sandstone show initial rises of around 1.5%, and then decreases as the sample becomes anelastic (i.e. at about 1% strain). The velocity increases seen for Darley Dale sandstone at this confining pressure are; an increase in Vp of ≈5%, and an increase in Vs of ≈2%.

Sample failure at 50MPa confining pressure (GS2) is similar to the 30MPa test result; i.e. a peak stress of 185MPa is followed by a small stress drop of about 10MPa. Darley Dale sandstone showed a peak stress of about 250MPa and a stress drop of about 50MPa, at the same confining pressure. Both Vp and Vs for the Gosford sandstone show similarly small increases (1.5% to 2%); these are of the same order as seen for Darley Dale sandstone. However, Vp increases noticeably more than Vs in Darley Dale sandstone (≈3% and 1% respectively).

At 100MPa and 200MPa confining pressures, Gosford sandstone (GS6 and GS10 respectively) shows typical pseudo-ductile deformation. The stress/strain curves rise linearly, then rolls over, and finally gently strain harden. At 200MPa confining pressure the peak stress (240MPa) is much less than that observed for Darley Dale sandstone (450MPa) at the same confining pressure.

At 100MPa confining pressure the compressional wave velocity shows a small increase of about 0.5% upon initial differential loading, while Vs remains approximately constant. Both the velocities decrease as the sample becomes dilatant. Vp decreases by about only 2% and then shows a slight increase during strain hardening.

Vs also continues to decrease throughout the test performed at 200MPa confining pressure; firstly at a slow rate (during the linear stress/strain response) and then at a faster rate as the sample becomes anelastic and then work hardens. Vp also decreases during the linear stress/strain response of the rock. However, Vp appears to increase slightly ($\approx$0.5%) as the sample work hardens.

9:3 Discussion.

The form of the mechanical and acoustic results for Gosford sandstone are generally in agreement with those obtained for Darley Dale sandstone. There are a number of easily recognisable features, such as: (i) A pressure dependent sample strength. (ii) A reduced stress drop with increasing confining pressure. (iii) A slight increase in the tangent modulus with confining pressure. (iv) The stages of brittle deformation outlined in section 2:6. The stages observed include compaction, a near-linear stress/strain response, anelasticity, work softening and catastrophic failure. (v) As seen in the Darley Dale sandstone, the respective velocity curves (Vp and Vs) decrease less with increasing confining pressure. (vi) Furthermore, Vs decreases proportionately more than Vp in all the tests. However, there are clear differences in the way in which the two sandstones behave, these are discussed below along with how they may reflect differences in the damage processes occurring in each rock.

At each confining pressure at which a test was conducted, the Gosford sandstone is much weaker than the Darley Dale sandstone and the stress drop at failure was also much smaller. The stress/strain curves for this rock show a well defined linear period, during which the elastic wave velocities generally increase (at least at low confining pressures). Both the compressional and shear wave velocities increase at a similar rate, whereas for the Darley Dale sandstone there is a distinct velocity anisotropy upon initial differential loading (i.e. Vp increases relatively more than Vs). Why Vp and

Vs should increase by similar amounts is not entirely clear. However, it appears that Gosford sandstone has an easily closed crack-porosity, and this is because significant inelastic compaction is only seen at the lowest confining pressure (15MPa). At higher pressures the stress/strain curves rise linearly upon loading. Therefore, as the sample is loaded the velocity increase is probably the result of the closing of the more spherical pore space. This would lead to less velocity anisotropy than the closing of thin cracks aligned perpendicular to the maximum loading axis (e.g. Walsh, 1965). The low rock strength, and the easily closed crack porosity suggest that Gosford sandstone is a weakly cemented rock. The velocities show no initial increase at 200MPa confining pressure (and Vp shows only a small increase at 100MPa confining pressure while Vs decreases). Therefore, it appears that most of the pore space is closed by 100MPa confining pressure. This velocity decrease probably results from the elastic opening of cracks or pores closed by the confining pressure.

As the rock becomes dilatant the elastic wave velocities decrease, the shear wave velocity proportionately more than the compressional wave velocity. This again (as in Chapter 7) suggests that axial cracking is an important damage mechanism. It seems reasonable to assume that in this rock the cracking is predominantly grain boundary in character because of the weak grain cementation.

The brittle-ductile transition is difficult to determine for the Gosford sandstone. The stress/strain curves show that the rock strain hardens at confining pressures above 100MPa. They also suggest that the rock fails catastrophically below 30MPa. Between 30MPa and 50MPa confining pressure, although the samples work soften, they deform in a stable way. Post-experiment examination of the samples showed that only at the lowest confining pressure of 15MPa was a clear fault plane impression seen in the soft copper jacket. Following the definition of Heard (1960), the brittle-ductile transition can be considered to occur at around 30MPa confining pressure for this rock.

As the rock fails in a pseudo-ductile manner and strain hardens, the compressional wave velocity appears to show relatively little change (and may even increase slightly), whereas the shear wave velocity continues to decrease at a steady rate. In Darley Dale sandstone it was seen that both Vp and Vs continue to decrease at high strains, reflecting continued sample damage. The reason why Vp does not continue to

decrease at high strains is not clear. However, extensive grain boundary cracking could loosen grains such that grain-rotation and eventual cataclastic flow occurs. During cataclastic flow the grains may readjust their packing in a similar way to soils and loosely consolidated sediments. This process could possibly result in slight temporary rise in Vp (and be accompanied by short-lived stiffening of the rock). However, in order for Vs to continue to decrease the process of axial (and probably grain boundary) cracking would have to persist.

In conclusion, it appears that the general framework of brittle failure outlined in sections 2:6 and 8:10 is also applicable to Gosford sandstone. There are, however, marked differences in its response (compared with that of Darley Dale sandstone), which are revealed by the stress/strain curves and elastic wave velocities. Most cracking is closed at very modest confining pressures (about 25MPa), and pore closure, which is probably predominantly elastic in character, occurs during the linear stress/strain climb. Most of the pore structure appears to be closed by about 100MPa. Dilatant cracking again appears to be predominantly axial in character. It appears that the matrix is much weaker than the average grain strength, thus making grain boundary cracking, grain loosening and eventually cataclastic flow likely.

CHAPTER 10

ELASTIC WAVE VELOCITY MEASUREMENTS ON SOLENHOFEN LIMESTONE.

10:1 Introduction.

A set of experimental results are presented for Solenhofen limestone deformed at confining pressures ranging from 75MPa to 200MPa. The stress/strain curves and the elastic wave velocity changes are described, and the possible micromechanisms of failure are discussed in detail at the end of the chapter. These results are also presented in the context of previous experimental results reported in the literature.

10:2 The mechanical response and elastic wave velocity changes.

Fig. 10:1 shows the stress/strain response and elastic wave velocity changes for a Solenhofen limestone sample deformed at a confining pressure of 75MPa (experiment S324). The stress/strain curve shows an initial upward concavity, followed by a well-defined linear-elastic phase between ≈0.9 and 1.6% strain. This is followed by a very short period of anelasticity before the sample fails abruptly at around 2.2% strain. A peak stress of 450MPa is reached; after failure the sample shows little residual strength (≈50MPa). Post-experiment examination of the sample revealed that it failed on a single, well-defined, fracture plane inclined at ≈27° to the differential loading axis. Neither Vp nor Vs show much variation before macroscopic failure of the sample, although there is a slight increase in Vp relative to Vs upon initial loading. Then after about 1% strain (and during the essentially linear elastic stress/strain response of the sample) both Vp and Vs decrease gently at a similar rate. The small velocity anisotropy between Vp and Vs prior to failure, their similar rates of change, and the small amount of total velocity decrease (≈2%) contrast markedly with the elastic wave velocity variations reported for both Darley Dale and Gosford sandstones in the previous three chapters. At failure the shear wave trigger was lost due to severe attenuation of the interrogating wave.

At 100MPa confining pressure (test S322) the stress/strain curve (fig. 10:2) shows a near-linear elastic climb (between ≈0.4% and 1.4% strain). There is a reduced

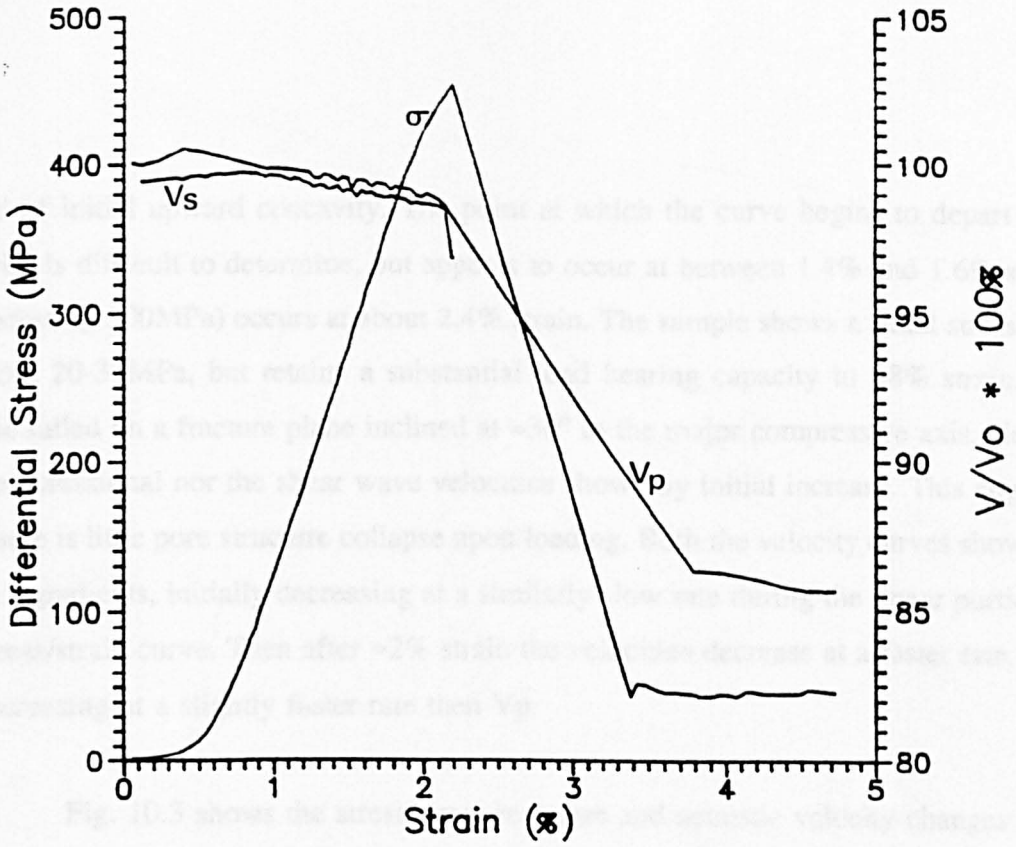

Fig. 10:1 The stress/strain curve and velocity changes for Solenhofen limestone deformed at 75MPa confining pressure (test nos. S324).

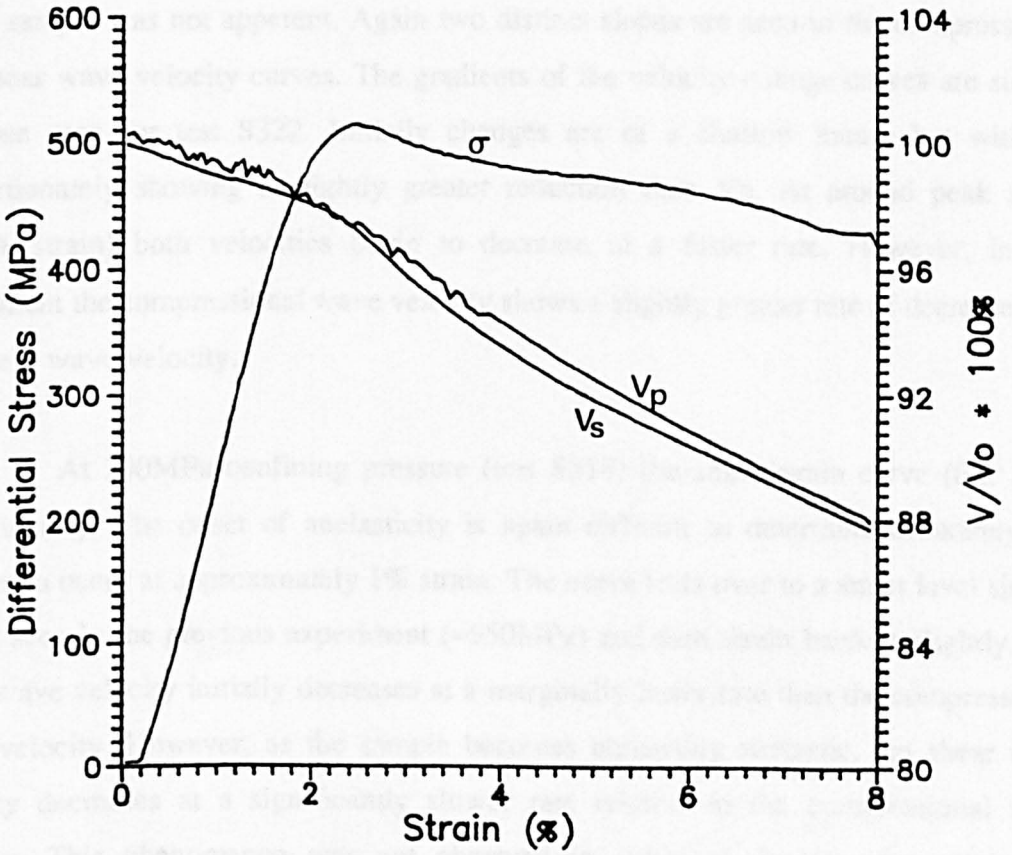

Fig. 10:2 The stress/strain curve and velocity changes for Solenhofen limestone deformed at 100MPa confining pressure (test nos. S322).

period of initial upward concavity. The point at which the curve begins to depart from linearity is difficult to determine, but appears to occur at between 1.4% and 1.6% strain; peak stress (≈500MPa) occurs at about 2.4% strain. The sample shows a small stress drop of about 20-30MPa, but retains a substantial load bearing capacity to >8% strain. The sample failed on a fracture plane inclined at ≈30° to the major compressive axis. Neither the compressional nor the shear wave velocities show any initial increase. This suggests that there is little pore structure collapse upon loading. Both the velocity curves show two distinct gradients, initially decreasing at a similarly slow rate during the linear portion of the stress/strain curve. Then after ≈2% strain the velocities decrease at a faster rate, with Vs decreasing at a slightly faster rate then Vp.

Fig. 10:3 shows the stress/strain response and acoustic velocity changes for a sample deformed at a confining pressure of 150MPa (test S320). The stress/strain curve rises steeply to a peak stress of about 550MPa at 3% strain. After peak stress the rock remains competent, showing only a gentle work softening. Examination of the sample after deformation showed no fault plane impression in the copper jacket, but barrelling of the sample was not apparent. Again two distinct slopes are seen in the compressional and shear wave velocity curves. The gradients of the velocity change curves are similar to those seen for test S322. Initially changes are of a shallow nature but with Vs proportionately showing a slightly greater reduction than Vp. At around peak stress (≈2.7% strain) both velocities begin to decrease at a faster rate. However, in this experiment the compressional wave velocity shows a slightly greater rate of decrease than the shear wave velocity.

At 200MPa confining pressure (test S518) the stress/strain curve (fig. 10:4) rises linearly. The onset of anelasticity is again difficult to determine accurately but appears to occur at approximately 1% strain. The curve rolls over to a stress level similar to that seen in the previous experiment (≈550MPa) and then strain hardens slightly. The shear wave velocity initially decreases at a marginally faster rate than the compressional wave velocity. However, as the sample becomes noticeably anelastic, the shear wave velocity decreases at a significantly slower rate relative to the compressional wave velocity. This phenomenon was not observed in either of the previous sandstones examined.

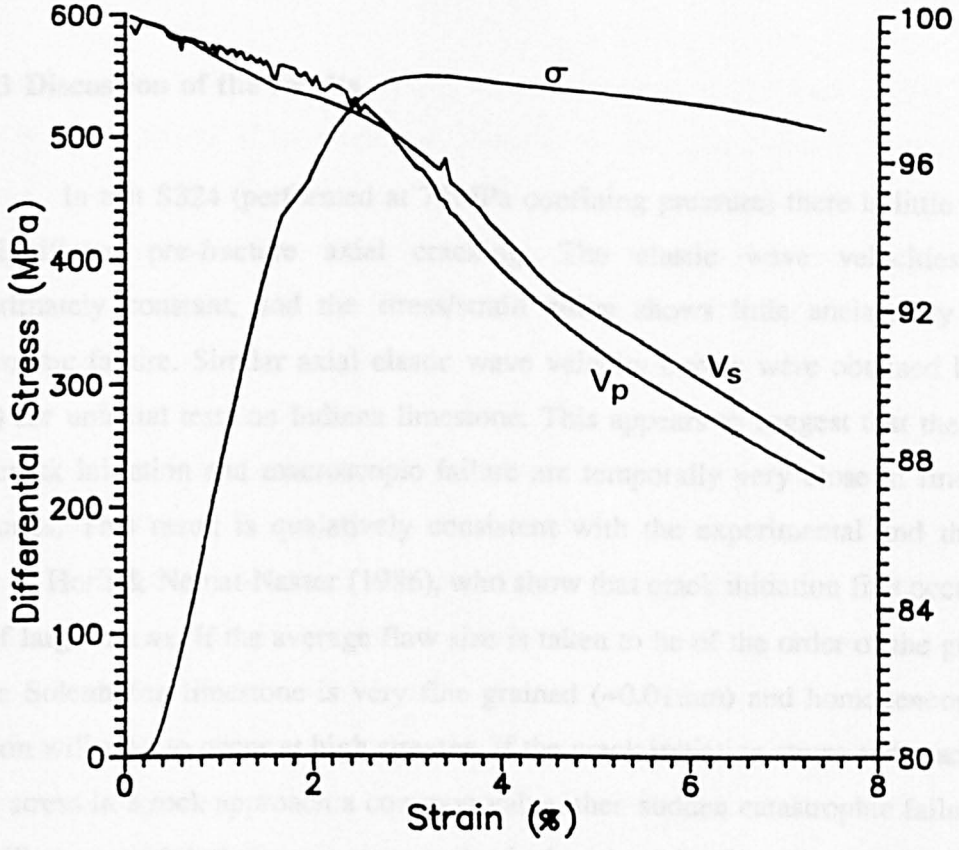

Fig. 10:3 The stress/strain curve and velocity changes for Solenhofen limestone deformed at 150MPa confining pressure (test nos. S320).

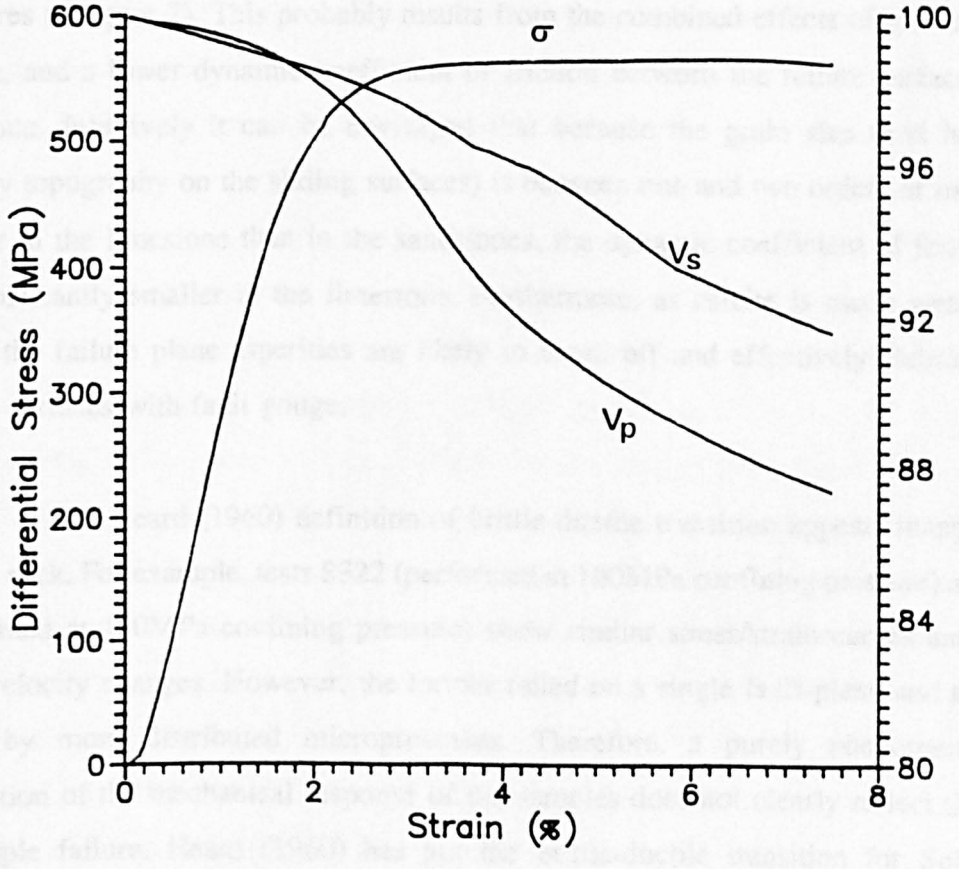

Fig. 10:4 The stress/strain curve and velocity changes for Solenhofen limestone deformed at 200MPa confining pressure (test nos. S518).

10:3 Discussion of the results.

In test S324 (performed at 75MPa confining pressure) there is little evidence for significant pre-fracture axial cracking. The elastic wave velocities remain approximately constant, and the stress/strain curve shows little anelasticity prior to catastrophic failure. Similar axial elastic wave velocity curves were obtained by Gupta (1973) for uniaxial tests on Indiana limestone. This appears to suggest that the onset of microcrack initiation and macroscopic failure are temporally very close in fine-grained limestones. This result is qualatively consistent with the experimental and theoretical results of Horii & Nemat-Nasser (1986), who show that crack initiation first occurs at the sites of larger flaws. If the average flaw size is taken to be of the order of the grain size, then as Solenhofen limestone is very fine grained (≈0.01mm) and homogeneous, crack initiation will tend to occur at high stresses. If the crack initiation stress and macroscopic failure stress in a rock approach a common value, then sudden catastrophic failure of the rock will occur with little pre-cursory mechanical anelasticity. Houpert (1974b) has noted that preliminary cracking in Solenhofen limestone is not very pronounced and that failure seems to occur initially by shear fracturing. It is worth noting that the stress drop seen for this sample is much greater than that seen for the sandstones at comparable confining pressures (Chapter 7). This probably results from the combined effects of greater energy release, and a lower dynamic coefficient of friction between the failure surfaces in the limestone. Intuitively it can be envisaged that because the grain size (and hence the asperity topography on the sliding surfaces) is between one and two orders of magnitude smaller in the limestone than in the sandstones, the dynamic coefficient of friction will be significantly smaller in the limestone. Furthermore, as calcite is much weaker than quartz the failure plane asperities are likely to break off and effectively "lubricate" the sliding surfaces with fault gouge.

The Heard (1960) definition of brittle-ductile transition appears inappropriate for this rock. For example, tests S322 (performed at 100MPa confining pressure) and S320 (performed at 150MPa confining pressure) show similar stress/strain curves and elastic wave velocity changes. However, the former failed on a single fault plane and the latter failed by more distributed microprocesses. Therefore, a purely phenomenological description of the mechanical response of the samples does not clearly reflect the mode of sample failure. Heard (1960) has put the brittle-ductile transition for Solenhofen

limestone at around 100MPa confining pressure, and Edmond & Paterson (1972) between 100MPa and 200MPa. If the transition, is taken as the point where the mode of failure changes from failure on an inclined failure plane to a more distributed microprocess (which may be brittle microcracking, plastic processes, or both), then the brittle-ductile transition can be placed between 100MPa and 150MPa confining pressure for this set of experiments.

At higher confining pressures the limestone samples tend to show a mechanical behaviour that is similar to the pseudo-ductile deformation seen in sandstones. However, in limestone, the elastic wave velocity curves show that the shear wave velocity decreases less relative to the compressional wave velocity as the confining pressure increases. The velocity changes seen in the sandstones (Chapters 7 and 9) can be interpreted in terms of the classical brittle failure process outlined at the end of Chapter 2; with dilatancy essentially being controlled by axially orientated microcracking. However, it seems difficult, to interpret ductility in Solenhofen limestone in the same way.

There are a number of possible mechanisms that could explain the elastic wave velocity changes seen for this limestone in the ductile regime. These include the specific case of randomly orientated cracking, grain/crystal rotation, and intracrystalline plastic processes; the likelihood of any of these processes (or a combination of these processes) occurring in the rock are examined in detail below:

1) Brittle microprocesses.

Although initially it appears difficult to reconcile the elastic wave velocity changes seen for limestone with traditional microcracking processes, there are conditions under which they may account for the velocity observations. If the microcracking was distributed and of near-random orientation, then following from the analysis of O'Connell & Budiansky (1974), Vp would be proportionately more affected than Vs. There appears to be no clear reasoning as to why cracking should be more distributed and random in Solenhofen limestone than in other materials. Axial cracking appears to be a fundamental process of brittle deformation (section 2:3), and as Solenhofen limestone is fine grained and homogeneous, it should be a near-ideal brittle material. However, it is possible that

if cracking preferentially nucleates in sites of, for example cleavage, glide or twin planes of calcite crystals then, over the whole sample the net result of the microcracking may appear random. Indeed, if the O'Connell & Budiansky (1974) model is used to determine the change in crack density parameter for test S518 (performed at 200MPa confining pressure), feasible results are obtained (fig. 10:5). The crack density parameter begins to increase as the sample becomes anelastic, and increases to a peak value as the stress/strain curve rolls over. However, if the same model is applied to test S322 (performed at 100MPa confining pressure) the model suggests that very little cracking is occurring in the sample even though the effective dynamic Young's modulus decreases by ≈24% (fig. 10:6). Apparently then, even though the rock is becoming increasingly more compliant throughout the test, the model shows little evidence of microcracking. It is unlikely that brittle microcracking is occurring at 200MPa confining pressure and not at 100MPa, as the O'Connell & Budiansky model suggests. An important point highlighted by this example, is that although the model may yield reasonable results (as it does for test S518), it does not necessarily follow that the damage mechanisms upon which the model is based are actually the mechanisms that are occurring in the rock sample.

Independent evidence for dilatant microprocesses (such as cracking) occurring in Solenhofen limestone is difficult to obtain. Attempts to record acoustic emission activity in deforming Solenhofen limestone samples have failed to detect events above the background level (Jones, 1989). This could be because either, no microcracking is occurring, or because the amplitude of AE events (which can be related to the source size; Savage, 1972), are of too low an amplitude. Conventional microscopic techniques are of limited use in attempting to directly observe cracking in such a fine grained rock. Direct dilatancy measurements using internal pore-fluid volume changes are also difficult because of the rock's low porosity and permeability. However, Edmond & Paterson (1972) have carried out tests on Solenhofen limestone using the dilatometer technique (section 2:1) to determine dilatant volume changes at confining pressures ranging from 100MPa to 800MPa. They found that although dilatancy occurred at relatively low confining pressures, by 250MPa little dilatancy was occurring, and at higher confining pressures compaction occurs. Figs. 10:7a,b show the stress/strain and the volumetric-strain/axial-strain plots (calculated by equating the dynamic and static Poisson's ratio) for test S518 (performed at 200MPa confining pressure). For comparative purposes, the curves calculated for a Gosford sandstone sample (GS10) also deformed at 200MPa confining

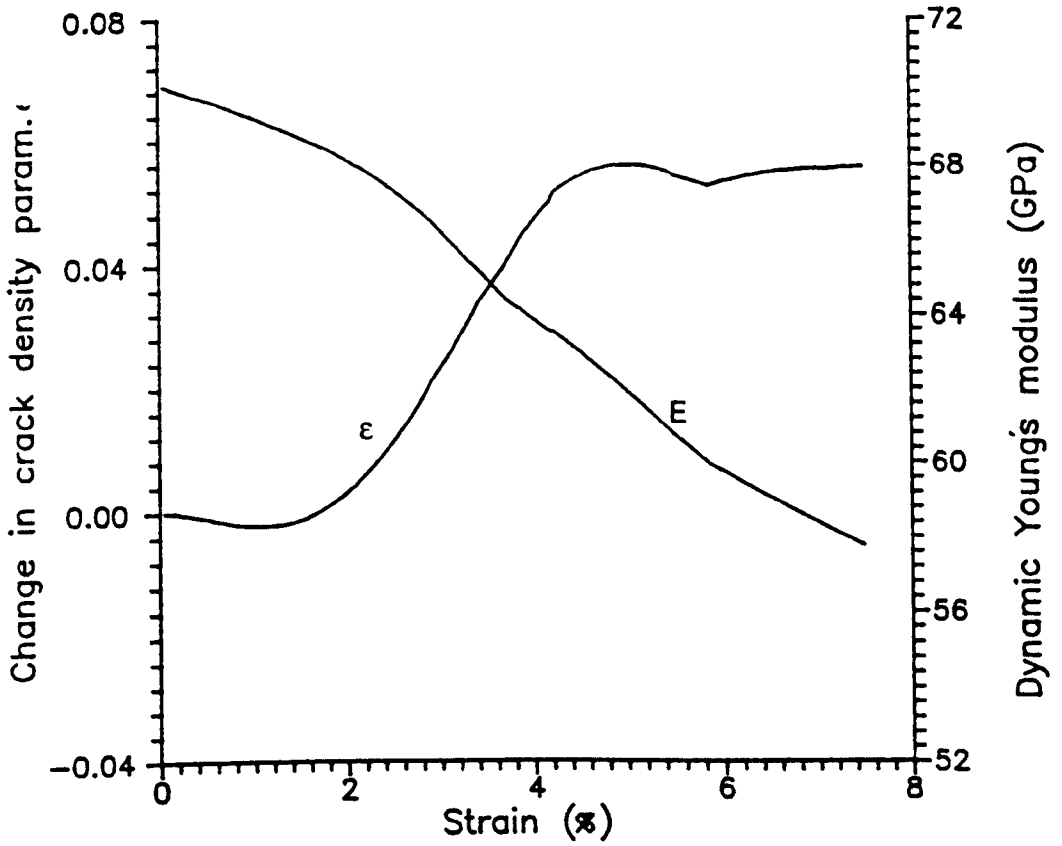

Fig. 10:5 The change in crack density parameter (ε), determined using the O'Connell & Budiansky (1974) model, is shown for a Solenhofen limestone sample deformed at 200MPa confining pressure (S518). The effective dynamic Young's modulus is also shown.

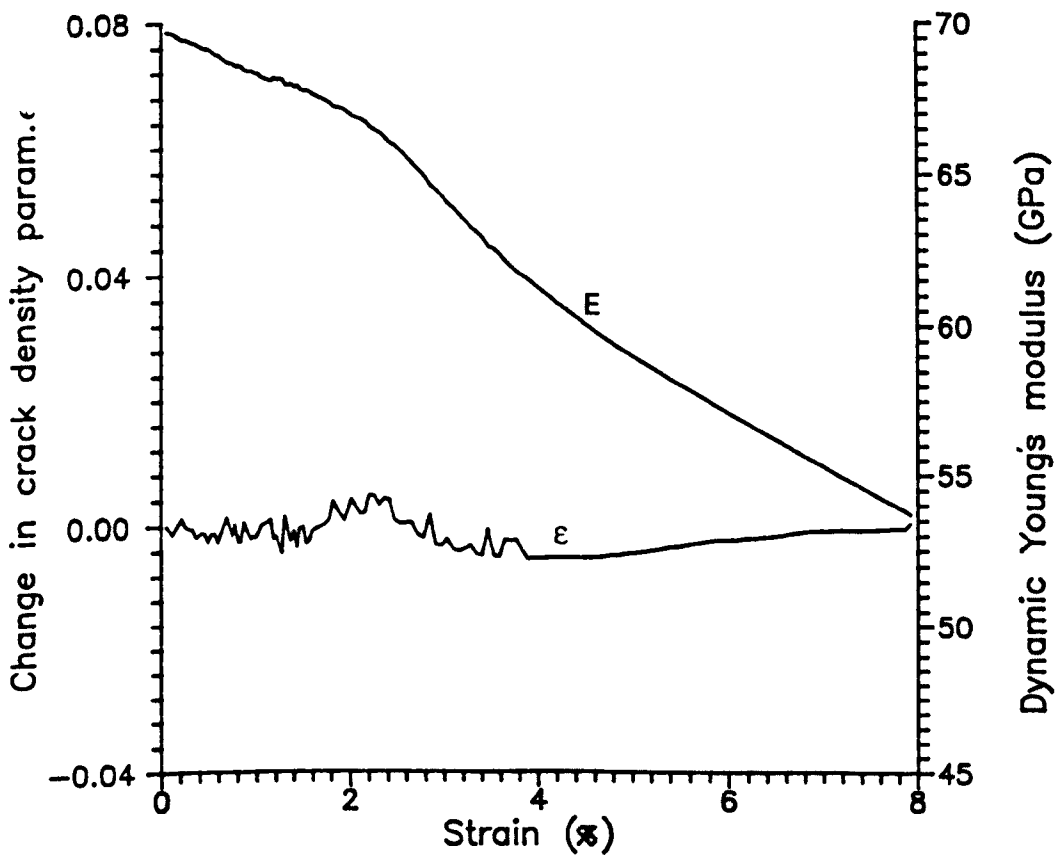

Fig. 10:6 The change in crack density parameter (ε), determined using the O'Connell & Budiansky (1974) model, is shown for a Solenhofen limestone sample deformed at 100MPa confining pressure (S322). The effective dynamic Young's modulus is also shown.

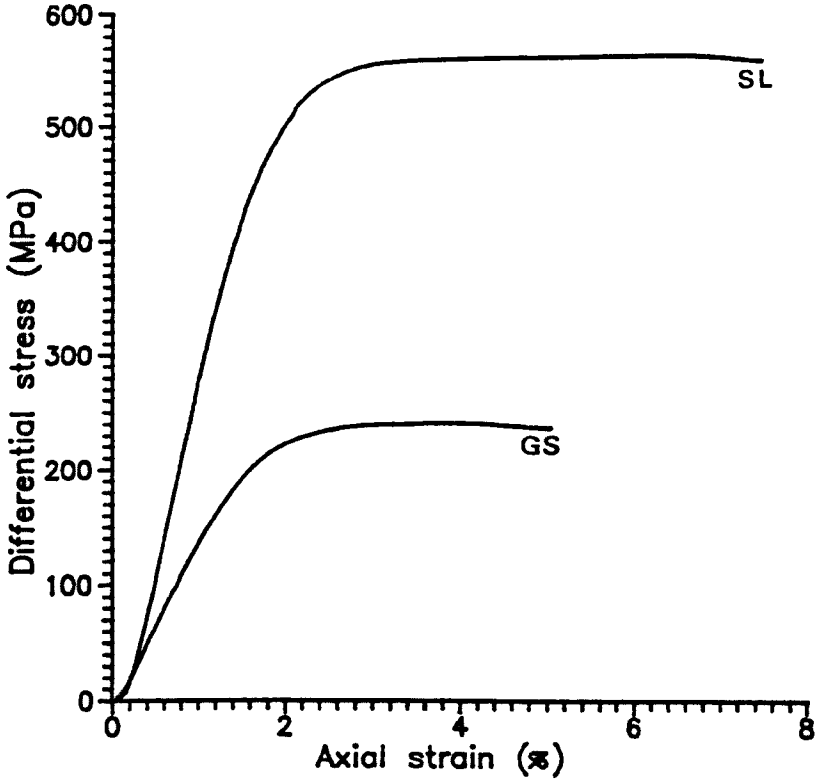

a

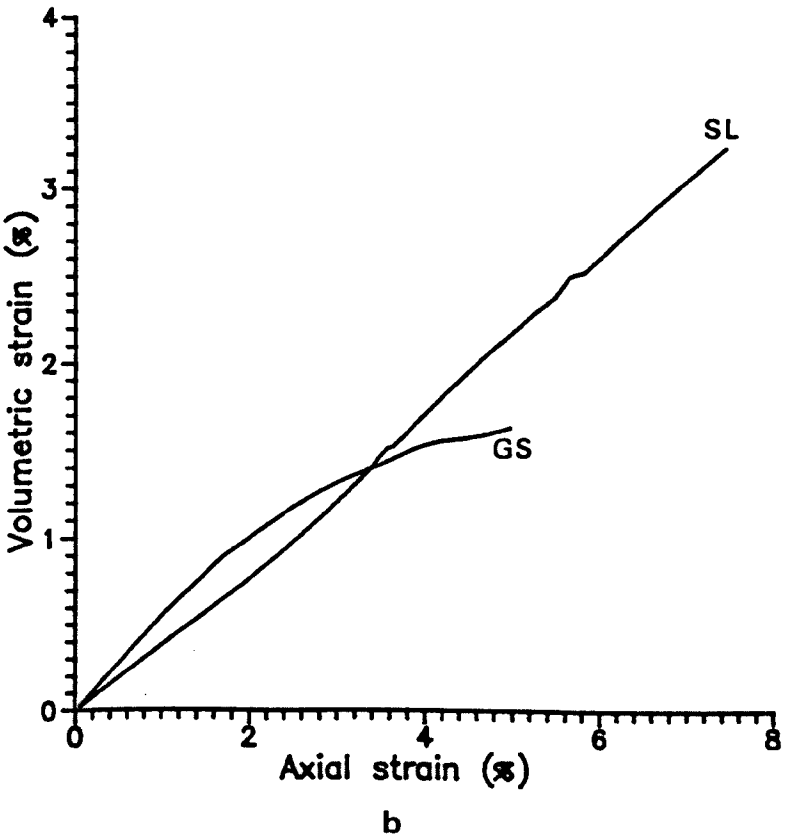

b

Figs. 10:7a,b The stress/strain curves for Solenhofen limestone and Gosford sandstone samples deformed at 200MPa confining pressure (tests S518, GS10 respectively) are shown (a). The calculated volumetric-strain/axial-strain plots for these two tests are also shown (b). GS - Gosford sandstone, SL - Solenhofen limestone.

pressure (Chapter 9), are given. As can be seen the limestone shows an essentially elastic strain up to 1.8 strain, after which slight compaction occurs. The volumetric plot for the Gosford sandstone (which shows a good resemblance to that reported by Edmond & Paterson for this sandstone) shows significant dilatancy as the sample becomes anelastic. Although the stress/strain curves for the two rocks show qualatively similar forms, the deformation mechanisms appear to be different, with the sandstone showing inelastic volume increase and the limestone compaction.

Thus there appears to be little evidence to suggest that brittle microcracking is an important mechanism during the ductile deformation of Solenhofen limestone. Although this does not necessarily mean that it is not occurring on a fine, grain-scale, level.

2) Grain rotation and calcite crystallographic alignment.

It has been noted that compressional wave velocity anisotropy occurs in rocks which show significant calcite crystallographic alignment (for example, in Yule marble by Thill & Willard, 1969, and Hohe Tauern marble by Kern & Fakhimi, 1975). Whether such grain rotation and alignment could be occurring in triaxially deformed samples of limestone is not known. Kern & Fakhimi (1975) noted a 7% compressional wave velocity anisotropy for about 40% alignment of calcite crystals relative to a uniform background distribution (Vp was low parallel to the aligned a-axes and high parallel to the aligned c-axes of the calcite crystals). Therefore, if it is assumed that initially, there is an isotropic distribution of calcite grains in the Solenhofen limestone samples, about 50% of the crystals would need to be aligned at 8% strain to achieve the percentage drop in compressional wave velocity seen in tests S320 and S518. However, as grain rotation would necessarily be accompanied by microcracking, such a high percentage of crystal alignment may not necessarily be needed to cause the observed compressional wave velocity decreases. Strain shortening of 8% represents ≈3.5mm of sample shortening, and as the average grain size is about 0.01mm, grain rotation is mechanically feasible. However, firstly, it is not clear how the crystals would align in the triaxial stress field, and secondly, it is difficult to see how such a process would account for the shear wave velocity changes. That is, why the shear wave velocity decreases proportionately less than the compressional wave velocity with increasing confining pressure.

3) Intracrystalline plasticity.

Intragranular deformation processes such as cleavage plane slip, twinning, and crystallographic gliding accounts for the ductility in some metals such as polycrystalline copper. Such processes may be important in fine grained limestone. These mechanisms essentially involve no volume increase, and constant volume deformation of limestone is seen at higher confining pressures. Also, the peak strength of the rock appears to show little pressure dependence (for the experiments carried out at 100MPa, 150MPa and 200MPa confining pressure). This too suggests that brittle processes may be suppressed and that plastic processes become more important as the confining pressure is increased. Twinning is often seen to occur in calcite in response to strain shortening, although this can only account for small strains and is likely to be of only minor importance at large strains (Paterson, 1978, p178). Edmond & Paterson (1972) state that intracrystalline plasticity may contribute largely to the total strain in the ductile field in limestone. But it is not clear how such plastic processes would affect the elastic wave velocity profiles. Limited experiments by Jones (1989), (see also Jones & Murrell, 1990), on Solenhofen limestone at 200MPa confining pressure and at temperatures up to 400°C, show that the effect on the compressional wave velocity becomes less as plastic processes become more dominant. At full plasticity, Vp may even continue to increase with strain. It is not known how the shear wave velocity would be affected by plastic processes.

In summary, it is at present not possible to say with certainty which mechanism is causing the ductility in Solenhofen limestone. Indeed it is likely that more than one mechanism is operating, with different mechanisms becoming dominant at different confining pressures or strains. However, it appears that brittle microprocesses may be important at lower confining pressures, but as the confining pressures increase these mechanisms will probably give way to plastic processes.

CHAPTER 11

ELASTIC WAVE VELOCITY ANISOTROPY MEASUREMENTS ON SAMPLES OF TENNESSEE SANDSTONE.

11:1 Introduction.

Tennessee sandstone is a highly anisotropic brittle sandstone with a low porosity and a fine well-developed bedding structure of millimetre scale. Samples were cored perpendicular and parallel to the bedding plane. Three tests carried out at 50MPa confining pressure are described in this chapter. Essentially the experiments investigate the mechanical and acoustic anisotropy of the rock introduced by the strong bedding structure. One test was carried out with the bedding perpendicular to the major stress axis; referred to as test (A). The other two tests were carried out with the bedding parallel to the major stress axis. In these latter two tests, the shear wave was polarised parallel to the bedding plane in one test (referred to as test (B)), and perpendicular to the bedding plane in the other (test (C)). Tests (A), (B) and (C) are experiments TEN7, TEN8, and TEN6 respectively, in table 6.1. The arrangement of the bedding plane with respect to the shear wave polarisation direction in each test is shown in fig. 11:1, (the initial compressional and shear wave velocities for each of the tests are also given). Great care must be taken when comparing single tests such as these, as sample variability is difficult to quantify. In the previous chapters essentially trends are discussed, where systematic changes in mechanical and acoustic responses can clearly be seen with increasing confining pressure. However, in this chapter only very general comparisons and conclusions can be drawn.

Assuming that crack alignment preferentially occurs in the bedding plane (in the undeformed rock), then the initial experimentally determined velocities can be compared to Anderson et al's (1974) theoretical analysis (outlined in section 5:6:1). In their analysis, elastic wave velocities travelling along three mutually orthogonal axes of an elliptical crack are considered. Following on from Anderson et al., the initial Vp in test (A) should be less than in tests (B) and (C) (which should be the same). In fact, Vp in test (C) is 1.6% faster than in test (B), and Vp in test (A) 2.1% slower than in test (B), (the relative error in these measurements is about 1.5%). Also, following from Anderson et al., Vs in test (C) should be less than in test (B); and is in fact about 10% less. Therefore, it appears

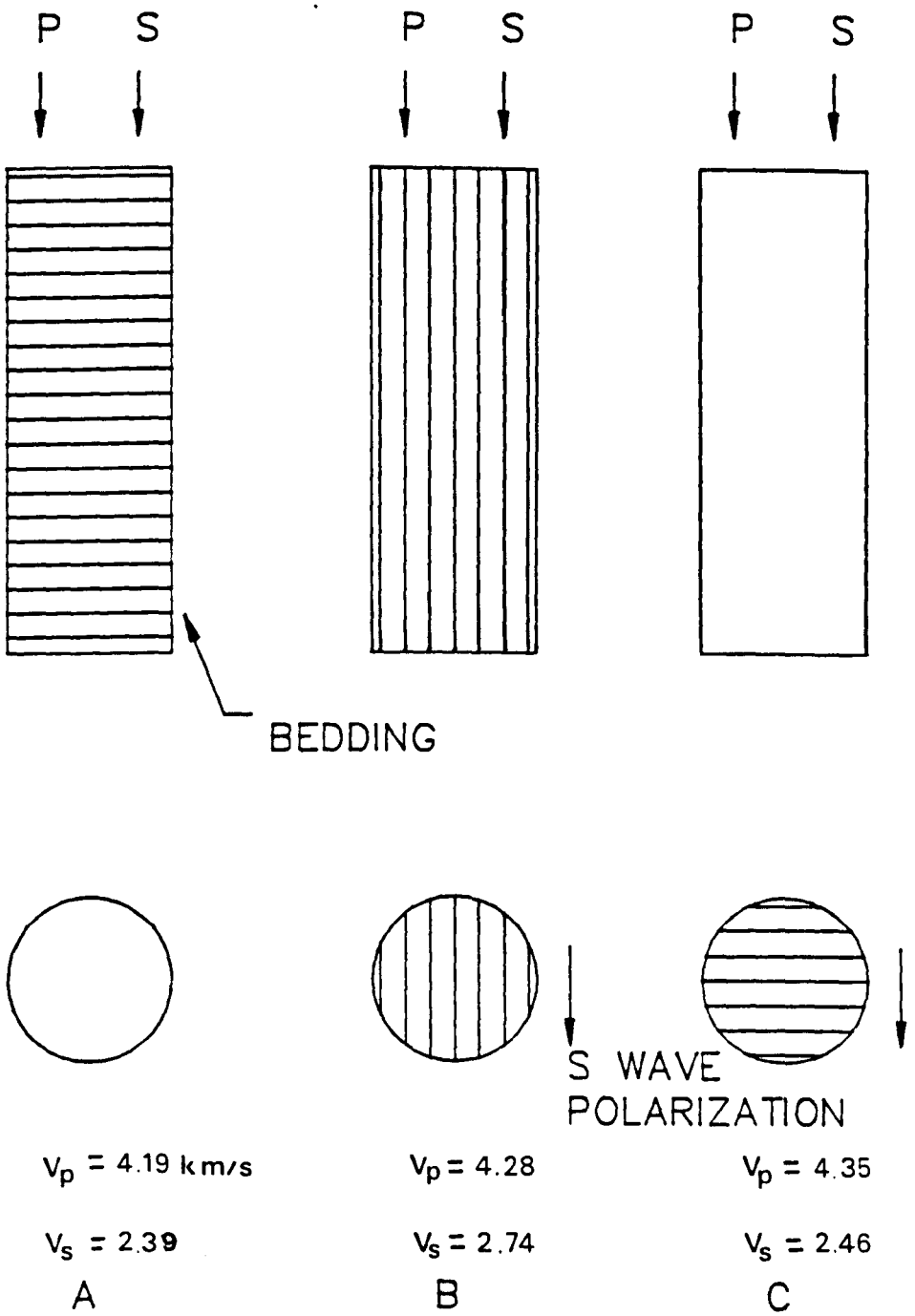

Fig. 11:1 Experimental arrangement for three tests carried out on Tennessee sandstone. In test (A) the bedding plane is perpendicular to the major stress axis. In tests (B) and (C) the bedding plane is parallel to the unique axis, in the former the shear is polarised in the bedding plane, in the latter the shear wave is polarised perpendicular to the bedding plane. The initial absolute velocities are also given for each test, these velocities are subject to 1.5% error.

that the results from these tests are consistent with the predictions of Anderson et al.

11:2 The stress/strain curves.

Fig. 11:2a. shows the stress/strain curves for the three experiments. Tests (B) and (C) produced similar stress/strain curves; that is, a well defined linear climb followed by a small anelastic region. Catastrophic failure occurs at, or around, peak stress (≈300MPa). The "knee" at the beginning of the stress/strain curve in case (B), is a commonly observed experimental feature (probably the result of an imperfection or inclusion at the ram/sample interface), that has little noticeable effect on the fundamental properties of the rock. Test (A) produced a significantly different stress/strain response from the other two tests. There is a slight stiffening of the sample upon initial loading, the form of which is familiar from previous chapters. There is clearly an increased tangent modulus, and a gentle roll over leading to a higher peak stress of 400MPa. A sustained period of strain weakening occurs prior to macroscopic failure.

11:3 The elastic wave velocity changes.

Fig. 11:2b,c shows the compressional and shear wave velocity changes in the three tests, respectively. Vp for test (A) increases less than in either test (B) or (C) (despite having a lower initial value), peaks at around 1.5% strain and then decreases. Vp for tests (B) and (C) show approximately similar forms (although the increase in test (C) may be slightly less, and appears to be displaced to higher strains with respect to test (B)). This displacement, however, is exactly as expected from the stress/strain curves for these two samples; that is, the peak velocities in (B) and (C) occur at the same stress level (about 200MPa). The increase in Vp in all three tests is substantial (≈6% to 9%). Surprisingly, in none of the tests does Vp decrease to below its initial value before the sample fails catastrophically; although the velocity for test (A) comes closest.

In all three tests the shear wave velocity increases by a significant amount (between 4% and 6%). The shear wave velocity increase seen for test (C), is somewhat less than for tests (A) and (B). If this is so, then it probably reflects a slight bowing and opening of cracks in the bedding plane upon initial differential loading. This would reduce

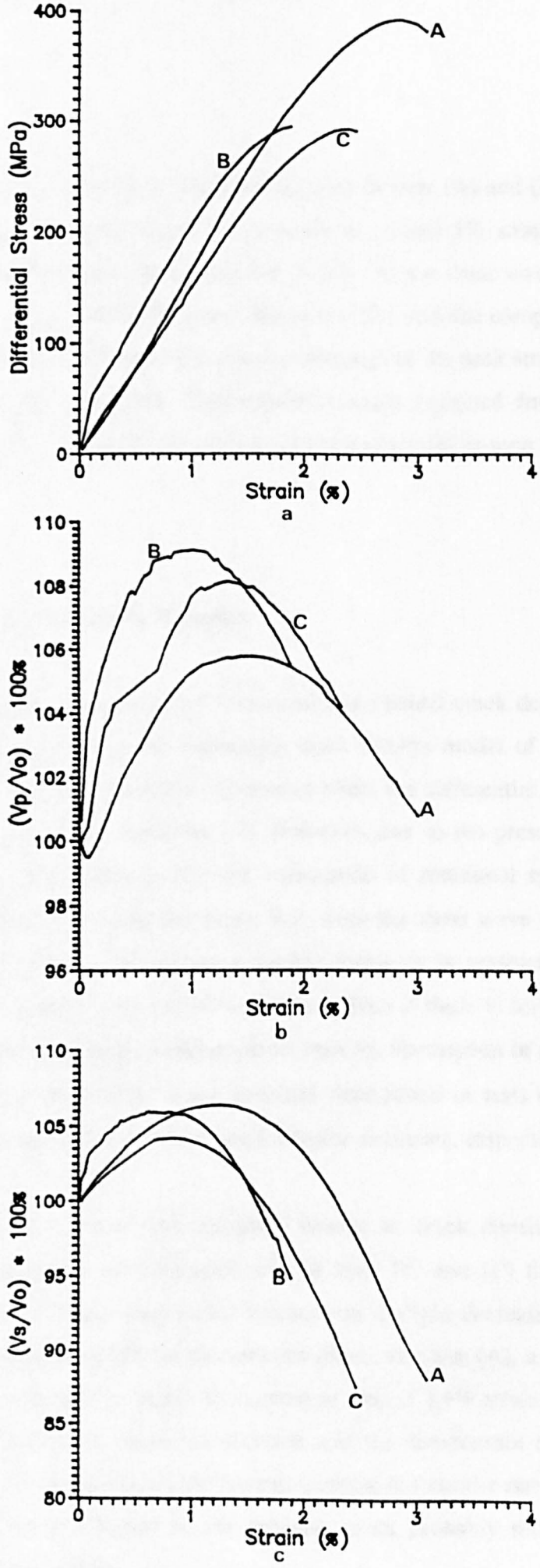

Figs. 11:2a,b,c The stress/strain curves (a), the compressional wave velocity changes (b), and the shear wave velocity changes (c) are shown for the three tests (marked, A,B,C).

the shear wave increase in test (C) relative to those in tests (A) and (B). In tests (B) and (C) the shear wave velocity begins to decrease at around 1% strain, which coincides approximately with the onset of anelasticity. In test (A) the shear wave velocity peaks at higher strain of 1.4%. It should be noted that in test (A) both the compressional and shear wave velocities begin to decrease at a lower percentage of the peak stress (i.e.≈55%), than in tests (B) and (C), (65-70%). This feature is again expected from the stress/strain response for test (A), where an extended period of anelasticity is seen before macrosocpic failure.

11:4 The changes in crack densities.

As before, changes in the horizontal and vertical crack densities during these tests can be estimated using the anisotropic crack density model of Soga et al. (1978). Since the model assumes cylindrical symmetry about the differential loading axis, it can be applied directly to test condition (A). However, due to the presence of the vertical bedding plane in tests (B) and (C), the assumption of rotational symmetry cannot be justified automatically in these two cases. But, since the shear wave velocity profiles for tests (B) and (C) show approximately similar forms, it is reasonable to assume that dilatant crack anisotropy may not be significant. Even if there is some dilatant cracking preferentially orientated in the bedding plane, then the assumption of rotational symmetry merely means that the vertical crack densities determined in tests (B) and (C) can be considered minimum and maximum crack density estimates, respectively.

Fig. 11:3a shows the estimated change in crack density parameter of the axially orientated cracks (εx) for each test. In tests (B) and (C) the changes in crack densities are very similar; upon initial compaction a slight decrease occurs. The crack densities then increase rapidly as the samples dilate. For test (A), a broader decrease is observed. The crack density begins to increase at around 1.4% strain, which corresponds to the point at which Vs begins to decrease and the stress/strain curve deviates from linearity. The crack density then continues to increase at a similar rate as that for the other tests. As discussed in Chapter 8, the decrease in εx probably reflects the closing of obliquely orientated cracks.

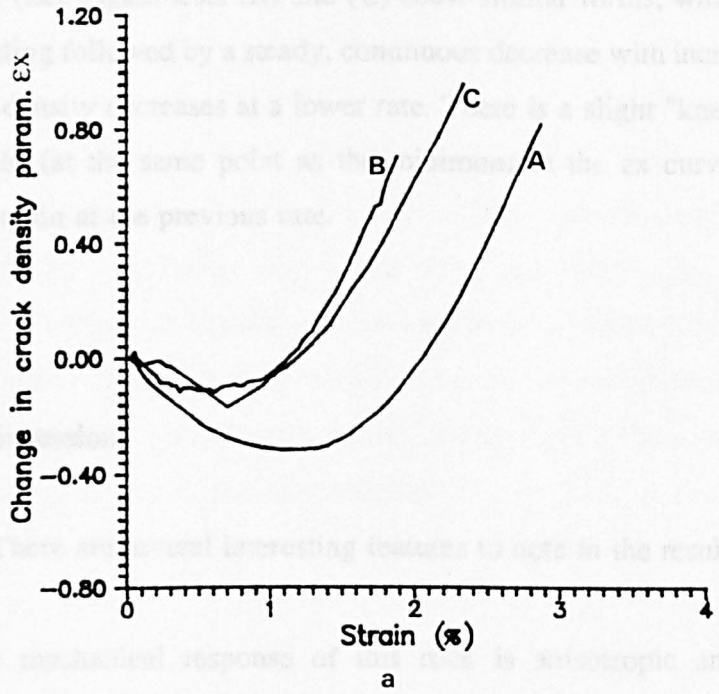

a

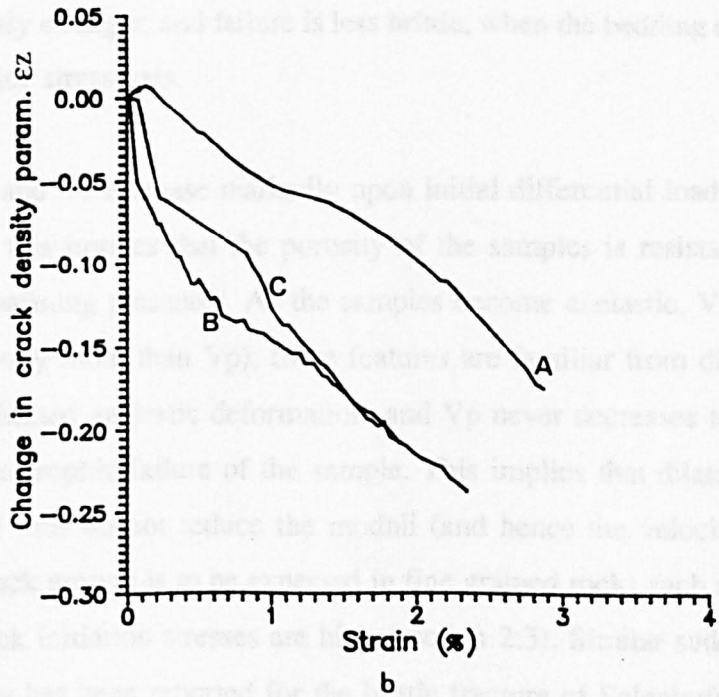

b

Figs. 11:3a,b The change in vertical and horizontal crack density parameters (εx, εz, respectively) for the three tests.

Fig. 11:3b shows the estimated change in the horizontal crack density parameter (ϵz). Again tests (B) and (C) show similar forms, with a sharp decrease upon initial loading followed by a steady, continuous decrease with increasing strain. In test (A) the crack density decreases at a lower rate. There is a slight "knee" in the curve at about 1.2% strain (at the same point as the minimum in the ϵx curve). It then continues to decrease again at the previous rate.

11:5 Discussion.

There are several interesting features to note in the results of this series of tests.

(i) The mechanical response of this rock is anisotropic and dependent upon the orientation of the bedding plane with respect to the major loading axis. The rock is significantly stronger, and failure is less brittle, when the bedding orientation is orthogonal to the major stress axis.

(ii) Vp and Vs increase markedly upon initial differential loading (Vp relatively more than Vs); this implies that the porosity of the samples is resistant to the application of modest confining pressures. As the samples become anelastic, Vp and Vs both decrease (Vs relatively more than Vp); these features are familiar from discussions in Chapter 7. There is limited anelastic deformation, and Vp never decreases to below its initial value before catastrophic failure of the sample. This implies that dilatant cracks are generally small, and thus do not reduce the moduli (and hence the velocities) very quickly. This limited crack growth is to be expected in fine grained rocks such as Tennessee sandstone, where crack initiation stresses are high (section 2:3). Similar sudden failure with limited anelasticity has been reported for the brittle fracture of Solenhofen limestone in Chapter 10.

(iii) Following on from (ii), because Vs decreases proportionally more than Vp in each test, it can be assumed that dilatant cracking is predominantly axial in nature (see Chapters 7 and 8). The similarity between the vertical crack density curves for tests (B) and (C) suggests that dilatant cracks are not preferentially located in the bedding plane

to any significant degree, although, as ε_x in tests (B) and (C) tends to commence increasing slightly earlier than in test (A), it appears that cracking initiates preferentially in the bedding plane.

In conclusion, even though comparisons between individual tests are problematical, some broad mechanical and acoustic anisotropic effects can be noted. The rock is stronger and failure less brittle when the bedding is at a high angle to the differential loading axis. Cracking appears not to grow preferentially in the bedding plane, but does appear to preferentially initiate there. For more subtle crack and pore structure delineations, acoustic measurements would ideally have to be made simultaneously along all three principle axes of the rock samples.

CHAPTER 12

RESULTS OF TESTS ON WATER SATURATED SAMPLES OF DARLEY DALE SANDSTONE AND SOLENHOFEN LIMESTONE UNDER BOTH DRAINED AND UNDRAINED CONDITIONS.

12:1 Introduction.

Before the pore fluid pressure intensifier and volumometer became available, only simple, poorly controlled "undrained" tests or "drained" tests were possible. In the simple undrained tests, a known volume of water was sealed inside the copper jacket with the specimen. Since sample deformation involves volume change (i.e. compaction followed by dilatancy) the pore fluid pressure varied in an unknown way during tests. This condition is analogous to the in situ crustal condition where fluid expulsion or infiltration during deformation is impeded either by the fluid bearing rock's own permeability or by an impermeable cap rock. In the drained test, a quantity of water was again introduced with the test specimen. However, in this case the pore fluid was vented to atmosphere via a bore through the top ram. Assuming the fluid can move freely throughout the sample then a constant (atmospheric) pore fluid pressure is maintained as the sample deforms.

Previous to this current study the drained test condition did not allow the acoustic wave velocities to be measured during deformation. This was because the limited space at the ram end only allows either an acoustic transducer, or a vent pipe to be emplaced, but not both. This problem was partially overcome by designing a simple fluid reservoir that was placed between a slightly shorter sample (35mm as against 45mm) and the standard acoustic top ram. This enabled P and S wave velocities to be measured through a deforming sample under drained conditions at atmospheric pressures. The fluid reservoir was specifically designed to have a solid central portion of diameter ≈6mm (i.e. the same dimensions as the acoustic transducer) which allowed optimum transmission of the elastic waves. Around this solid central portion 12 holes were drilled (1mm in diameter and 15mm in length) providing a total reservoir volume of ≈140mm^3; sufficient to accommodate the volume of water expelled from the sample (see also Chapter 13). These holes were interconnected by a series of radial grooves to facilitate fluid movement.

The reservoir was placed between the sample and the top ram for two reasons. Firstly, if there was any delay in running the test then the sample pore fluid would not drain into the reservoir. Secondly, as compaction occurred water would be expelled into the reservoir, then as dilatancy ensued pore fluid would be gravity-fed back into the sample. This method gave approximate constant pore fluid pressure conditions, provided complete saturation of the sample is maintained.

Three tests were performed on Darley Dale sandstone under a confining pressure of 100MPa. These were under dry, undrained water-saturated, and drained water-saturated conditions (D519, D100S, D520 respectively). Two additional tests were carried out on samples of Solenhofen limestone at 100MPa confining pressure for the dry and the undrained water-saturated conditions (S322, S121).

12:2 The stress/strain response for Darley Dale sandstone.

The stress/strain curves are shown in fig. 12:1a for the three sandstone samples deformed at 100MPa confining pressure under dry, drained and undrained conditions. The curve for the dry sample shows a form familiar from Chapter 7. That is, the stress/strain curve rises linearly, rolls over to a peak stress of 345MPa, and maintains this high load up to substantial strains. The drained saturated sample is considerably weaker, the curve rolls over to a peak stress of 215MPa. This peak stress is similar to those seen at ≈30MPa confining pressure for dry samples of the same rock. There is no large stress drop after the peak stress but a gentle roll over and stable post-peak deformation. The undrained test, as expected, was weakest. The curve rises linearly, rolls over to a peak stress of about 155MPa, and again sustains this load with increasing strain without any sign of catastrophic failure.

12:3 The elastic wave velocity change curves.

Fig. 12:1b shows the compressional wave velocity changes for the three tests. The compressional wave velocity for the dry sample varies in a by now familiar manner. That is, there is an initial increase (≈2.5%), followed by a gentle roll over as the sample starts to dilate, and finally, a gentle decrease at a steady rate. As before, the observation

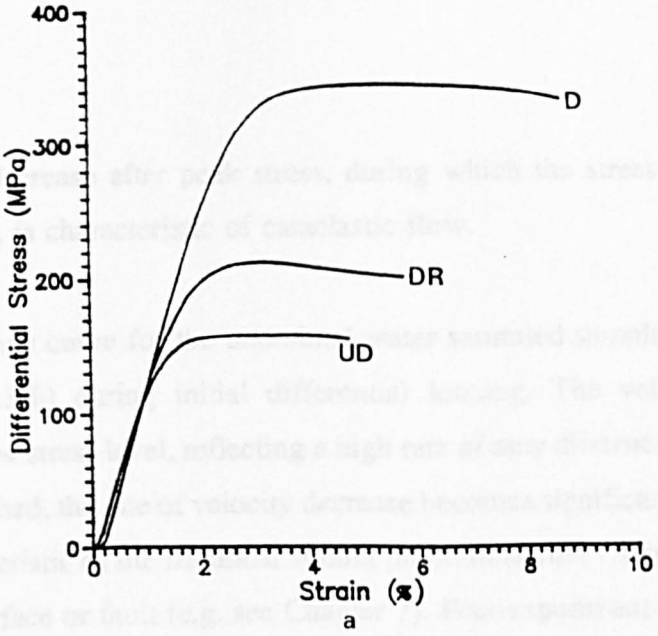

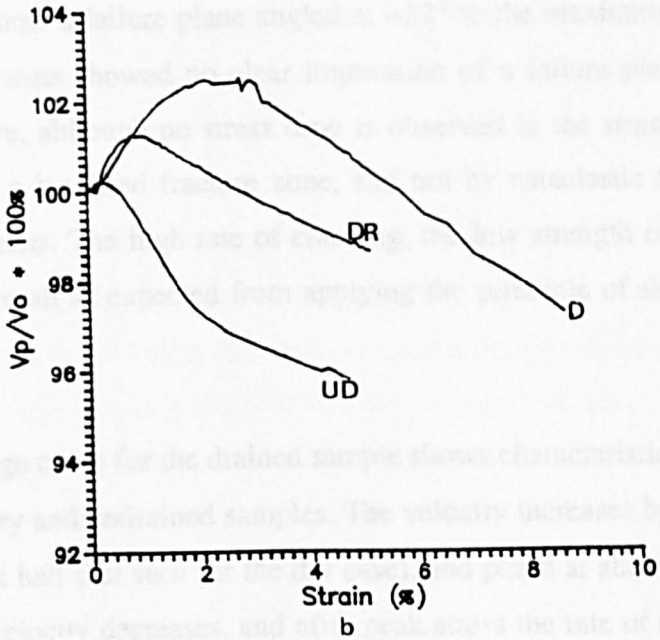

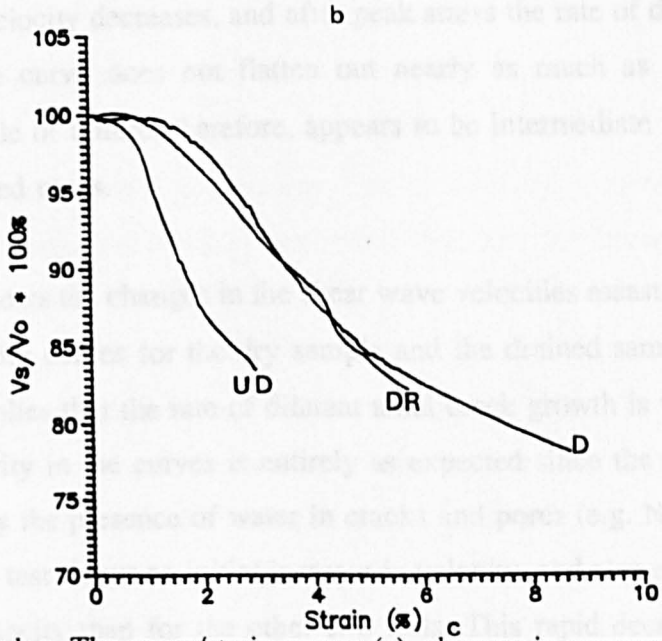

Figs. 12:1a,b,c The stress/strain curves (a), changes in compressional wave velocity (b), and changes in shear wave velocity (c) for three tests on Darley Dale sandstone samples, dry, drained and undrained conditions (D519, D520, D100S respectively) at 100MPa confining pressure. D-dry, DR-drained, and UD-undrained.

of continued velocity decrease after peak stress, during which the stress level remains approximately constant, is characteristic of cataclastic flow.

The Vp change curve for the undrained water saturated sample shows only a marginal increase (≈0.3%) during initial differential loading. The velocity starts to decrease sharply at a low stress level, reflecting a high rate of new dilatant cracking. After maximum stress is reached, the rate of velocity decrease becomes significantly lower. This phenomenon is characteristic of the frictional sliding phase in samples that have failed on an inclined fracture surface or fault (e.g. see Chapter 7). Post-experiment examination of the sample did indeed show a failure plane angled at ≈32° to the maximum loading axis (whereas the other two tests showed no clear impression of a failure plane in the soft copper jacket). Therefore, although no stress drop is observed in the stress/strain curve, failure has occurred on a localised fracture zone, and not by cataclastic flow as seems likely in the other two tests. The high rate of cracking, the low strength of the rock and the manner of failure are all as expected from applying the principle of simple effective stress.

The Vp change curve for the drained sample shows characteristics intermediate between those for the dry and undrained samples. The velocity increases by ≈1.2% as the sample compacts (about half that seen for the dry case), and peaks at about 1% strain. As the sample dilates the velocity decreases, and after peak stress the rate of decrease of Vp is lower. However, the curve does not flatten out nearly as much as the curve for undrained test. The mode of failure, therefore, appears to be intermediate between those for the dry and undrained cases.

Fig. 12:1c shows the changes in the shear wave velocities measured during the same three tests. Velocity curves for the dry sample and the drained sample show very similar trends. This implies that the rate of dilatant axial crack growth is very similar in both cases. The similarity in the curves is entirely as expected since the shear modulus is very little affected by the presence of water in cracks and pores (e.g. Nur, 1989). The curve for the undrained test shows no initial increase in velocity, and also exhibits a much sharper decrease in velocity than for the other two tests. This rapid decrease reflects a sharp increase in the rate of cracking. This is interpreted as being due to the reduced effective confining pressure caused by the increase in pore fluid pressure during pore

compaction.

12:4 The change in the crack density parameter.

Fig. 12:2 shows the change in the total crack density parameter ($2\varepsilon x+\varepsilon z$) for the three tests. It should be noted that the constants used in the crack density formulation are based on an analytical analysis of gas-filled pore spaces (see section 5:6:1). However, a comparison can be made between changes seen for the drained and the undrained tests without ambiguity. Also, as only the change in crack density parameter is considered the error introduced into the analysis when comparing the wet and dry cases is expected to be minimised.

A comparison of the crack density curves for the drained and undrained tests shows that a faster rate of cracking is seen to occur in the undrained test. It is, however, surprising that the crack density curves are very similar for the dry and the drained tests. Although the rate of dilatant cracking is about the same in each sample (as evidenced by the Vs curves), the stress/strain curves show that the water saturated sample is much weaker. This observation is discussed later in section 12:6.

12:5 Tests on Solenhofen limestone.

Two experiments were also performed on Solenhofen limestone samples at 100MPa confining pressure; one sample was tested dry, and the other tested water-saturated but undrained (S322, S121).

Fig. 12:3a shows the stress/strain curves for the two tests. The two curves are virtually identical. This similarity in deformation behaviour is also reflected in nearly identical compressional wave velocity changes curves (fig. 12:3b). Furthermore, the changes in the shear wave velocities, are also very similar (fig. 12:3c). However, there is some indication that after peak stress the shear wave velocity decreases slightly faster in the saturated sample. This could reflect marginally increased cracking resulting from a reduced effective stress. The overall strength of the rock seems not to be affected by this.

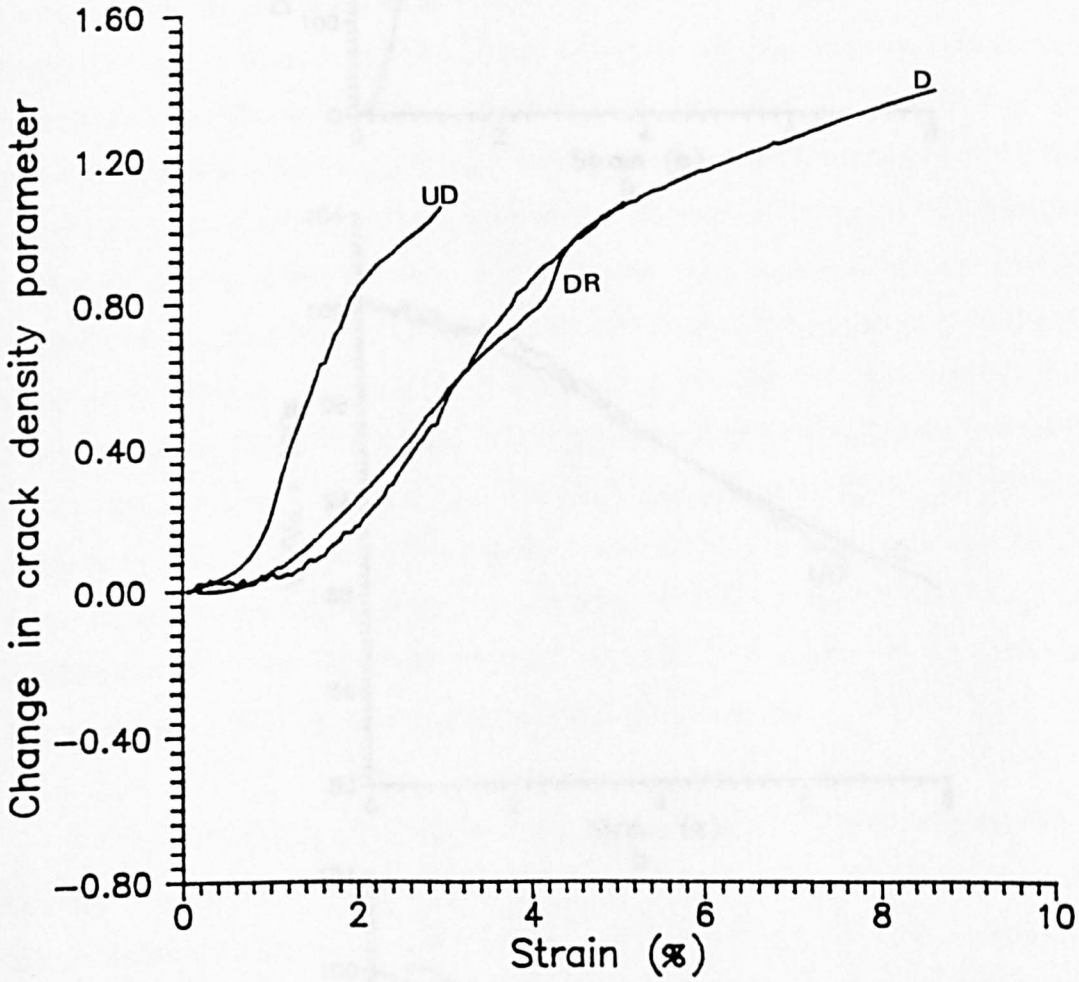

Fig . 12:2. Change in total crack density parameter ($\varepsilon_{total}=2\varepsilon_x+\varepsilon_z$) for the three tests, determined using the Soga et al. (1978) model.

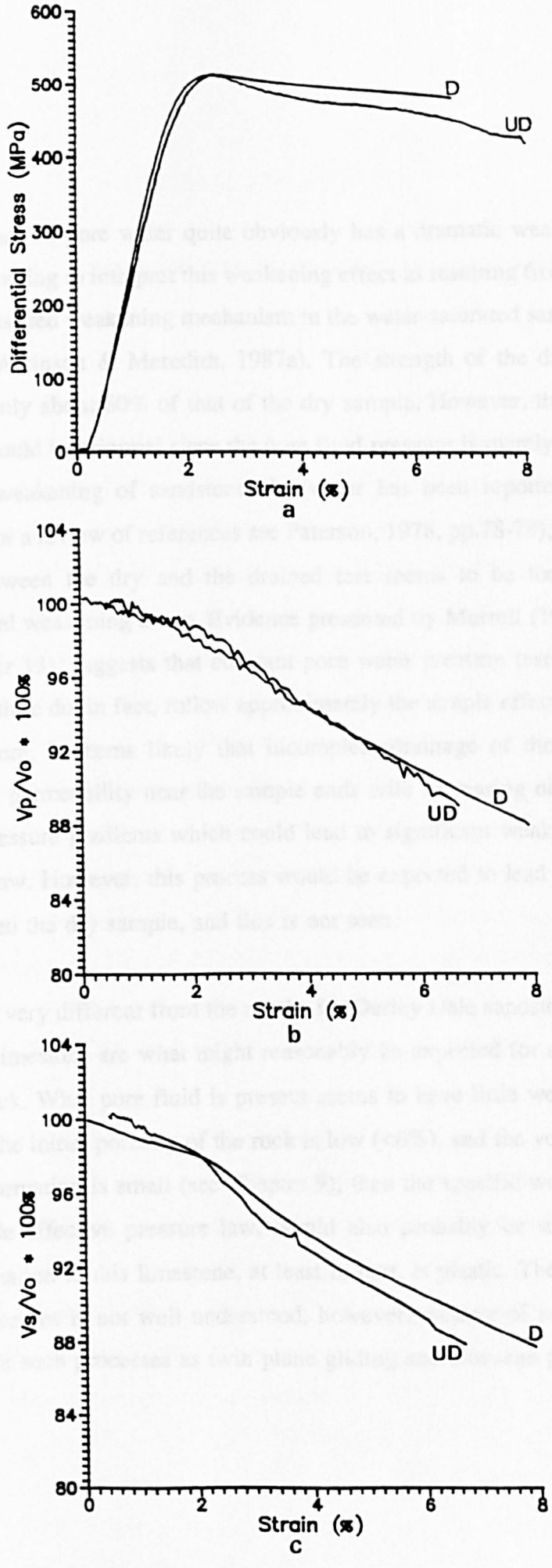

12.3a,b,c The stress/strain curves (a), changes in compressional wave velocity (b), and changes in shear wave velocity (c) for two tests on Solenhofen limestone samples, dry and undrained conditions (S322, S121 respectively) at 100MPa confining pressure. D-dry, UD-undrained.

12:6 Discussion.

The presence of pore water quite obviously has a dramatic weakening effect on sandstone. It is tempting to interpret this weakening effect as resulting from some form of environmentally assisted weakening mechanism in the water-saturated sandstones such as stress corrosion (Atkinson & Meredith, 1987a). The strength of the drained water-saturated sample is only about 60% of that of the dry sample. However, the mechanical effect of the water should be minimal since the pore fluid pressure is merely atmospheric. Although chemical weakening of sandstones by water has been reported by a large number of authors (for a review of references see Paterson, 1978, pp.78-79), the reduction in strength seen between the dry and the drained test seems to be too great to be explained by chemical weakening alone. Evidence presented by Murrell (1965) and later in this study (Chapter 13), suggests that constant pore water pressure tests on this rock undergoing brittle failure do, in fact, follow approximately the simple effective stress law of Terzaghi. Therefore, it seems likely that incomplete drainage of the sample (due primarily to reduced permeability near the sample ends with increasing deviatoric load) causes local pore pressure gradients which could lead to significant weakening through the effective stress law. However, this process would be expected to lead to an increase in cracking relative to the dry sample, and this is not seen.

Although very different from the results for Darley Dale sandstone, the results for the Solenhofen limestone are what might reasonably be expected for a low porosity, low permeability rock. What pore fluid is present seems to have little weakening effect on this rock. Since the initial porosity of the rock is low (<6%), and the volumetric crack increase during deformation is small (see Chapter 9), then the specific weakening effect following the simple effective pressure law, would also probably be small. It is also possible that deformation in this limestone, at least in part, is plastic. The effect of pore fluid on plastic processes is not well understood, however, wetting of surfaces may be expected to facilitate such processes as twin plane gliding and cleavage plane slip.

CHAPTER 13

CONTROLLED PORE FLUID PRESSURE EXPERIMENTS.

13:1 Introduction.

A series of experiments have been performed on Darley Dale sandstone samples with a new servo-controlled pore fluid pressure intensifier (described in section 3:7) used to maintain a constant elevated pore-fluid pressure during deformation. As the sample compacts and dilates water is either expelled or injected into the sample, respectively, in order to maintain constant pore pressure. The volume of fluid expelled from or injected into the sample is recorded. Thus a measure of the change in connected porosity during deformation can be monitored directly. Three experiments are examined in detail in this chapter. Phenomenologically, these experiments represent; (i) catastrophic brittle failure, (ii) pseudo-ductile deformation, and (iii) the brittle-ductile transition. In total 13 constant pore pressure tests were carried out. Of the remaining tests, five experiments were carried out at similar effective pressures as those reported here to test repeatability. The others were either only partially successful or suffered from problems such as jacket sealing, or blockage of the pore fluid inlet pipe. In the experiments reported here the differential stress, axial strain, acoustic emission rate, acoustic emission waveforms and pore fluid volume changes were all measured simultaneously.

Evidence from the "drained-to-atmosphere" tests on Darley Dale sandstone (Chapter 12) suggests that complete drainage of the sample may be impeded by its compaction near the ram ends. Therefore, for these tests an axial hole, 1.5mm in diameter and ≈2cm long, was drilled into the sample end, and located with the pore fluid inlet hole. Great care was needed in drilling these holes, in order not to damage the samples. Each sample was carefully examined after the drilling process, if any sign of macroscopic damage was found then the sample was discarded.

13:2 Description of a test carried out at 20MPa effective pressure (PERM21).

Fig. 13:1 shows the stress/strain curve and the acoustic emission (AE) rate, for a Darley Dale sandstone sample deformed under triaxial conditions with a total confining pressure of 30MPa and a pore fluid pressure of 10MPa. The AE threshold for this test was set at 28dB. The stress/strain curve rises linearly; it then deviates from linearity at about 1.1% axial strain. The curve rolls over and forms a fairly narrow peak at 200MPa stress. The sample becomes more compliant until it fails catastrophically at 2% axial strain. Macroscopic failure is marked by a sharp and sudden stress drop of ≈25MPa. There then follows a period of stable sliding along the failure plane. Visual inspection of the sample after deformation showed the sample had failed along a well defined failure plane angled at ≈34° to the major compression axis. If the simple effective pressure law applies, then the specimen should exhibit the same mechanical response as that of a dry sample deformed under a confining pressure of 20MPa (neglecting any chemical effects of the pore fluid). However, the curve shows a response that is less brittle than would have been expected (see data in Chapter 7). The peak stress is about at the level that would be expected. Either the pore fluid column acts somehow to support the sample at the point of catastrophic failure or, more likely, rapid dilatancy near macroscopic failure may lead to locally incomplete saturation thus increasing the effective stress and stabilising the failure. This is known as dilatancy hardening and is discussed in section 2:2, (see also Sholz, 1990 for details).

The AE rate begins to rise above the background level at about 0.7% strain. This is prior to the stress/strain curve deviating from linearity. This onset could reflect either; (i) the growth of thin microcracking which does not significantly reduce the axial elastic moduli of the sample, or (ii) the result of inelastic pore collapse. The AE rate begins to increase sharply above about 1.5% strain, coinciding with the stress/strain curve showing significant sample anelasticity. The AE rate peaks (about 16000 events per minute) as the sample fails macroscopically. After failure the rate decreases sharply to the relatively low value of ≈1000 events per minute. This low AE rate is approximately constant and probably results from asperities sliding across each other on the failure plane. The AE events are unlikely to be due to significant dilatant cracking as evidence from previous acoustic velocity experiments (Chapter 7) show that elastic wave velocities tend to remain constant after catastrophic sample failure.

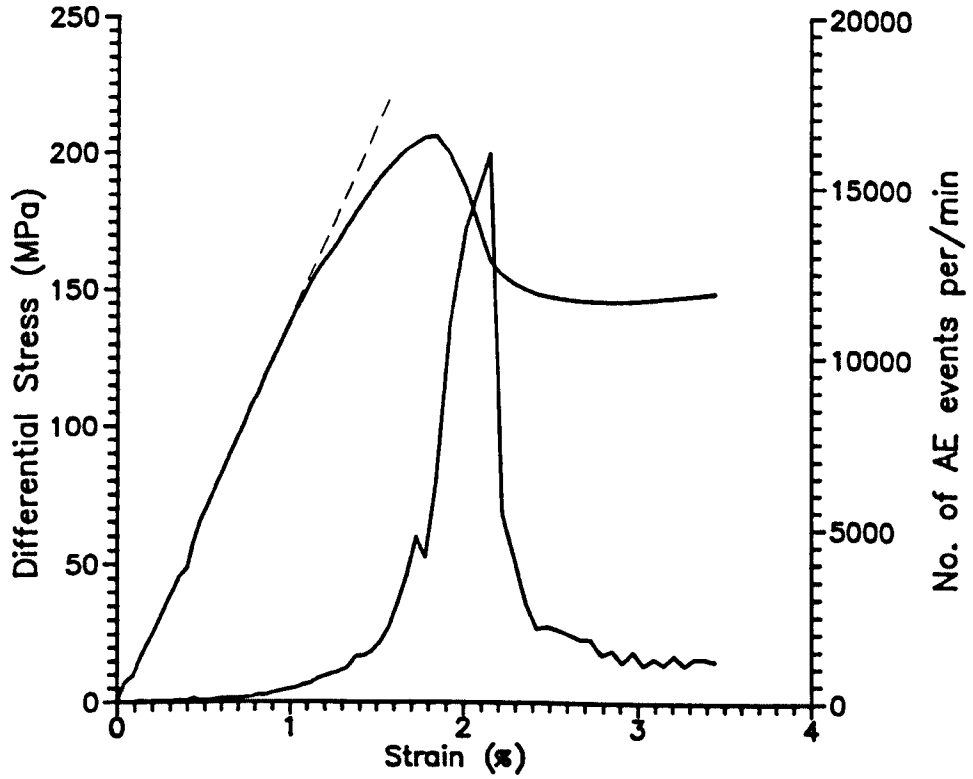

Fig. 13:1 The stress/strain curve and acoustic emission rate for experiment PERM21; carried out at 20MPa effective pressure.

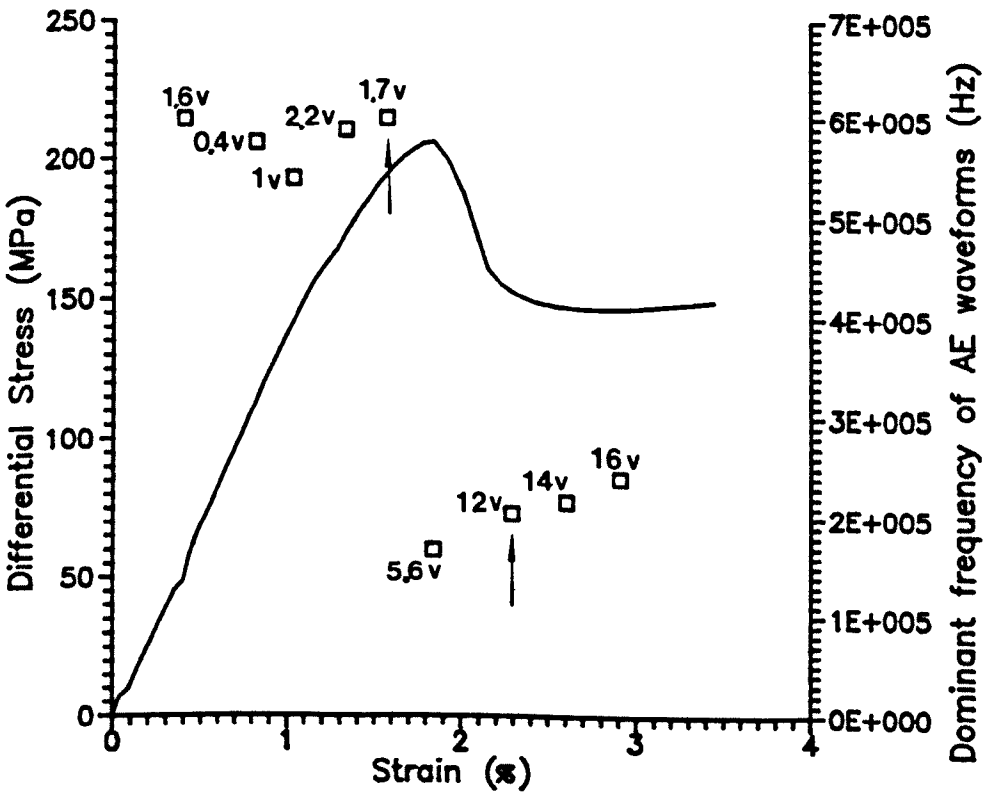

Fig. 13:2 A plot of the dominant frequency component of captured AE waveforms. The peak amplitudes are also shown. The stress/strain curve is shown for reference. The arrows mark the positions at which two AE waveforms occurred the amplitude spectrums of which are shown in fig. 13:3. The upper arrow refers to fig. 13:3a and the lower to fig. 13:3b.

Fig. 13:2 shows a plot of the dominant frequency of digitised AE waveforms recorded throughout the test, also shown are the amplitudes of these frequency components. The complete amplitude spectra of two AE waveforms (marked with arrows on fig. 13:2) are shown in fig. 13:3. These are typical spectra of AE waveforms recorded before peak stress and after macroscopic failure, respectively. It can be seen that high frequency components dominate in the former waveform, while lower frequency components dominate in the latter. It was also found that most of the AE events had a common signature on their amplitude spectrums; that is, peaks in energy are seen to occur at about 200kHz and 600kHz (with a smaller peak at ≈400kHz). This waveform signature can be explained in terms of the geometry of the sample. Taking $V=f.\lambda$, where V is the velocity, f the frequency, and λ the wavelength; then if the average compressional wave velocity through the sample is around 4000m/s, the wavelengths corresponding to frequencies of 200KHz and 600Khz are about 20mm and 7mm, respectively. These correspond to approximately half the length and half the width of the sample, respectively. Therefore, these energy peaks in the amplitude spectra are likely to be caused by vertical and horizontal standing waves excited in the specimen by the AE events. As the test proceeds and the sample shortens axially and expands radially, then the peak at about 200khz should tend to move to higher frequencies and the peak at 600khz should move to lower frequencies. This shift, however, is likely to be small because the strains involved are small. Even with these limitations, fig. 13:2 provides very useful information, and can be interpreted in terms of the changing mechanisms of deformation. The plot shows that as the sample is initially loaded the dominant frequencies of the waveforms are high, and that little change in frequency is seen with strain. The amplitudes of the AE waveforms are low, and generally less than two volts. However, either just prior to, or at, peak stress the waveforms change dramatically. The amplitudes increase by an order of magnitude and the dominant frequency components of the waveforms are much lower. There appear to be three possible explanations for these changes in character of the waveforms:

(i) The increasing heterogeneity of the rock caused by progressive microcracking could preferentially attenuate the high frequency components of the waves thus causing the frequency shift seen in the waveform spectra. This, however, does not explain the dramatic increase in AE amplitudes at high strains.

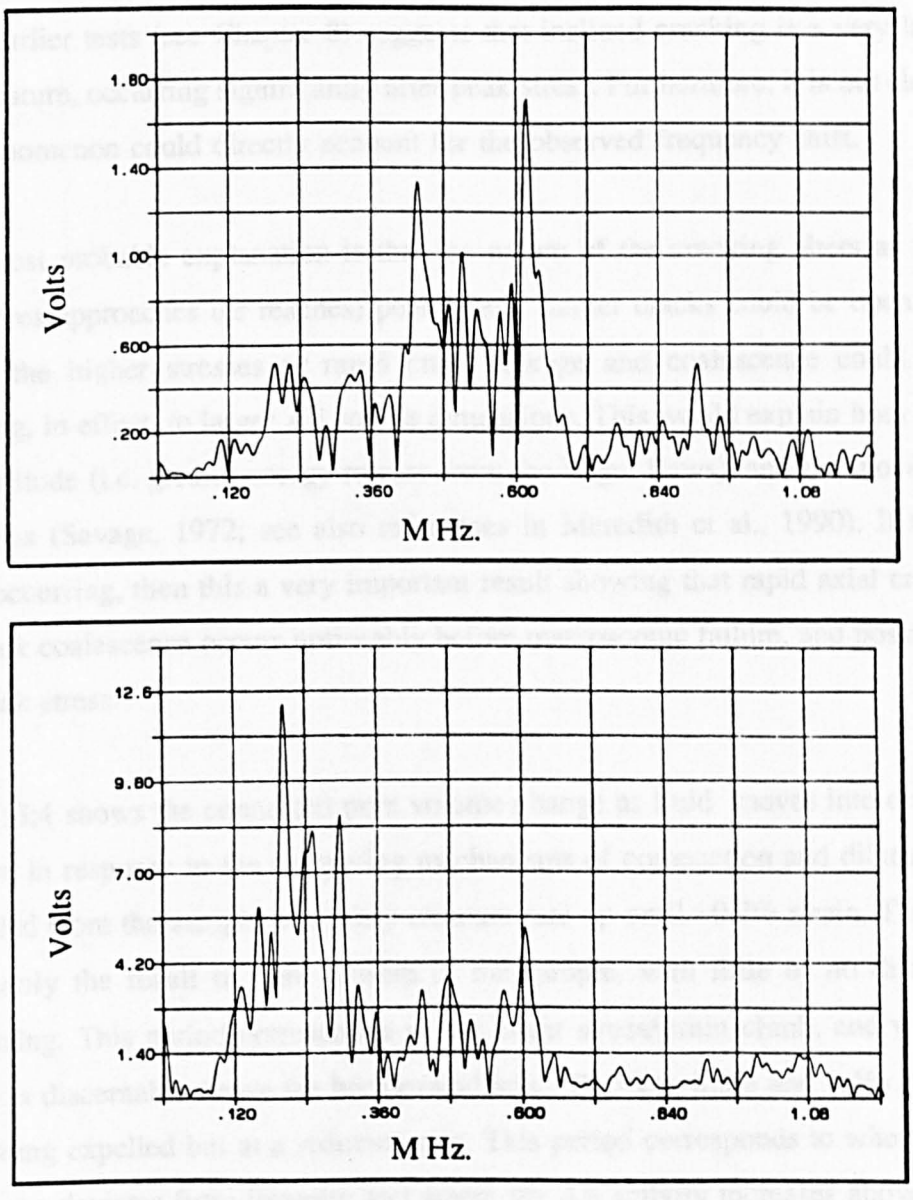

Figs. 13:3 a,b Two amplitude spectra plots of AE waveforms, one of which occurred prior to peak stress (see fig. 13:2, first arrow),(a), the second occurred after peak stress (see fig. 13:2, second arrow), (b).

(ii) The crack population could be changing from predominantly axial cracks to predominantly inclined cracks. This would alter the azimuthal direction of the source with respect to the receiver, and could account for a change in amplitude of the waveforms. This, however, is unlikely to be solely responsible for such large amplitude changes. Also, evidence from earlier tests (see Chapter 8) suggests that inclined cracking is a very late deformational feature, occurring significantly after peak stress. Furthermore, it is not clear how such a phenomenon could directly account for the observed frequency shift.

(iii) The most probable explanation is that the nature of the cracking alters as the stress/strain curves approaches (or reaches) peak stress. Larger cracks could be opening in response to the higher stresses or rapid crack linkage and coalescence could be occurring leading, in effect, to larger AE source dimensions. This would explain both the increase in amplitude (i.e. greater energy release from the larger flaws), and the move to lower frequencies (Savage, 1972; see also references in Meredith et al., 1990). If this mechanism is occurring, then this a very important result showing that rapid axial crack growth and crack coalescence occurs noticeably before macroscopic failure, and possibly even before peak stress.

Fig. 13:4 shows the connected pore volume change as fluid moves into or out of the specimen in response to the competing mechanisms of compaction and dilatancy. Water is expelled from the sample at a fairly constant rate up until ≈0.7% strain. This is probably primarily the result of pore closure in the sample, with little or no dilatant cracking occurring. This period corresponds to the linear stress/strain climb, and where no AE activity is discernable above the background level. Between 0.8% and 1.4% strain water is still being expelled but at a reducing rate. This period corresponds to where the stress/strain curve deviates from linearity and where the AE activity increases above the background level. This period probably reflects crack growth occurring concurrently with the continuing closure of the pore structure. Hydrostatic pore volume tests show that porosity is not completely closed in this rock until about 400MPa (M.D. Read, personal communication; although as previously stated velocity data of Jones (1989) suggests most of the cracks are closed 200MPa confining pressure). As the rock becomes noticeably anelastic, and the AE activity increases sharply (above 1.4% strain), the sample dilates significantly, and for the first time there is a net take-up of pore fluid. The sample steadily becomes more dilatant until macroscopic failure, after which the connected pore volume

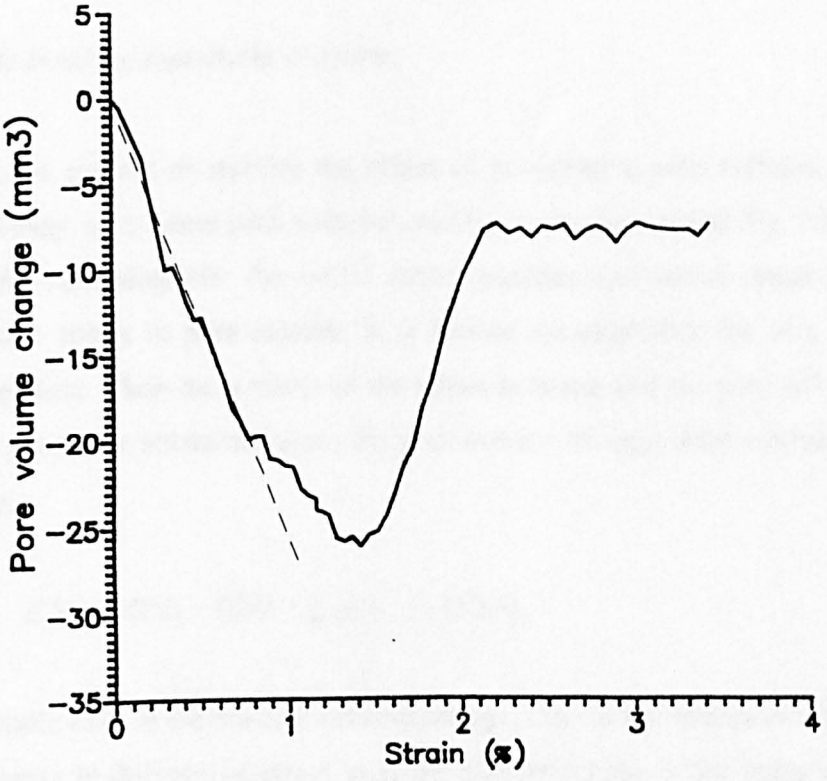

Fig. 13:4 The pore volume change measured during experiment PERM21 (see text for details).

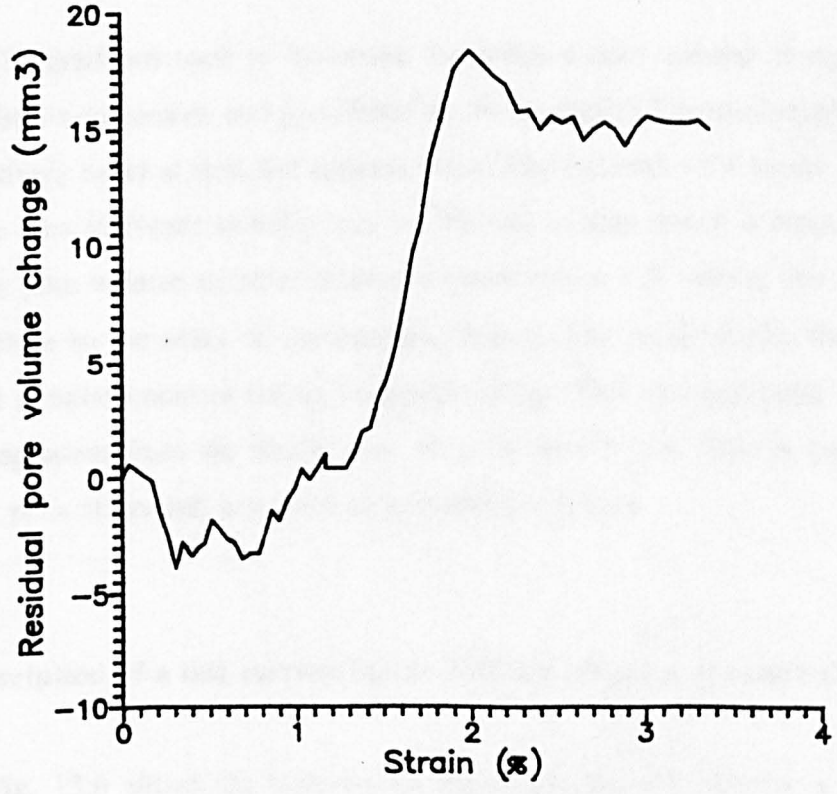

Fig. 13:5 This shows the residual pore volume change for test PERM21 (see text for details).

of the sample remains essentially constant.

In an attempt to remove the effect of progressive pore collapse masking the onset of dilatancy, a "residual pore volume" plot has been determined (fig. 13:5). This plot is obtained by assuming that the initial stress gradient and initial linear pore volume decrease is due solely to pore closure. It is further assumed that this is a constant and continuing process. Then the product of the stress increase and the pore volume decrease per strain increment is subtracted from the pore volume change. Mathematically this may be written as;

$$\Delta V_R = \Delta V_T - (\Delta\sigma * g_2/g_1) \qquad (13.1)$$

where ΔV_R is the residual volume change, ΔV_T is the total pore volume change, $\Delta\sigma$ is the change in differential stress, g_2 is the gradient of the initial linear portion of the pore volume/strain curve, and g_1 is the corresponding gradient of the linear part of the stress/strain curve.

The gradients used to determine the residual pore volume change plot were g_1=135MPa/strain-increment, and g_2=-25mm^3/strain-increment. The residual plot (fig. 13:5) appears relatively noisy at first, but appears essentially flat until ≈1% strain. The residual pore volume then increases steadily until ≈1.3% strain, after which it increases sharply. The inelastic pore volume increase reaches a maximum at ≈2% strain; this is after peak stress and close to the point of macroscopic failure. The residual plot then decreases slightly, and remains constant during frictional sliding. This plot highlights an important feature not apparent from the simple pore volume change plot. That is, peak dilatancy occurs after peak stress and just prior to macroscopic failure.

13:3 Description of a test carried out at 100MPa effective pressure (PERM2).

Fig. 13:6 shows the stress/strain curve and the AE rate for a Darley Dale sandstone sample deformed under a total confining pressure of 110MPa, but with a constant pore fluid pressure of 10MPa. The AE threshold for this test was 30dB. The stress/strain curve shows typical pseudo-ductile behaviour as illustrated for this sandstone

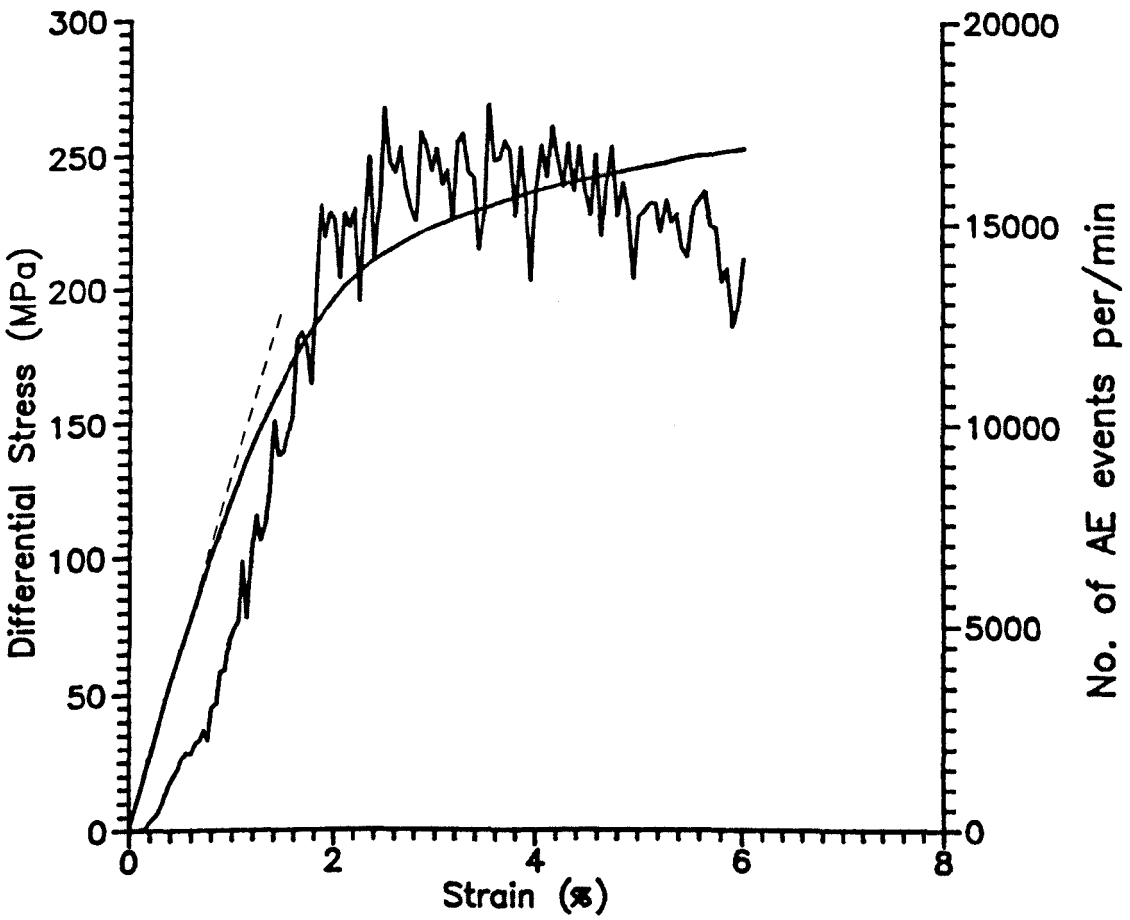

Fig. 13:6 The stress/strain curve and the AE rate for experiment PERM2; performed at 100MPa effective pressure.

under dry conditions in Chapter 7. An initial linear increase in the stress/strain curve gives way to sample anelasticity (at ≈0.8%), rolls over, and subsequently strain hardens. The AE rate rises sharply as the sample becomes significantly anelastic, reaching a high, relatively constant value (16000 events per minute) at ≈2% strain as the sample strain hardens. The strength of the sample is lower than would be expected from the simple effective stress law (see Chapter 7), a characteristic discussed in Chapter 12. It again appears that the diffuse nature of dilatant cracking during pseudo-ductile deformation could be resulting in incomplete sample drainage. This in turn could lead to local pore pressure gradients which reduce the effective confining pressure and weaken the sample.

Fig. 13:7 shows the pore volume change curve for this experiment. The pore volume decreases at a near-constant rate until about 3.5% strain, at which point pore closure and dilatant crack opening approximately balance. This balance of fluid expulsion and fluid intake does not occur until the rock is well within its anelastic regime. This suggests that early dilatant cracking is volumetrically small compared with the continuing process of pore closure during differential loading.

The residual dilatant pore volume, ΔV_R, plot is shown in fig. 13:8. The gradients used to correct for the fluid expulsion due to pore structure closure are g_1=125MPa/strain-increment and g_2=-40mm^3/strain-increment. The residual plot, although noisy, indicates that the sample starts to dilate at about 2% strain (which is earlier than suggested by the simple pore volume change plot). However, this is later than the onset of increased AE activity which occurs at ≈1% strain. A clear indication of the onset of dilatancy from this residual pore volume plot is precluded by its erratic nature. The residual plot peaks at ≈3.5% strain, after which it remains essentially constant. The total dilatant crack volume is about four times greater in this experiment than in the previous one (PERM21). This highlights the localised nature of cracking at lower confining pressures where less total damage occurs in the sample (volumetrically), and yet it still fails catastrophically.

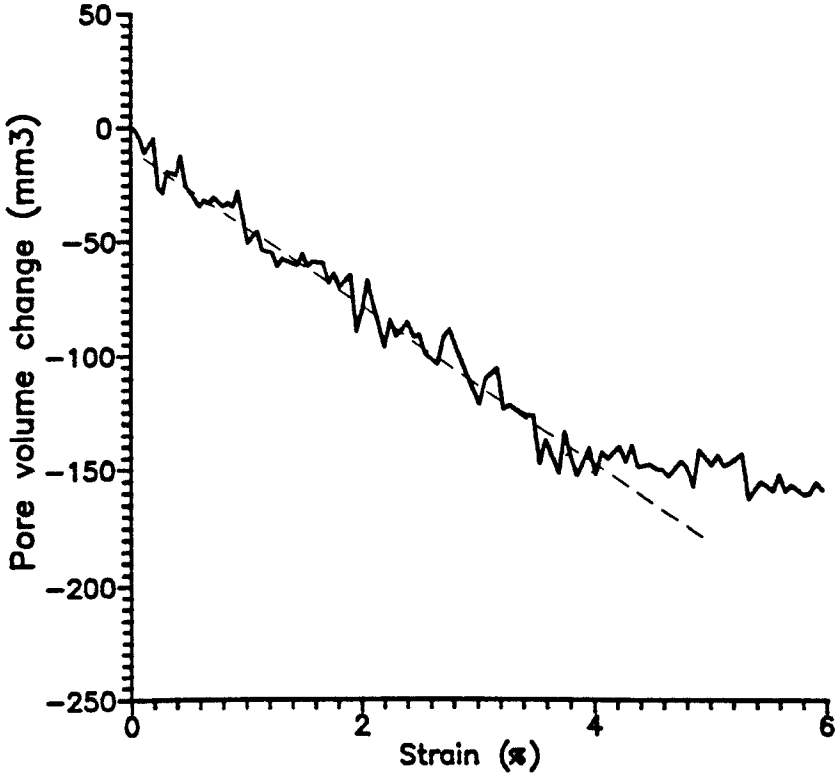

Fig. 13:7 The pore volume change for experiment PERM2.

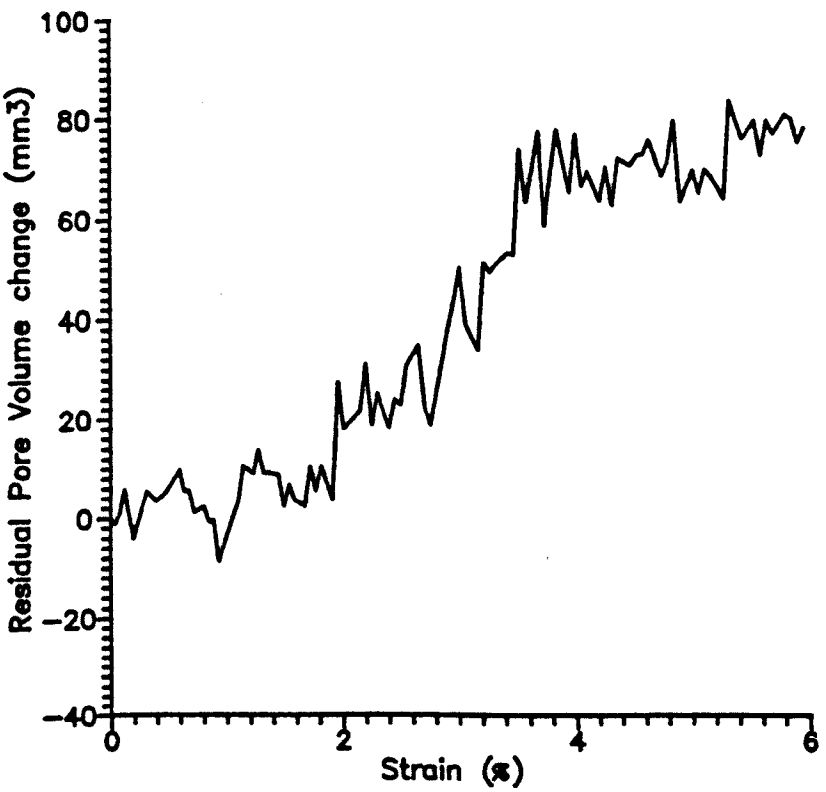

Fig. 13:8 The residual pore volume plot determined for test PERM2 (see text for details).

13:4 Description of a test carried out at 50MPa effective pressure (PERM12).

Fig. 13:9 shows the stress/strain curve and AE rate for a test performed at a confining pressure of 80MPa and a constant pore fluid pressure of 30MPa. The AE threshold on this test was 28dB. The stress/strain curve shows a slight initial upward concavity, which then gives way to a well defined linearity. The curve begins to deviate from linearity at around 1.1% strain. The curve rolls over to a peak stress of around 250MPa and then gently strain softens. There is a small stress drop of around 15MPa, although failure appears stable. The AE rate becomes emergent from the background level at ≈0.5% strain; but only increases sharply above about 1.5% strain. This latter point coincides with significant deviation from linearity of the stress/strain curve. The AE rate reaches a peak value (≈15000 events per minute) just after peak stress and then decreases to an intermediate level of about 7000 events per minute.

The stress/strain profile and the AE rate suggest that the mode of failure in this sample is transitional between brittle and ductile. Examination of the sample after testing showed no evidence for failure having taken place on a localised inclined failure plane. From the simple effective stress law it would be expected that the sample would fail catastrophically on a single inclined fault. This follows from the results presented in Chapter 7 where it is clear that the brittle-ductile transition occurs at around 75MPa confining pressure for dry samples of this rock. The peak strength of this sample is as expected from the effective stress law. Therefore, it is open to question as to whether or not chemical weakening was significant in this test.

The pore volume change curve (fig. 13:10) shows that the total pore volume initially decreases at an approximately constant rate. At ≈1.4% strain (at which point the AE rate is increasing sharply and the sample becomes significantly anelastic) the rate of fluid expulsion slowly decreases. However, net fluid expulsion continues throughout the test.

The residual dilatant pore volume plot (fig. 13:11), is determined using the gradients g_1=135MPa/strain-increment and g_2=-50mm^3/strain-increment. This plot shows significant scatter, but does indicate that dilatancy is increasing at a reasonably constant rate and reaches a maximum value at about 2% strain (close to peak stress). After

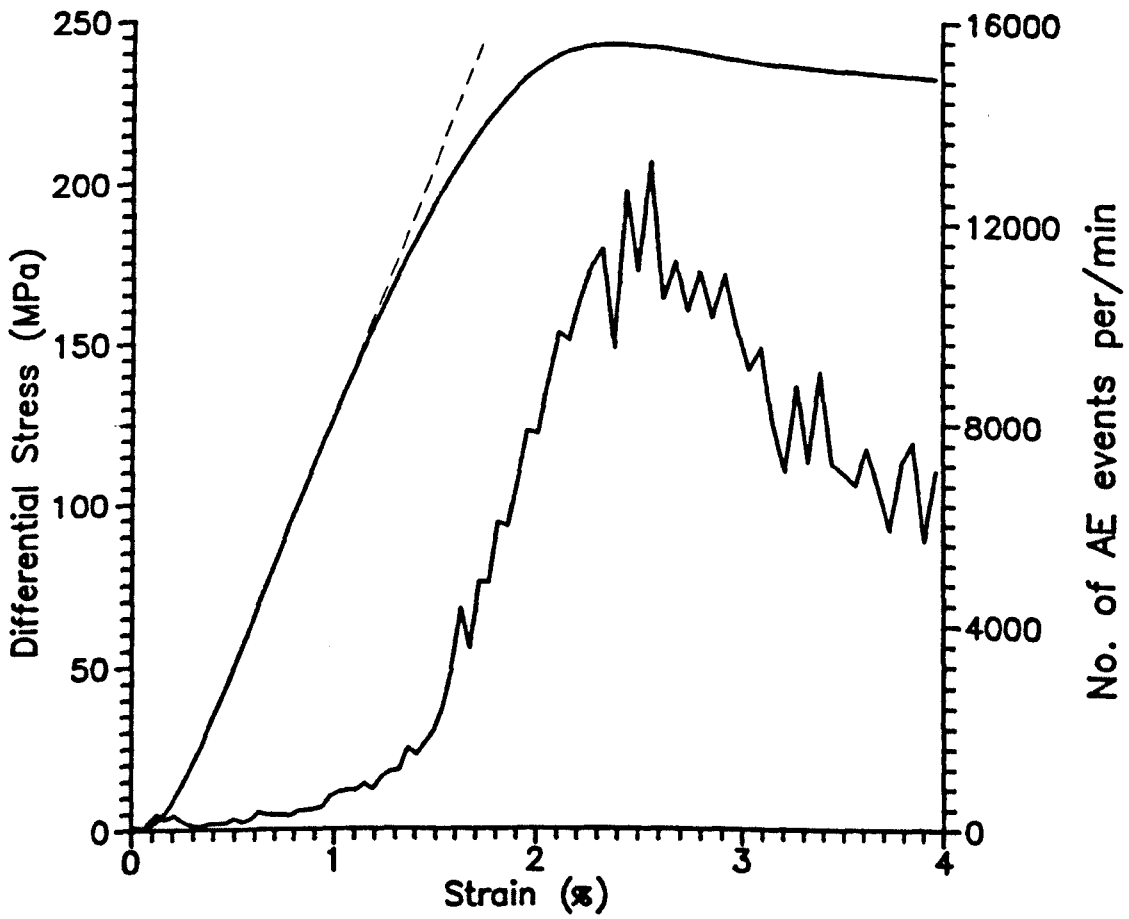

Fig. 13:9 The stress/strain curve and AE rate for experiment PERM12; performed at 50MPa effective pressure (see text for details).

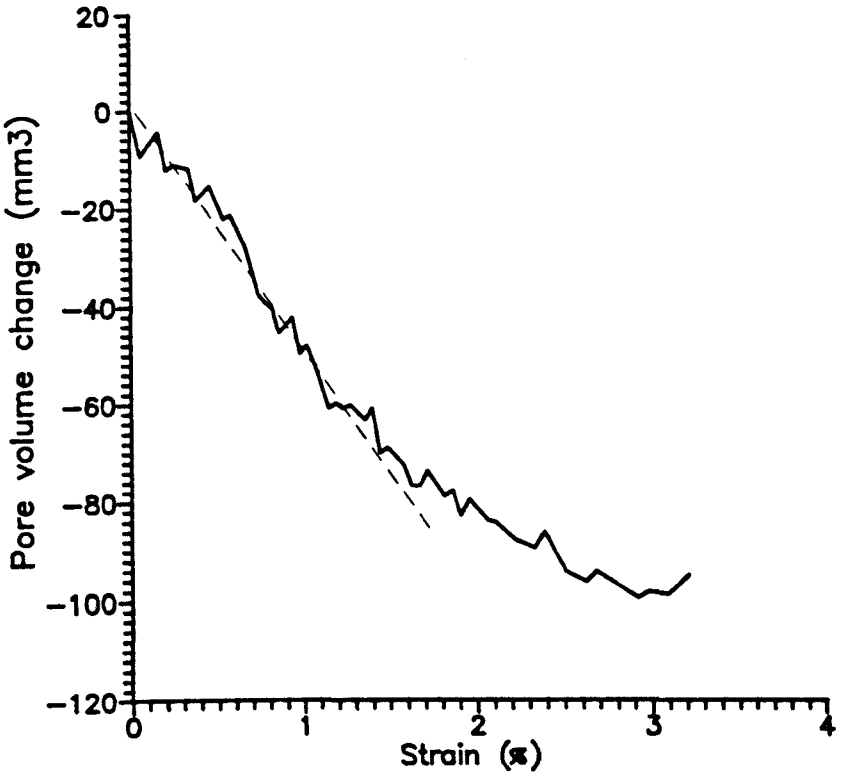

Fig. 13:10 The pore volume change for experiment PERM12.

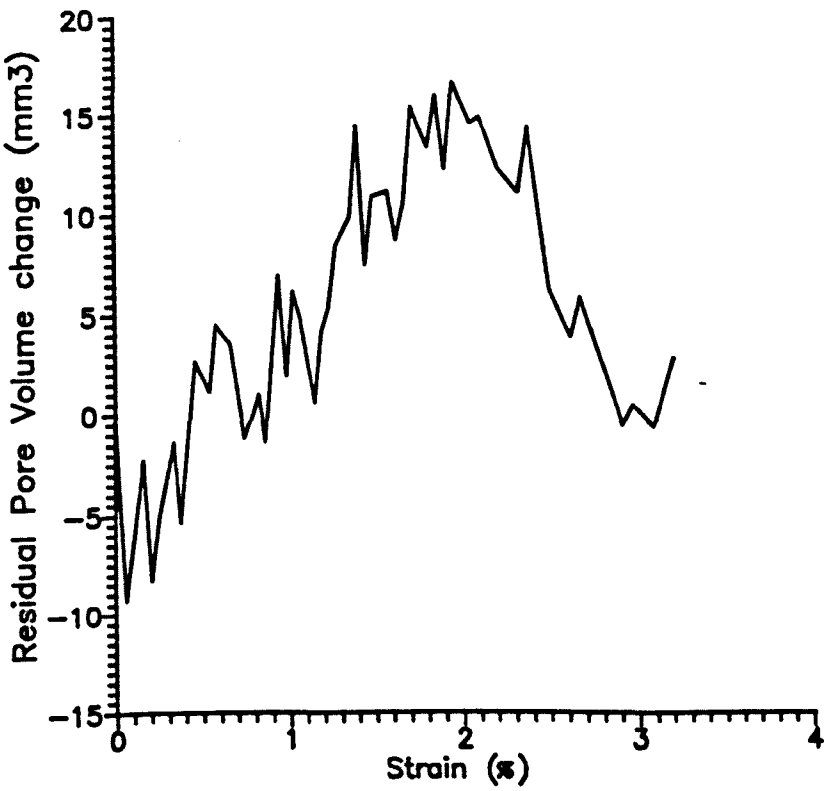

Fig. 13:11 The residual pore volume plot for test PERM12 (see text for details).

reaching a maximum the residual pore fluid volume decreases. The dilatant crack volume is similar to that measured in experiment PERM21 (carried out at 20MPa effective pressure).

13:5 Discussion.

The presence of water in sandstone seems to have effects on the behaviour of the rock other than those expected from the application of simple effective stress law. The presence of pressurised pore fluids appear to stabilise brittle behaviour which leads to less catastrophic failures and to reduce stress drops. However, the strength of the rock does not appear to be significantly affected. The most likely explanation of this is that rapid cracking can reduce the pore fluid pressure locally and lead to dilatancy hardening as macroscopic failure is approached.

AE evidence suggests that rapid crack growth and crack coalescence may occur at, or even before peak stress. This observation fits in well with the results of elastic wave velocity reported in Chapter 8. Furthermore, the residual pore volume plots suggest that peak dilatancy occurs close to macroscopic failure and well after peak stress (see fig. 13:5). Again, this fits in well with the evidence from the vertical crack density plots reported in Chapter 8. It can be seen that there is at least an approximate correlation between the vertical crack density parameter plots (εx) in Chapter 8 and residual pore volume plots (figs. 8:9 and 13.5, respectively) presented here. Although, this point is discussed further in the following chapter, it immediately suggests that; (i) dilatancy in this rock is controlled mainly by axial cracking, (ii) cracking is linked to a reasonably well-connected pore structure from an early stage (at least during brittle deformation), and (iii) again axial cracking is shown to be important even during pseudo-ductile deformation of this rock.

Pore closure volumetrically outweighs the effects of dilatant cracking. Therefore, the residual pore volume change plot is important in determining the onset of dilatancy. Also, the total crack density ($\varepsilon t=2\varepsilon x+\varepsilon z$) will significantly underestimate the amount of pore closure. This argument follows from the observation of relatively small reductions in εz seen in the analysis carried out in Chapter 8, and the large volumes of

fluid expulsion reported for the tests presented in this chapter. This is to be expected since ε_z is effectively a measure of crack closure, and fluid expulsion is a measure of both crack and pore closure; and Walsh (1966) and O'Connell & Budiansky (1974) have shown that velocity measurements are much less affected by spherical pores than thin cracks.

CHAPTER 14

DISCUSSION, CONCLUSIONS AND RECOMMENDATIONS FOR FUTURE WORK.

14:1 Discussion: Estimate of changes in the pore aspect ratio of dilatant cracking during progressive deformation.

Following from the arguments Chapter 13 an estimate of changes in the average aspect ratio of cracks during deformation can be obtained using pore volume change data combined with crack density parameter estimates. From the definition of the crack density parameter (eqn. 5:7) it can be seen that the crack aspect ratio can be determined (i.e. $\phi/\varepsilon = (4\pi/3)(c/a)$ where ϕ is the crack porosity, ε the crack density parameter and c/a the crack aspect ratio; see section 2:4:3). As previously discussed in section 8:4, there could again be a problem of relating a tensor quantity like the velocity matrix (and through this ε) to a volumetric quantity like porosity. However, the vertical crack density parameter can be related to the "residual pore volume" plot without ambiguity if it is assumed that most of the dilatant crack growth is aligned along the differential stress axis. There is little point, however, in trying to relate the total calculated crack density parameter ε_t to the total measured pore volumes (see section 13:5). The change in the crack density parameter for axially (or vertically orientated) cracks can be determined for Darley Dale sandstone, along with the increase in porosity resulting from dilatant cracking (see Chapters 8 and 13) in both the ductile and brittle regimes. Therefore, an estimate of the change in the crack aspect ratio for vertical dilatant cracks can be found for the first time in a triaxially deformed samples of this rock. However, there is some evidence for incomplete drainage of the rock samples deforming in a pseudo-ductile manner (i.e. the reduced strength of samples seen in Chapters 12 and 13). This may result in an underestimate of the average crack aspect ratio at high strains.

To calculate the crack aspect ratio of a sample showing typical catastrophic brittle failure, the data from the dry experiment performed at 50MPa confining pressure (DDA1; discussed in Chapters 7 and 8) was used in conjunction with the constant pore fluid pressure test at 50MPa effective pressure (PERM12; described in section 13:4). For the calculation of the change in vertical crack aspect ratio during pseudo-ductile

deformation, data from the dry experiment performed at 100MPa confining pressure (D519; described in Chapter 12), is used in conjunction with data from the constant pore fluid pressure test at 100MPa effective pressure (PERM2; described in section 13:3).

The stress/strain curves for the four tests are shown in figs. 14:1a,b. As can be seen, the two curves at 50MPa effective pressure show similar forms except that the stress drop seen for the constant pore fluid pressure test is less. The stress/strain curves at 100MPa effective pressure are much less similar, with the water-saturated sample exhibiting a considerably lower strength. However, the forms of the latter curves are similar. Figs. 14:1c,e show the vertical crack density parameter and residual pore volume change respectively, for 50MPa effective pressure. Due to scatter on the residual pore volume plot only an approximate likeness between the graphs can be noted. However, both are seen to increase as the sample dilates. After macroscopic failure of the sample the residual pore volume decreases markedly, whereas the vertical crack density decreases only marginally. Figs. 14:1d,f show the calculated vertical crack density and the residual pore volume changes at 100MPa effective pressure, respectively. These show reasonably similar forms. There is little change during the linear stress/strain climb, a sharp increase as the sample becomes anelastic, and then a continued increase (but at a reduced rate) during strain hardening of the sample. The initial crack density parameter at 100MPa confining pressure has a considerably lower value than at 50MPa confining pressure reflecting the increased number of cracks closed at the higher confining pressure.

In order to calculate the crack aspect ratio the initial vertical crack porosity is required. The porosity of undeformed Darley Dale sandstone at 50MPa and 100MPa effective hydrostatic pressure is about 0.085 and 0.035 respectively (M.D. Read, personal communication). Assuming that this porosity can be represented by three sets of aligned cracks, with the plane of their alignment perpendicular to three mutually orthogonal axes x,y,z; where z is the unique axis (c.f. Soga et al., 1978 and section 5:6:1), then the initial vertical crack porosity (perpendicular to the x axis) can be approximated by one-third the total porosity. This gives vertical crack porosities of about 0.028 and 0.012 at 50MPa and 100MPa effective pressures, respectively. These initial porosities can now be used with the residual pore volume change data, and the vertical crack density data (εx) to estimate the aspect ratios of dilatant cracks.

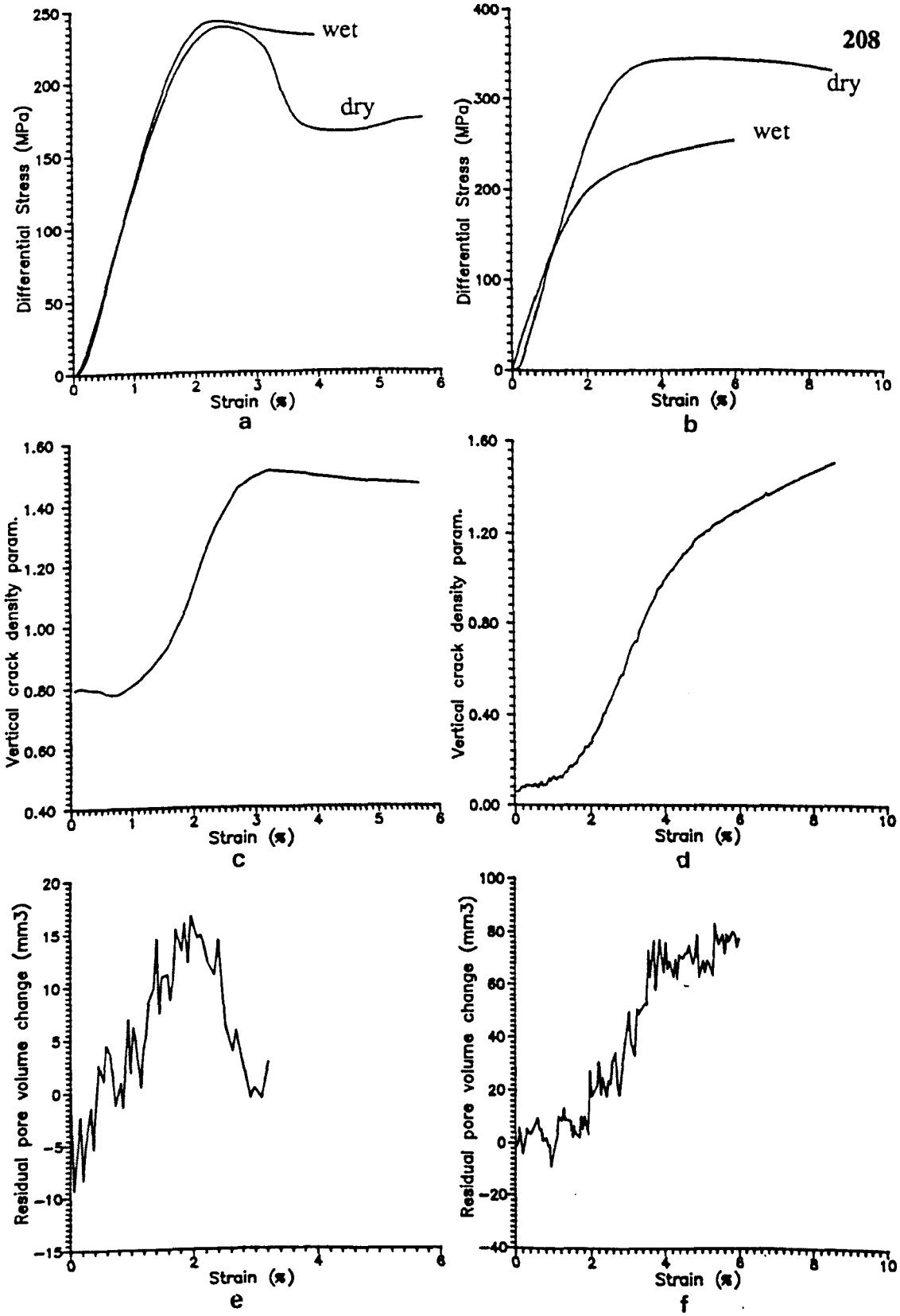

Figs. 14:1a,b,c,d,e,f The stress/strain curves for dry and wet Darley Dale sandstone deformed at 50MPa effective pressure (DDA1, PERM12, respectively), (a). The vertical crack density parameter εx for DDA1, and the residual pore volume plot, (c) and (e) respectively. The stress/strain curves for dry and wet Darley Dale sandstone deformed at 100MPa effective pressure (D519, PERM2), (b). The vertical crack density parameter for D519 and the residual pore volume plot for PERM2, (d) and (f) respectively.

Fig. 14:2a shows the calculated vertical crack aspect ratio during deformation at 50MPa and 100MPa effective pressure, and fig. 14:2b shows the percentage change in crack aspect ratio. At 50MPa effective pressure the crack aspect ratio increases slightly from 0.008 (≈1/120) to a peak of about 0.009 (≈1/113). This increase probably reflects elastic bowing of the vertical cracks upon initial differential loading, without much accompanying crack growth, and occurs during the linear elastic portion of stress/strain curve. After about 1% strain (the point at which the rock begins to become anelastic) the crack aspect ratio begins to decrease. As the rock becomes significantly anelastic the crack aspect ratio decreases sharply to a final value of about 0.0045 (≈1/220). This decrease in aspect ratio represents significant crack growth relative to increase in crack width.

The vertical crack aspect ratio for 100MPa effective pressure has an initial value of 0.04 (≈1/25). This higher aspect ratio reflects the more spherical nature of the open cracks and pores, as most of the low aspect ratio cracks (i.e. thin cracks) have already been closed at this confining pressure. As the sample is loaded, the crack aspect ratio decreases. This would appear to imply that rapid crack growth is occurring directly from initial differential loading even though the stress/strain curve for the sample appears linear. However, this explanation seems unlikely because of the small changes seen in Vp and Vs and the absence (or low level) of AE activity during the early stages of loading. A more likely explanation is that axially orientated cracks closed by the application of the confining pressure are merely opening in response to the application of a differential load. The crack aspect ratio decreases throughout the test, even during pseudo-ductile deformation (albeit at a markedly slower rate). The final crack aspect ratio is about 0.003 (≈1/360).

These calculations highlight some interesting features. Firstly, when cracks reach an average aspect ratio of about 0.005 (≈1/200), crack growth appears to be stable. That is, the cracks grow by a set increment per strain increment. Secondly, during the linear portion of the stress/strain curve of the experiment carried out at 50MPa confining pressure, an increase in crack width relative to crack length occurs. This suggests that elastic crack opening processes occur during this linear elastic deformation. At higher confining pressures there also appears to be a similar re-opening of cracks previously closed by the application of confining pressure, and this process is again likely to be reversible.

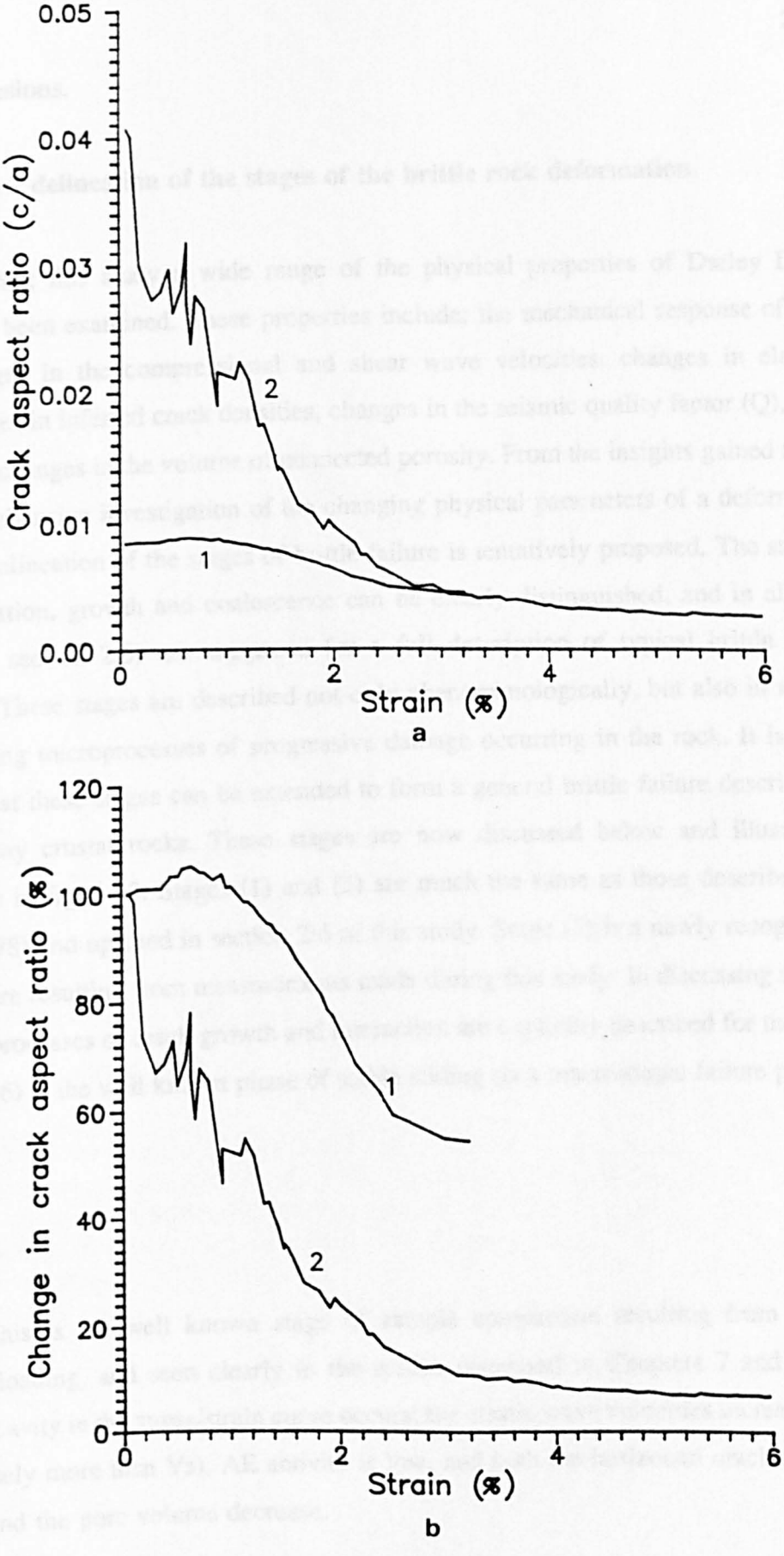

Figs. 14:2a,b The determined crack aspect ratio for new dilatant cracking in Darley Dale sandstone at 50MPa effective pressure (1) and 100MPa effective pressure (2), diagram (a). The percentage change in crack aspect ratio normalised to the initial value is also shown, diagram (b).

14:2 Conclusions.

14:2:1 A new delineation of the stages of the brittle rock deformation.

During this study a wide range of the physical properties of Darley Dale sandstone has been examined. These properties include; the mechanical response of the sample, changes in the compressional and shear wave velocities, changes in elastic moduli, changes in inferred crack densities, changes in the seismic quality factor (Q), AE statistics, and changes in the volume of connected porosity. From the insights gained after such a comprehensive investigation of the changing physical parameters of a deforming rock, a new delineation of the stages of brittle failure is tentatively proposed. The stages of crack initiation, growth and coalescence can be clearly distinguished, and in all six stages (as in section 2:6) are suggested for a full description of typical brittle rock deformation. These stages are described not only phenomenologically, but also in terms of the changing microprocesses of progressive damage occurring in the rock. It is also considered that these stages can be extended to form a general brittle failure description valid for many crustal rocks. These stages are now discussed below and illustrated schematically in fig. 14:3. Stages (1) and (2) are much the same as those described by Paterson (1978) and updated in section 2:6 of this study. Stage (3) is a newly recognised stage of failure resulting from measurements made during this study. In discussing stages (4) and (5), processes of crack growth and interaction are explicitly described for the first time. Stage (6) is the well known phase of stable sliding on a macroscopic failure plane.

Stage 1

This is the well known stage of sample compaction resulting from initial differential loading, and seen clearly in the results discussed in Chapters 7 and 9. An upward concavity in the stress/strain curve occurs; the elastic wave velocities increase (Vp proportionately more than Vs); AE activity is low; and both the horizontal crack density parameter and the pore volume decrease.

This stage is clearly associated with the closing of favourably orientated cracks upon initial differential loading, and is most noticeable at low confining pressures.

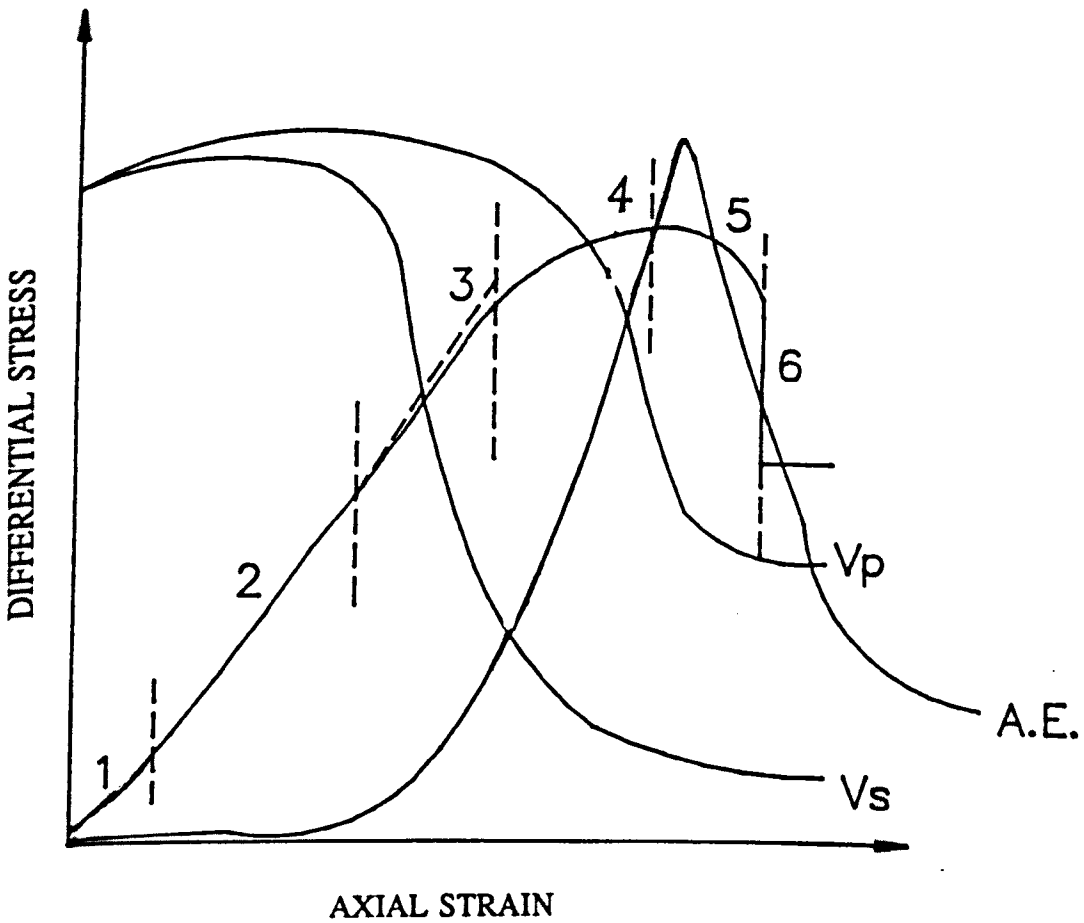

Fig. 14:3 An idealised stress/strain curve for brittle failure of rock. A new delineation of the stages of failure is given (see text). The AE rate, and shear and compressional wave velocity changes are also shown as evidence to support help with the delineation of the various stages.

Stage 2

In this stage, the stress/strain curve is quasi-linear elastic. Vp and Vs both peak, with the Vp peak being somewhat broader. AE activity is again low or non-existent. Both vertical and horizontal crack density parameters show little change, and the crack aspect ratio increases slightly at low confining pressures as vertical cracks bow open. At higher confining pressures the vertical crack aspect ratio decreases as thin cracks closed by the application of the confining pressure are re-opened.

During this stage competing mechanisms of elastic pore closure and vertical crack opening by bowing are probably occurring. These processes are mostly reversible.

Stage 3

This region is difficult to define merely by considering the stress/strain curve. It is better defined by considering the shear wave velocity curve and the volumetric strain/axial strain plot. The region extends from the point at which the shear wave velocity begins to decrease sharply (and where the volumetric strain plot deviates from linearity) to the point at which the sample becomes "significantly" anelastic. The exact position of this latter point is somewhat subjective, but can be reasonably well defined as where the stress/strain curve begins to become concave towards the strain axis. The stress/strain response during this stage appears to be approximately linear, but with a slope which is slightly less than that seen for stage (2). AE activity during this period becomes emergent from the background level (although the extent of this is necessarily dependent on the background threshold setting). Vs begins to decrease sharply, however, Vp only begins to decrease slowly from its peak value. The vertical crack density parameter also increases, while the dilatant crack aspect ratio decreases. The total pore volume continues to decrease at approximately the same rate as in earlier stages, but the dilatant crack aspect ratio decreases significantly.

This stage is considered to mark the onset of inelastic axial crack growth. It is suggested that these cracks are generally thin, thus contributing only marginally to the deviation of the stress/strain curve from linearity. These processes are again mostly

recoverable. The definition of this stage is important because it separates crack initiation (which occurs during this stage), from significant crack growth contributing to high levels of dilatancy (which does not occur until the following stage).

Stage 4

In this stage, rock becomes recognisably anelastic, and the stress/strain curve rolls over to reach peak stress. Vs decreases sharply, with its maximum rate of change occurring during this stage. Vp also decreases but at a slower rate than Vs. The vertical crack density continues to increase steeply, and the AE activity increases exponentially. Even though the pore volume continues to decrease, it is at a much reduced rate and may eventually begin to increase in the final part of this stage. The AE events increase markedly in amplitude, and low frequency components become dominant in the AE waveforms. The dilatant crack aspect ratio continues to decrease, and sample dilatant volume increases significantly.

Following from the theory of, among others, Horii & Nemat-Nasser (1985, 1986) we note that large flaws reduce the modulus of a solid much more rapidly than smaller flaws. Thus it seems reasonable to assume that the greatest rate of decrease in acoustic velocities marks the point at which crack linkage occurs (as velocity is dependent on the modulus of the material through which it travels). The rate of Vs decrease is most rapid at this stage. Therefore, it appears that accelerated crack growth is occurring at the sites of maximum damage and crack linkage is occurring locally. The cracking is mainly orientated along the axis of deviatoric stress. All the changes in the other parameters also support this interpretation of the cracking during this stage.

Stage 5

During this stage dilatancy, as determined from pore volume measurements, reaches a peak. The AE rate also peaks and so does the vertical crack density parameter. The rock fails macroscopically while the horizontal crack density increases slightly. The acoustic velocities are still decreasing but at a much reduced rate. The decrease in dilatant

crack aspect ratio becomes less.

When this stage commences significant crack linkage has already occurred. This process appears to continue during stage 5 but at a reduced rate. This results from previous crack linkage which has led to a lesser number of larger cracks. Because these larger cracks are not increasing in length as much as when crack linkage was dominant (i.e. in stage 4) the rate of decrease in Vp and Vs becomes less, and the rate of decrease in vertical crack aspect ratio also becomes less. At the point of catastrophic failure, dilatancy is a maximum, and an increase in the horizontal crack density parameter (εz) is seen. This increase in εz is thought to result from the onset of angled cracking. Therefore, it seems likely that cracking remains predominantly axial in nature until immediately before macroscopic failure of the sample.

Stage 6

This stage is characterised by stable sliding on the macroscopic fault, with little new cracking. Vp and Vs, and the pore volume remain essentially constant. The AE rate is modest (and constant) and is the result of frictional sliding on the failure plane.

The above scenario of brittle deformation and failure shows several important features distinguishing it from previous classifications (e.g. Paterson, 1978). Firstly, a stage of onset of thin crack growth is clearly defined (stage 3). The elastic wave velocities are crucial in defining this stage. Secondly, crack linkage is clearly seen to occur prior to peak stress. Before peak stress and for a period following it cracking is predominantly axial. Thirdly, the onset of angled crack growth is shown to be an extremely late feature occurring only immediately before catastrophic failure of the rock.

It is worth noting that the experimental evidence presented above (and the subsequently derived damage processes) suggests that rock failure is occurring in a manner similar to that outlined in the analogue model of Sammis and Ashby (1986). That is, axial crack growth and linkage occur until the rock is effectively supported by a series of vertical beams (this coincides with peak stress). These rock beams then begin to flex

and bow open reducing the stiffness of the rock. This process occurs mainly during the strain weakening period (stage 5, above). The flexing increases the crack length by causing further growth at the crack tips, hence cracking remains essentially axial in character. The arc of flexure would be greatest in the centre of the sample. When the beams bend beyond a certain limit, angled cracking breaks across the sample (at the point of maximum curvature of beams) and is virtually contemporaneous with macroscopic failure.

14:2:2 General summary of the experimental results.

Simultaneous compressional and shear wave velocity changes have been extensively and systematically examined for a suite of rocks at different confining pressures. A detailed scenario of crack closure followed by axial crack opening, growth and coalescence has been proposed to explain the physical parameter changes seen in Darley Dale sandstone. It is considered that these processes of damage outlined for this rock will have a general application to many brittle rocks.

Acoustic velocity changes during deformation of Gosford sandstone have been measured for the first time, and a detailed examination of the rock's response in the brittle field has been reported. This rock has a lower strength and is more variable than Darley Dale sandstone. However, a similar regime of crack closure and subsequent axially orientated dilatant cracking can be invoked to explain the velocity changes for both rock types, although, the weakly cemented Gosford sandstone shows signs of considerable cataclastic flow even at moderate confining pressures.

Solenhofen limestone has been examined in the brittle, ductile and transitional deformation regimes. The brittle results are in agreement with those of previous authors, and the brittle-ductile transition occurs at a confining pressure also seen by others. A close examination of the acoustic results in the ductile field implies that brittle microprocesses are probably not the only mechanisms of deformation. More likely, a combination of plastic processes that may include cleavage slip, twin plane gliding, and/or intracrystalline plasticity, together with axial cracking of limited extent is occurring.

An investigation of the effects of strong anisotropic bedding on the mechanical and acoustic properties of Tennessee sandstone has been carried out. There is some evidence for seismic anisotropy of the sample at 50MPa hydrostatic pressure; this evidence suggests that alignment of cracking is in the bedding plane. However, as the sample is deformed there is no evidence that the new dilatant cracking is preferentially orientated in the bedding plane. The orientation of the bedding plane with respect to the maximum loading axis has a significant effect on the mechanical response of the rock.

Results from three tests on Darley Dale sandstone under dry, water saturated-drained, and water saturated-undrained conditions at 100MPa confining pressure, are reported. Initially, by considering changes in the crack densities of the samples, it appeared that the mechanical and chemical effects of pore water on the deformation properties of the rock could be separated. It seemed as though chemical weakening could have a considerable effect on the peak strength of this sandstone. However, in subsequent tests conducted under pore fluid pressure control in the brittle field, it was shown that the strength of the rock approximately obeyed the simple effective pressure law. The weakening seen in saturated samples (at least for this sandstone deformed at relatively fast strain rates and undergoing pseudo-ductile deformation) is considered to be, primarily, the result of incomplete drainage of the sample causing local pressure gradients which in turn reduce the effective confining pressure locally.

Results from constant pore pressure tests carried out for Darley Dale sandstone samples in the brittle, ductile and transitional regimes are also reported. The pore fluid volume changes show that volumetric pore closure dominates over the crack opening, up to effective pressures of at least 100MPa. By subtracting the fluid expulsion effect caused by pore collapse, dilatancy can be seen in all the samples, although the scatter in the measurements makes the onset of dilatant cracking less easy to see than when it is determined from the acoustic velocity measurements. The "residual dilatant pore volume" plots agree approximately with the vertical crack density plots (εx) determined for dry samples at the equivalent effective pressure. These results taken together further imply that most of the dilatant cracking at medium to low confining pressures is in the vertical (axial) direction and is linked to a saturated and inter-connected pore volume matrix. For the brittle samples, chemical weakening is seen to have only a small effect on the peak strength of the rock. In the ductile regime, wet samples show a marked reduction in

strength. This could possibly be due to the diffuse nature of the cracking at high effective pressures making complete fluid saturation and drainage of the sample difficult when there is a pore-fluid inlet at only one end of the sample. The weakening effect of water on sandstones, therefore, appears to be the result of pore pressure effects, according to effective stress principles.

14:3 The wider geological implications of the laboratory investigations.

A clear understanding of the fundamental processes involved in rock failure on the microscopic level is of prime importance in understanding much larger geological processes. This has been discussed by, among others, Meredith et al. (1990), as have the scaling problems involved in relating microprocesses to macroscopic geological processes. Research into the stress build-up and failure processes occurring in rocks is particularly important in the fields of earthquake source physics and mine safety. The rock physical property changes measured in this study, along with measurements of fluid connectivity changes, are potentially important in developing far-field interrogation techniques to determine in situ porosity and permeability changes at depth. This could be important in such fields as nuclear waste disposal and oil exploration and exploitation.

Laboratory data on the mechanical and elastic properties of rocks can be of direct application to many geological problems today. Primarily, it can be envisaged that laboratory data can provide boundary conditions for the computer modelling of such processes as sedimentary basin formation (McKenzie, 1978), mountain building and regional metamorphism (Murrell, 1986a), and the development of subduction zones.

14:4 Recommendations for future work.

There are certain mechanical restrictions to the sample size and geometry which make the interactions of the sample and interrogating acoustic wave complicated (Chapter 4). However, more advanced signal processing techniques could perhaps be useful in extending the interpretation of acoustic wave data from the present triaxial cell. These

might include deconvolution of the input and output waveforms, that is, the waveform obtained at the beginning of the test (which will have propagated through an undeformed and relatively isotropic sample) and the subsequent waveforms recorded at different stages of deformation. At small strains the change in the waveform due to the sample shortening is likely to be small and can easily be corrected for. This would mean that any changes seen in the deconvolved waveforms would directly reflect changes in the internal structure of the sample. Furthermore, a direct comparison of the changes in seismic Q of laboratory samples with the changes in coda Q for field data as reported by Aki (1981) could be made. However, care would be needed, since previous attempts to measure coda Q in the laboratory (e.g. Warren et al., 1974) have found values that are an order of magnitude higher than those determined by first arrival half-width methods. The seismic Q determinations reported here have been very limited and this work should be extended, as such measurements provide a potential way of separating elastic and non-elastic components of rock deformation. As most of the crust is fluid-saturated, this work could also be extended to saturated samples in which the role of fluid attenuation mechanisms could be examined. Different types of saturants such as hydrocarbons or CO_2 could also be examined, to provide a link between acoustic velocity, attenuation changes and the transport properties of the rock; such experiments would be especially important to the oil industry.

More complex waveform interpretations are precluded in the present experimental arrangement primarily because of the complicated waveform-sample geometry interaction. Also, unique crack density determinations are not possible because the acoustic velocity changes can only be measured along the major axis of compression. The crack aspect ratio determinations are also subject to error resulting from differences between the mechanical response of the different samples which are compared. Therefore, it is important to take a "holistic" approach to physical parameter measurements on deforming rock samples. That is, a range of different parameters should be measured simultaneously on the same sample. This approach could be developed further by utilising the newly-constructed, large-volume triaxial deformation and rock physics ensemble at U.C.L. In this new system the sample size has been increased to 40mm diameter, 120mm long. The system also affords greater access to the sample to enable multi-parameter measurements to be made synchronously. This new apparatus is designed to simulate conditions in the upper 15km of the Earth's crust i.e. up to 400MPa and 400°C. This

corresponds broadly to the depth of the crust's seismogenic zone, or schizosphere (Scholz, 1990). It will enable the whole range of syn-deformational physical property measurements to be made simultaneously. These will include P and S wave velocity measurements, AE event rate and location, independent pore fluid control as well as electrolytic conductivity measurements. More complete velocity measurements carried out along three mutually orthogonal axes will allow unique crack orientation distributions to be determined without the need for assumptions about the elastic properties of the rock to be made (e.g. Sayers, 1988). Increased access to the sample will also allow direct strain gauging of the sample. This equipment should lead to exciting new discoveries about the processes of rock deformation and failure, and lead to a greater clarity of understanding of fundamental processes of crack growth and linkage.

APPENDIX 1

DESCRIPTION OF THE ROCKS USED IN THIS STUDY.

Darley Dale sandstone.

This rock comes from Stancliffe quarry in Derbyshire, and has been described fully elsewhere (e.g. Ismail & Murrell, 1976). It is a well-indurated felspathic sandstone, the grains are angular to sub-angular and range from 0.08mm to 0.8mm in size. The cementing material is silicious. The approximate composition of the rock is 75% quartz, 15% felspar and 10% clays and micas. The average bulk density is 2.42g/cm^3 and average porosity is ≈12%.

Gosford sandstone.

Gosford sandstone comes from New South Wales in Australia, and stress-induced dilatancy has been reported for this rock by Edmond & Paterson (1972). They give the stress/strain response at confining pressures between 200MPa and 600MPa, and volume changes determined using the dilatometer method. The grain size in this rock range from 0.1mm to 1mm. There is moderate sorting of the grains which are mostly sub-angular to sub-rounded, the grains are tightly packed. The approximate composition is 70% quartz (65% monocrystalline and 5% polycrystalline), 5% muscovite, 1% biotite and <1% sphene. The matrix is 20%, mostly clays and polycrystalline micas. It has a bulk density of 2.45g/cm^3, and a porosity of ≈13%.

Solenhofen limestone.

This well known rock has also been described elsewhere (Edmond & Paterson, 1972). This is a fine grained (0.01mm) lithographic limestone with a density of 2.56g/cm^3 and an average porosity of <1%

Tennessee sandstone.

This sandstone comes from Tennessee in the U.S.A., and has been described by Rutter & White (1979). It comprises of about 85% quartz, with 15% fine-grained phillosilicate and limonite cement. The average grain size of the quartz is about 0.15mm. The rock shows a strong laminar cross-bedding ranging from about 1mm to 10mm in thickness. The average porosity of this rock is 5%, and has an average bulk density of 2.63g/cm^3.

LIST OF REFERENCES.

Adams, F.D. An experimental investigation into the action of differential pressure on certain minerals and rocks, employing the process suggested by Professor Kick. J. Geol. **18**, 489-525 (1910).

Aki, K. Scattering and attenuation of high-frequency body waves (1-25Hz) in the lithosphere. Phys. Earth Planet. Int. **26**, 241-243 (1981).

Anderson, D.L., Minster, B., Cole, D. The effect of orientated cracks on seismic velocities. J. Geophys. Res. **79**, 4011-4015 (1974).

Ashby, M.F., Hallam, S.D. The failure of brittle solids containing small cracks under compressive stress states. Acta Metall. **34/3**, 497-510 (1986).

ASTM Standard Method for Laboratory Determination of Pulse velocities and Ultrasonic Elastic Constants of Rock. Vol 04.08 D 2845-83 (1988).

Atkinson, B.K., Meredith, P.G. Stress corrosion of quartz: a note on the influence of chemical environment. Tectonophysics **77**, T1-T11, (1983).

Atkinson, B.K., Meredith, P.G. The theory of subcritical crack growth with application to minerals and rocks. In: Fracture Mechanics of Rock. Academic Press, London, 111-166 (1987a).

Atkinson, B.K., Meredith, P.G. Experimental fracture mechanics data for rocks and minerals. In: Fracture Mechanics of Rock. Academic Press, London, 477-525 (1987b).

Attewal, P.B., Ramana, Y.V. Wave attenuation and internal friction as functions of frequency in rocks. Geophys. **31**, 1049-1056 (1966).

Barasch, S. Strain guages for the measurement of strain waves on the surface of fused quartz. IEEE Trans. on Sonics and Ultrasonics, Vol. SU-**17**, No.1 30-34 (1970).

Birch, F. The velocities of compressional waves in rocks up to 10 Kilobars, Part I. J. Geophys. Res. **65**, 1083-1102 (1960).

Birch, F. Velocity and attenuation from resonant vibrations of spheres of rock, glass and steel. J. Geophys. Res. **80**, 756-764 (1967).

Biot, M.A. Theory of propagation of elastic waves in a fluid-saturated porous solid. I. Low frequency range: J. Acoust. Soc. Am. **28**, 168-178 (1956a).

Biot, M.A. Theory of propagation of elastic waves in a fluid-saturated porous solid. II. High frequency range: J. Acoust. Soc. Am. **28**, 179-191 (1956b).

Bombolakis, E.G. Study of the brittle fracture process under uniaxial compression. Tectonophysics **18**, 231-248 (1973).

Bonner, B.P. Shear wave birefringence in dilating granite. Geophys. Res. Lett. **1**, 217-220 (1974).

Brace, W.F. Brittle fracture of rocks. In: State of Stress in the Earth's Crust. Judd. W.R. (ed.). New York: Elsevier 1964a, pp. 111-174.

Brace, W.F. The mechanical effects of pore pressure on fracturing of rocks. In: Proc. Conf. on Research in tectonics (Kink Bands and Brittle Deformation), Ottawa, March 1968. Baer, A.J., Norris, D.K. (eds). Geol Surv. Canada, Paper **68-52**, 1969a, pp. 113-123.

Brace, W.F., Bombolakis, E.G. A note on brittle crack growth in compression. J. Geophys. Res. **68**, 3709-3713 (1963).

Brace, W.F., Martin, R.J. A test of the law of effective stressfor crystalline rocks of low porosity. Int. J. Rock. Mech. Min. Sci. **5**, 415-426 (1968).

Brace, W.F., Orange, A.S. Electrical resistivity changes in saturated rocks during fracture and frictional sliding. J. Geophys. Res. **73,** 1433-1445 (1968).

Brace, W.F., Paulding, B.W., Scholz, C. Dilatancy in the fracture of crystalline rocks. J. Geophys. Res. **71,** 3939-3953 (1966).

Brookes, S.G. Siesmic velocities from crustal sections in northern Scandinavia. PhD thesis, University of East Anglia (1984).

Bruner, W.M. Comment on "Seismic velocities in dry and saturated cracked solids" by Richard J. O'Connell and Bernard Budiansky. J. Geophys. Res. **81,** 2573-2576 (1976).

Bylerlee, J.D. Frictional characteristics of granite under high confining pressure. J. Geophys. Res. **72,** 3639-3648 (1967a).

Byerlee, J.D. Acoustic emission in rock during fluid injection. In: Advances in Rock Mechanics Proc. 3rd Int. Soc. Rock Mech., Denver, 1974 Vol. II, part A pp633-637.

Callerame, J., Tancrell, R.H., Wilson, D.T. IEEE Cat. 79CH 1482-9SU (London:IEEE), p.119 (1979).

Carmichael, R.S. Practical handbook of physical proerties of rocks and minerals, CRC Press, Florida, (1989).

Carter, N.L., Christie, J.M., Griggs, D.T. Experimental deformation and recrystallization of quartz. J. Geol. **72,** 687-733 (1964).

Costin, L.S. A microcrack model for the deformation and failure of brittle rock. J. Geophys. Res. **88,** 9485-9492 (1983).

Costin, L.S. Damage mechanics in the post failure regime. Mechanics of materials **4,** 149-160 (1985).

Crampin, S. A review of wave motion in anistropic and cracked elastic media. Wave motion **3,** 341-391 (1981).

Crampin, S., McGonigle, R. The variation of delays in stress-induced anisotropic polarization anomalies. Geophys. J.R. astr. Soc. **64,** 115-131 (1981).

Edmond, J.M., Paterson, M.S. Volume changes during the deformation of rocks at high pressures. Int. J. Rock Mech. Min. Sci. **9,** 161-182 (1972).

Edmond, O., Murrell, S.A.F. Experimental observations on rock fracture at pressures up to 7 kbar and the implications for earthquake faulting. Tectonophysics **16,** 71-87 (1973).

Eshelby, J.D. The determination of the elastic field of an ellipsoidal inclusion and related problems. Proc. Roy. Soc. Ser. A. **241,** 376-396 (1957).

Fjaer, E., Holt, R.M., Raaen, A.M. Rock mechanics and rock acoustics. In: Rock at great depth. Proc. Int. Symp., Pau, 1990, Vol. III, pp. 355-362.

Fonseka, G.M., Murrell, S.A.F., Barnes, P. Scanning electron microscope and acoustic emission studies of crack development in rocks. Int. J. Rock Mech. Min. Sci. **22,** 273-289 (1985).

Gordon, J.B., Davies, L.A. Velocity and attenuation of seismic waves in imperfectly elastic rock. J. Geophys. Res. **73,** 3917-3935 (1968).

Griffith, A.A. The phenomena of rupture and flow in solids. Phil. Trans. R. Soc. Ser. A **221,** 163-198 (1920).

Griffith, A.A. The theory of rupture. In: Proc. 1st Int. Congr. Appl. Mech. Biezeno, C.B., Burgers, J.M. (eds.). Delft: Tech. Boekhandel en Drukkerij J. Waltman Jr., 1924, pp.54-63.

Griggs, D.T. Deformation of rocks under high confining pressures. J. Geol. **44,** 541-577 (1936).

Gupta, I.N. Seismic velocities in rock subjected to axial loading up to shear fracture. J. Geophys. Res. **78,** 6936-6942 (1973).

Hadley, K. Vp/Vs anomalis in dilatant rock samples. Pure Appl. Geophys. **113,** 1-23 (1975a).

Hadley, K. Comparison of calculated and observed crack densities and seismic velocities in Westerly granite. J. Geophys. Res. **81,** 3484-3494 (1976b).

Hallbauer, D.K., Wagner, H., Cook, N.G.W. Some observations concerning the microscopic and mechanical behaviour of quartzite specimens in stiff, triaxial compression tests. Int. J. Rock Mech. Min. Sci. **10,** 713-726 (1973).

Handin, J., Hager, R.V., Friedman, M., Feather, J.N. Experimental deformation of sedimentary rocks under confining pressure; pore pressure effects. Bull. Am. Assoc, Petrol. Geol. **47,** 717-755 (1963).

Hamilton, E.L. Compressional wave attenuation in marine sediments. Geophys. **37,** 620-646 (1972).

Heard, H.C. Transition from brittle fracture to ductile flow in Solenhofen limestone as a function of temperature, confining pressure, and interstitial fluid pressure. In: Rock Deformation. Griggs, D., Handin, J.(eds.). Geol. Soc. Am., Memoir **79,** 1960, pp. 193-226.

Heard, H.C. Effect of large changes in strain rate in the experimental deformation of Yule marble. J. Geol. **71,** 162-195 (1963).

Heck, W.J. Development of equipment for studying pore pressure effects in rock. In: Basic and Applied Rock Mechanics. Gray, K.E. (ed). 10th Symp. Rock Mech., Austin, Texas, May 1968. New York: A.I.M.E. 1972, pp. 243-266.

Holloway, J.R. Internally heated pressure vessels: In Research techniques at high pressures and temperatures. Springer-Verlag, N.Y. 1971, pp217-258.

Horii, H., Nemat-Nasser, S. Compression induced microcrack growth in brittle solids: axial splitting shear failure. J. Geophys. Res. **87 B4,** 3105-3125 (1985).

Horii, H., Nemat-Nasser, S. Brittle failure in compression: splitting, faulting and brittle ductile transition. Phil. Trans. R. Soc. Lond. **A319,** 337-374 (1986).

Houpert, R. Comportement fragile en compression simple et structure des roches. In: Proc. 2nd Int. Congr. Int. Assoc.Eng. Geol. Sao Paolo, Aug. 1974, 1974b, Vol. 1, pp. IV-25.1-IV-25.10 (1974).

Ismail, I.A.H. Experimental studies of mechanical instabilities in rocks. Ph.D. thesis, University of London (1974).

Jackson, D.D., Anderson, D.L. Physical mechanisms of seismic wave attenuation. Rev. Geophys. Space Phys. **8,** 1-63 (1970).

Jaeger, J.C., Cook, N.G.W. Fundamentals of Rock Mechanics. 3rd. ed. London: Chapman and Hall, 1979.

Johnston, D.H., Toksoz, M.N. Ultrasonic P- and S-wave attenuation in dry and saturated rocks under pressure. J. Geophys. Res. **85,** 925-936 (1980).

Johnston, D.H., Toksoz, M.N., Timur, A. Attenuation of seismic waves in dry and saturated rocks: II. mechanisms. Geophys. **44,** 691-711 (1979).

Jones, C. An experimental study of the relationships between P wave velocity, acoustic emission and deformation in rocks under simulated crustal conditions. Ph.D. Thesis, University of London (1989).

Jones, C, Murrell, S.A.F. Acoustic compressional wave velocity and dilatancy in triaxially stressed rock. In: Rock at great depth. Proc. Int. Symp., Pau, 1990, Vol. I. pp. 241-249.

Kern, H. The effect of high temperature and high confining pressure on compressional wave velocities in quartz-bearing and quartz-free igneous and metamorphic rocks. Tectonophysics **44**, 185-203 (1978).

Kern, H., Fakhimi, M., Effect of fabric anisotropy on compressional wave propagation in various metamorphic rocks for the range 20-700°C at 2Kbars. Tectonophysiocs **28**, 227-244 (1975).

Knopoff, L., Q. Rev. Geophys. **2**, 625-660 (1964).

Kranz, R., Microcracks in rock: A review. Tectonophysics **100**, 449-480 (1983).

Kuster, G.T., Toksoz, M.N., Velocity and attenuation of seismic waves in two-phase media: Part I. Theoretical formulations. Geophysiscs **39**, 587-606 (1974).

Lawn, B.R., Wilshaw, T.R. Fracture of brittle solids. Cambridge: Univ. Press. 1975b, 204pp.

Lo, T., Coyner, K.B., Toksoz, M.N. Experimental determination of elastic anistotropy of Berea sandstone, Chicopee shale, and Chelmsford granite. Geophys. **51**, 164-171 (1986).

Lockner, D., Byerlee, J.D. Acoustic emission and fault formation in rocks. In: Proc. First Conf. on Acoustic Emission/Microseismic Activity in Geologic Structures and materials. Penn. State Univ., June 1975. Hardy, H.R., Leighton, F.W. (eds.). Clausthal:Trans. Tech. Publ. 1977c, pp. 99-107.

Lockner, D., Byerlee, J.D. development of fracture plane during creep in granite. In: Proceedings of the 2nd Conference on Acoustic Emission/Microseismic Activity in Geologic Structures and Materials. Hardy, Jr., H.R., Leighton, F.W. (eds.), Trans. Tech. Publications, Clausthal-Zellerfeld, Federal Republic of Germany, 1980, pp.1-15.

Lockner, D.A., Walsh, J.B., Byerlee, J.D. Changes in seismic velocity and attenuation during deformation of granite. J. Geophys. Res. **82**, 5374-5378 (1977).

Maeda, I. Spectral and source parameters of acoustic signals emitted by microcrack generation in a granite sample. J. Phys. Earth **29,** 241-253 (1981).

Main, I.G., Meredith, P.G., Sammonds, P.R., Jones, C. Influence of fractal flaw distributions on rock deformation in the brittle field. In: Deformation Mechanisms and Tectonics. Geol. Soc. Special Publication, 1990. Knipe, R.J., Rutter, E.H. (eds.) No. 54, pp. 71-79.

Martin, R.J., Durham, W.B. Mechanics of crack growth in quartz. J. Geophys. Res. **80,** 4837-4844 (1975).

Mattaboni, P., Schreiber, E. Method of pulse transmission measurements for determining sound velocities. J. Geophys. Res. **72,** 5160-5163 (1974).

Mavko, G.M. Frictional attenuation: An inherent amplitude dependence. J. Geophys. Res. **84,** 4769-4775 (1979).

Mavko, G., Nur, A. Melt squirt in the asthenosphere. J. Geophys. Res. **80,** 1444-1447 (1975).

Mavko, G., Nur, A. The effect of nonelliptical cracks on the compressibility of rocks. J. Geophys. Res. **83,** 4459-4468 (1978).

Mavko, G., Kjartansson, E., Winkler, K. Seismic wave attenuation in rocks. Rev. Geophys. and Space Physics, Vol. **17,** No. 6 1155-1164 (1979).

McDonal, F.J., Angona, F.A., Mills, R.L., Sengbush, R.L., Van Nostrand, R.G., and White, J.E. Attenuation of shear and compressional waves in Pierre shale. Geophys. **23,** 421-439 (1958).

McKenzie, D.P. Some remarks on the development of sedimentary basins. Earth Planet. Sci. Lett. **48,** 25-32 (1978).

McLintock, F.A., Walsh, J.B. Friction on Griffith cracks in rocks under pressure. In: Proc. 4th U.S. Nat. Congr. Appl. Mech., Vol II. New York: Am. Soc. Mech. Eng. 1962, pp. 1015-1021.

Meredith, P.G., Atkinson, B.K., Stress corrosion and acoustic emission during tensile crack propagation in Whin Sill dolerite and other basic rocks. Geophys. J.R. Astro. Soc. **75** 1-21 (1983).

Meredith, P.G., Main, I.G., Jones, C. Temporal variations in seismicity during quasi-static and dynamic rock failure. Tectonophysics **175,** 249-268 (1990).

Murrell, S.A.F. The strength of coal under triaxial compression. In: Mechanical Properties of Non-Metallic Brittle Materials. Walton, W.H. (ed.). London: Butterworths 1958, pp. 123-145.

Murrell, S.A.F. A criterion for brittle fracture of rocks and concrete under triaxial stress, and the effect of pore pressure on the criterion. In: Rock Mechanics. Fairhurst, C. (ed.), Proc. 5th Symp. Rock Mech. New York: Pergammon Press 1963, pp. 563-577.

Murrell, S.A.F. The theory of the propagation of elliptical Griffith cracks under various conditions of plane strain or plane stress. Part I. Br. J. Appl. Phys. **15,** 1195-1210: Part II and III:ibid., 1211-1223 (1964).

Murrell, S.A.F. The effect of triaxial stress systems on the strength of rocks at atmospheric temperatures. Geophys. J.R. Astron. Soc. **10,** 231-281 (1965).

Murrell, S.A.F. The role of deformation, heat and thermal processes in the formation of the lower continental crust. In: The Nature of the Lower Continental Crust, J.B. Dawson et al. (eds.), Oxford:Blackwells, Geol. Soc. Lond. Spec. Publ. No 19, 1986a, pp. 107-117.

Murrell, S.A.F. General report: The measurement of the properties at great depth of rocks and rock masses. In: Rock at great depth. Proc. Int. Symp., Pau, 1990, Vol. III, pp. 1219-1229.

Murrell, S.A.F., Digby, P.J. The theory of brittle fracture initiation under triaxial stress conditions. **I.** Geophys. J.R. Astron. Soc. **19,** 309-334; **II.** ibid, 499-512 (1970)

Murrell, S.A.F., Ismail, I.A.H. The effect of decomposition of hydrous minerals on the mechanical properties of rocks at high pressures and temperatures. Tectonophysics **31,** 207-258(1976a).

Nemat-Nasser, S., Horii, H. Compression induced nonplanar crack extension with application to splitting, exfoliation and rockburst. J. Geophys. Res. **87 B8,** 6805-6821 (1982).

Nishizawa, O. Seismic velocity anisotropy in a m edium containing orientated cracks - transversly isotropic case. J. Phys. Earth **30,** 331-347 (1982).

Nishizawa, O., Onai, K., Kusunose, K. Hypocenter distribution and focal mechanism of AE events during two stress stage creep in Yugawara andesite. Pure Appl. Geophys. **122,** 36-52 (1985).

Nur, A. General report: Seismic rock properties for rock mas descriptions and fluid flow monitoring. In: Rock at great depth. Proc. Int. Symp., Pau, 1990, Vol **III,** pp. 1081-1102.

Nur, A., Simmons, G. The effect of saturation on velocity in low porosity rocks. Earth Planet. Sci. Lett. **7,** 6414-6419 (1969a).

Nur, A., Simmons, G. Stress-induced velocity anisotropy in rock: an experimental study. J.Geophys. Res. **74,** 6667-6674 (1969b).

Obert, L., Duvall, W. Use of subaudible noises for predicting rock bursts. Part **2** U.S. Bur. Min., Rep. Invest. 3654, pp22 (1942).

O'Connell, R.J., Budiansky, B. Seismic velocities in dry and saturated cracked solids. J. Geophys. Res. **79/35,** 5412-5426 (1974).

O'Connell, R.J., Budiansky, B. Viscoelastic properties of fluid saturated cracked solids. J. Geophys. Res. **82,** 5719-5736 (1977).

Ohnaka, M., Mogi, K. Frequency characteristics of acoustic emission in rocks under uniaxial compression and their relation to the fracturing process of failure. J. Geophys. Res. **87,** 3873-3884 (1982).

Pandit, B.I., Savage, J.C. An experimental test of Lomnitz's theory of internal friction in rocks. J. Geophys. Res. **78,** (1973).

Paterson, M.S. Experimental deformation and faulting in Wombeyan marble. Bull. Geol. Soc. Am. **69,** 465-476 (1958).

Paterson, M.S. Experimental Rock Deformation - The Brittle Field, Springer-Verlag, Berlin (1978).

Peselnick, L., Outerbridge, W.F. Internal friction and rigidity modulus of Solenhofen limestone over a wide frequency range. U.S.G.S. Prof. paper no. 400B (1961).

Read, M.D., Meredith, P.G., Murrell, S.A.F. Permeability measurement techniques under hydrostatic and deviatoric stress conditions. In: Rock at great depth. Proc. Int. Symp., Pau, 1990, Vol. **I,** pp. 211-219.

Rist, M.A. The effect of temperature and strain rate on the triaxial deformation and strength of pure polycrystalline ice: An experiemntal study. Ph.D. Thesis, University of London (1989)

Rist, M.A., Sammonds, P.R., Murrell, S.A.F. Strain rate control during deformation of ice: An assessment of the performance of a new servo-controlled triaxial testing system. Cold Regions Science and Technology **19,** pp.189-200 (1991).

Rutter, E.H. The effects of strain-rate changes on the strength and ductility of Solenhofen limestone at low temperatures and confining pressures. Int. J. Rock Mech. Min. Sci. **9,** 183-189 (1972a).

Rutter, E.H. The influence of interstitial water on the rheological behaviour of calcite rocks. Tectonophysics **14**, 13-33 (1972b).

Rutter, E.H., White, S.H. The microstructure and rheology of fault gouges produced experimentally under wet and dry conditions at temperatures up to 400°C. Bull. Mineral. **102**, 101-109 (1979).

Salganik, R.L. Mechanics of bodies with many cracks. Mechs. Solids **8(4)**, 135-143 (1973).

Sammis, C.G., Ashby, M.F. The failure of brittle porous solids under compressive stress states. Acta Metall. **34/3**, 511-526 (1986).

Sammonds, P.R. triaxial deformation experiments on natural sea ice as a function of temperature and strain rate. Ph.D. Thesis, University of London, (1988).

Sammonds, P.R., Murrell, S.A.F., Rist, M.A., Butler, D. The design of a high-pressure low-temperature triaxial deformation cell for ice. Cold Regions Science and Technology **19**, pp.177-188 (1991).

Savage, J.C. Comments on paper by R.B. Gordon and L.A. Davies, "Velocity and attenuation of seismic waves in imperfectly elastic rock". J. Geophys. Res. **74**, 726-728 (1969).

Savage, J.C. Relation of corner frequency to fault dimensions. J. Geophys. Res. **77**, 3788-3795 (1972).

Sayers, C.M. Inversion of ultrasonic wave velocity measurements to obtain the microcrack orientation distribution function in rocks. Ultrasonics **26**, 73-77 (1988).

Sayers, C.M. Stress-induced ultrasonic wave velocity anisotropy in fractured rock. Ultrasonics **26**, 311-317 (1988).

Sayers, C.M. Technical note: Orientation of microcracks formed in rocks during strain relaxation. Int. J. Rock Mech. Min. Sci. & Geomech. **27,** No. 5. pp. 437-439 (1990).

Scholz, C.H. Microfracturing and the anelastic deformation of rock in compression. J. Geophys. Res. **73,** 1417-1432 (1968a).

Scholz, C.H. The mechanics of earthquakes and faulting. Cambridge University Press, Cambridge, pp439 (1990)

Scholz, C.H., Sykes, L.R., Aggerwal, Y.P. Earthquake prediction: a physical basis. Science **181,** 803-810 (1973).

Sears, F.M., Bonner, B.P. Ultrasonic attenuation measurement by spectral ratios utilizing signal processing techniques. Trans. Geosci. Remote Sensing, Vol. GE-**19,** No.2 95-99 (1981).

Serdengecti, S., Boozer, G.D. The effects of strain rate and temperature on the behaviour of rocks subjected to triaxial compression. In: Proc. 4th Symp. Rock Mechanics. Hartman, H.L. (ed.). Penn. State Univ., Bull. Min. Ind. Exp. Sta. No. 76, 1961, pp. 83-97.

Shaw, H.R., Gartner, A.E. On the graphical interpretation of palaeoseismic data. United States geological Survey Open File Report, 86-394 (1986).

Sheriff, R.E. Factors affecting siesmic amplitudes. Geophys. Prosp. **23,** 125-138 (1975).

Silk, M.G. Ultrasonic transducers for nondestructive testing. Adam Hilger Ltd., Bristol (1984).

Simmons, G. Velocity of shear waves in rocks to 10 Kilobars, I. J. Geophys. Res. **69,** 1123-1130 (1964).

Simmons, G., Richter, D. Microcracks in rocks. In: The Physics and Chemistry of Minerals and Rocks. Strens, R.G.J. (ed.). NATO Institute, Newcastle-upon-Tyne, April 1974. London: Wiley 1976, pp. 105-137.

Soga, N., Mizutani, H., Spetzler H., Martin, R.J. The effect of dilatancy on velocity anisotropy in Westerly granite. J. Geophys. Res. **83 B9,** 4451-4456 (1978).

Sondergeld, C.H., Estey, L.H. Acoustic emission study of microfracture during the cyclic loading of Westerly granite. J. Geophys. Res. **86 B4,** 2915-2924 (1981).

Spetzler, H., Anderson, D.L. The effect of temperatureand partial melting on velocity and attenuation in a simple binary system. J. Geophys. Res. **73,** 6051-6060 (1968).

Thill, R.E. Acoustic methods for monitoring failure in rock. In: New Horizons in Rock mechanics. 14th Symp. Rock Mechanics, University Park, Penn., June 1972. Hardy, H.R., Stefanko, R. (eds.). New York: Am. Soc. Civ. Eng. 1973, pp. 649-687.

Thill, R.E, Peng, S.S. Statistical comparison of the pulse and resonance methods for determining elastic moduli. U.S. Bereau of mines. Report of investigations 7831, (1974).

Thill, R.E., Willard, R.I. Correlation of longitudinal velocity variation with rock fabric. J. Geophys. Res. **74,** 4897-4909 (1969).

Toksoz, M.N., Cheng, C.H., and Timur, A. Velocities of seismic waves in porous rocks. Geophys. **41,** 621-645 (1976).

Tullis, T.E., Tullis, J. Experimental rock deformation techniques. In: Mineral and Rock Deformation: Laboratory Studies, geophys. Monogr. Am. Geophys. Un., Washington D.C., pp. 297-324 (1986).

Volarovich, M.P., Budnikov, V.A. Velocities of elastic waves and Vp/Vs ratios in water-saturated rock samples at high pressure. Pageoph. Vol. **117,** 795-805 (1978/79).

Von Karmen, T.H. Festigkeitsversuche unter allseitigem. Druck. Z. Ver. dt. Ing. **55,** 1749-1757 (1911).

Walsh, J.B. The effect of cracks on the compressibility of rock. J. Geophys. Res. **70,** 381-389 (1965).

Walsh, J.B. Seiemic wave attenuation in rock due to friction. J. Geophys. Res. **71,** (1966).

Walsh, J.B. New analysis of attenuation in partially melted rock. J. Geophys. Res. **74,** 4333-2599 (1969).

Walsh, J.B. Effect of pore pressure and confining pressure on fracture permeability. Int. J. Rock Mech. Min. Sci. & Geomech. Abstr. **18,** 429-435 (1981).

Walsh, J.B., Grosenbaugh, M.A. A new model for analyzing the effect of fractures on compressibility. J. Geophys. Res. **84,** 3532-3536 (1979).

Wang, C.-Y., Lin, W. Velocity ratios for rocks with orientated microcracks. Nature (London) **248,** 579-580 (1974).

Warren, N., Trice, R., Stephens, J. Ultrasonic attenuation: Q measuements on 70215, 29: Geochim. Cosmochim. Acta, Supp. **5,** 2927-2938, (1974).

Wawersik, B.R., Brace, W.F. Post-failure behaviour of a granite and a diabase. Rock Mech. **3,** 61-85 (1971).

Wawersik, B.R., Fairhurst, C. A study of brittle rock farcture inlaboratory compression experiments. Int. J. Rock Mech. Min. Sci. **7,** 561-571 (1970).

Winkler, K.W., Plona, T.J. Technique for measuring ultrasonic velocity and attenuation spectra in rocks under pressure. J. Geophys. Res. **87,** pp.10,776-10,780 (1982).

Winkler, K.W., Nur, A. Seismic attenuation: Effects of pore fluids and frictional sliding. Geophys. Vol. **47,** 1-15 (1982).

Winkler, K., Nur, A., Gladwin, M. Friction and seismic attenuation in rocks. Geophys. Res. Lett. **6,** 1-4 (1979).

Xu, S., King, M.S. Attenuation of elastic waves in a cracked solid. Geophys. J. Int. **101,** 169-180 (1990).

Yamamoto, K., Kosuga, M., Hirasawa, T. A theoretical method for determination of effective elastic constants of isotropic composite. Sci. Rep. Tohoku Univ., Ser. 5 (Tohoku Geophys. J.) **28**, 47-67 (1981).

Yanagidani, T., Shoji, E., Nishizawa, O., Kusunose, K., Terada, M. Localisation of dilatancy in Okshima granite under constant uniaxial stress. J. Geophys. Res. **90/8** pp 6840 (1985).

Yukutake, H., Fracturing process of granite inferred from measurements of spatial and temporal variations in velocity during triaxial deformations. J. Geophys. Res. **94**, 15639-15651 (1989).

Zheng, Z., Cook, N.G.W., Doyle, F. A new technique to observe 3D microcracks in rocks. EOS **68**, 1477 (1987).

Zimmerman, R.W., King, M.S. Propagation of acoustic waves through cracked rock. 26th US Symposium on Rock Mechnaics, Rapid City, SD, 739-745 (1985).